Spring 2013

Numerical evaluation of deflector performance in the tailrace of Hells Canyon Dam

Michael Joseph Carbone
University of Iowa

NUMERICAL EVALUATION OF DEFLECTOR PERFORMANCE IN THE TAILRACE OF HELLS CANYON DAM

by

Michael Joseph Carbone

A thesis submitted in partial fulfillment
of the requirements for the Master of
Science degree in Engineering
in the Graduate College of
The University of Iowa

May 2013

Thesis Supervisor: Adjunct Associate Professor Marcela Politano
Associate Professor Pablo Carrica

Graduate College
The University of Iowa
Iowa City, Iowa

CERTIFICATE OF APPROVAL

_____

MASTER'S THESIS

_____

This is to certify that the Master's thesis of

Michael Joseph Carbone

has been approved by the Examining Committee
for the thesis requirement for the Master of Science
degree in Engineering at the May 2013 graduation.

Thesis Committee: _____
Marcela Politano, Thesis Supervisor

_____
Pablo Carrica, Thesis Supervisor

_____
James Buchholz

To my family: John, Mary, Nina, Robert and Meka.

ACKNOWLEDGMENTS

Primarily I would like to thank the Idaho Power Company for sponsoring this numerical study. I would then like to graciously thank my advisor Marcela Politano for her guidance, encouragement and knowledge throughout the entire process of writing this thesis. As well as Pablo Carrica, for encouraging me to take the opportunity to participate in the research opportunities at the University of Iowa. I am indebted to Antonio Arenas and Yuwei Li for their patience, wisdom and otherwise good fortune. Craig Wojcik for his assistance reviewing and revising my writing. I would like to thank Daniel Seabra for his expertise in generating time save data reduction programs.

I would particularly like to thank my family for their encouragement in my pursuit of a higher education; without their love and support I would not have come this far.

ABSTRACT

The purpose of this thesis was to perform a comprehensive evaluation of proposed sluiceway deflectors in Hells Canyon Dam with the use of Computational Fluid Dynamics (CFD). A CFD model developed and validated by Politano et al. (2010) was used to assess the downstream performance of the deflectors. Relative performance was measured by effects of the deflectors on the flow field, Total Dissolved Gas (TDG) production, and probability of mechanical fish injury.

The deflectors evaluated in this model included the deflector with dimensions determined from a physical model as well as three additional deflector geometries that adjusted elevation, length and transition radius based on the physical model deflector. Physical model testing, at a 1:48 scale, of deflectors on Hells Canyon Dam performed by Haug and Weber (2002) provided a baseline deflector for the deflectors modeled in this study. The physical model was built and tested by IIHR-Hydroscience and Engineering.

The performance study that this thesis focuses on was performed at two different tailwater elevations, established with two different total river flow rates of 25 Kcfs and 45 Kcfs. Each deflector was evaluated considering the spillway jet regime, tailrace flow pattern, and total dissolved gas (TDG) production. According to the model, decreasing the deflector length or increasing the transition radius results in more TDG production at all tailwater elevations. At 45 Kcfs, the height of the deflector does not appreciably affect the spillway jet regime or the TDG distribution in the tailrace. However, increasing the deflector elevation at this river flow increases the amount of powerhouse entrainment and induces a recirculation in the western region of the tailrace. The baseline deflector

performed best because it had the smallest impact on the tailrace flow pattern and produced the least TDG.

The performance of the selected deflector was further evaluated for additional river flow rates of 37 Kcfs, 45 Kcfs and a 7Q10 flow condition of 71.5 Kcfs, with the 7Q10 condition being tested with and without the deflector. Although the deflector was able to prevent the spillway flow from creating a large amount of downstream TDG, the 7Q10 flow condition significantly increased the TDG values downstream of the deflector relative to the other tested conditions. With the chosen deflector TDG, values returned to forebay levels after 1 and 3.5 miles for the 37 Kcfs and 45 Kcfs river flow rates, respectively. With the deflector installed the 7Q10 flow condition creates considerable TDG production however the deflectors were able to reduce TDG production by 10% from the test without a deflector installed.

For all evaluated river flows, with the chosen deflector, entrainment from the powerhouse was observed in the simulations; this entrainment was caused by the sluiceway surface jets. As powerhouse flow increases there was an observed decrease in entrainment. This was due to the increase of flow velocity in the streamwise direction, or perpendicular to the direction of entrainment. An important western recirculation that was prominent in the 7Q10 flow condition was also caused by the introduction of deflectors onto the spillways. Reversed flows near the fish trap region and water directed back into the aerated section of the spillway were consequences of this recirculation. The effect causes a 25% percent increase of entrained flow relative to the no deflector 7Q10 flow.

Mechanical injury of fish traveling over the spillway and through the sluiceway was estimated with the use of inert spherical particles and the computed flow field.

Acceleration and strain experienced by the particles was calculated over the length of the spillway region. Numerical results were compared against literature values published by Deng (2005). Including the deflectors in the design increases the probability that fish will be injured. The most extreme cases of fish injury probability were for 37 Kcfs and the 7Q10 Kcfs flow rates. For these cases, injuries experienced by the fish were 10% and 3% for minor and major injuries respectively. With comparison of the 7Q10 flows it appears that the inclusion of the deflector increases the induced minor injury induce from 5% to 10% and the major injury from 1% to 3%.

Fish tailrace residence time was calculated using inert particles introduced to the computed fluid flow field. These particles were tracked for 650 feet past the sluiceway inlets and their time to completion was recorded. Particles were released from the sluiceways as well as the powerhouses for the 37 Kcfs, 45Kcfs and 7Q10 flow conditions. Particles released from the sluiceways generally had an inverse relationship of residence time and flow rate; where an increase in flow rate caused a decrease in residence time for a given powerhouse flow rate. Some amount of powerhouse entrainment increased the residence time of the particles released from the powerhouse draft tubes. These particles follow the entrainment to the deep low velocity region in the stilling basin. As the lateral flow increases some of the particles released from the spillway will join the high speed jets produced by the deflectors and their residence time will be reduced. According to the model, deflectors consistently reduce overall residence time and were therefore not expected to increase fish migration time.

Water surface elevation near the fish trap was measured for the 25 Kcfs, 37 Kcfs, 45 Kcfs and 7Q10 flow conditions. The wave height near the fish trap for the 7Q10

deflector case was predicted to be about one foot above the estimated water surface elevation. According to the model the inclusion of the deflector reduces the wave height.

TABLE OF CONTENTS

LIST OF TABLES

LIST OF FIGURES

CHAPTER I
INTRODUCTION

Hydropower in the United States accounts for nearly 9 percent of all the total electrical supply and in the Pacific Northwest Hydropower is responsible for about two thirds of the power delivered to the grid (EPA, 2012). Hydropower plants are also considered a form of green energy since there is no fossil fuel cost or a greenhouse gas emission associated with their operation. However, even as hydropower has no impact on air quality, it is not without negative environmental effects. Many of those impacts come from the dam structure altering the water level or quality and not the generation of electricity. Some of those impacts include changing the upstream water elevation, temperature of downstream water, changing the migratory paths of fish, as well as altering the gas concentration of the downstream water (EPA, 2012). These changes are not intrinsic to dams, however their intensity is subject to dam location, design and operation.

Many dams in the United States have made efforts to reduce the environmental impacts of their existence and operation according to the regulations enacted by the Environmental Protection Agency (EPA). These efforts include the addition of fish ladders for upstream migrating fish, upgrading to more fish friendly turbines, adjusting the season spill to encourage fish passage downstream as well as installing spillway deflectors to reduce the gasification of downstream flow.

Introduction to Hells Canyon Dam

Hells Canyon is a dam in the Pacific Northwest, specifically located in the Snake River basin. Hells Canyon Dam was constructed in 1967 by the Idaho Power Company (IPC) and located in the path of migrating salmon and steelhead fish. Although the design for the dam included permanent upstream fish passage when the project was first built it did not contain a permanent method for fish passage, nor did the upstream neighboring dams Oxbow and Brownlee. During the construction of each dam a temporary fish collector was installed at the base of the construction to move fish above the construction zone. The three dams were constructed from upstream to downstream, starting with Brownlee, the most upstream, and ending with Hells Canyon, the furthest downstream. The fish trap was moved downstream and rebuilt at the base of each dam just before construction on that dam began. In 1964 a permanent fish trap was built at the base of Hells Canyon Dam. Part of the license to build a dam in Hells Canyon included annually allocating two hundred and fifty thousand dollars to study fish runs and determine how to alleviate loss of fish life due to the operation of the dams (Harrison, 2008).

Hells Canyon Dam consists of a powerhouse, spillway, sluiceway, stilling basin, left bank guide wall, and fish trap; the modeled structure can be seen in Figure 1. The maximum head of the dam is 330 ft, with an installed electrical capacity of 391.5 megawatts generated from three powerhouse units. The three powerhouse units allow a flow of 30 Kcfs when operating at full capacity ("Hells Canyon Dam - Hydroelectric Project Information", 1997).

Flows from the spillways and sluiceways are deposited directly into the stilling basin. Where the stilling basin is located immediately after the sluiceway and spillway

and is in line with the draft tubes of the powerhouse units. The stilling basin is made of poured concrete and does not contain any appurtenances that are sometimes present in stilling basins to dissipate energy. The basin is designed to reduce the velocity of the flow and prevent downstream erosion. The basin is deeper than the river bed by approximately 18ft, at a depth of 1354 ft.

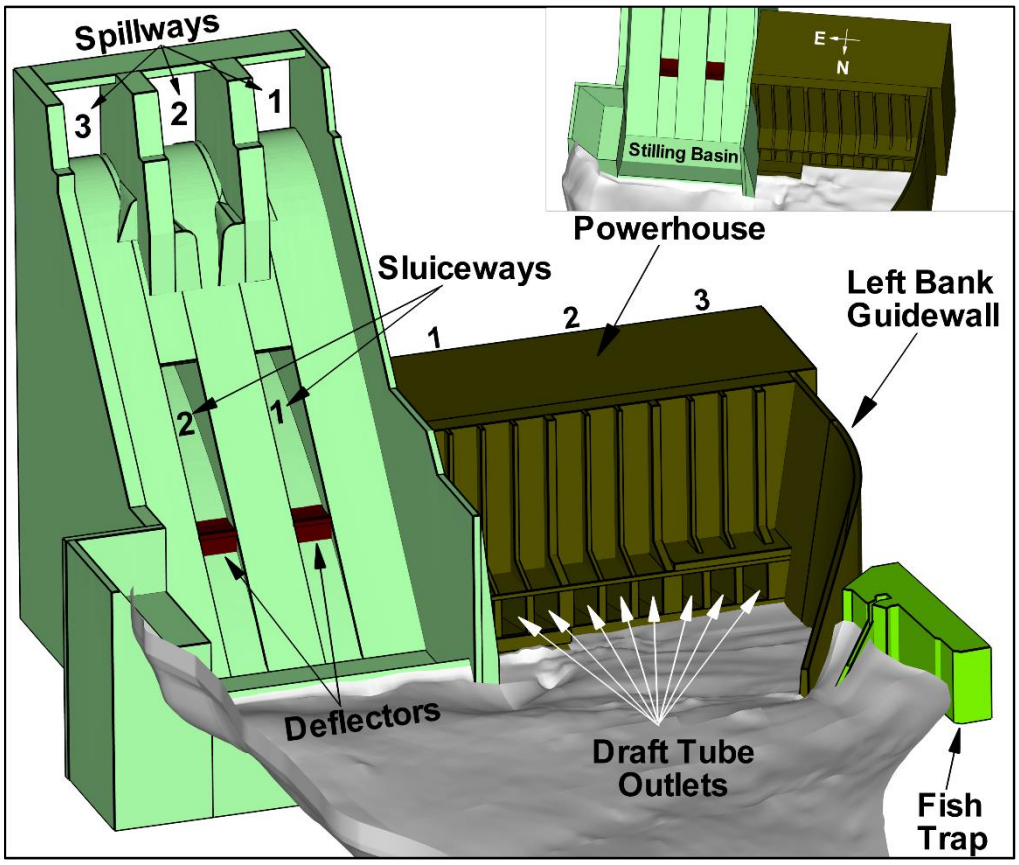

Figure 1. Important structures included in the Hells Canyon Dam model

The powerhouse is to the west and the spillway is to the east. To the west of the powerhouse is a wall known as the left bank guide wall. This wall gradually conducts the powerhouse flow toward the center of the river and returns the river to its original width. Just north of the left bank guide wall exist the current fish trap.

The initial fish trap constructed at Hells Canyon was designed to collect upstream migrating fish to be transported by truck a distance of approximately 39 miles and deposited a mile upstream of the Brownlee Dam. This method was used to transport fish from the beginning of construction in 1956 until 1964. Post 1964 the fish were collected and transported by truck upstream, however instead of depositing them into the river they were introduce to the Oxbow Fish Hatchery (Harrison, 2008). Since 1964 the original fish trap has been modified, it currently consists of an attraction channel 150 ft of fish ladder, a holding area and a truck loading mechanism. Fish from the hatchery are then returned to the area downstream of the Hells Canyon Dam to complete the adult life cycle ("Oxbow Fish Hatchery", 2012).

Thesis Objectives

IPC with concern for the health of fish on the Snake River as well as the relicensing of Hells Canyon Dam has made reducing the Total Dissolved Gas (TDG) downstream of Hells Canyon a recent goal. The installation of sluiceway deflectors was the method selected to reduce downstream TDG and will be tested in this numerical study. The main goals of this thesis were to evaluate the performance of different spillway deflectors using a numerical model considering:

1. Changes in the tailrace flow field due to geometrical variation of the deflector and changing flow rate.
2. TDG generation and transport.
3. Probability of fish mechanical injury due to the installation of deflectors.
4. Fish residence time with the selected deflector.

Installing deflectors onto the face of a spillway or sluiceway will inevitably change the flow in the tailrace, the region immediately downstream of the dam. The extent of those changes must be qualitatively and quantitatively analyzed to determine if the flow changes were acceptable. Jets produced by the installed deflectors can cause back rolls below the jets or large recirculations in the tailrace immediately after the deflectors. Criteria for positive and negative tailrace effects will be discussed in more detail in Chapter II. This study was following two physical model studies of Hells Canyon, performed by Haug and Weber (2002), to determine deflector performance.

TDG production will be calculated using a multiphase flow program, developed by Politano et al. (2009a), and implemented in Fluent's flow solvers. This program will monitor the transport of bubbly flow and determine whether air will be dissolved into water or released from solution.

Determining some probability of fish mechanical injury from the installation of the deflectors was also important while rating the deflector performance. The nature of a deflector is to change the direction of the water flow, in turn causing flow deceleration. Since fish will be at times traveling through this flow it will be necessary to determine if they can withstand the deceleration and the shear forces from the flow through the deflector and jet region.

CHAPTER II
LITERATURE REVIEW

Chapter I covered the structures present in Hells Canyon Dam as well as the importance of reducing the tailrace TDG. This chapter contains a detailed discussion about TDG, past and current modeling methods for downstream TDG, deflector performance, and fish mechanical injury.

Total Dissolved Gas

TDG is a term used to quantify the total dissolved gas relative to the level of dissolved gas present at atmospheric pressure. TDG is generally oxygen, nitrogen and carbon dioxide. The generation of TDG occurs when air is entrained by flow and brought to regions with large hydrostatic pressure (Weitkamp, 2008). Air is dissolved more intensely when it is brought to a deeper region of the tailrace where higher hydrostatic pressures are present, increasing TDG. According to Henry's Law solubility of air into water increases with the increase of pressure, but decreases with an increase in temperature. The pressure at the point of exchange is determined by both atmospheric and hydrostatic pressures. The total pressure exerted on a point of exchange, air water interface, will determine the equilibrium concentration of dissolved gases. Equilibrium concentration is defined as the level where no dissolution or release of gas is occurring. At equilibrium there is a balance of the partial pressure of the gas dissolved in the fluid as well as the gas present at the point of exchange. According to IPC temperature will not change significantly over the length of the reach, therefor it can be assumed to not play a significant role in the variability of solubility. When the maximum solubility of water is greater than the current amount of gas dissolved in the water, and bubbles are present,

more air can be dissolved by the water until equilibrium of the solution is reached (Politano et al., 2010). When TDG present in the water is above 100% of the maximum saturation, at atmospheric pressure, it is considered a supersaturated fluid and can be harmful to fish (Weitkamp, 2008).

When high TDG water flows downstream some degasification occurs naturally through rapids, mass transfer with present bubbles, and through mass transfer at the surface of the flow (Politano et al., 2009a). Fish present in highly saturated flow instinctively match their blood gas content with the gas content of the surrounding water. TDG would not be a problem if the fish that entered the deep, highly saturated, region never left. However, it is the case that the fish, and the highly saturated water, are transported downstream where the hydrostatic pressure is lower. In the shallow downstream region the hydrostatic pressure is less, lowering the equilibrium saturation value, and the highly saturated flow becomes supersaturated flow. As the fish swims to a region of lower pressure with the high TDG water natural degasification occurs within the fish. During this natural degasification bubbles will become present inside of the fish and potentially causing life threatening effects. When degasification occurs inside fish it is known as gas bubble disease (Meyers et al., 2008). Gas bubble disease is typically present in the eyes, gills, and fins of the fish. Figure 2 and Figure 3 show bubbles formed around the eyes and inside the gills, respectively.

Figure 2. Bubbles formed around the fish's eye due to gas bubble disease (Meyers et al., 2008)

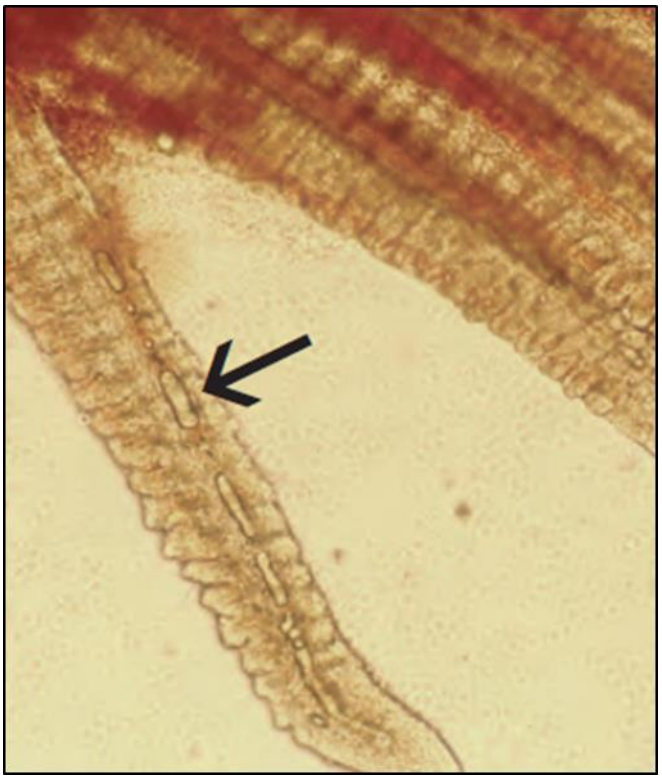

Figure 3. Trapped bubbles located inside the gills of a fish (Meyers et al., 2008)

Total Dissolved Gas Modeling

Roesner and Norton (1971) began the modeling of dissolved gases in tailraces with a coefficient based model that used field data to correlate the coefficients (Urban et al., 2008). The coefficients are based on the effective saturation of the downstream and upstream flow as well as the transfer coefficient and residence time of the bubbles. Transfer coefficients and residence time data were based on field data that would have to be obtained, a major drawback for this early method. Orlins and Gulliver (2000) used a two dimensional simulation with a laterally averaged transport equation with convection, turbulent diffusion, and surface mass transfer. The laterally averaged values were collected by the development of a small scale three dimensional laboratory model and field data. Reduced scaled three dimensional laboratory models are expensive and take time to build and conduct tests, an immense drawback since this must be done for each dam (Urban et al., 2008).

Politano et al. (2009a) used a three dimensional CFD simulation to determine the tailrace flow characteristics and TDG production at Wanapum Dam. The three dimensional simulations are full scale and utilize a two-step approach. The first step determines the free surface shape of the flow using a volume of fluid (VOF) simulation. Although this method is computationally expensive, it is now feasible to utilize with modern computer systems and monetarily less expensive than a physical model. This form of modeling was preferred over the previous methods because it can effectively take into account the full hydrodynamics of the flow.

The second part of the simulation comes after the initial hydrodynamics are determined. Free surface information of the VOF simulation was extracted and used in

this subsequent simulation as the stationary surface of the computational domain, known as the rigid-lid simulation. Air bubbles were then introduced into the domain through the flow inlet boundary conditions. The two phase-air water flow is solved, effectively altering the equations used to determine hydrodynamics. Air is considered soluble in water and obeys Henry's law; the air is considered a single gas with molar averaged properties (Politano et al., 2010). Once bubbles were introduced into the domain the solver is adjusted to take into account changes in density and viscosity due to the air-water mixture. This model coupled the local flow field effects and the bubble characteristics. Meaning when the local pressure increases the bubbles size then decreases following the rules laid out by the Ideal Gas Law. Movement of the bubbles for this model are dependent on drag and turbulent dispersion forces, where lift and virtual mass are negligible due to their small magnitude. The solution of air into water was determined with the use of Henry's Law that describes the total solubility of a liquid at a given pressure and temperature as well as the Henry's constant (Politano et al., 2009a).

Spillway Deflector Performance

Bubbly flow can be deterred from entering the deep region of a spillway with the use of a spillway deflector. Spillway deflectors operate changing the flow direction. The objective of a spillway deflector was to create a surface jet. However, deflectors are rated for different flow rates and can create either surface jumps, surface jets, vented surface jets, or plunging flow (Dierking and Weber, 2001). Pictures of these jet types for a two dimensional model of Hells Canyon was provided by the previously created physical model. Figure 4 is showing a surface jump where the tailwater elevation is above the height of the jet, effectively submerging the jet. Figure 5 shows a surface jet where the

flow moves across the surface of the flow and tends to be angled slightly above horizontal, which is the most desirable flow regime for reducing downstream TDG (Dierking and Weber, 2001). Figure 6 displays the vented surface jet. This flow regime contains a pocket of air below the deflector; also a prominent vertical recirculation is observed in the stilling basin. Figure 7 shows a plunging flow which is the least desirable flow when attempting to alleviate TDG production in the tailrace. When comparing the jet types, it is important to notice that both the tailrace water elevation and the height of the jet, which depends on the flow rate, play a crucial role in the type of jet produced. The jets displayed are from a more idealized two dimensional modeling approach, which does not incorporate powerhouse entrainment effects on the shape of the jet.

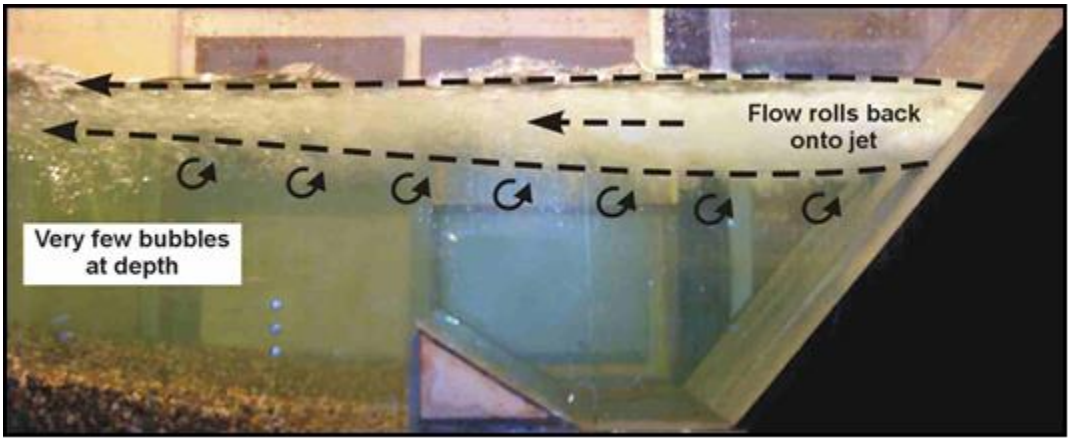

Figure 4. Surface jump flow regime (Dierking and Weber, 2001)

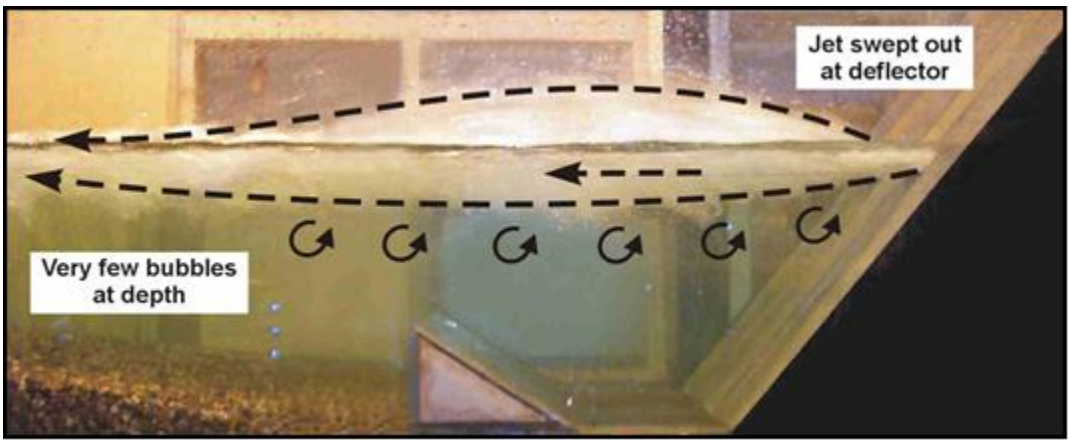

Figure 5. Surface jet flow regime (Dierking and Weber, 2001)

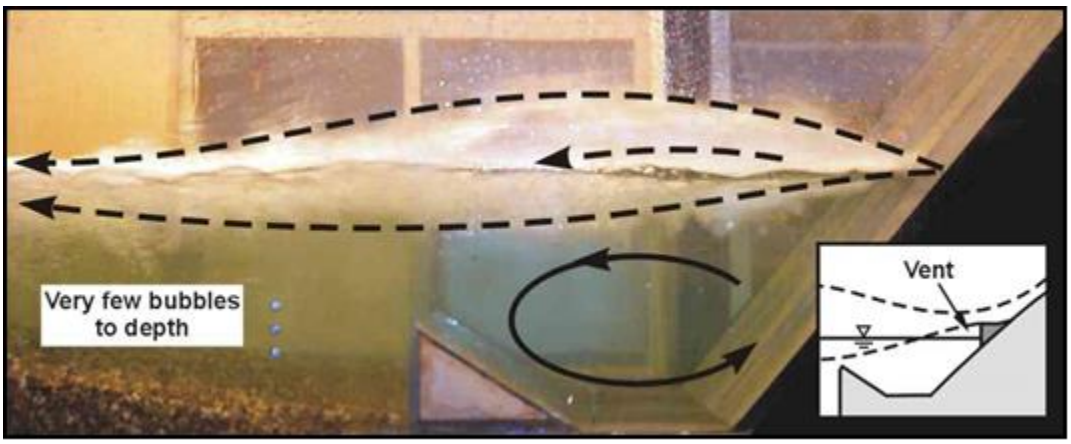

Figure 6. Vented surface jet flow regime (Dierking and Weber, 2001)

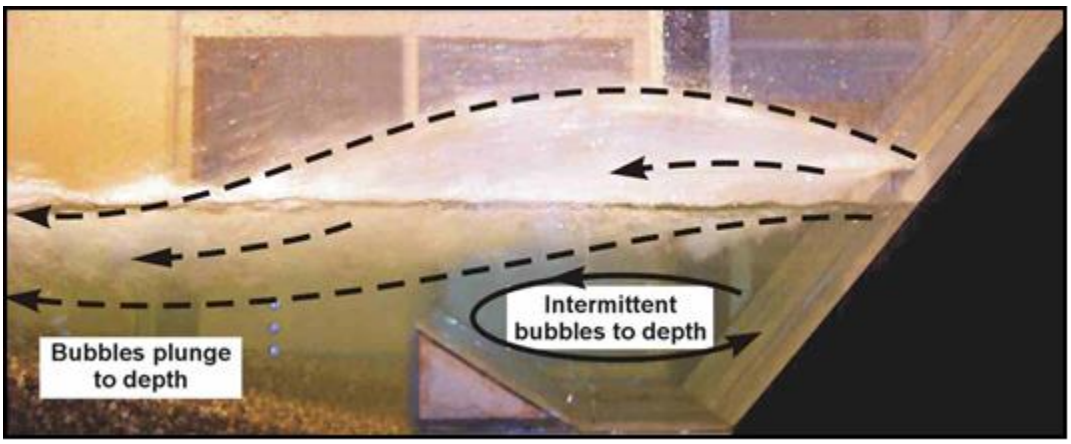

Figure 7. Plunging flow regime (Dierking and Weber, 2001)

Desirable flow characteristics were defined by IPC. They consist of making minimal changes to the natural state of the river, in other words minimizing recirculation

regions, reducing the entrainment of powerhouse flow into the region where bubbles are present, as well as minimizing wave generation near the installed fish trap. Hells Canyon's fish trap was designed to operate with the local flow tending downstream such that upstream migrating fish would head toward the inlet of the trap. If the deflector changes the flow pattern near the fish trap it may alter the efficiency of the fish trap.

Fish Mechanical Injury

Deng et al. (2005) exposed juvenile salmonids to a laboratory-generated shear environment. Curves of fish injury probabilities as a function of flow acceleration were determined from qualitative results. For an acceleration of approximately 300 ft/s^2 the probability of injury is below 0.05. At about 1500 ft/s^2 the probabilities of fish suffering minor and major injuries were 0.50 and 0.18, respectively. Life-threatening injuries were almost certainly caused by an acceleration above 4200 ft/s^2. Foust et al. (2010) reports that values of strain rate above 360 s^{-1} were harmful to fish. According to the authors, acceleration was the strongest predictive variable to correlate eye, operculum injuries and overall injury. Acceleration was proposed as a link between laboratory, field, and numerical studies of fish injury. Neitzel et al. (2000) reported that exposures to shear strain rates above 850 s^{-1} would be harmful to juvenile fish. Later, Foust et al. (2010) found that values of strain rate above 360 s^{-1} can be harmful to fish. Neitzel et al. (2000) reported that injury or mortality was unlikely to occur at strain rates less than about 500 s^{-1}, and Neitzel et al. (2004) reported that major injuries were not observed at or below a strain rate of 517 s^{-1}. Strain rates of this magnitude are generally experienced by fish as they pass through turbines.

CHAPTER III
STUDY AREA

Hells Canyon Dam is located in a deep canyon at river mile (RM) 247.7 of Idaho's Snake River. The total study area extends to 7 miles downstream of the dam; Figure 8 shows a contour of the elevation information provided by the Idaho Power Company imposed onto a map of Hells Canyon's tailrace. The VOF simulations extend to a maximum of approximately 4500 ft past the spillway inlets. After that distance the solution was considered steady open channel flow, where the slope of the river bed and the slope of the water elevation were matched and the height of the flow does not rapidly change. This being said there was no need to continue the computationally expensive VOF simulation far downstream of the dam. A multiphase rigid-lid TDG modeling was implemented the entire distance of the VOF model until bubbles were no longer present in the system. A single phase TDG model was run for the remainder of the reach to determine the location where the TDG levels matched that of the dam's forebay. At this location the TDG generation effects of the dam are considered ended.

Coordinates for the Idaho Power Company provided tailrace bathymetry were adjusted from the established northing and easting units to a normalized system to allow for tighter tolerances. The following conversion was used to adjust the coordinate system $(X_m, Y_m) = \left(X_{IPC} - 1.33141(10^6), Y_{IPC} - 1.51213(10^6)\right)$. A $-54°$ rotation about a vertical axis located at $(0.55472, 3.76919)$ was performed to align the streamwise direction with the model's X-axis, this was done after the coordinate translation.

Hells Canyon Dam consists of 4 major parts: 3 spillway bays, 2 sluiceways bays, 3 powerhouse units each including 3 draft tubes, and downstream fish trap. These important parts of the model are shown in Figure 1. Noting the location of the deflectors attached to the face of the spillway.

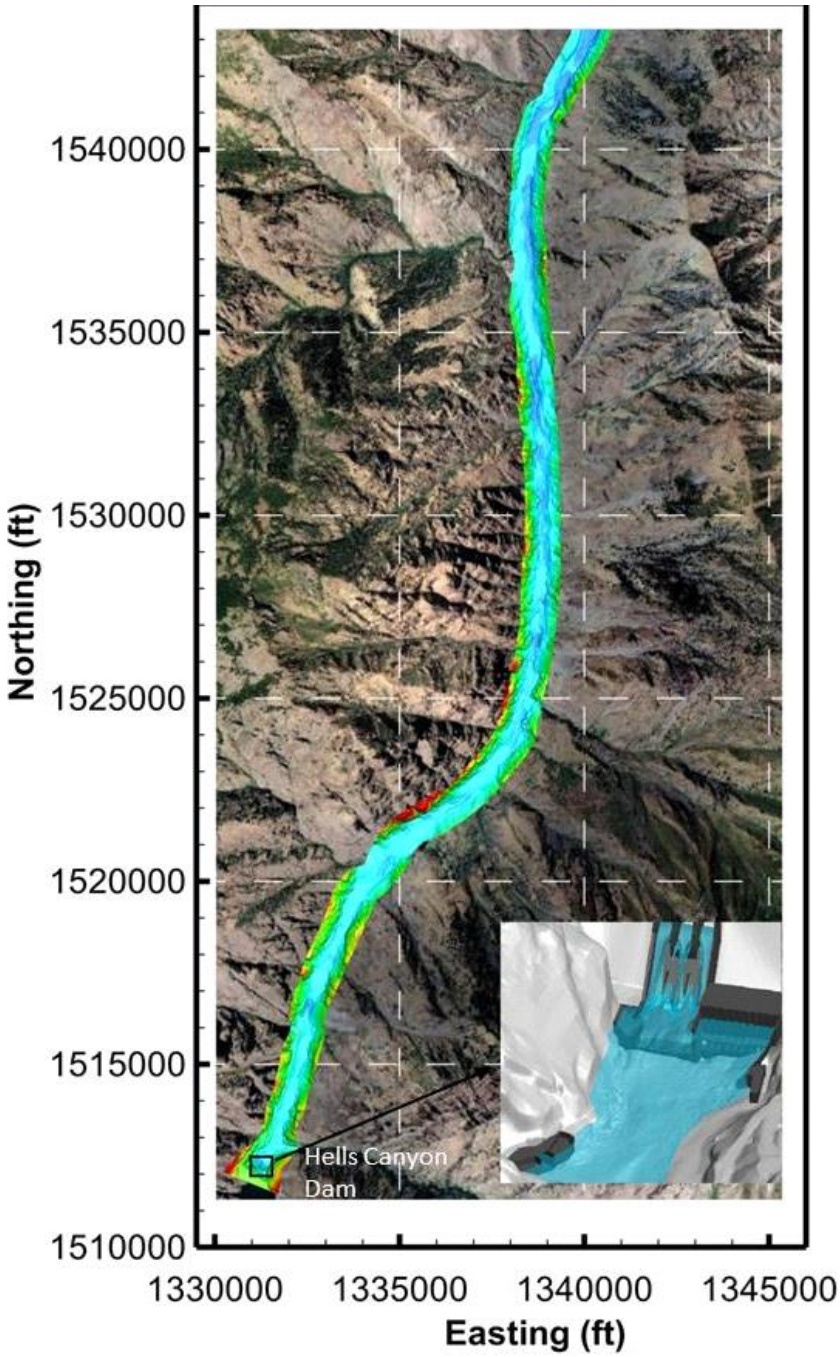

Figure 8. Study area for the tailrace model of Hells Canyon Dam

Geometric changes between the base deflector case and the three other modeled deflectors are shown in Figure 9. It should be observed that the physical changes between the different deflectors were not large suggesting that the changes in the flow pattern, although significant, may not be extreme.

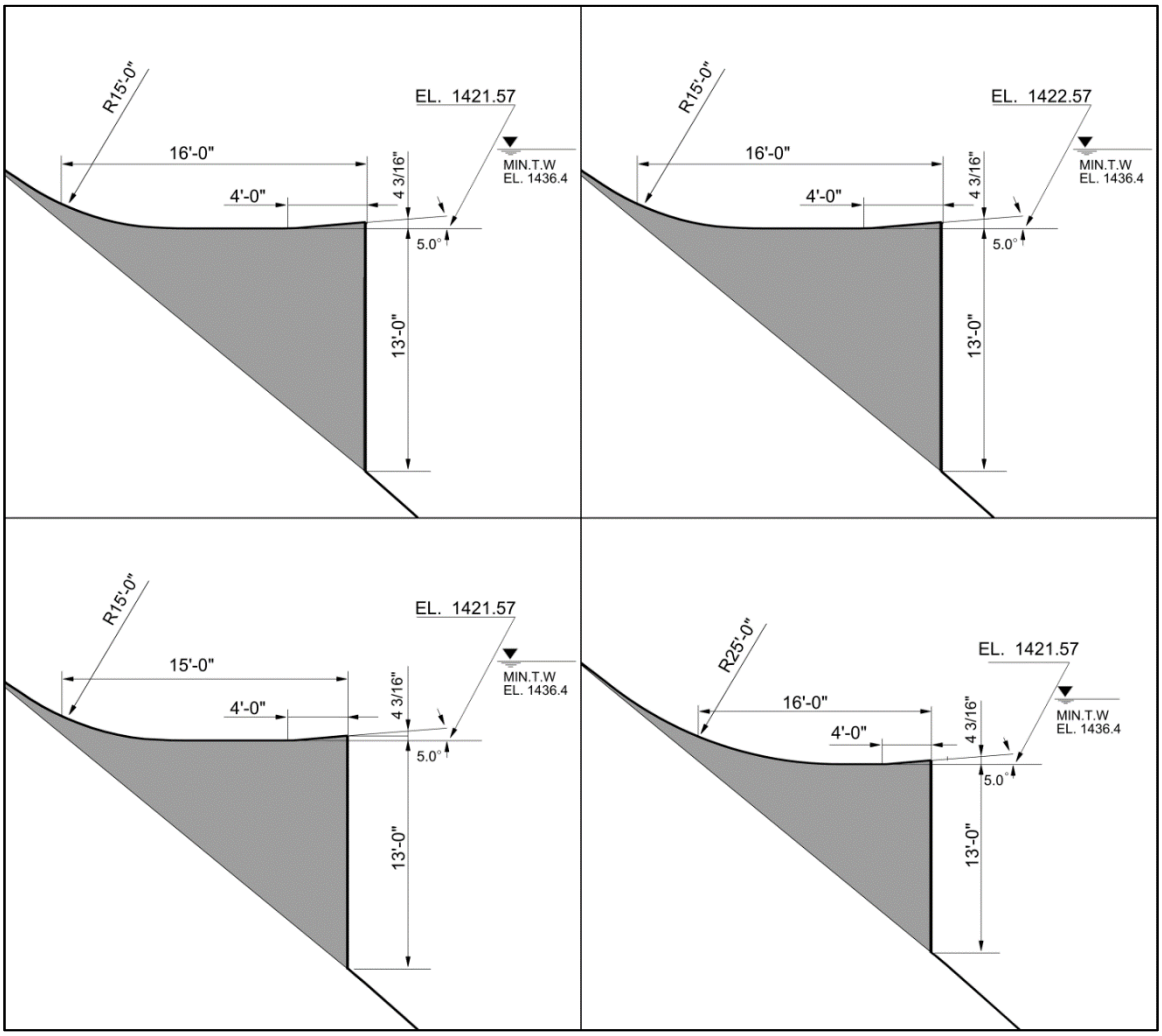

Figure 9. Dimensions of the four simulated deflectors

CHAPTER IV
METHODOLOGY

Model Overview

Fluid flow simulations were run using commercially available Ansys Fluent together with programs developed at IIHR-Hydroscience and Engineering. Fluent uses the Reynolds-averaged Navier-Stokes (RANS) equations to solve the flow field. The equations are based on the cell centered finite volume scheme. The three models included in this study were: VOF model, rigid-lid Eulerian model, and a Lagrangian particle tracking model. To complete the performance analysis of the deflectors, the models were run in a distinct order. First, the multiphase VOF was run to determine the shape of the free surface. Then the rigid-lid model was run using the free surface shape determined from the VOF simulation. Finally, the Lagrangian model was used in the established rigid-lid flow to determine the paths and experiences of inert particles. This was done for the deflectors shown in Figure 9, with the flow rates of 25 Kcfs and 45 Kcfs.

The VOF model required a small computational time step, approximately 0.004 seconds, and three weeks of computational time to achieve a steady-state. Each simulation was solved with thirty two cores, in parallel, on the University of Iowa Helium Cluster. For this reason, the simulation was limited to 1200 ft downstream of the dam for the optimization cases. When the flow of water out of the computational domain remained constant and matched the flow into the domain, it was determined the simulation had reached steady-state. Computational fluctuations were seen during the beginning of a simulation, diminishing as the computation progressed. Those fluctuations propagate into and out of the computation domain through the river outlet as well as around the domain by reflecting off the walls. Once the fluctuations were diminished and

the mass flow rate out of the domain matches the mass flow rate into the domain the solution was considered converged. After convergence was achieved in the VOF model the free surface, defined as an isosurface with a gas volume fraction of 0.5, was extracted. This was used as the top of the computational domain in the rigid-lid model.

The rigid-lid model, the second simulation, extended 7 miles downstream of the dam. The mixture model was used for at minimum the length of each respective VOF simulation grid. If the bubbles were present exiting the domain of the rigid-lid model it was extended until less than 0.33% of bubbles were not present at the outflow of the computational domain. The mixture model included the dissolution of air into water and the degasification of air out of solution with water. A single phase model transporting the TDG scalar represented the flow for the remained of the 7 miles, only including the mass transfer of air at the free surface.

In Fluent, the two phase mixture model was chosen to simulate the flow and transport of bubbles within the flow. The mixture model solves the continuity, Equation 1; momentum, Equation 2; and energy equations for the mixture (Fluent, 2001a). The energy equation is not used in this simulation since no heat transfer will be considered. The model also solves the volume fraction equation and the relative velocities of the phases. The relative velocities of the phases are solved within Fluent as algebraic equations using the concept of slip velocities (Fluent, 2001a). However, the mixture model was run with a supplementary code written by Politano et al. (2009a) that changed the method of calculating relative velocity of the gas phase, including the size of the bubbles, in determining the velocity of the gas phase. Equations that govern the mixture

model are listed below, where the subscripts g, l, and m denote gas, liquid, and mixture, respectively:

$$\frac{\delta \rho_m}{\delta t} + \nabla \cdot [\rho_m \vec{u}_m] = 0 \tag{1}$$

$$\frac{\delta}{\delta t}(\rho_m \vec{\mathrm{u}}_m) + \nabla \cdot (\rho_m \vec{\mathrm{u}}_m \vec{\mathrm{u}}_m) = -\nabla \mathrm{P} + \nabla \cdot (\sigma_m^{Re} + \tau_m) + \rho_m \vec{g} - \nabla \cdot \left(\sum_{k=g,l} \alpha_k \rho_k \vec{u}_k \vec{u}_{dr,k} \right) \tag{2}$$

where P is the total pressure, $\vec{\mathrm{g}}$ is the gravitational acceleration, σ_m^{Re} is the turbulent shear stress and $\tau_m = \rho_m v_m (\nabla \vec{u}_m + \nabla \vec{u}_m^T)$ is the molecular shear stress. ρ_m, μ_m, and $\vec{\mathrm{u}}_m$ are the mixture density, viscosity and mass-averaged velocity defined as:

$$\rho_m = \sum_{k=g,l} \alpha_k \rho_k \tag{3}$$

$$\mu_m = \sum_{k=g,l} \alpha_k \mu_g \tag{4}$$

$$\vec{\mathrm{u}}_m = \frac{1}{\rho_m} \sum_{k=g,l} \alpha_k \rho_k \vec{\mathrm{u}}_k \tag{5}$$

where α_g is the gas volume fraction and $\vec{\mathrm{u}}_{dr,k}$ is the drift velocity defined as the velocity of phase k relative to the mixture velocity, $\vec{\mathrm{u}}_{dr,k} = \vec{u}_k - \vec{u}_m$.

The below equation is used to ensure momentum conservation (Antal et al., 1991; Lopez de Bertodano et al., 1994):

$$0 = -\alpha_g \nabla P + \alpha_g \rho_g \vec{g} + \vec{M}_g \tag{6}$$

the above equation considers inertia and viscous shear stresses are negligible compared to pressure, body forces, and interfacial forces (Politano et al., 2009a). The momentum of

the gas phase is calculated with the inclusion of the drag and turbulent dispersion forces. Interfacial momentum is determined by the solution of the following equation:

$$\vec{M}_g = \vec{M}_g^D + \vec{M}_g^{TD} \tag{7}$$

where $\vec{M}_g^D$ and $\vec{M}_g^{TD}$ are the drag and turbulent dispersion terms, respectively. The turbulent dispersion term is modeled as (Carrica et al., 1999). $\vec{M}_g^D$ and $\vec{M}_g^{TD}$ are defined below:

$$\vec{M}_g^D = -\frac{3}{8}\rho_m \alpha_g \frac{C^D}{R}\vec{u}_r|\vec{u}_r| \tag{8}$$

$$\vec{M}_g^{TD} = -\frac{3}{8}\frac{\nu^t}{Sc_b}\rho_m \frac{C^D}{R}|\vec{u}_r|\nabla\alpha_g \tag{9}$$

where $\vec{u}_r$ is the relative velocity of the gas phase respect to the liquid phase, R is the bubble radius, Sc_b is the bubble Schmidt number and C^D is the drag defined below for different bubble radii (Lane et al., 2005):

$$C^D = \begin{cases} \dfrac{24}{\mathrm{Re}_b} & if\ R < 0.0002 \\ \dfrac{24\left(1+0.15\,\mathrm{Re}_b^{0.687}\right)}{\mathrm{Re}_b} & if\ 0.0002 < R < 0.00222 \\ 0.56 & if\ R > 0.00222 \end{cases} \tag{10}$$

where $\mathrm{Re}_b = 2\rho_l|\vec{u}_r|R/\mu_l$ defines the bubble Reynolds number.

The mixture model enables the interaction between the two phases; phase interaction generates a more accurate prediction of the tailrace velocities. The mixture

model considers each cell of the computational mesh as a volume occupied by some percentage of air and water, called gas volume fraction. Different viscosities, μ_m, and densities, ρ_m, are attributed to the cells with different percentages of air and water. Gas volume fraction and bubble number density are computed throughout the domain. Bubble number density is transported by the following equation:

$$\frac{\partial N}{\partial t} + \nabla \cdot \left[\vec{u}_g \, N \right] = 0 \tag{11}$$

where Equation 11 is a derivation of the Boltzmann transport equation with N describing the bubble number density. With the bubble number density and the gas volume fraction the bubble radius, R, can be determined:

$$\frac{\delta}{\delta t}(\alpha_g \rho_g) + \nabla \cdot (\alpha_g \rho_g U_m) = -\nabla \cdot (\alpha_g \rho_g \vec{u}_{dr,g}) - S \tag{12}$$

$$R = \left(\frac{3\alpha_g}{4\pi N} \right)^{\frac{1}{3}} \tag{13}$$

where Equation 12 shows the gas volume fraction and how it is transported by the mixture model. The code generated by Politano (2009a) adds a source term to the gas phase continuity equation (Drew and Passman, 1998):

$$\frac{\delta}{\delta t}(\alpha_g \rho_g) + \nabla \cdot (\alpha_g \rho_g U_g) = -S \tag{14}$$

where U_g is the velocity of the gas phase and $-S$ is a gas mass source. The gas mass source describes the TDG in this model. With the source term defined as:

$$S = 4\pi N R^2 k_l \left(\frac{P + \sigma/R}{He} - C \right) \tag{15}$$

where σ is the interfacial tension, He is Henry's constant and C is the TDG concentration. TDG concentration is calculated with a two-phase transport equation described in Politano et al. (2007):

$$\frac{\partial \alpha_l C}{\partial t} + \nabla \cdot (\vec{u}_l \alpha_l C) = \nabla \cdot \left(\left(\nu_m + \frac{\nu_t}{Sc_C} \right) \alpha_l \nabla C \right) + S \tag{16}$$

where ν_m and ν_t are the molecular and turbulent kinematic viscosity, respectively. Sc_c is the Schmidt number, a standard value of 0.7 was used in the studies (Politano et al., 2010). Equations written into this model also include the production and suppression of turbulence by the bubbles. All of the previously listed factors consequently effect the overall flow field giving more appropriate and realistic values of tailrace velocity and TDG.

Proper tailrace velocities were important in accurately determining the path of the bubbly flow; where TDG can only be produced where bubbles are present. User Defined Functions (UDFs) were implemented in Fluent to create this specific two phase flow model and subsequent boundary conditions. The distribution of TDG as well as the bubble number density were calculated using scalar transport equations defined in Fluent as User Defined Scalars (UDSs), equations 11 and 16 respectively. For the far downstream region, defined as the region were 99.67% of the bubbles have left the computational domain, a single phase model was used. A gas volume fraction value of 10^{-4} constrained the end of the multi-phase model. In this region TDG creation by bubble dissolution can be ignored, since there are almost no bubbles remaining. However, the free surface will allow degasification with the constant $k_l = 0.001\ m/s$ as

previously used in the mixture model. Natural mixing of secondary flows throughout the winding reach will change the TDG distribution.

Trajectories of neutrally buoyant spherical particles released from the sluiceway gates, into the VOF solution, were calculated using a Lagrangian model. The model integrated the forces on the particles determined from the surrounding flow and the specifications of the particles. Fluent integrates the below equation for each Cartesian coordinate:

$$\frac{\delta u_p}{\delta t} = F_D(u_m - u_p) + \frac{g_x(\rho_p - \rho_m)}{\rho_p} \tag{17}$$

where u_p is the velocity of the particle, ρ_p is the density of the particle, F_D is the drag force experience by the particle and g_x is the gravitational force in a given Cartesian direction (Fluent, 2009b). Since the particle is neutrally buoyant, the second term on the right side of Equation 17 is zero, i.e. the effect of gravity is removed. F_D is defined below:

$$F_D = \frac{18\mu_m}{d_p^2 \rho_p} \frac{C_D Re}{24} \tag{18}$$

where the Reynolds number is $Re = \rho d_p |u_p - u_m| / \mu_m$, d_p is the diameter of the particle, and μ_m is the viscosity of the mixture. C_D is the drag coefficient determined by:

$$C_D = a_1 + \frac{a_2}{Re} + \frac{a_3}{Re^2} \tag{19}$$

with a_1, a_2, and a_3 defined as constants (Fluent, 2001b).

This model is used to extract accelerations and strain rates experienced by the particles as they travel through the flow. Information was extracted to estimate experiences of a fish traveling down the spillway face and evaluate the mechanical injury

caused to the fish. Particle trajectories were determined by using the converged velocity flow field from the VOF model. Injury probability was determined with the strain rate extracted from Fluent as well as the flow acceleration interpolated onto the particle locations. The flow acceleration was extracted from Fluent and the data field was brought into Tecplot, along with the particle tracks. Tecplot's linear interpolation tool was used to impose the flow acceleration data onto the particles. The files were then exported to an ASCII point formatted file. Finally, a java program used a moving average over one second to reduce numerical outliers from the data. The java program also determined if the particles were within cells with a gas volume fraction of 0.113. This value was determined from a trial and error approach, and is the minimum gas volume fraction that does not affect the probability of injury. Meaning decreasing the gas volume fraction to 0.0 from 0.113 would not change the resulting probability of mechanical injury. The program used the statistical curves from Chapter VI, Fish Injury, to create an output file with the fish injury statistics.

Tecplot 360 will be used to post process most of Fluent's CFD data. However, MATLAB, Microsoft Excel, and a Java program written by Daniel Seabra are also used during the data reduction process.

Numerical Method and Initial Conditions

Continuity throughout the computational cells was enforced using the mainstream Semi-Implicit Method for Pressure-Linked (SIMPLE) algorithm. Pressure at the cell faces was solved for using a body force weighted scheme. Momentum and turbulent effects were solved using the first-order upwind scheme.

The solver allowed time-steps between 0.002 and 0.004 seconds, for VOF simulations. Larger flow rate, higher velocity flow, required a smaller time-step. rigid-lid simulations used a larger time-step ranging between 0.5 and 1 seconds. Time step values were selected to achieve two internal iterations within each time-step to converge all variables to a L_2 norm of the error less than 10^{-3}. The L_2 norm is defined below (NPARC, 2002):

$$L_2 = \sqrt{\frac{\sum_{i=1}^{N}\sum_{m=1}^{M}(\delta Q_{i,m})^2}{M * N}} \tag{20}$$

where Q is the equations in use, M is the number of elements in Q, and N is the total number of grid points. The L_2 represents the change in the solution over an iteration averaged over all the grid points and equations.

Initial conditions for the VOF simulation included a constant water surface height across the domain and zero velocities and turbulent values. The converged solution from a model with a similar flow rate could be used as the initial condition for a VOF that had not been run. Velocity and turbulence data were interpolated into an unsolved computational domain acting as initial conditions.

The mixture model was run in three steps to avoid the divergence of the code. First, the steady-state solution of the flow field was solved until convergence. Bubbles were then introduced to the flow through the spillway boundary condition. Finally, the TDG production equation was included once the bubbly flow has covered a significant portion of the computational domain.

Simulation Conditions

Flow rates of 25 Kcfs and 45 Kcfs were used to evaluate the four different deflector geometries. Table 1 contains information regarding the deflector geometry, dam operations, river flow rate, and tailwater elevation used in each simulation. Odd numbered simulations SI, SIII, SV and SVII were run with a river flow rate of 25 Kcfs. Even numbered simulations SII, SIV, SVI and SVIII were run with a river flow rate of 45 Kcfs. In both sets of simulations, the flow rate of water through the sluiceways was a constant 7.5 Kcfs. No flow was included discharging from the spillway gates in these simulations.

Simulations SI and SII had a deflector that was designed during the IIHR Hydroscience and Engineering 1:48 laboratory scale model testing of Hells Canyon Dam spillway (Dierking and Weber, 2002), which will be referred to as the baseline deflector. Simulations SIII and SIV have a spillway deflector that was raised 1 ft from the baseline deflector. Simulations SV and SVI have a deflector that was 1 ft shorter in length than the baseline deflector. Finally, simulations SVII and SVIII increase the radius of curvature from the spillway face to the deflector surface; the radius increased from 15 ft to 25 ft.

Table 1. Important deflector geometries and related simulation conditions

	Deflector Optimization								
	SI	SII	SIII	SIV	SV_1	SV_3	SVI	SVII	SVIII
Forebay Elevation (ft)	1640.4	1640.4	1640.4	1640.4	1640.4	1640.4	1640.4	1640.4	1640.4
Tailwater Elevation (ft)	1430.5	1436.4	1430.5	1436.4	1430.5	1430.5	1436.4	1430.5	1436.4
River flow (kcfs)	25	45	25	45	25	25	45	25	45
Powerhouse Discharge (kcfs)									
Unit #1	0	10	0	10	10	0	10	0	10
Unit #2	0	10	0	10	0	0	10	0	10
Unit #3	10	10	10	10	0	10	10	10	10
	Sluice Structure								
Deflector Elevation (ft)	1421.6	1421.6	**1422.6**	**1422.6**	1421.6	1421.6	1421.6	1421.6	1421.6
Deflector Transition Radius (ft)	15	15	15	15	15	15	15	**25**	**25**
Deflector Length (ft)	16	16	16	16	**15**	**15**	**15**	16	16

Hells Canyon Dam has a maximum powerhouse flow rate of 30 Kcfs. For simulations with a river flow rate of 45 Kcfs, the powerhouse was operating at maximum capacity. However, at simulations with 25 Kcfs only one powerhouse unit was operating with a flow of 10 Kcfs. The flow field effects of the most east, unit number 1, and west, unit number 3, powerhouses were evaluated, refer to Figure 1. These simulations were evaluated using the deflector from SV. Where simulation SV_1 denotes the simulation with powerhouse 1 and SV_3 denotes the simulation operating with powerhouse number 3. It was observed that overall powerhouse entrainment and western recirculation was greater when operating with powerhouse number 3 and to make more conservative calculations powerhouse 3 was used for all other 25 Kcfs simulations. Detailed results of these simulations are covered in chapter 5.

Assumed TDG levels at the forebay, or TDG levels at the sluiceway inlet condition, are 1.15, or 115%, based on Forebay TDG criterion issued by the Washington and Oregon State Departments of Ecology (Washington State Department of Ecology and State of Oregon Department of Environmental Quality, 2009). This criteria was used

from the Wells Dam evaluation for TDG standards compliance (Politano et al., 2009b, Politano et al., 2011, Politano et al., 2012).

After the 9 optimization simulations reached convergence, an overall most effective deflector geometry was chosen. This deflector geometry was then evaluated for flow conditions of 37 Kcfs, 45 Kcfs and 71.5 Kcfs. These flow rates were selected by IPC as supplemental flow conditions. Table 2 describes the conditions for these supplemental simulations. The 71.5 Kcfs flow rate was chosen because it was the 7Q10 flow rate, or the largest flow rate that is expected to occur for 7 consecutive days every ten years judged by a statistical trend.

An additional simulation without a deflector was performed for the 7Q10 flow condition. This simulation uses the spillway gates following the recommendations of the reduced-scale model study of using spillway gates for high discharges when energy dissipation was important (Haug and Weber, 2002).

Table 2. Conditions for chosen deflector performance evaluation

	Performance Simulations			
	37kcfs	45kcfs	7Q10-D	7Q10-ND
Forebay Elevation (ft)	1640.4	1640.4	1640.4	1640.4
Tailwater Elevation (ft)	1433.9	1436.4	1441.6	1441.6
Sluiceway Discharge per bay (kcfs)	3.5	7.5	20.75	0
Spillway Discharge per bay (kcfs)	0	0	0	13.84
River flow (kcfs)	37	45	71.5	71.5
Powerhouse Discharge (kcfs)				
Unit #1	10	10	10	10
Unit #2	10	10	10	10
Unit #3	10	10	10	10
	Sluice Structure			
Deflector Elevation (ft)	1421.57	1421.57	1421.57	1421.57
Deflector Transition Radius (ft)	15	15	15	15
Deflector Length (ft)	16	16	16	16

Grid Generation

Computational grids were generated using Gridgen V15 in combination ANSYS ICEM. Most of the computational volumes were generated using Gridgen, however, ICEM was used to create a small part of the non-orthogonal unstructured mesh. At maximum four small volumes were non-orthogonal hexahedral mesh, most of the volumes generated were near orthogonal hexahedral blocks, Figure 10. Although, when the grid must respect the walls and bathymetry the nearby blocks will not be orthogonal. For the VOF model a grid refinement was included around the expected free surface elevation in an attempt to resolve the free surface shape and reduce numerical diffusion. Above the estimated free surface elevation, a block was included for air accommodation. At the bottom of each spillway face, in the stilling basin, ICEM was used to generate a quad unstructured surface mesh that was swept into a semi-structured volume mesh and merged with the original Gridgen volumes, Figure 11.

Each VOF grid contained approximately 2.0 million computational nodes. Figure 10 shows an overview of the mesh generated for the VOF simulations near the stilling basin, powerhouse and for each of the deflectors chosen to be tested. Near the sluiceway deflector the grid had a y-plus value of approximately 55000. This value of y-plus does not allow the boundary layer to be resolved. Fluent requires a y-plus of 1 to properly resolve the boundary layer. Fluent is also capable of using wall functions, that estimate the boundary layer effects, with a required y-plus between 30 and 300 (Fluent, 2009). However, not resolving the boundary layer on the sluiceway face does not preclude the

generation of a proper free surface shape; the flow in the sluiceway can be approximated as inviscid due to the high Reynolds number. As it will be shown later in this thesis, the grid density in the sluiceway is not sufficient to properly solve the flow on the spillway face and in turn does not allow the convergence of the particle acceleration data.

The number of computational nodes for the mixture model varied from 1.0 million to 2.7 million nodes. This variation was based on how far downstream the bubbles entrained from the spillway travel. For low flow rate simulations, 25 and 37 Kcfs, the computational domain extended to about 900 ft past the dam. The 45 Kcfs simulation extended to 1200 ft past the dam. Finally, the 7Q10 flow which extended to 4500 ft past the dam structure. Figure 11 shows the details on a slice through the sluiceway deflector, the unstructured mesh generated in ICEM and the grid at the calculated free surface.

The model that extends the rest of the 7 miles downstream of the dam contains near 2 million computational nodes. Meshes of the inlet boundary condition, river mile 246.5, river mile 241.6, and the exit boundary condition are shown in Figure 12 colored by elevation. The surface of this model was not extracted from any VOF model, but provided by IPC from a simulation using the MIKE11 software package.

Typical grid sizes for all of the simulations in the longitudinal, lateral, and vertical directions are shown in Table 3.

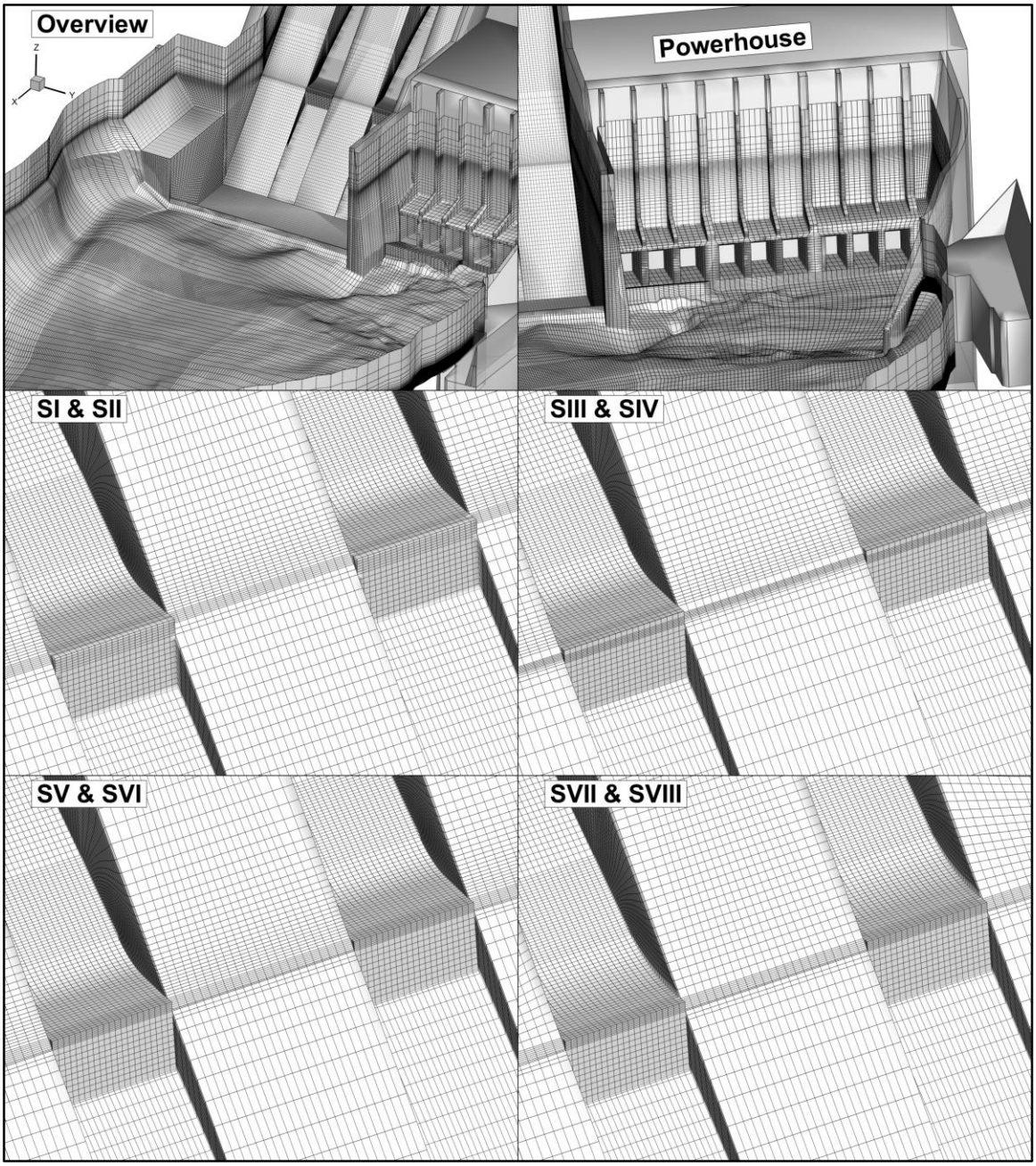

Figure 10. VOF grid overview for the tailrace, top. Mesh details near the deflector, middle and bottom

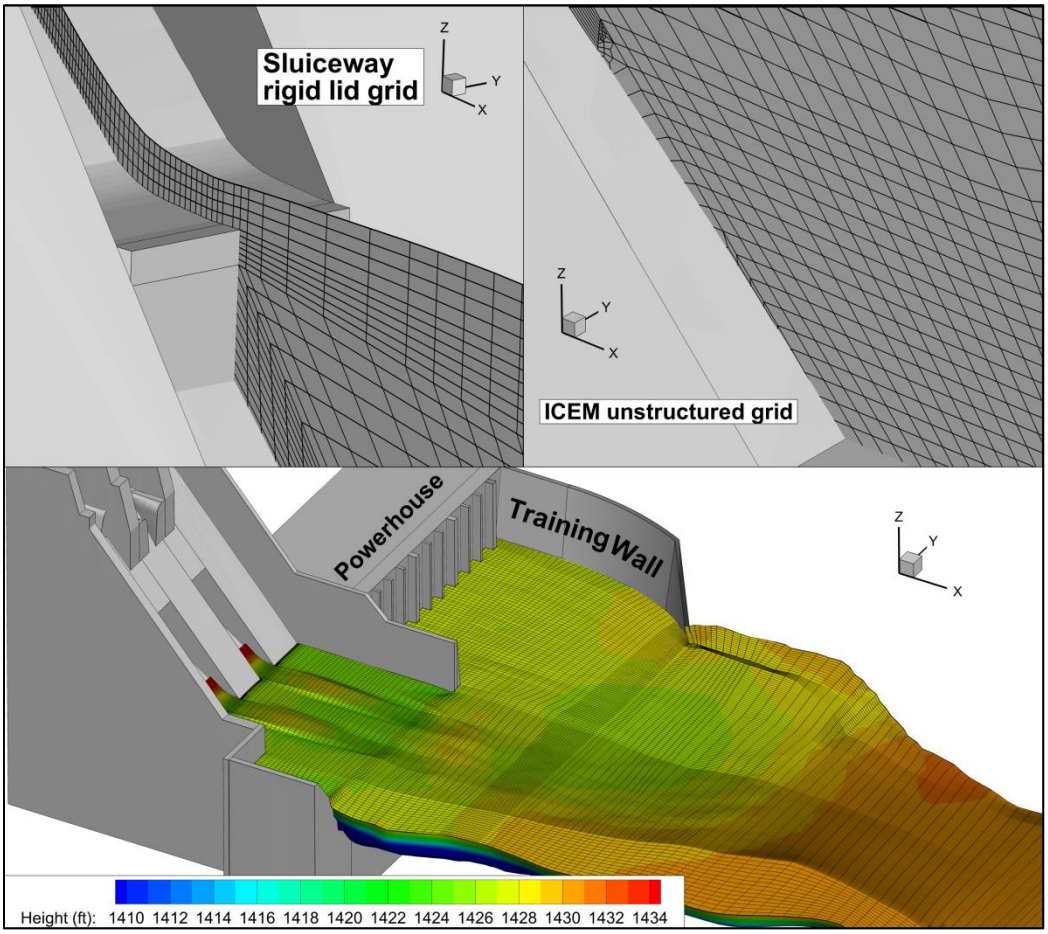

Figure 11. Grid details for the mixture model. A slice through the sluiceway and deflector, top left. The unstructured grid generated in ICEM, top right. Mesh at the constructed free surface, bottom.

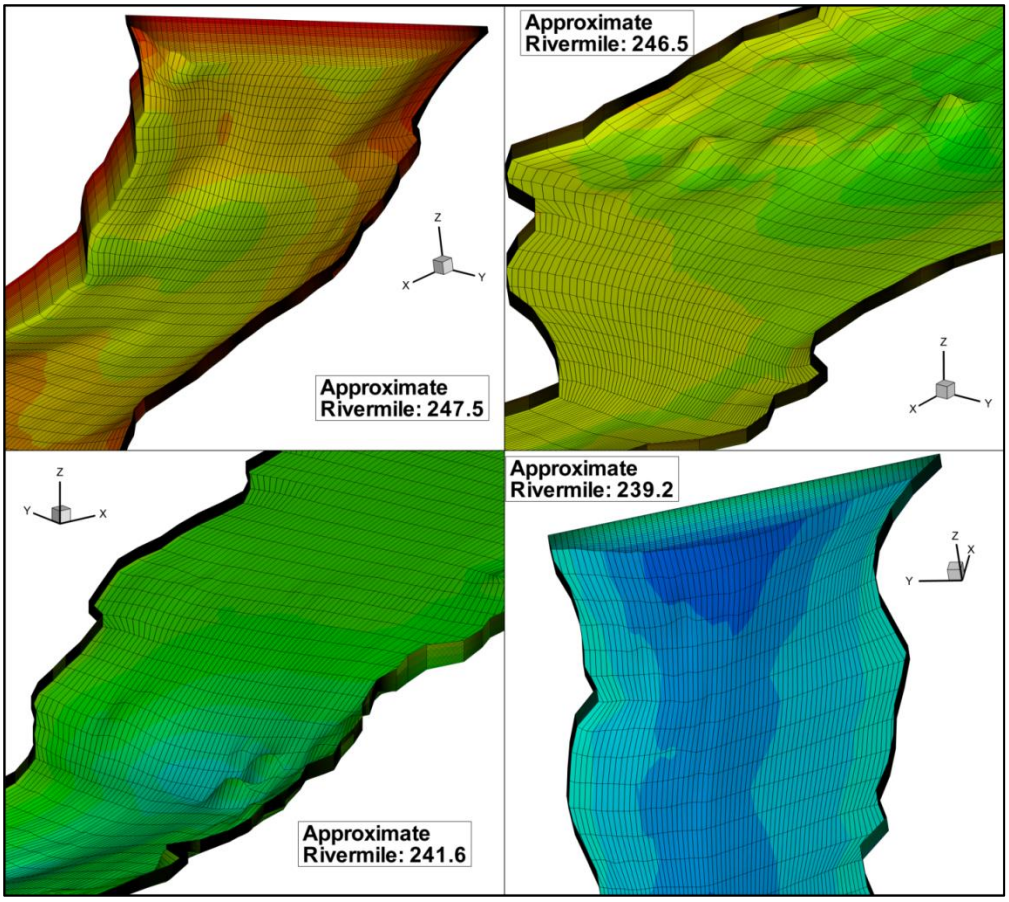

Figure 12. Grid details for the downstream TDG model

Table 3. Typical element dimensions for the VOF and TDG simulations

	Typical Element Size (ft)		
	Downstream Deflector	Fish Trap	Exit
VOF	(4.0,1.5,0.5)	(6.5,2.0,0.5)	(9.5,1.5,0.5)
TDG near Dam	(4.5,1.5,1.0)	(7.1,3.5,0.5)	(7.0,1.5,0.5)
TDG River Downstream	---	---	(30,3.0,0.5)

Boundary Conditions

Velocity at the spillway gate was an important boundary condition that can change the type and length of a spillway jet. Various spillway jets will alter the tailrace

flow field differently. For these simulations the velocity at the spillway gate was determined considering contraction at the gate and the velocity increase after the spillway gates, without energy loses. This allows for an accurate, however conservative, model of the sluiceway inlet. The velocity entering the sluiceway was calculated using the following equations:

$$g(\Delta H) = \frac{|V|^2}{2} \tag{21}$$

$$q = UhW \tag{22}$$

where $|V|$ is the velocity magnitude, U the velocity in longitudinal direction, q the gate flow rate, ΔH is the difference between forebay and gate elevations, h is the height of the gate opening, and W is the spillway width. For a forebay elevation of 1640.4 ft, $\Delta H = 138\ ft$ and $|V| = 94.2\ ft/s$.

Maximum allowable TDG in the forebay of Hells Canyon Dam was 115%, according to the 401 relicensing of the Snake and Columbia Rivers when encouraging downstream fish passage (Kolosseus, 2009). This value was added to the sluiceway inlet as a TDG initial condition. Entrainment by the sluiceway flow was quantified by altering the value of gas volume fraction and bubble size at the inlet. These values of gas volume fraction and bubble size were chosen to match experimental TDG data from May 21, 1998 and May 4, 2006 and were not changed between numerical simulations (Politano et al., 2010). For the model, including the far downstream simulations, a free surface mass transfer coefficient of air was determined to most closely match experimental data. The inlet model parameters were established as $\alpha = 0.03$ and $D_b = 0.8\ mm$ for gas volume fraction and bubble diameter, respectively. A value of $k_l = 0.001\ m/s$ was used for the free surface mass transfer coefficient (Politano et al., 2010). A bubble diameter of

0.8 mm produces an initial bubble number density of approximately $1.1(10^8)$ $bubbles/m^3$, for a gas volume fraction of 0.03.

The gate opening heights for a the 25 Kcfs and 45 Kcfs flow simulations were 5.36 ft and 5.41 ft for sluiceway 1 and sluiceway 2, respectively. For the 37 Kcfs flow the gate opening was 2.46 ft and 2.51 ft for sluiceway 1 and sluiceway 2, respectively. The 7Q10 simulation with the flow passing through the sluiceways had a gate openings of 15.3 ft for sluiceway 1 and sluiceway 2.

An inflow boundary condition for the rigid-lid model was created 33 ft upstream of the deflector and based on the shape of the flow from the VOF simulation. The velocity profile of the flow from the VOF simulation was extracted and used as the inlet flow for the rigid-lid cases. This inlet condition was imposed with the forebay TDG as well as the flow velocity profile extracted from the VOF model.

CHAPTER V
OPTIMIZATION OF THE DEFLECTOR

Grid Sensitivity Analysis

Prior to beginning the simulations to determine the performance of the deflector, a grid sensitivity analysis was conducted on the SVI case. Figure 13 and Figure 14 show the three mesh densities tested during the grid sensitivity analysis. The medium grid was the originally discretized mesh with the coarse and refined meshes being 1.4 times less and 1.4 times more refined, respectively. These grids were then simulated with the 45 Kcfs flow condition to compare the resulting free surface shapes and flow patterns. Figure 15 shows an instantaneous free surface shape at a slice passing through the deflector. The solid red line, the fine condition, shows a clearly occurring surface jump. Whereas the coarse case, dashed green line, shows a smooth surface with no surface jump present. The medium grid, solid blue line, shows the creation of a moderate surface jump. Although the flow is instantaneous it can be used to make a qualitative comparison of the free surface resolution. The fine level of refinement in the VOF model was too high to be reproduced when making the rigid-lid model. The spot of water above the jet in the refined case would not be considered in the rigid-lid model, since the surface of the rigid-lid model must be continuous. Also, the rigid-lid model cannot have two sections of fluid with airspace between them, removing the two significant features resolved by the refined case. All three conditions show a tight correlation after the initial surface jump.

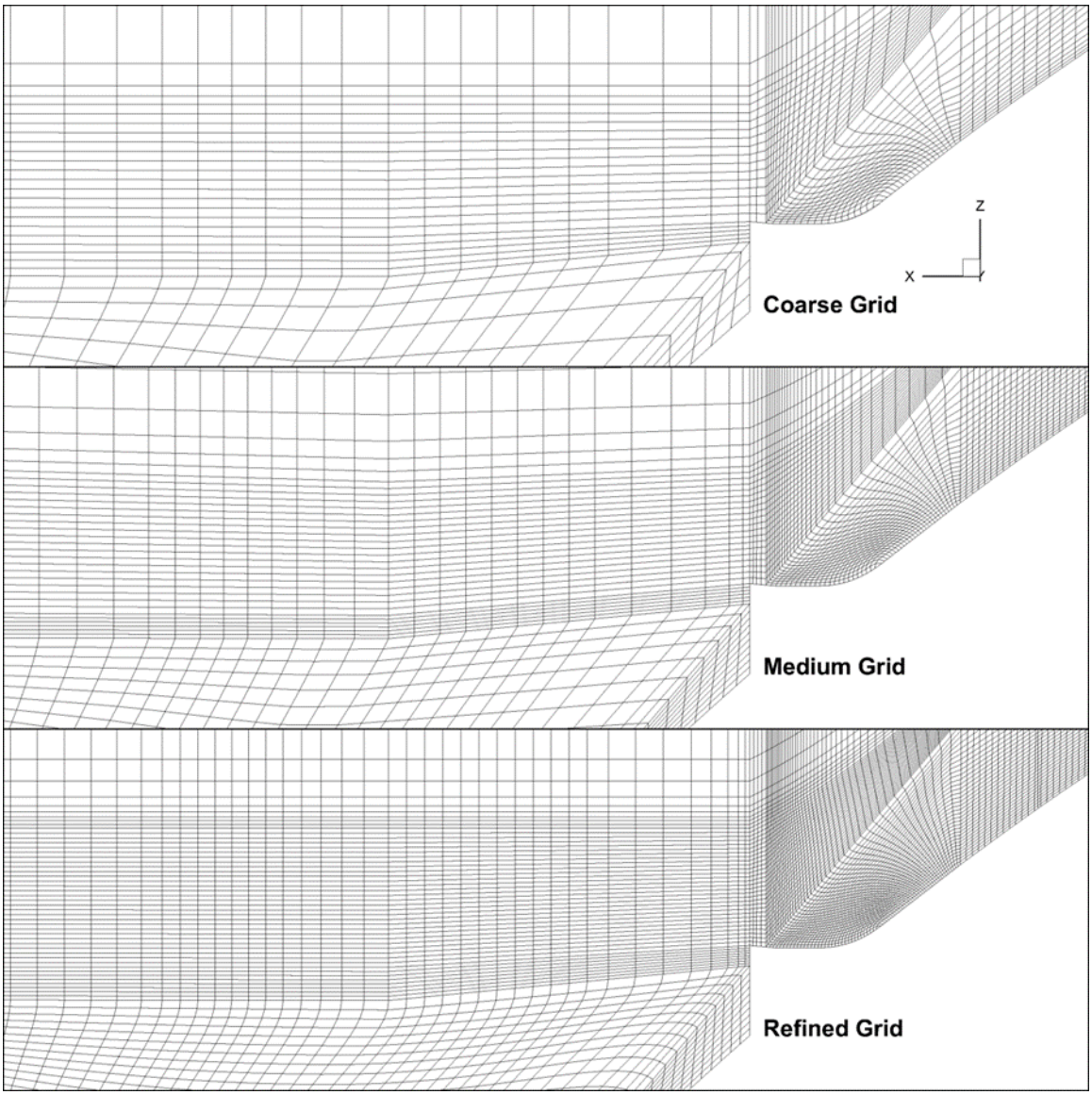

Figure 13. Tested meshes at a slice through the deflectors

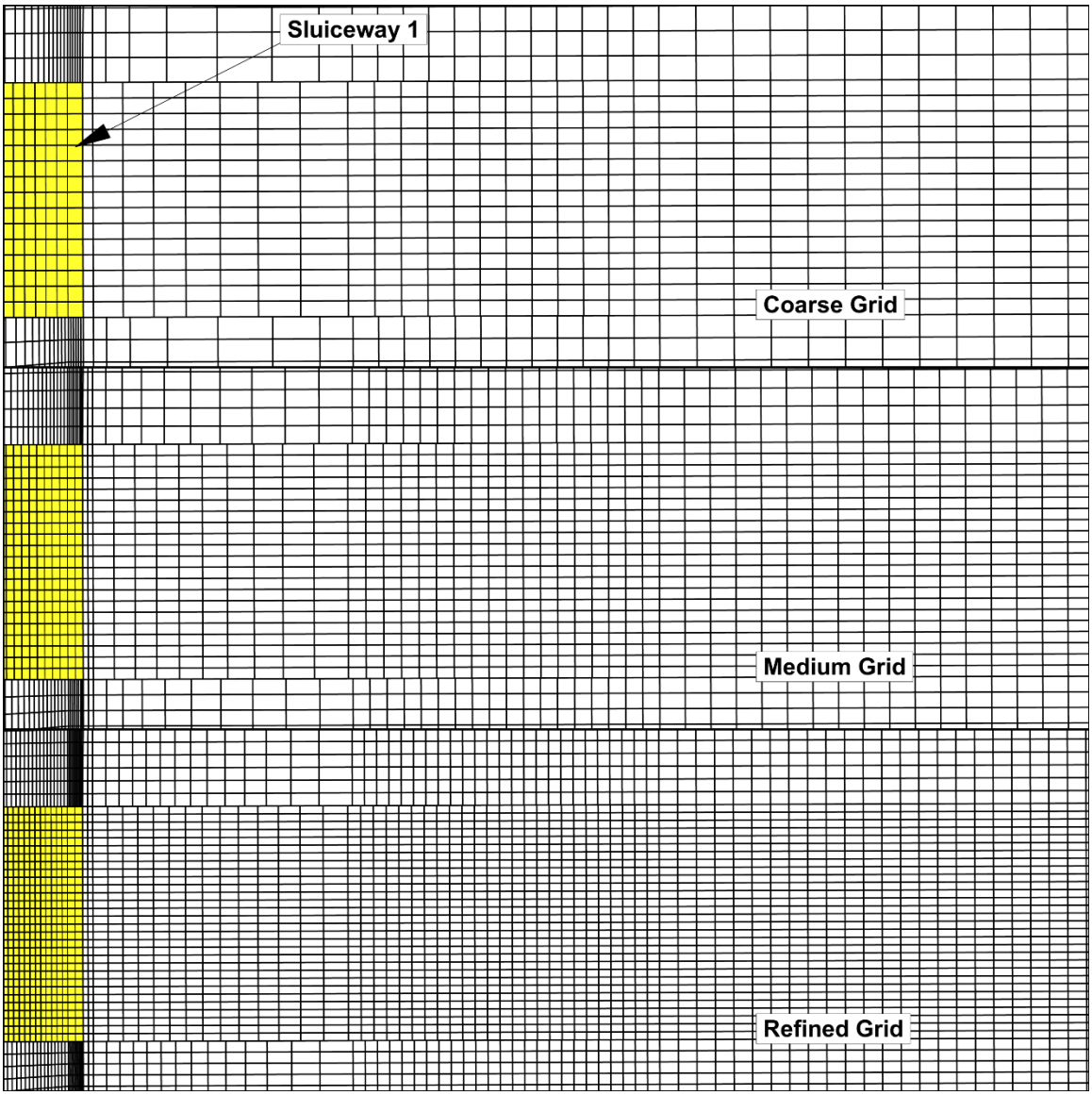

Figure 14. Tested meshes viewed orthogonally from above, near sluiceway 1

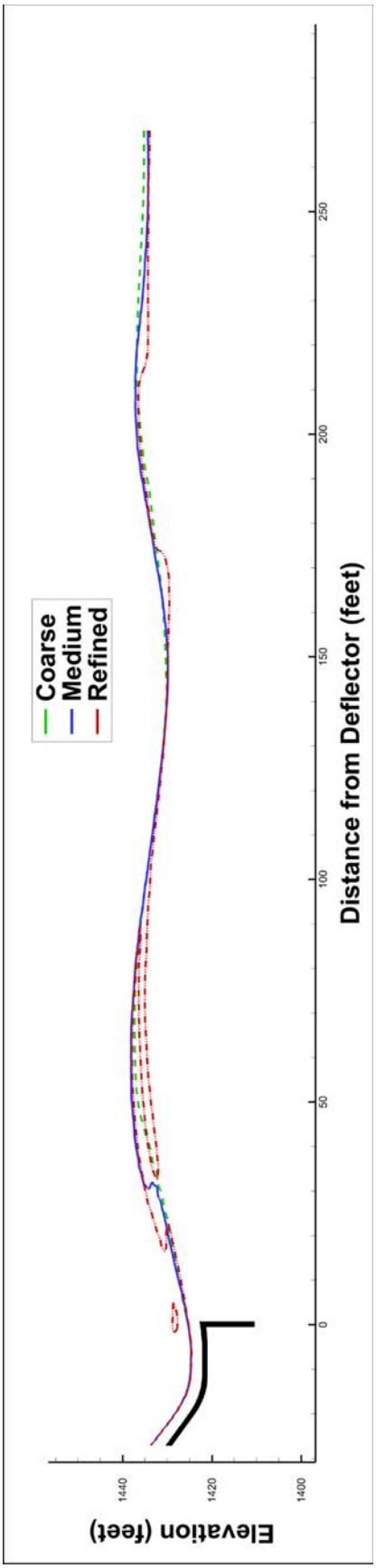

Figure 15. Different flow surface shapes on a slice passing through sluiceway 1

Another important aspect to the grid sensitivity analysis was the comparison of the flow fields between the three tests. A vertical slice of streamwise velocity from the three cases can be seen in Figure 16 and Figure 17, at 1424 ft and 1410 ft respectively. These vertical slices show no major changes in the main flow field between any of the three grid refinements. The important feature being the length and velocity of the jet seems to not be altered by the level of grid refinement. Effects of the jet at depth, shown in the low slices, seem to also not be altered by the grid refinement.

Figure 18 and Figure 19 show velocity vectors of the three grids at elevations of 1424 ft and 1410 ft respectively. Vectors were created by interpolating the flow field onto a 65 by 45 two dimensional structured grid. The vectors show minimal differences in the flow field downstream of the jet and powerhouse. Some differences in direction are seen near the deflector for the high slice as well as near the wall dividing the powerhouse and spillway flow.

Figure 20 and Figure 21 show velocity vectors on a slice through the sluiceway 1 and sluiceway 2 respectively. A blanking is performed on the data to show only the cells with more than 50% water content. This blanking is done to avoid confusion with the velocity vectors present in the air cells. These slices show the important back rolls that are shared among the three grids; the jet diffusion downstream of the stilling basin is also similar.

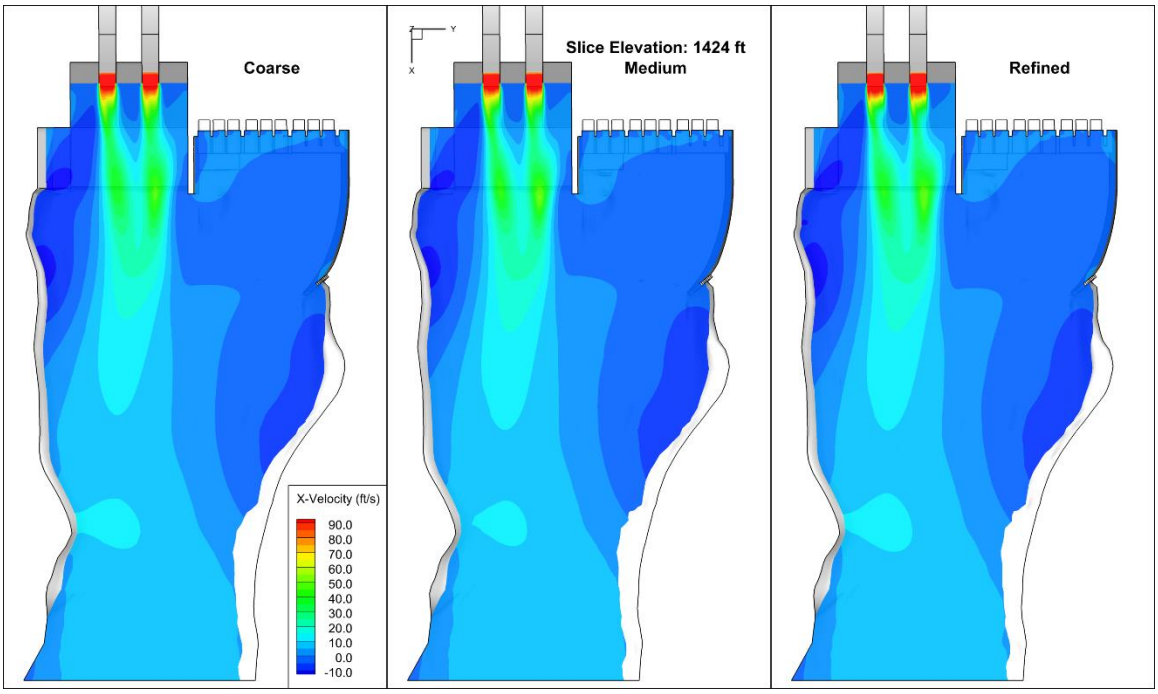

Figure 16. Velocity in the streamwise direction at 1424 ft for grid sensitivity analysis

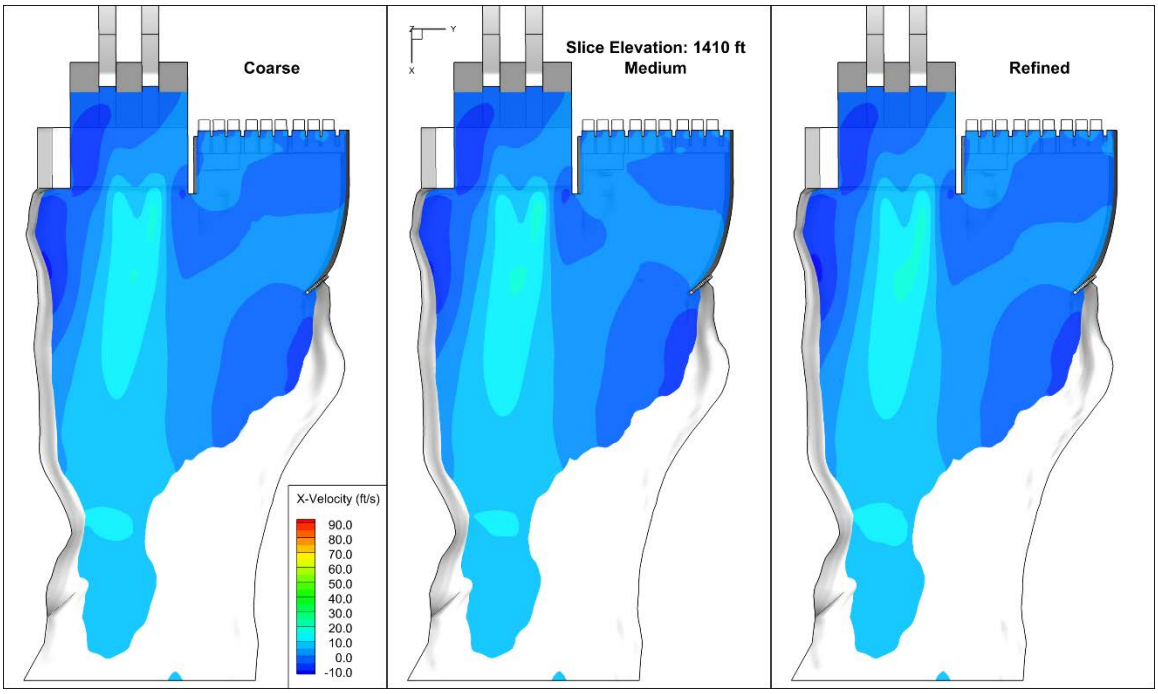

Figure 17. Velocity in the streamwise direction at 1410 ft for grid sensitivity analysis

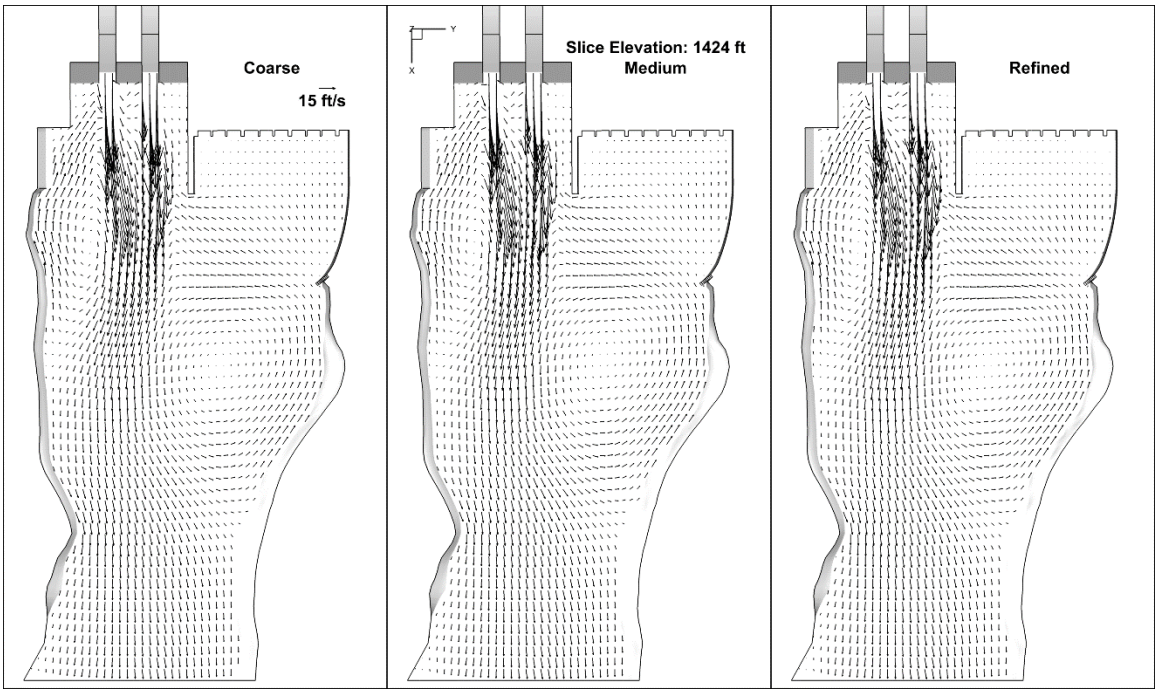

Figure 18. Velocity vectors at 1424 ft for grid sensitivity analysis

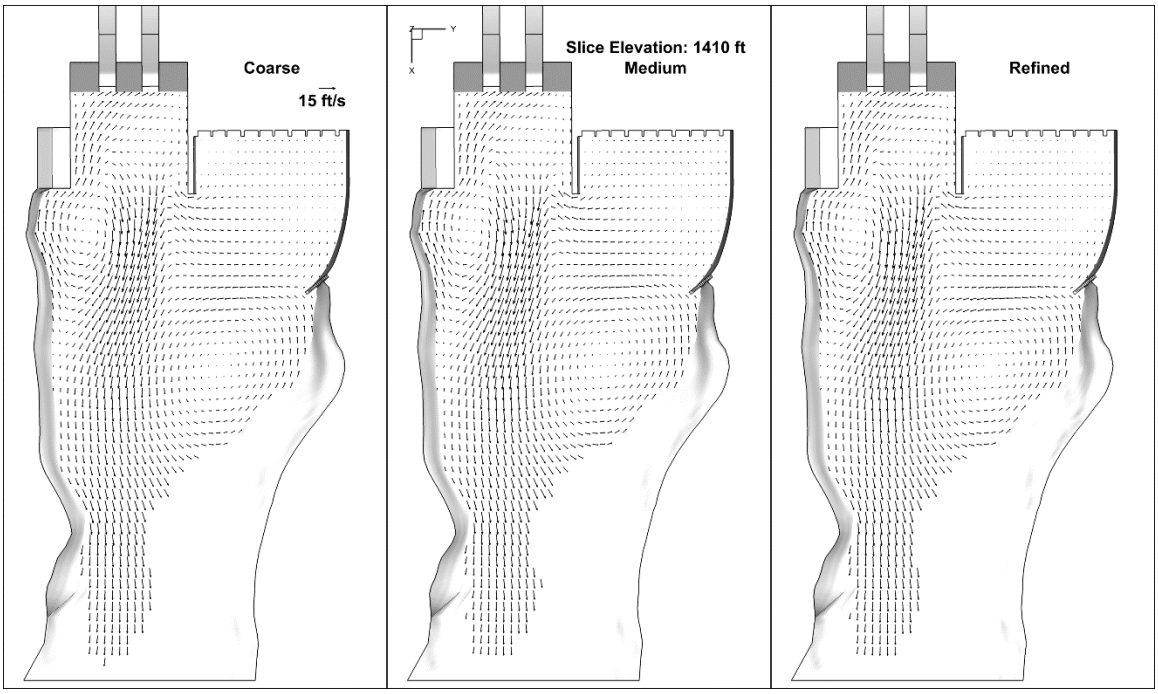

Figure 19. Velocity vectors at 1410 ft for grid sensitivity analysis

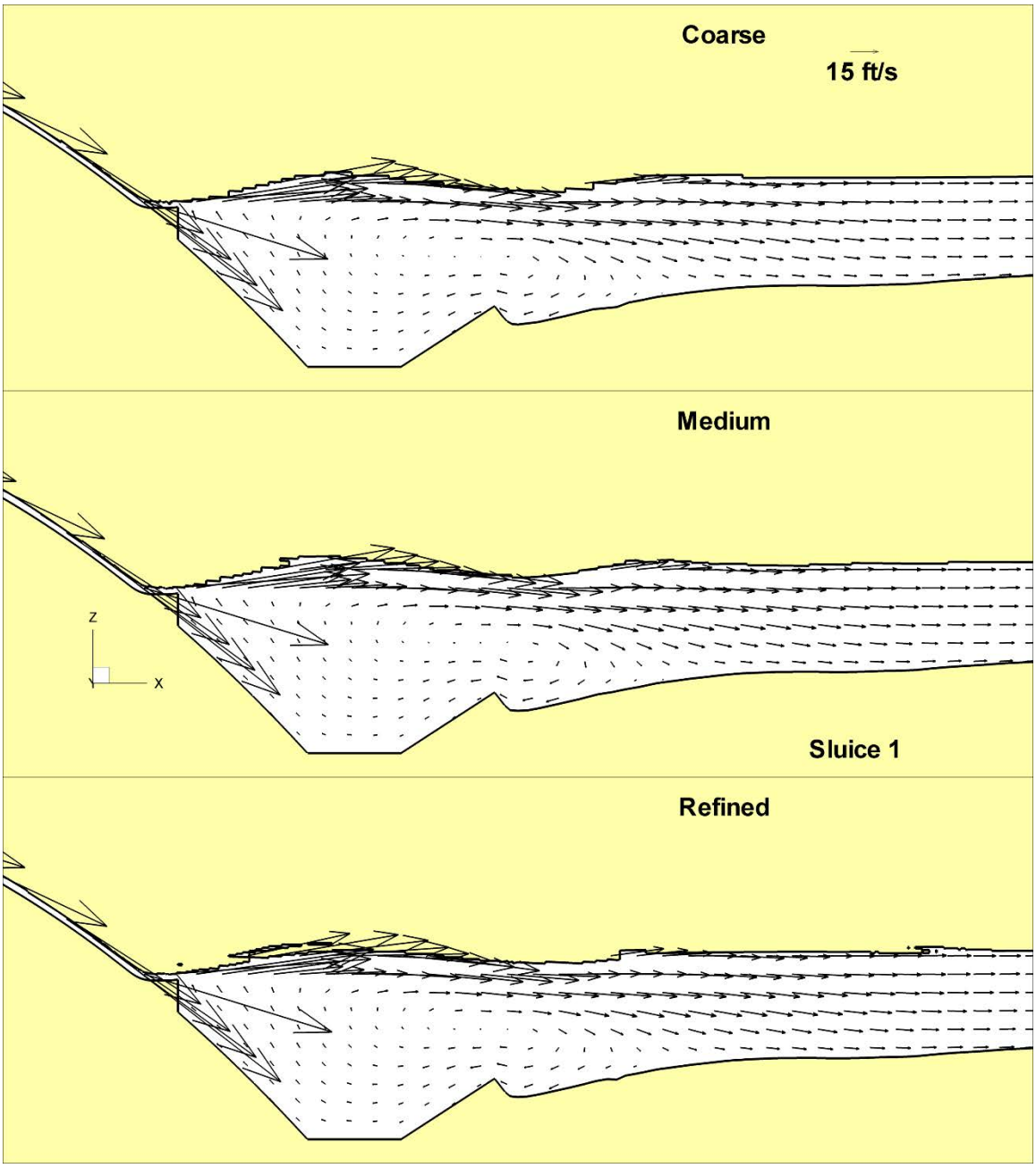

Figure 20. Velocity vectors from a slice through sluiceway 1 for the grid sensitivity analysis

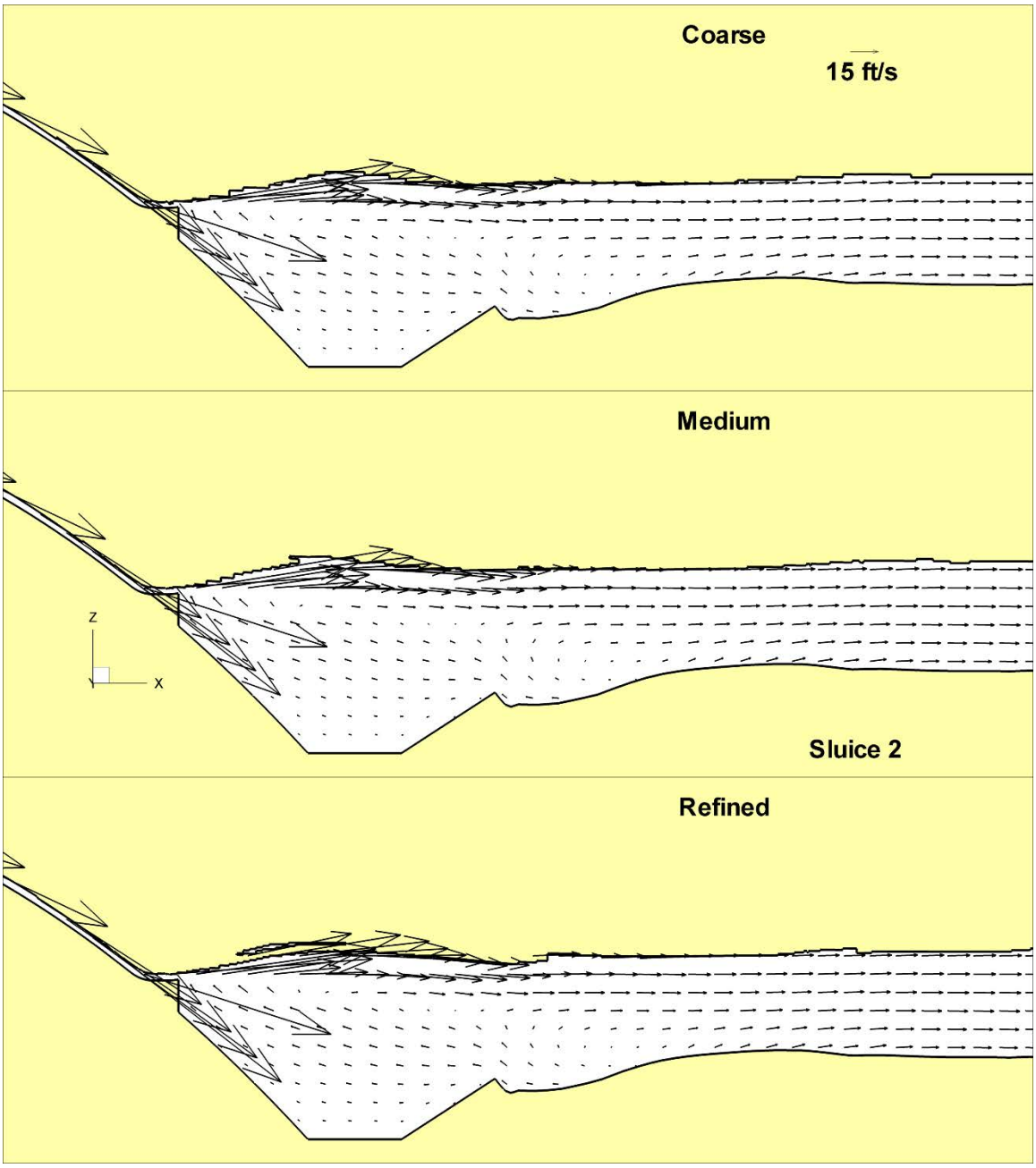

Figure 21. Velocity vectors from a slice through sluiceway 2 for the grid sensitivity analysis

The effects of grid density on powerhouse flow entrainment were tested to determine a quantitative difference between the three grids. Powerhouse flow entrainment is quantified by the amount of flow passing, from the powerhouse to the spillway region, through planes extending from the wall dividing the powerhouse and

spillway region. Figure 22 shows the differences in entrainment for the three grids during a VOF simulation. Lowest values of entrainment are seen in the simulation with the coarse mesh. The medium mesh has the highest value of entrainment, the total recorded entrainment is 4.6% larger than the entrainment of the fine mesh. The coarse mesh showed a maximum level of entrainment 3.2% smaller than the refined grid. Later in this chapter entrainment is calculated using the rigid-lid models, and it should be noted these values of entrainment from the VOF model are not comparable. The entrainment from the different models cannot be directly compared since an isotropic single-phase model under predicts the entrainment Politano et al. (2009a).

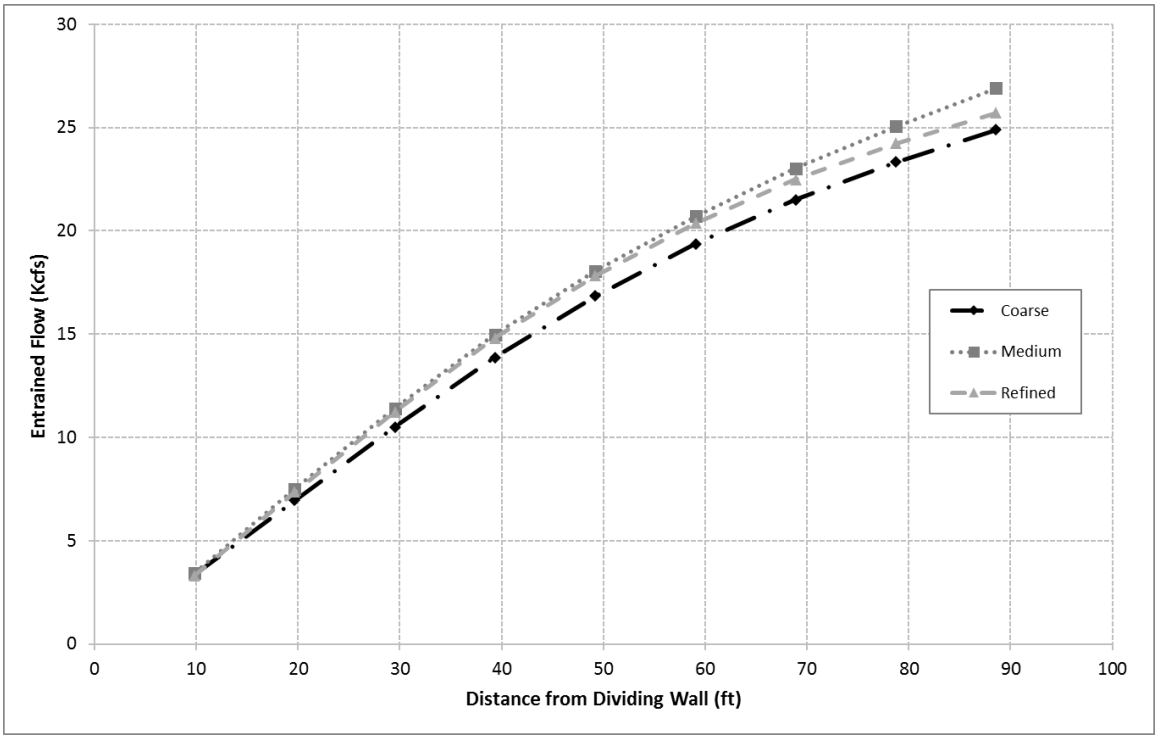

Figure 22. Powerhouse entrainment for the grid sensitivity simulations

The medium mesh was able to capture the presence of a surface jet at a resolution reproducible in the rigid-lid grid, as well as closely match the downstream elevation of

the refined condition. The medium grid was chosen to be the standard grid density for the remaining VOF cases. Between the meshes the overall flow field did not change. However, minor local differences near the sluiceway jets were observed.

Volume of Fluid Simulations

Simulations with 25 Kcfs River Flow

Evolution of the flow rates through the outflow for the 25 Kcfs cases are illustrated in Figure 23. In this figure the horizontal dashed line is the target flow rate of 25 Kcfs that the simulations were converging to. Each simulation converged in approximately 15 minutes of flow time. From an initialized condition of approximate target tailwater elevation and zero velocity the simulations took approximately 10 days of computational time to converge. Simulation SV_3 was interpolated from simulation SV_1 and took approximately 5 minutes to converge to the target flow rate. All simulations converged to approximately the same value.

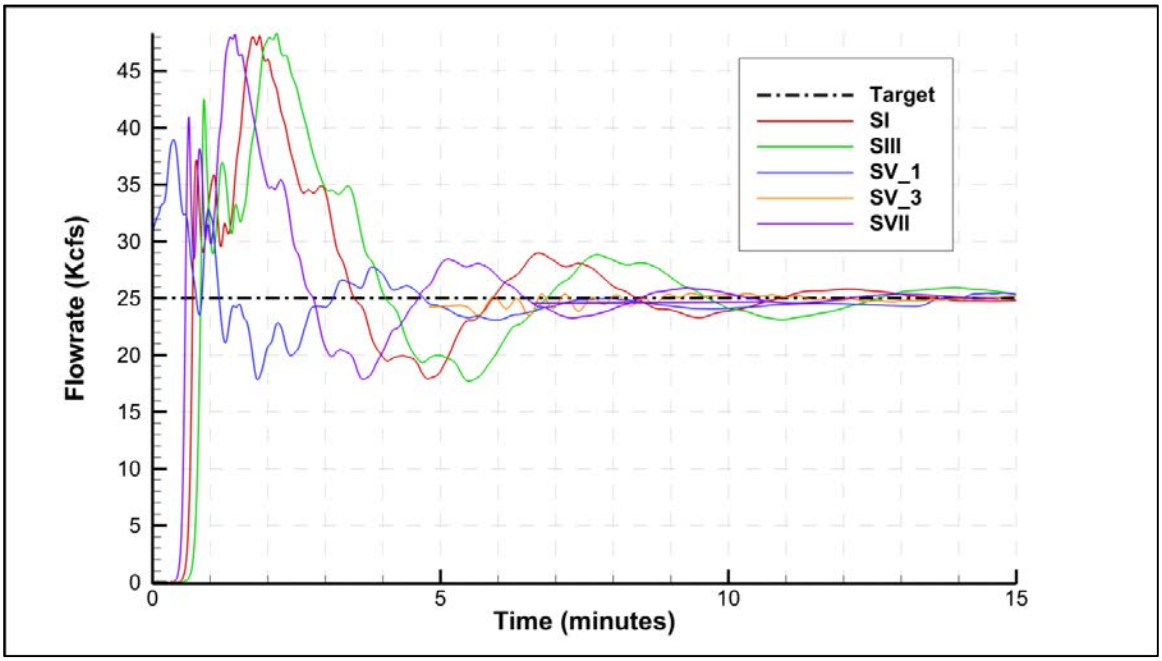

Figure 23. Flow rate evolution measured at the outflow for simulations with 25 Kcfs

A qualitative comparison of the flow solutions shows the differences in deflector dimensions plays a minor role in the shape of the free surface. Figure 24 shows the free surface shape colored by water elevation. This free surface shape was determined using a gas volume fraction of $\alpha = 0.5$, or cells containing half air and half water. Tecplot 360 smoothed the data by taking it from the cell centered information given by Fluent and interpolating it to the nodes belonging to that cell. Each of these free surfaces shown will become the rigid surface of a TDG simulation. Each simulation shared the occurrence of a lower water elevation above the stilling basin due to the increased velocity of the jets, approximately 3 feet of difference from the expected outflow elevation.

A horizontal bounded plane was used to determine the near surface velocity of the flow. This plane contained an eighty by eighty uniform orthogonal mesh generated within Tecplot. Linear interpolation imposed the velocity components onto the plane, displaying the velocity magnitude. This can be seen in Figure 25 as planes with an elevation of 1430.4 ft, approximately 0.1 ft from the estimated free surface. Each of these figures shows the presence of a large recirculation entraining water from the west bank into the jet region. This recirculation also reverses the natural local flow near the fish trap, changing it from flowing downstream to flowing upstream toward the powerhouse. Since this was present in all simulations it cannot be used as a criteria to determine the relative performance of the deflectors.

Determining the jet regimes was an important initial criteria for determining the performance of the deflectors. Figure 26 shows the slices through the deflectors and the interpolated velocity vectors. In this instance none of the deflectors operate outside of a surface jet. However, some plunging flow was seen deeper in the tailrace after sluiceway

number 1. Although these plots do not show the lateral flow it can be implied from the previous plots the entrained flow was the causing the jet to plunge downstream. A weak back roll was also present in all of the simulations downstream of sluiceway 1. There was no indication of backflow or plunging flow from sluiceway 2.

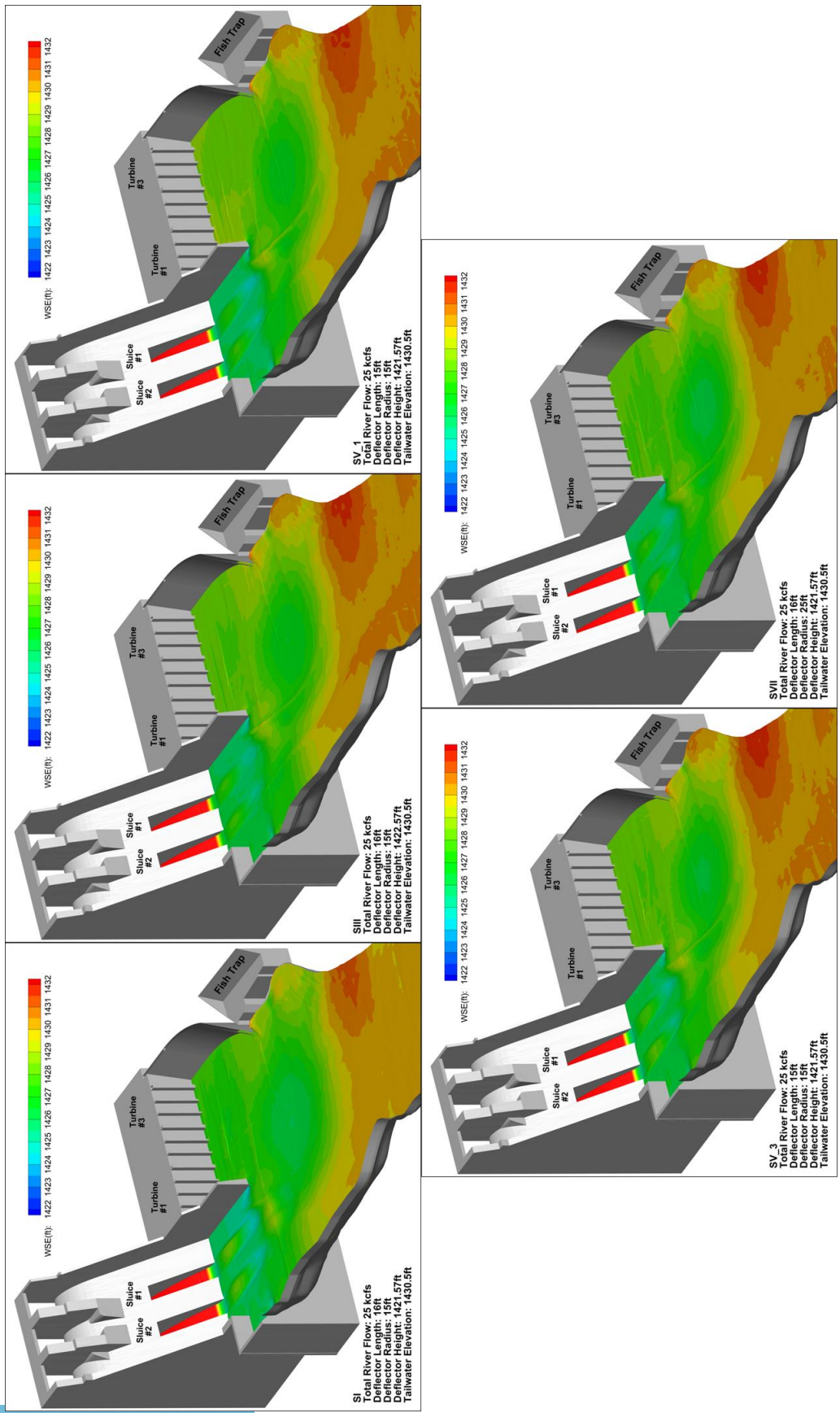

Figure 24. Free surface elevation of the 25 Kcfs simulations colored by water surface elevation

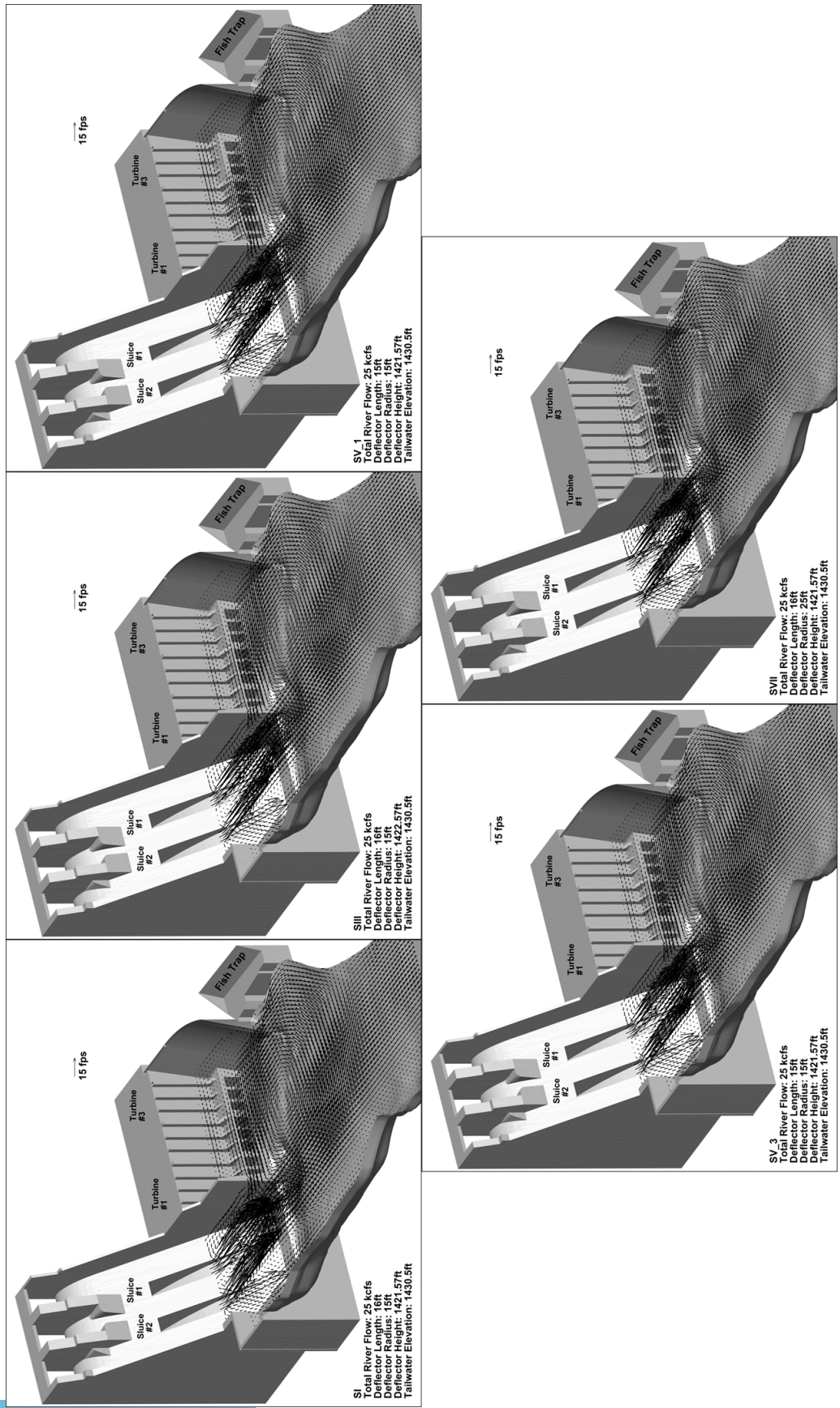

Figure 25. Near surface velocity vectors for the 25 Kcfs simulations, plane height of 1430.4 ft

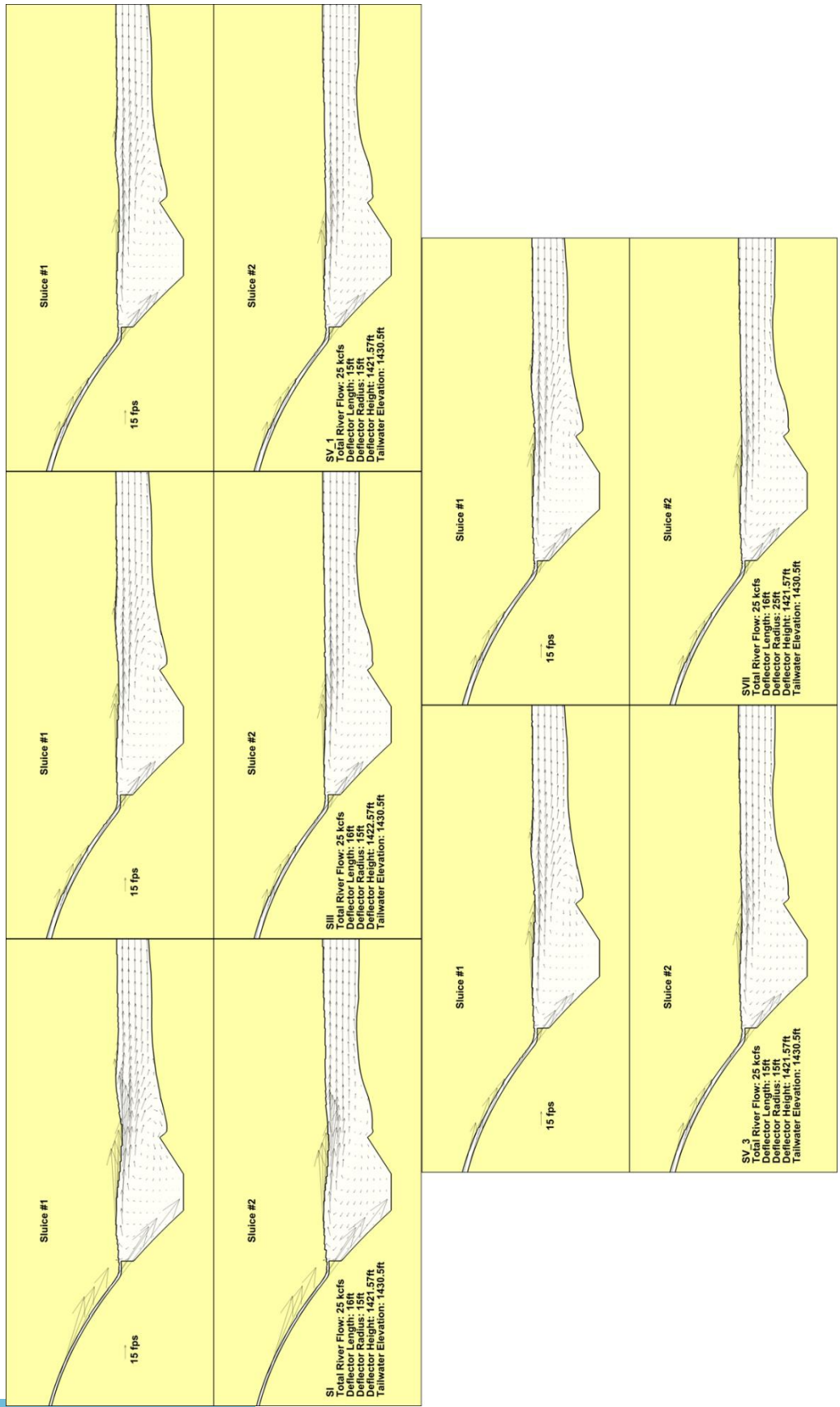

Figure 26. Slices through the sluiceways presenting the velocity vectors present in the water for the 25 Kcfs simulations

Simulations with 45 Kcfs River Flow

Evolution of the simulation outflow for the 45 Kcfs cases are illustrated in Figure 27. In this figure the horizontal dashed line is the target flow rate of 45 Kcfs that the simulations were converging to. Each simulation converged in approximately 20 minutes of flow time. From an initialized condition of approximate target tailwater elevation and zero velocity the simulations take approximately 12 days of computational time. Simulation SIV was interpolated from simulation SII and took approximately 5 minutes to converge to the target flow rate. All simulations converged to approximately the same value with some small differences due to numerical diffusion at the outflow.

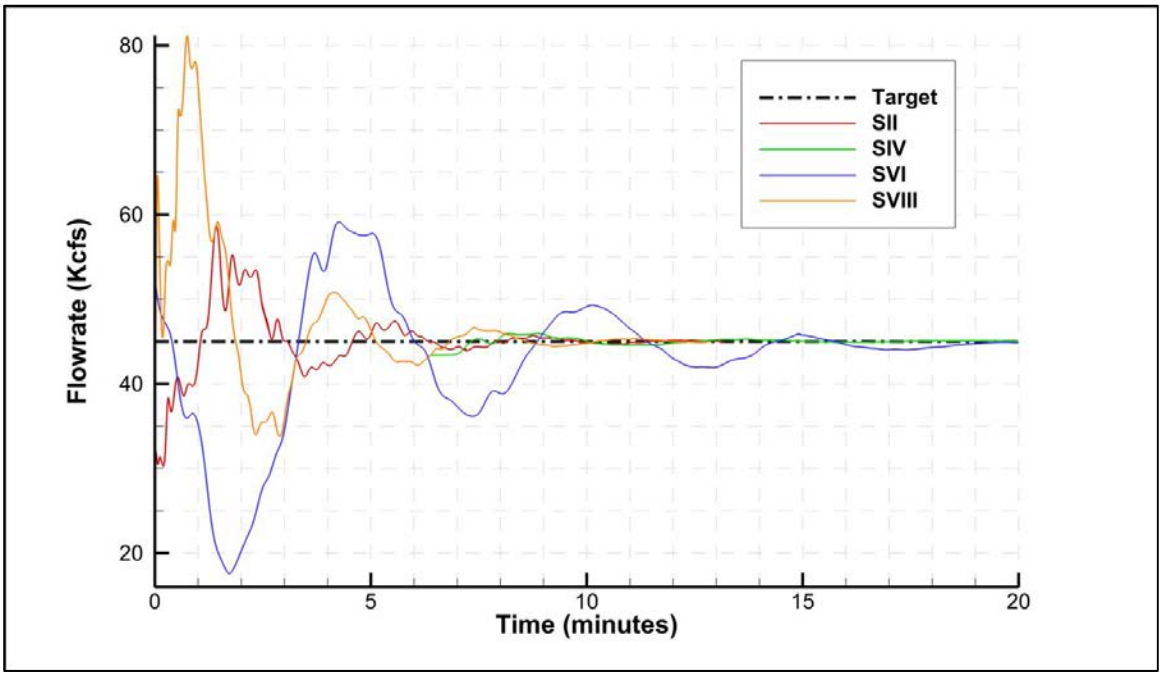

Figure 27. Flow rate evolution measured at the outflow for simulations with 45 Kcfs

Another qualitative comparison of the VOF solution shows the differences in surface shape and elevation were marginal. The free surface shape colored by elevation can be seen in Figure 28. Like the simulations with 25 Kcfs the free surface shape was extracted at a gas volume fraction of $\alpha = 0.5$. Once more, in the same way as the

previous flow solutions the region near the deflectors and stilling basin was lower than the downstream flow. In these cases the change in tailwater elevation from the stilling basin to the outflow was about 4 feet.

In order to properly compare the flow between the two cases it was decided to choose the same plane height and grid density for extracting flow velocity data and displaying vectors. The height of the plane was again 1430.4 ft however it was then 6 feet below the estimated water surface elevation. Figure 29 shows the velocity vector data at this plane. It can again be seen that every simulation shares a large recirculation. This recirculation appears weaker in relative magnitude that the recirculation seen in cases with 25 Kcfs. It should be noted that in these cases powerhouse flow was increased from 10 to 30 Kcfs effectively increasing the streamwise velocity present in the region.

Figure 30 shows vertical slices through the sluiceways similar to the 25 Kcfs simulations. In all cases sluiceway 1 produces some effect of a transition from surface jet to surface jump. The presence of a hydraulic roller, above the start of the jet and just downstream of the deflector, shows the beginning of the flow's transition from surface jet to surface jump. Water present above the jet becomes very aerated prior to moving downstream, likely causing an elevated level of TDG.

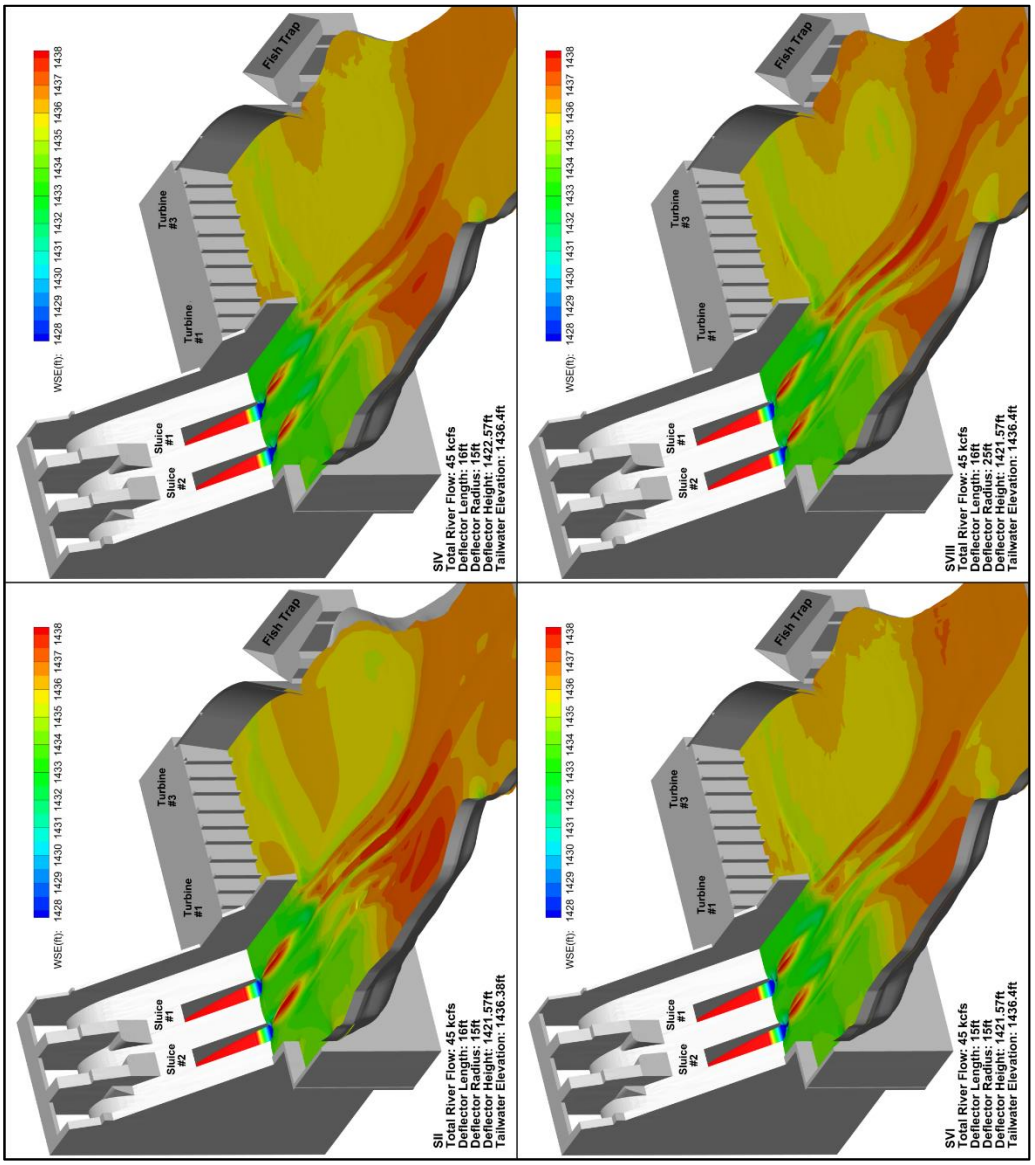

Figure 28. Free surface elevation of the 45 Kcfs simulations colored by water surface elevation

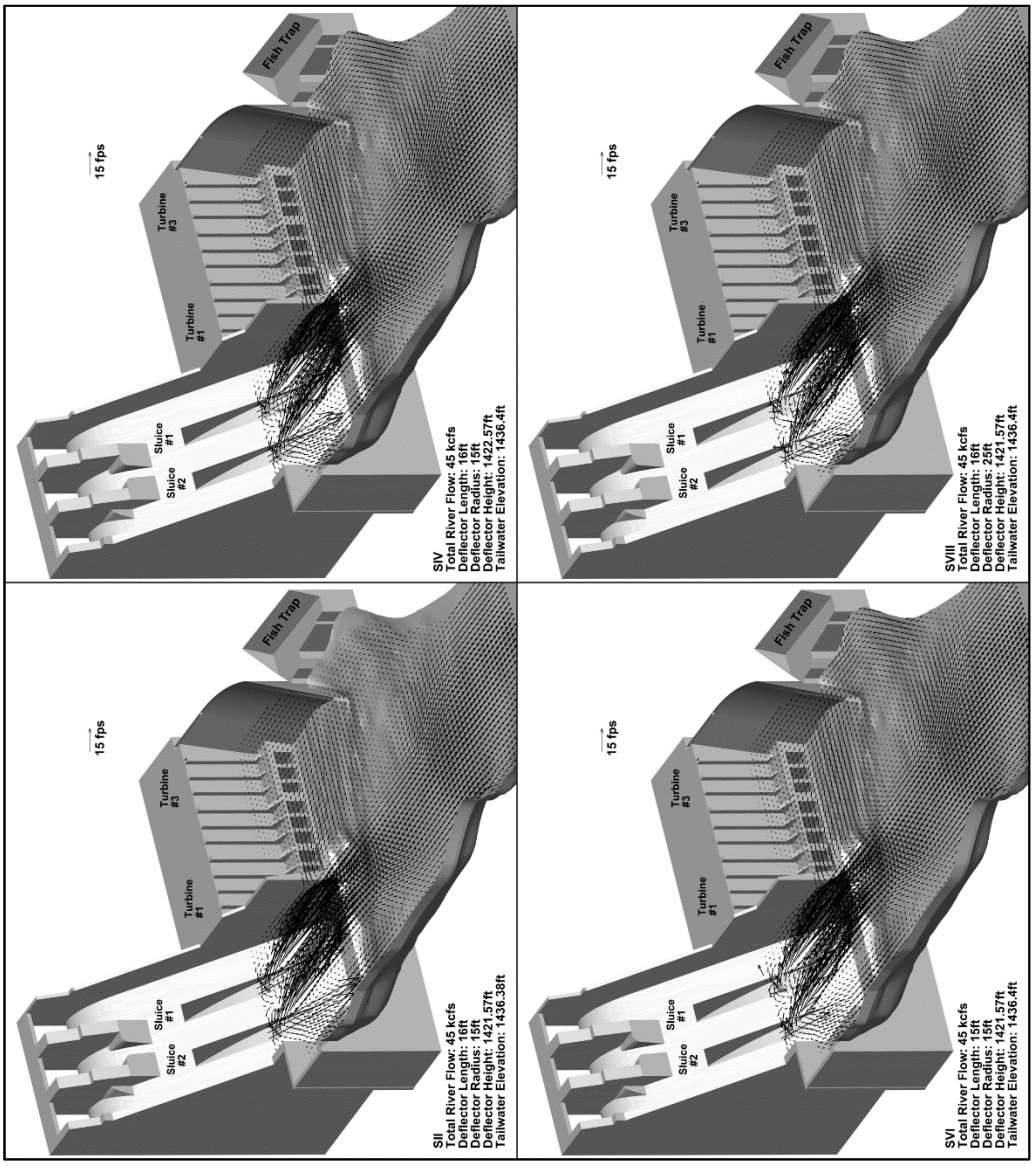

Figure 29. Near surface velocity vectors for the 45 Kcfs simulations, plane height of 1430.4 ft

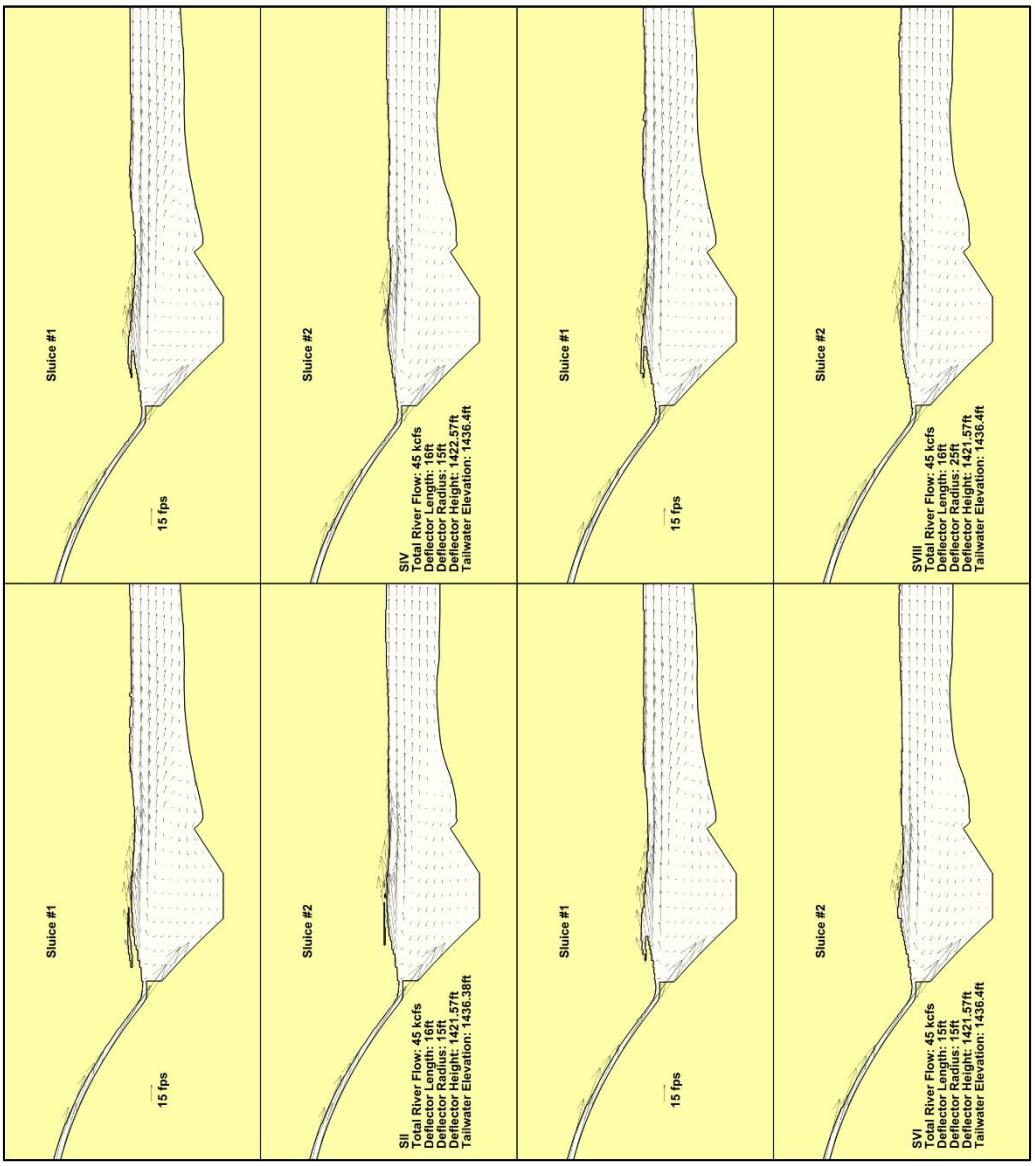

Figure 30. Slices through the sluiceways presenting the velocity vectors present in the water for the 45 Kcfs simulations

Rigid-lid Model

After collecting and extracting free surface information for all the deflector geometry cases 'rigid-lid' grids were created. These computational grids have a stationary free surface and were intended to model the new flow field with the imbedded TDG program. Each grid was made with a unique and corresponding free surface.

Simulations with 25 Kcfs River Flow

TDG assessment will be made at elevations of 1410 ft and 1418 ft for all 25 Kcfs simulations. Where 1410 ft was located 2 ft below the downstream edge of the deflector and 20 ft below the free surface. The information shown at 1418 ft was 12 ft below the estimated free surface.

Velocity vectors can show important entrainment and recirculation regions, as well as the location and strength of the jets. For their visualization in the rigid-lid model the velocity components were interpolated onto a coarser structured mesh generated by Tecplot. A linear interpolation was used to interpolate the data from the mesh to the structured grid containing sixty five nodes in the streamwise direction by forty five nodes in the transverse streamwise direction.

Figure 31 and Figure 32 show the velocity vectors from the interpolated flow. For all simulations and for both heights there were two present recirculations in the flow. One larger recirculation present near the fish trap and the left bank guide wall, this recirculation was also seen in the VOF simulations. A second recirculation becomes present on the east bank very close to the deflectors. Either recirculation was caused by jet entrained flow, however the larger western eddy was adding to powerhouse entrainment. The simulation with powerhouse one operating shows a slightly weaker

west bank recirculation. This simulation also reduces the strength of the jets, seen in Figure 33 and Figure 34 showing the streamwise velocity of the flow. Contours of streamwise velocity allows the judgment of the magnitude of the jets as well as the size of the regions that were affected by reversed flow.

Gas volume fraction was determined by the percent of the volume that was filled with water. High values of alpha indicate regions where there was a significant amount of air in the flow, this is usually called “white water”. Figure 35 and Figure 36 show the gas volume fraction at the two different horizontal slice elevations. The distribution of bubbles for each of the cases was similar. The western eddy entrains bubbles and bring them around the fish trap back to the spillway region. Although, in the case with powerhouse 1 operating the entrainment of bubbles back into the spillway region was less. This was expected since the previous results showed a weaker western recirculation while operating powerhouse 1.

Figure 37 shows vertical slices through sluiceway 1 and 2 for each of the simulations again colored by gas volume fraction. These figures show the effects of the western eddy’s entrainment of bubbles to depth as well as the deflectors’ ability to keep bubbles at the surface immediately after they exit the sluiceways. After the stilling basin the flow begins to plunge bubbles to half of the downstream depth. The plunging flow in conjunction with the powerhouse entrainment causes bubbles to be pulled into a back roll underneath the sluiceway jets, this was not a desirable effect given the depth of the stilling basin. Bubbles were drawn deeper in the stilling basin of SV_1 however the amount of bubbles present under the jets were minimal. This backflow was also seen in the three dimensional physical model of Hells Canyon (Haug and Weber, 2002).

TDG source is the numerical representation of the value *S* from Equation 14. Represented by the mass transfer of air from bubbles into and out of solution with water; positive values describe gas being dissolved into water and negative values describe degasification. Figure 38 shows TDG source on slices through the two sluiceways. It should be noted that for all simulations no major production of TDG was present in the stilling basin. However, the TDG production was evident just downstream of the stilling basin. From Figure 37 this region was shown to contain a high presence of bubbles as well as entrained powerhouse flow. It can be recalled from Chapter II that the presence of bubbles in water with a low gas concentration allows the dissolution of those bubbles to meet the equilibrium condition. At the surface of the flow, the gas volume fraction was very high, however the hydrostatic pressure was very low. The plots show degasification occurring at the surface, meaning the dissolved air content was greater than the equilibrium condition.

TDG distribution is shown in Figure 39 and Figure 40 at the horizontal slices used for the previous plots. SIII, SV_3 and SVII have very similar TDG values at the low and high elevations where TDG was more concentrated on the western bank. Whereas SI and SV_1 have an overall higher presence of downstream TDG occurring more uniformly. For all simulations the percentage increase of TDG from the forebay to tailrace was less than 5%, initially at 1.15.

Figure 41 shows streamlines colored by TDG values. This figure shows the important effects of the recirculation and consequential powerhouse entrainment. Both sluiceways contain three released streamlines and each powerhouse draft tube has one. Each simulations shows all three streamlines from the powerhouse were entrained into

the spillway flow. The entrainment appears to cause more significant back rolls in SV_1 and brings the water into the deep region of the stilling basin in SI.

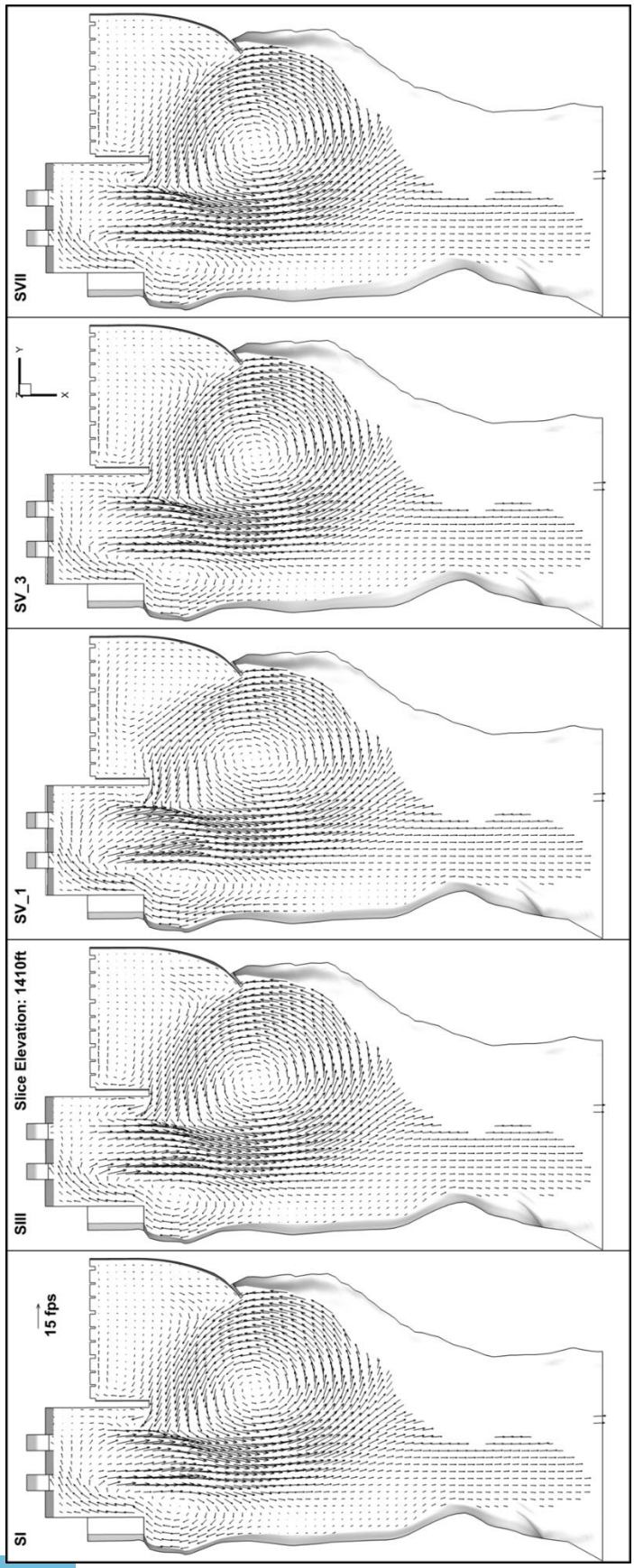

Figure 31. Velocity vectors at 1410 ft for 25 Kcfs

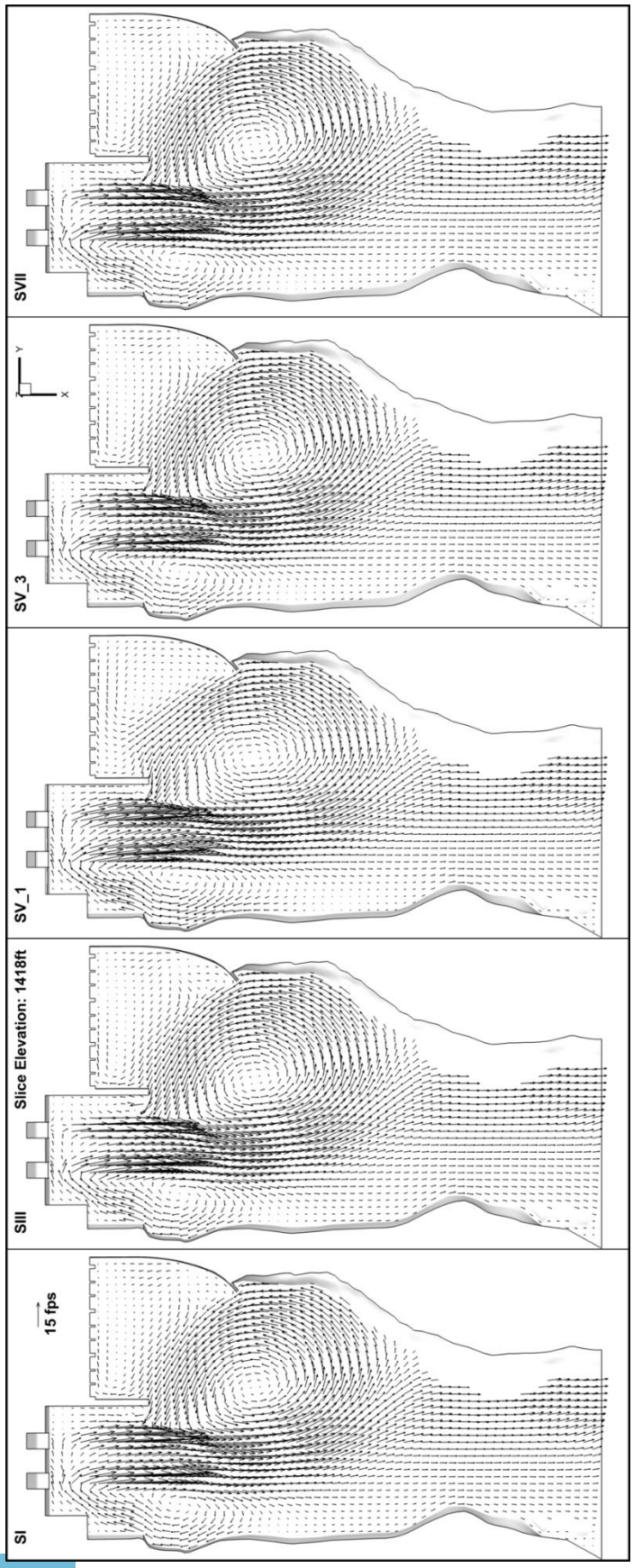

Figure 32. Velocity vectors at 1418 ft for 25 Kcfs

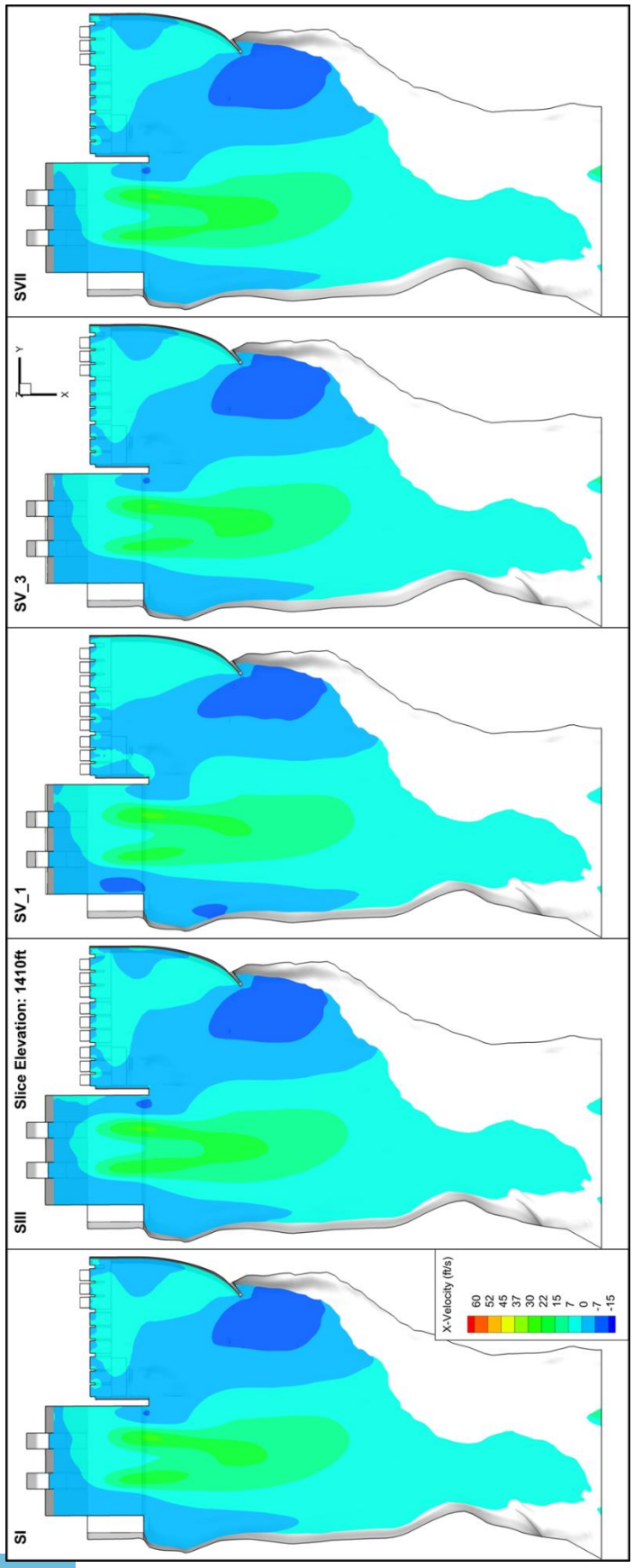

Figure 33. Velocity in the streamwise direction at 1410 ft for 25 Kcfs

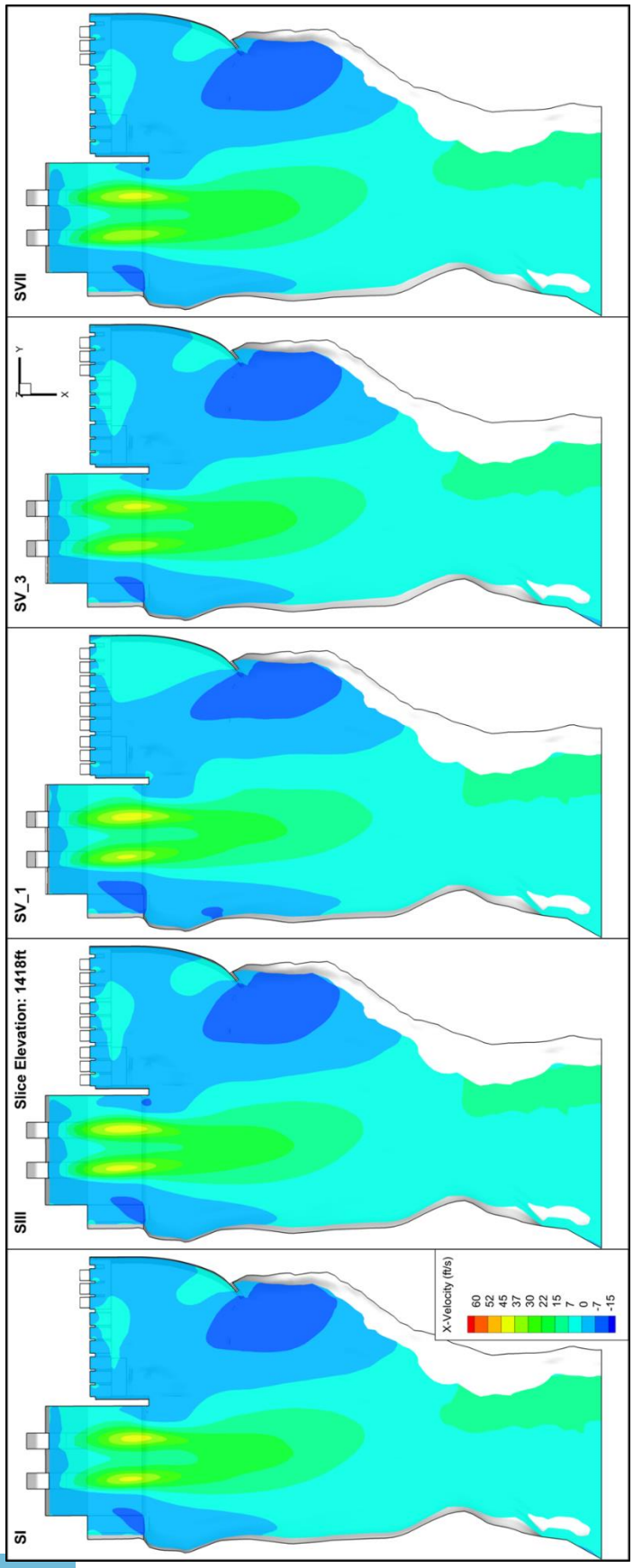

Figure 34. Velocity in the streamwise direction at 1418 ft for 25 Kcfs

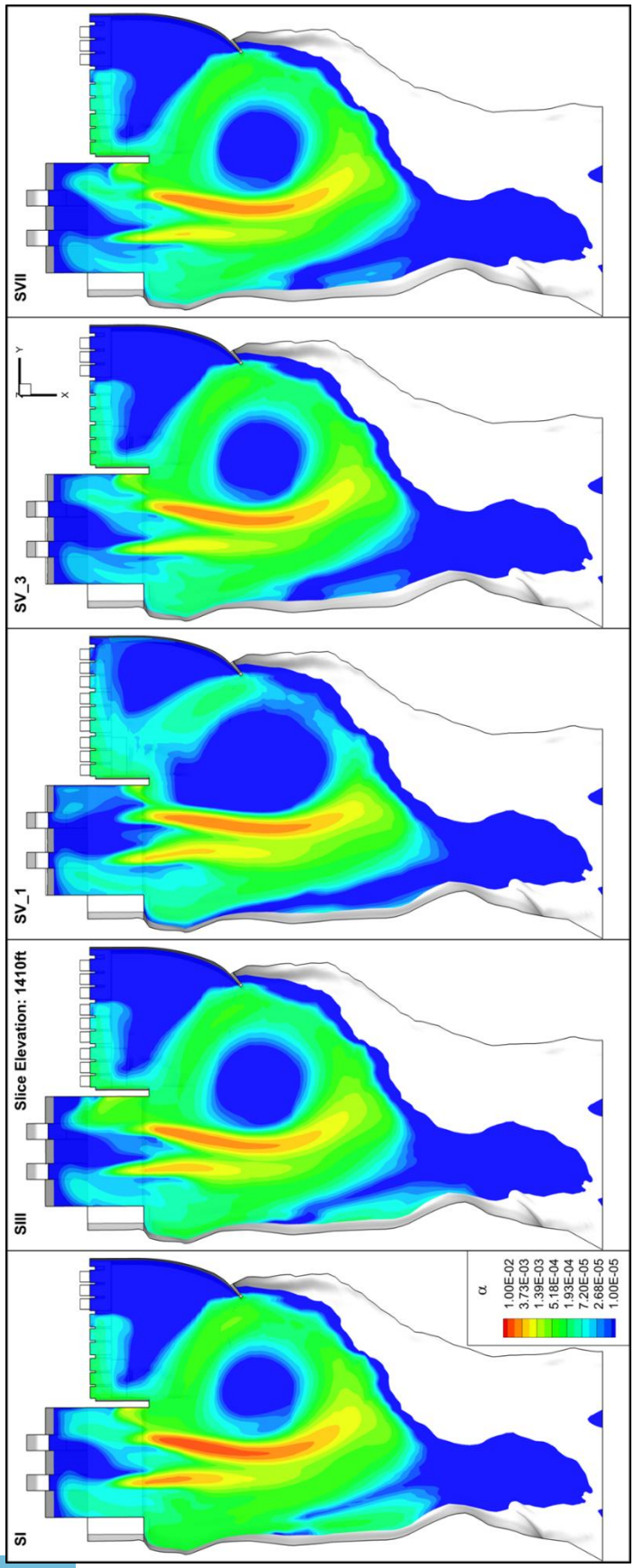

Figure 35. Gas volume fraction at 1410 ft for 25 Kcfs

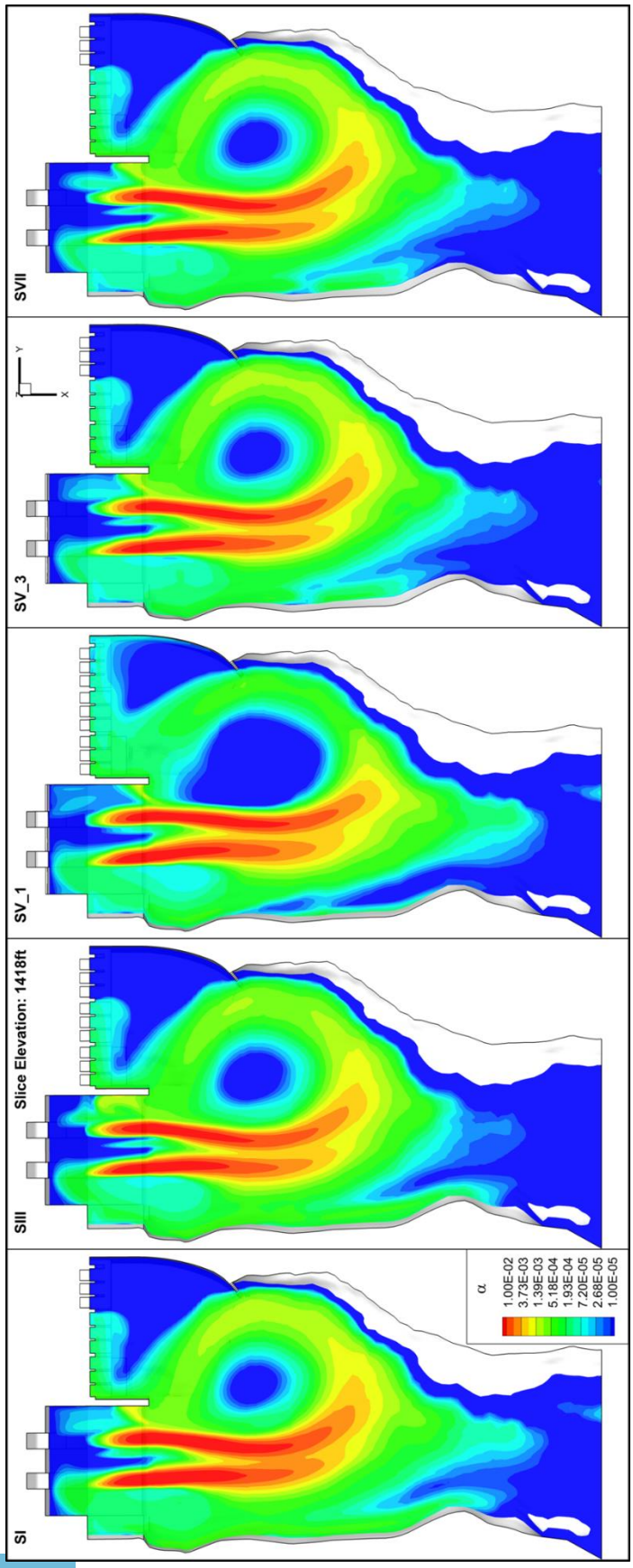

Figure 36. Gas volume fraction at 1418 ft for 25 Kcfs

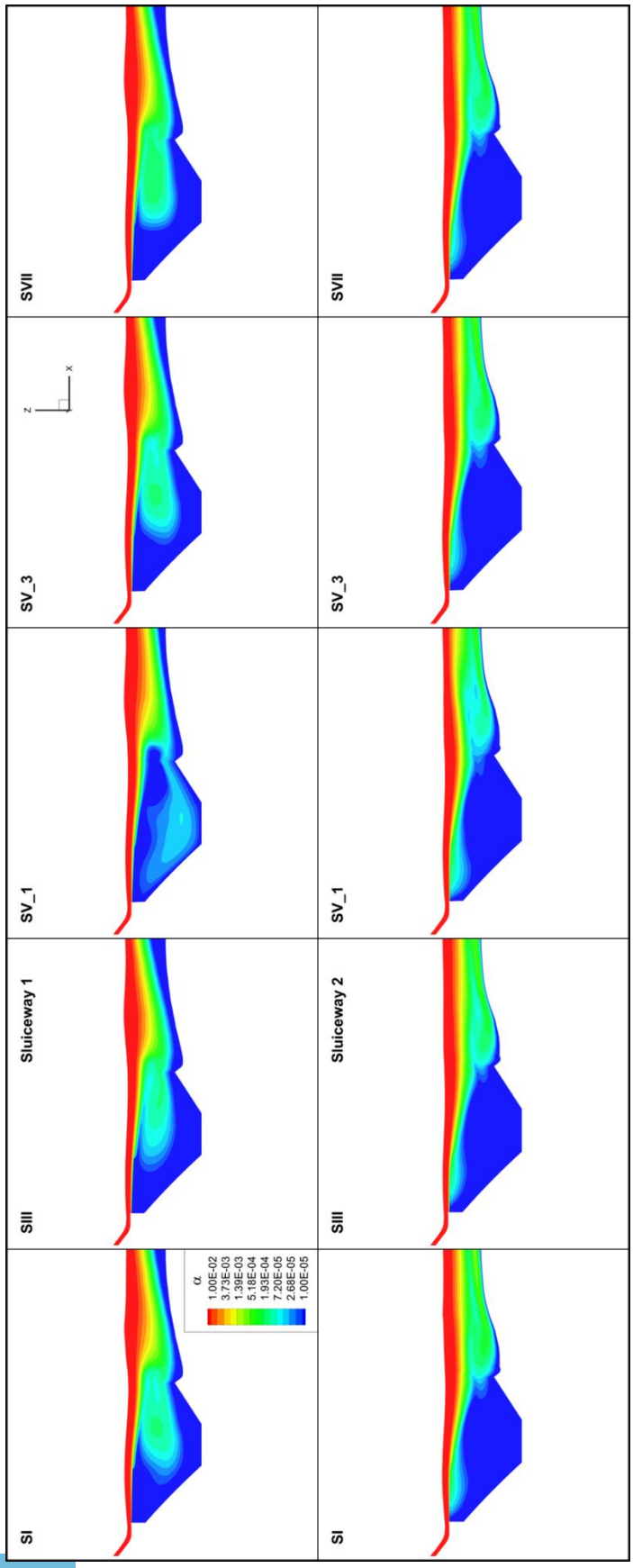

Figure 37. Gas volume fraction at vertical slices passing through sluiceway 1 and 2 for 25 Kcfs

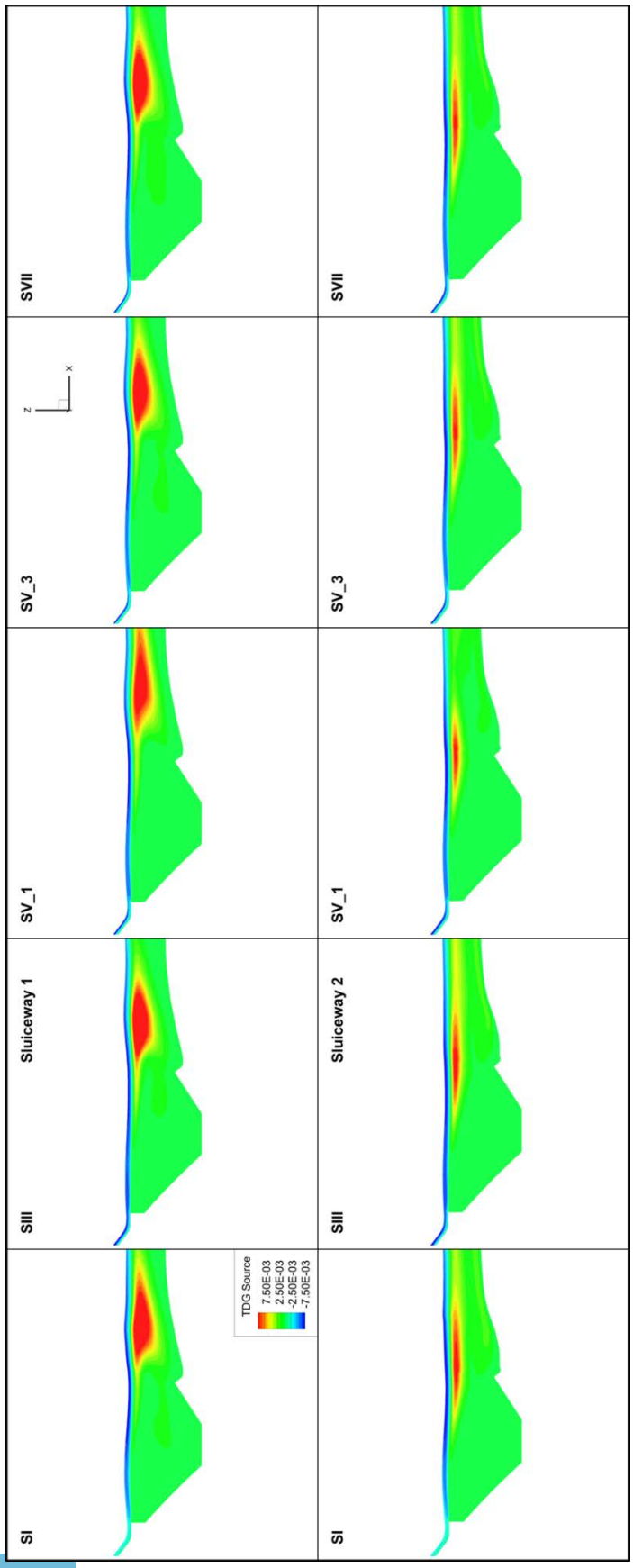

Figure 38. TDG source locations at vertical slices passing through sluiceway 1 and 2 for 25 Kcfs

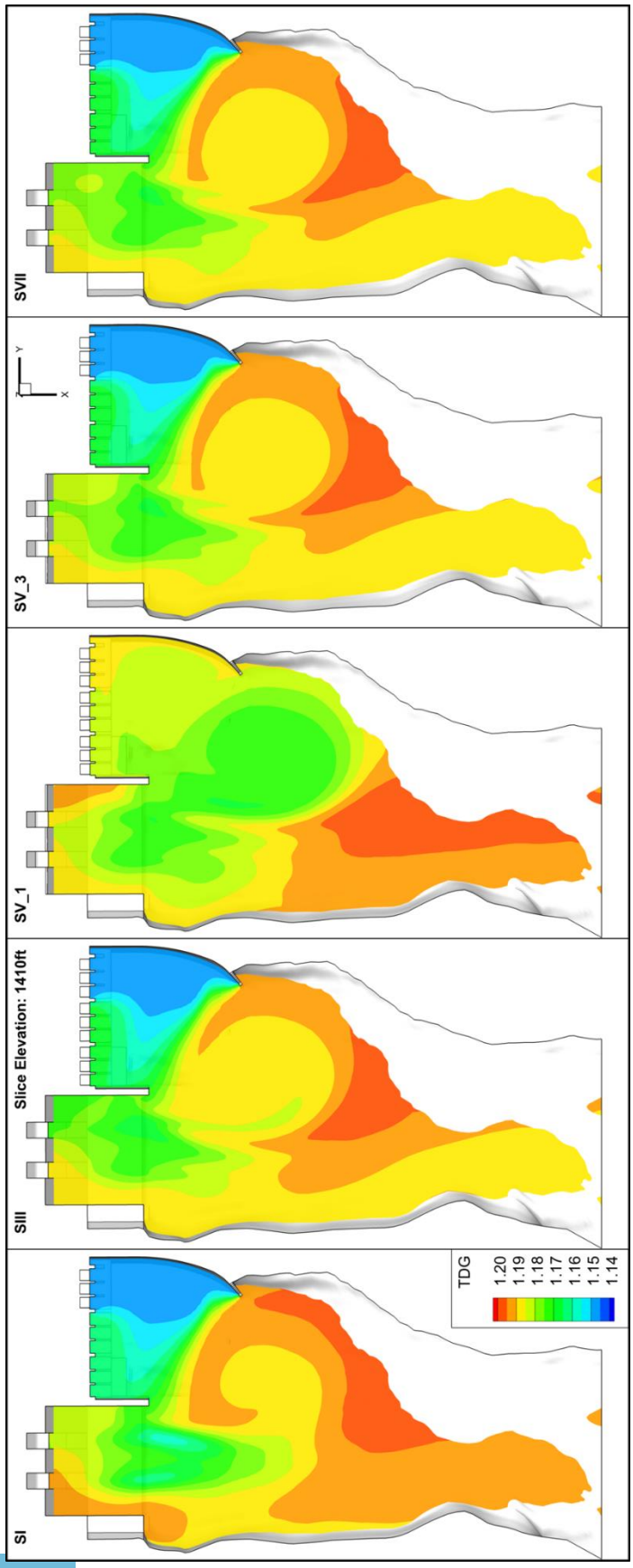

Figure 39. TDG distribution at 1410 ft for 25 Kcfs

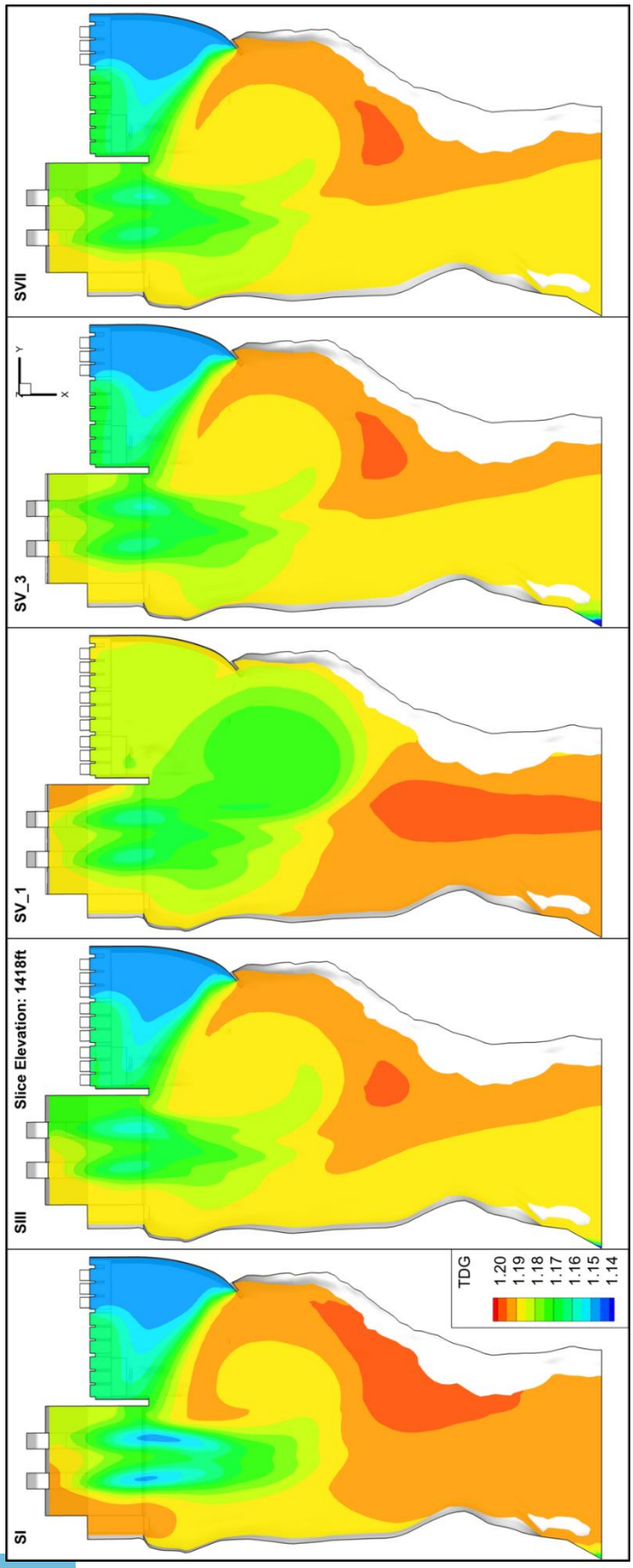

Figure 40. TDG distribution at 1418 ft for 25 Kcfs

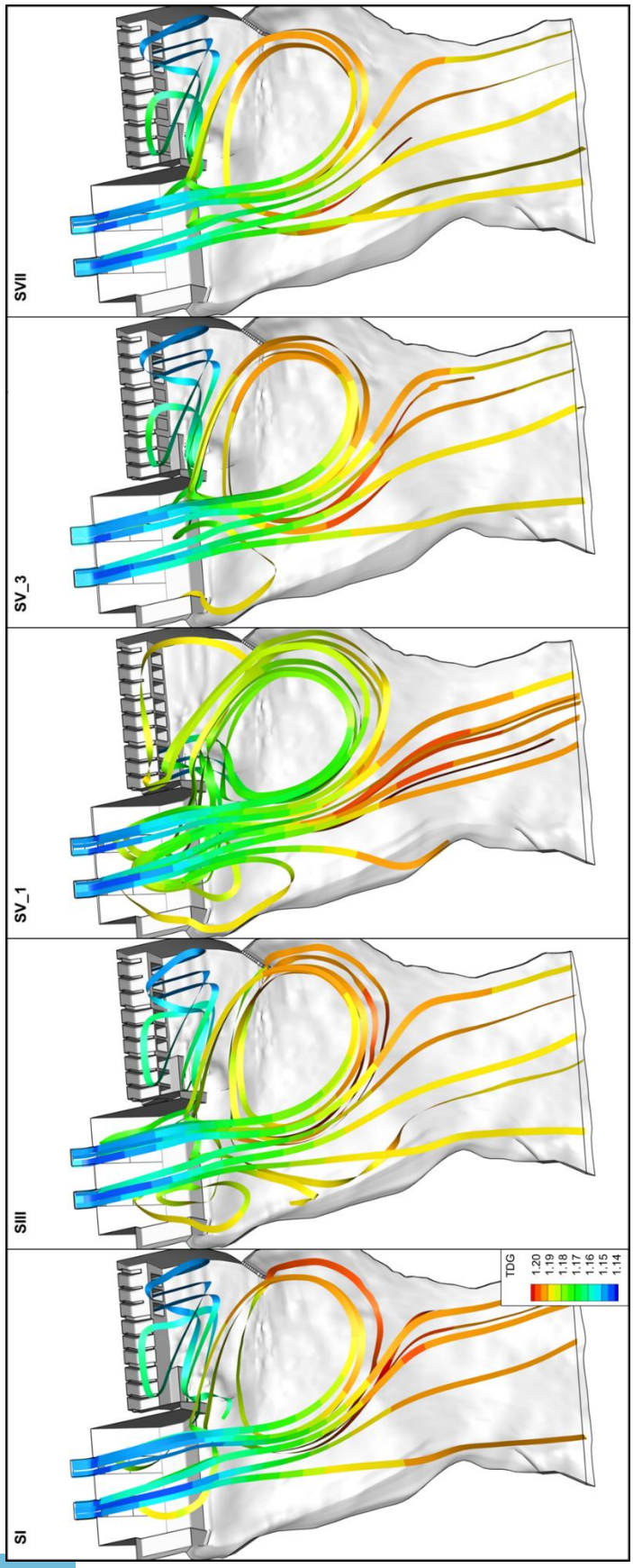

Figure 41. Streamlines colored by TDG distribution

Simulations with 45 Kcfs River Flow

For simulations with 45 Kcfs river flow rate, the elevation for the high slice was adjusted to 1424 ft to more properly capture the information near the free surface. The slice at an elevation of 1410 ft was maintained to allow for comparison to the 25 Kcfs cases.

Velocity vectors for the 45 Kcfs show two distinct differences from the 25 Kcfs simulations, one being the presence of a much longer jet and the other being the absence of the large western eddy in every simulation except for slightly higher deflector geometry, SIV. Although the eddy was diminished in strength or not existent powerhouse entrainment can be seen on all simulations just past the entraining wall of the stilling basin. The eastern eddy was equally as present in these high flow simulations. Figure 42 and Figure 43 show the velocity vectors at both tested elevations. Figure 44 and Figure 45 show contours of velocity in the streamwise direction. The combination of these figures shows that during this higher flow the deflectors more effectively keeps the jet near the surface, where Figure 44 shows a minimal increase in velocity due to the presence of the jets.

Gas volume fraction is shown in Figure 35 and Figure 36, at heights 1410 ft and 1424 ft respectively. For SVI, shortened deflectors, and SVIII, increased radius of curvature, the bubbles were transported into the stilling basin a more significant distance than in SIV, the raised deflector. SII, the baseline deflector seems to have a minimal presence of bubbles in the stilling basin. These figures also clearly show the distinction between flow coming from the sluiceways and flow from the powerhouse. Where flow from the powerhouse contains no bubbles and was seen as a solid blue. This also shows

the effect mentioned earlier that the increased streamwise flow from the powerhouse does not allow the eddy to form decreasing the amount of unsaturated water in the presence of bubbles. Alternatively, Figure 48 shows the gas volume fraction on slices through each of the sluiceways. This figure shows the effects of the powerhouse entrainment that was not seen in verticals slices. Below sluiceway 1, bubbles were pulled to depth in the stilling basin in all simulations. Although SVI does not show bubbles in significant depth the number of bubbles present below the jet was greater than the other simulations. For a higher flow rate the baseline deflector was more effective in keeping bubbles from tending to depth in the tailrace.

Figure 49 shows slices through the sluiceways of the TDG source where the location of the TDG production has moved upstream in comparison to the 25 Kcfs simulations. The TDG production for sluiceway 2 of SII appears to be significantly less than the other simulations at this location. SVIII, the increased radius of curvature deflector, shows significant TDG production downstream of sluiceway 1. Figure 50 and Figure 51 show TDG at vertical slices of 1410 ft and 1424 ft where it can be immediately noticed the TDG present in simulation SVI, the shortened deflector, was greater than any other simulation. This coincides with the information of gas volume fraction from previous figures where SVI had the highest level of bubbles present in the stilling basin and near the jets. Although both SII and SIV show similarly low levels of TDG, Figure 43 shows the presence of the western recirculation that could affect the proper operation of the fish trap. Streamlines colored by TDG are shown in Figure 52 where three streamlines were released from each sluiceway and one streamline was released from each powerhouse draft tube. Powerhouse entrainment can be seen for all simulations

mostly stemming from powerhouse unit 1 and 2. Powerhouse unit 3 does not contribute to entrainment in any simulation. In SIV, raised deflector, flow from powerhouse 3 was caught in the large western eddy. The streamlines show an increased and otherwise unseen effect of the eastern eddy. SVI shows a large eastern eddy that pushes the jet toward the center of the reach as well as transporting bubbly flow from the jets back upstream and underneath the deflectors. This flow passes underneath the sluiceway 2 deflector and rejoins the flow in the sluiceway 1 jet and was transported downstream as high TDG flow.

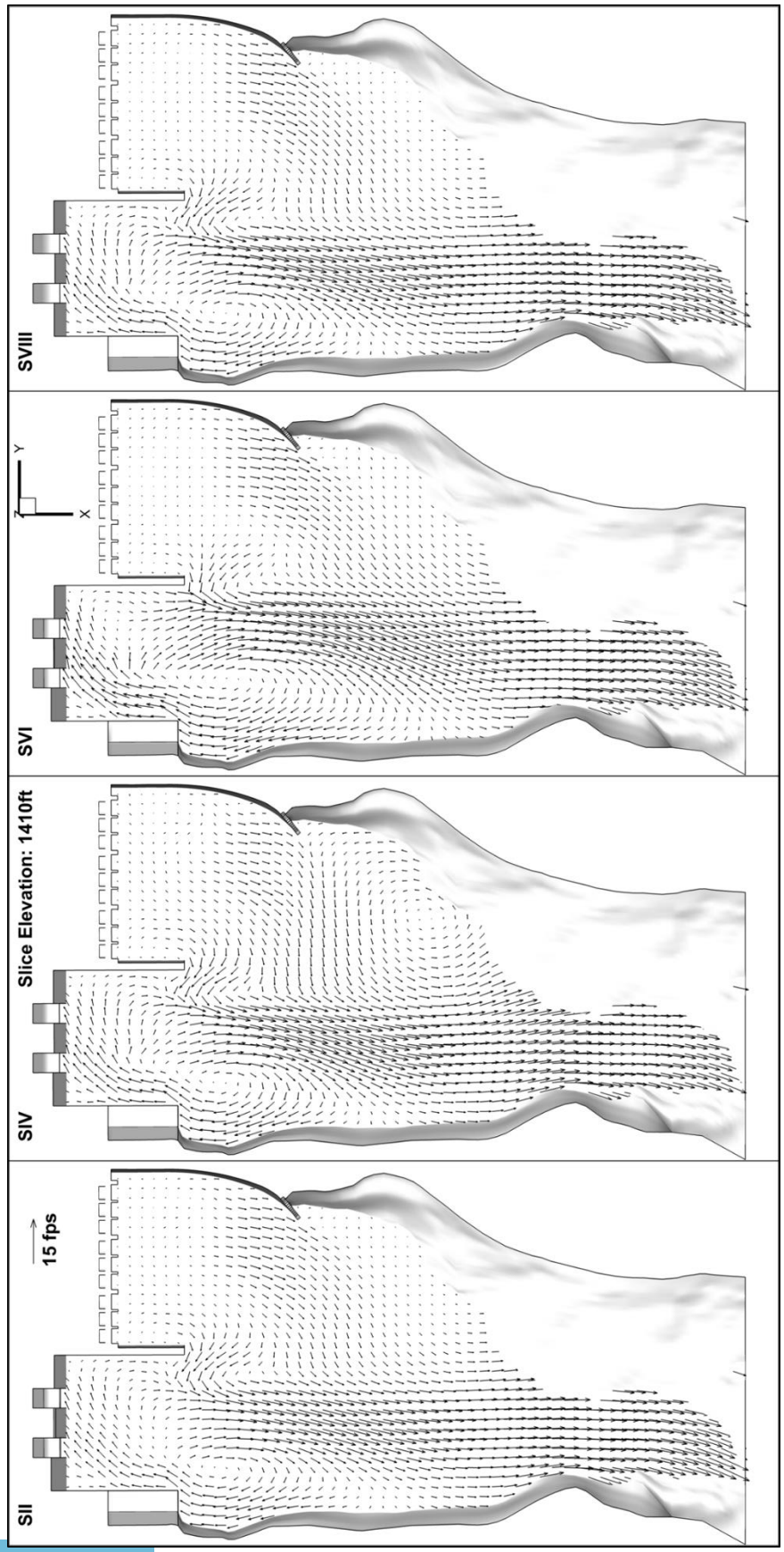

Figure 42. Velocity vectors at 1410 ft for 45 Kcfs

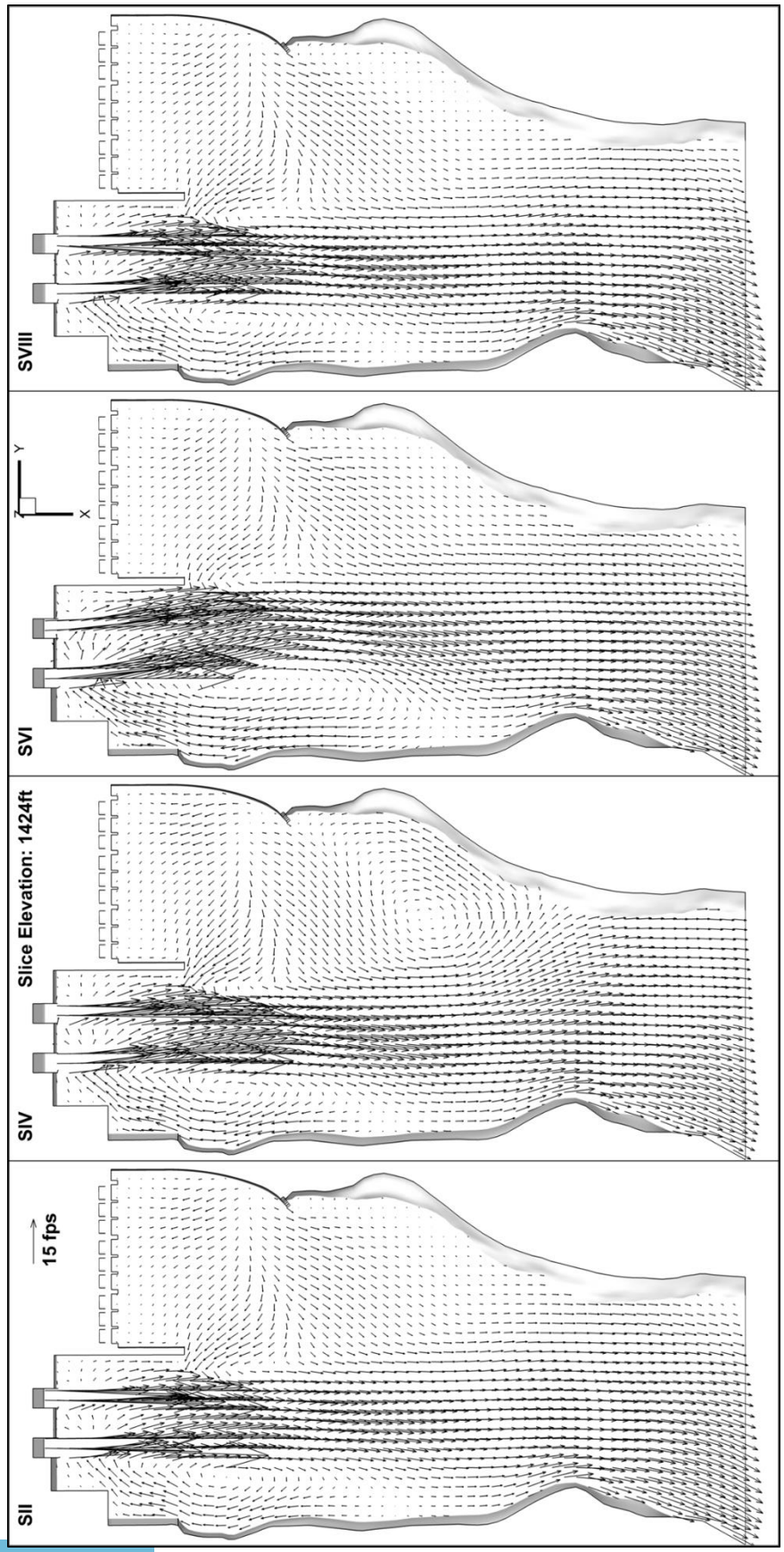

Figure 43. Velocity vectors at 1424 ft for 45 Kcfs

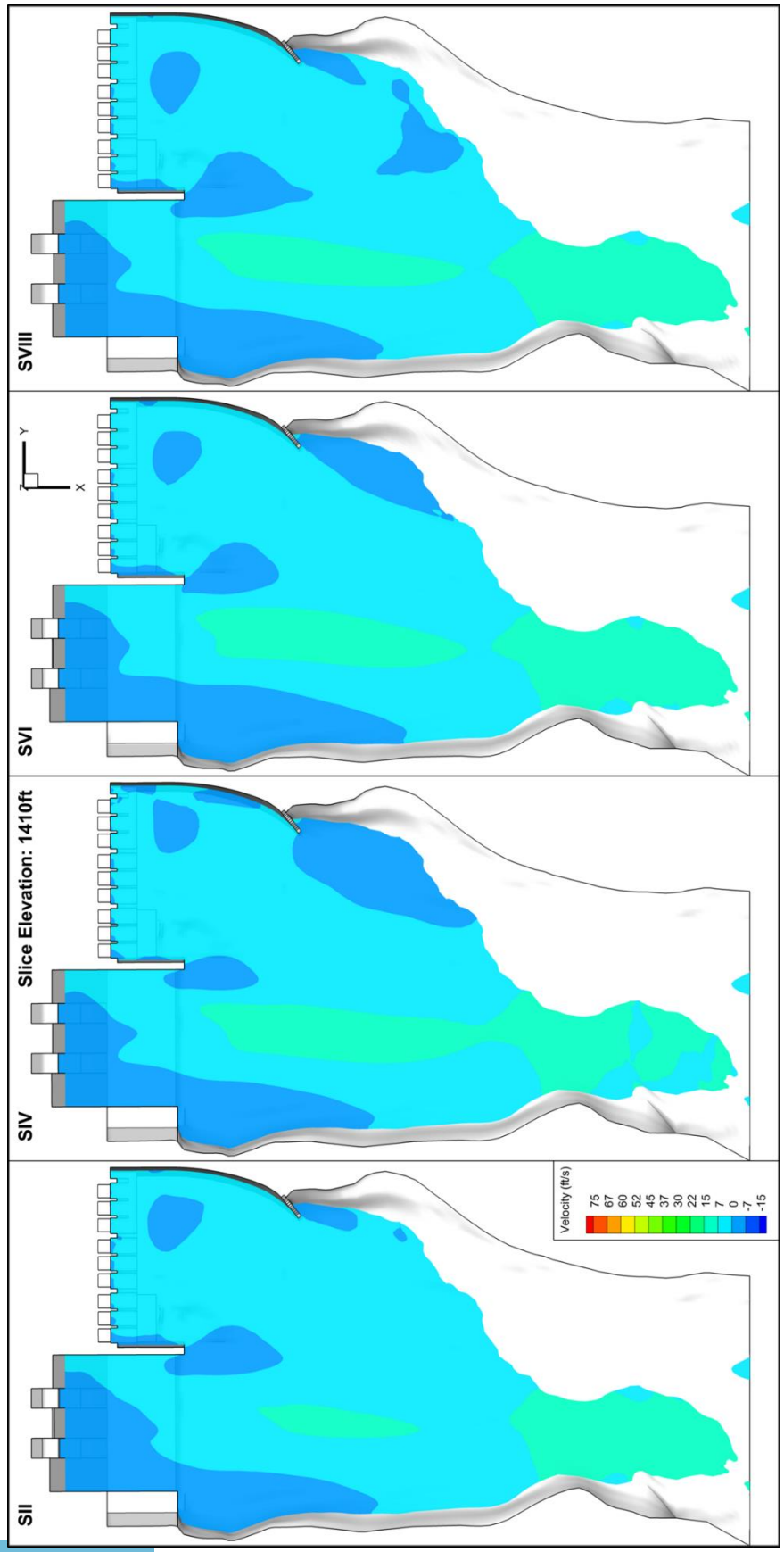

Figure 44. Velocity contours at 1410 ft for 45 Kcfs

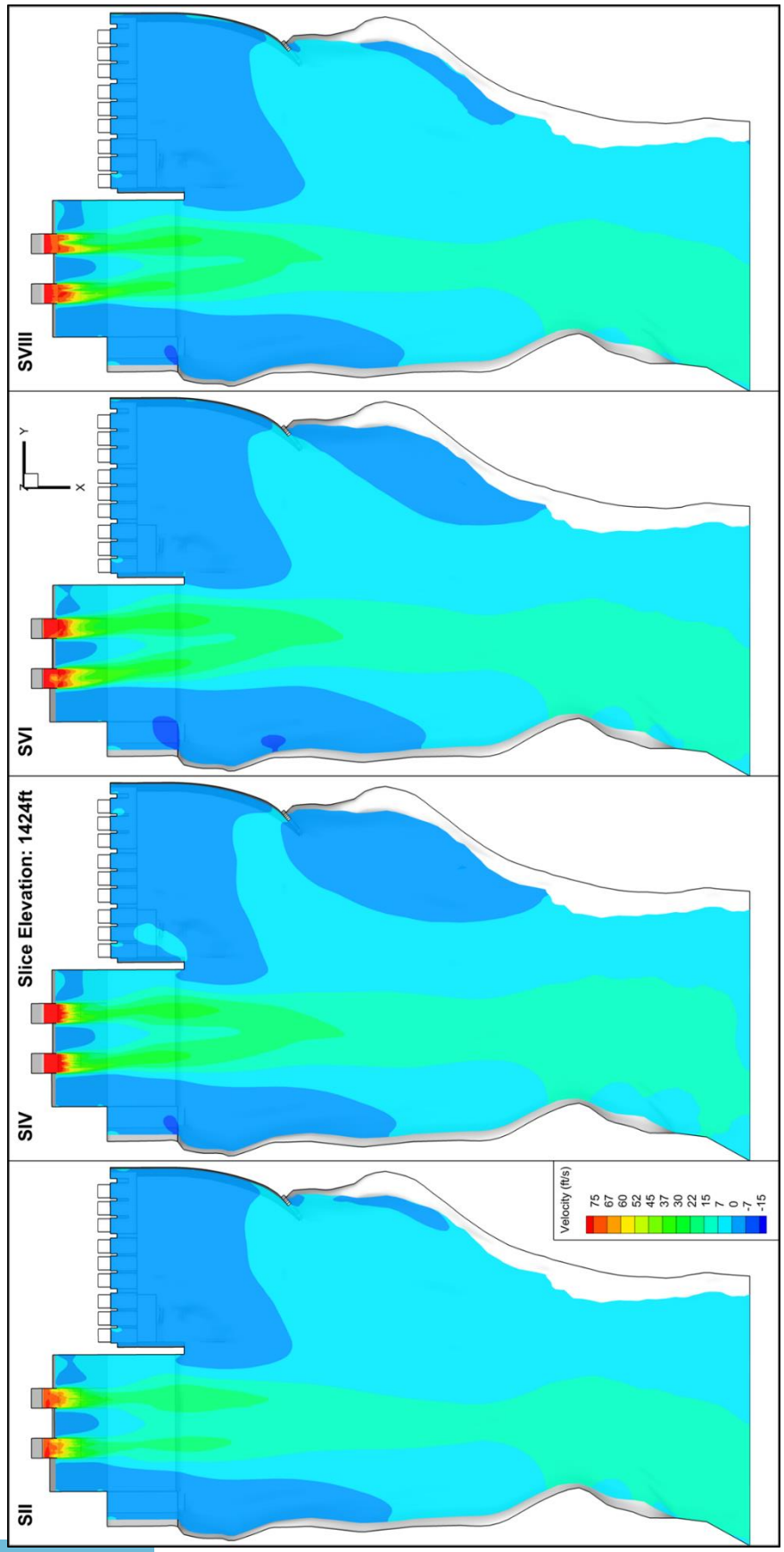

Figure 45. Velocity contours at 1424 ft for 45 Kcfs

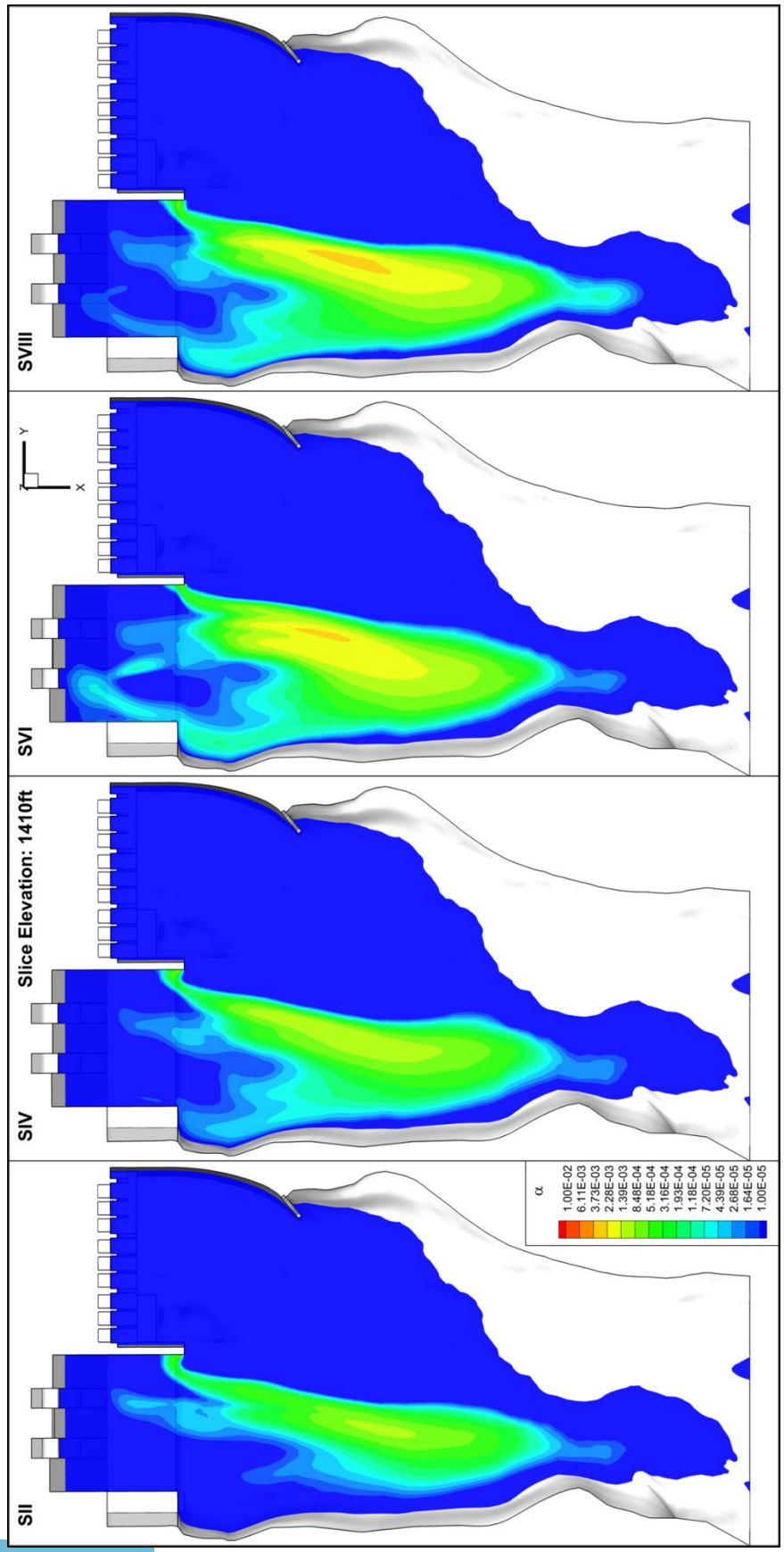

Figure 46. Gas volume fraction contours at 1410 ft for 45 Kcfs

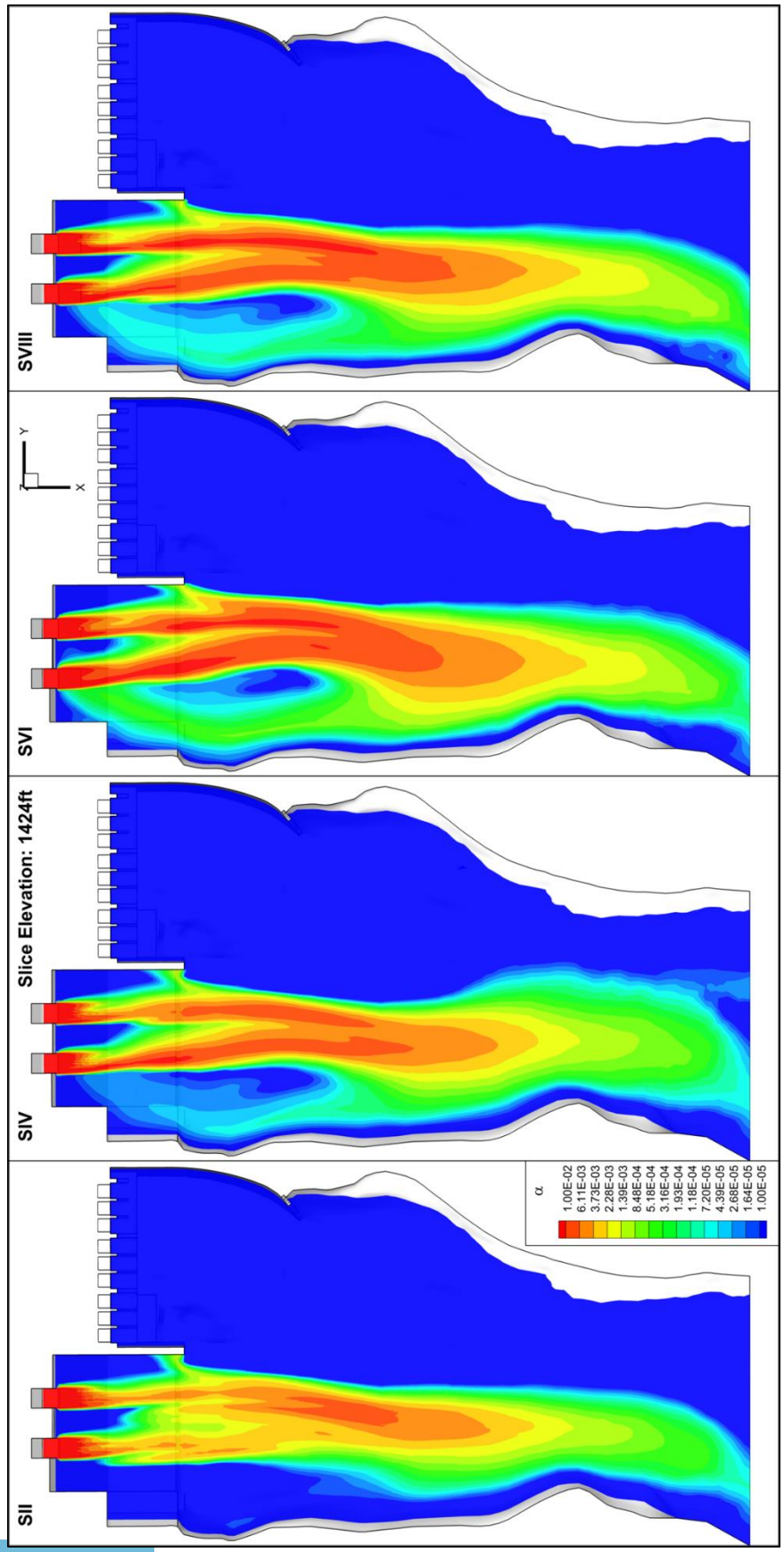

Figure 47. Gas volume fraction contours at 1424 ft for 45 Kcfs

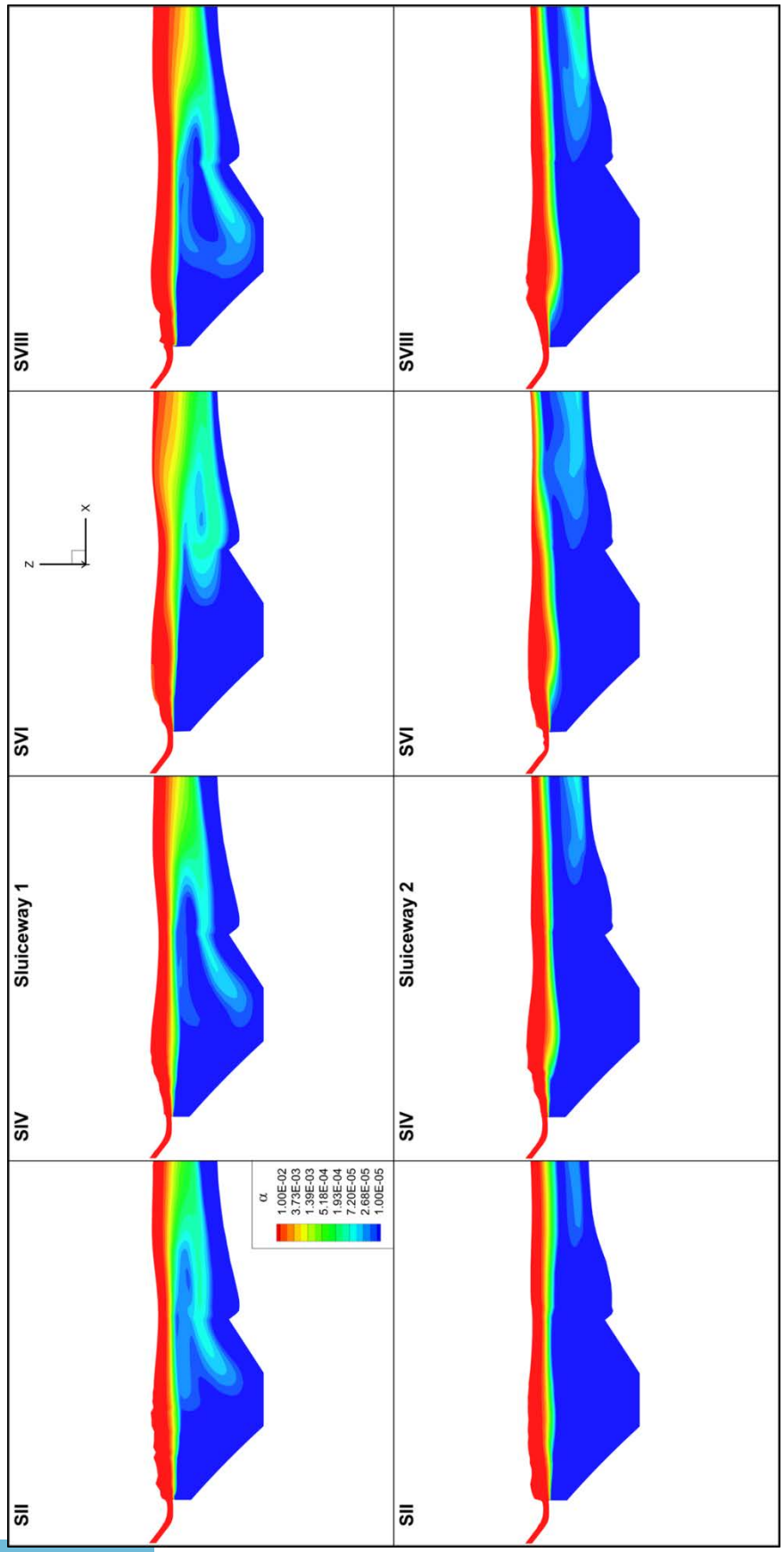

Figure 48. Gas volume fraction contours at vertical slices passing through sluiceway 1 and 2 for 45 Kcfs

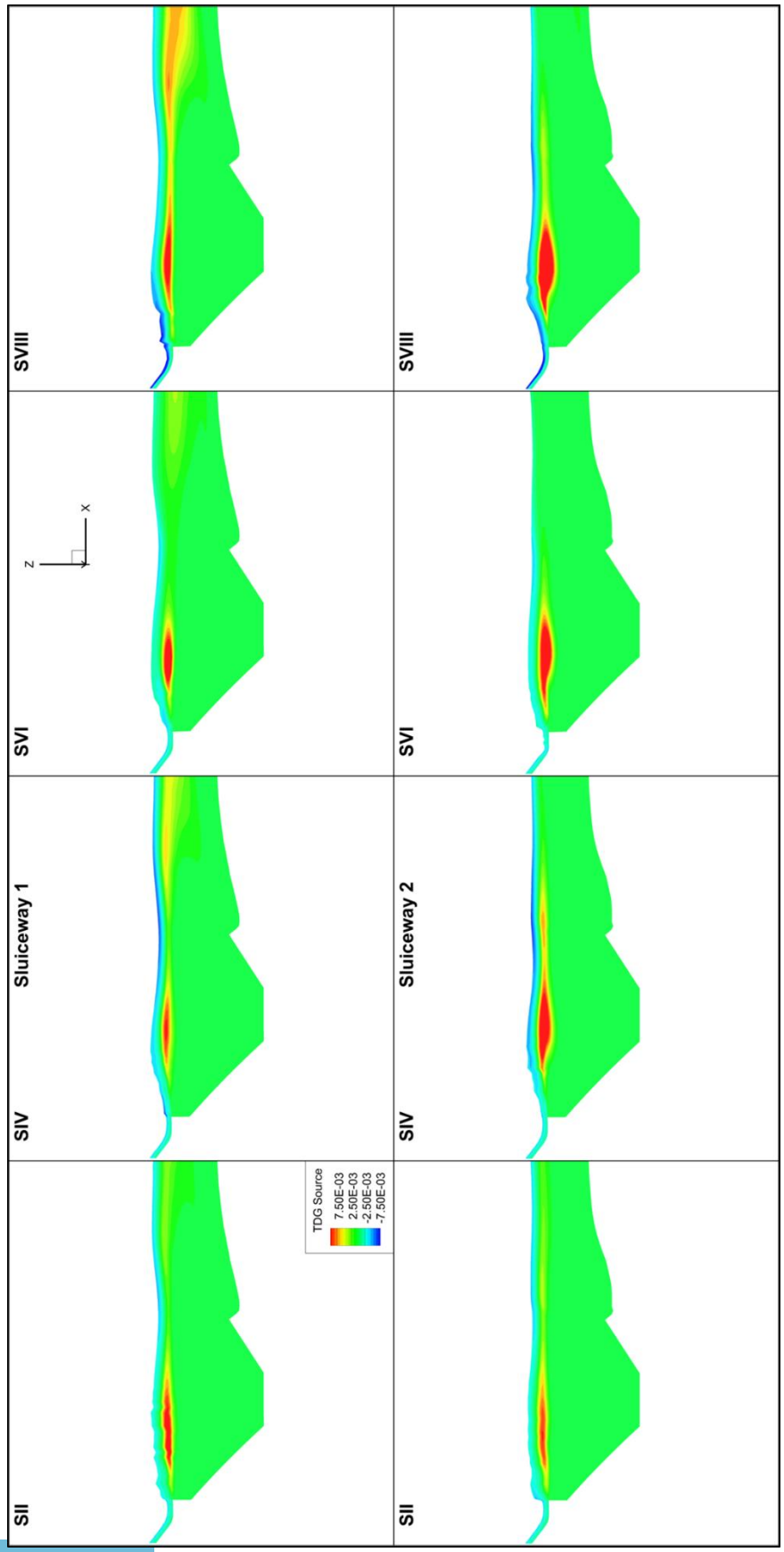

Figure 49. TDG source locations at vertical slices passing through sluiceway 1 and 2 for 45 Kcfs

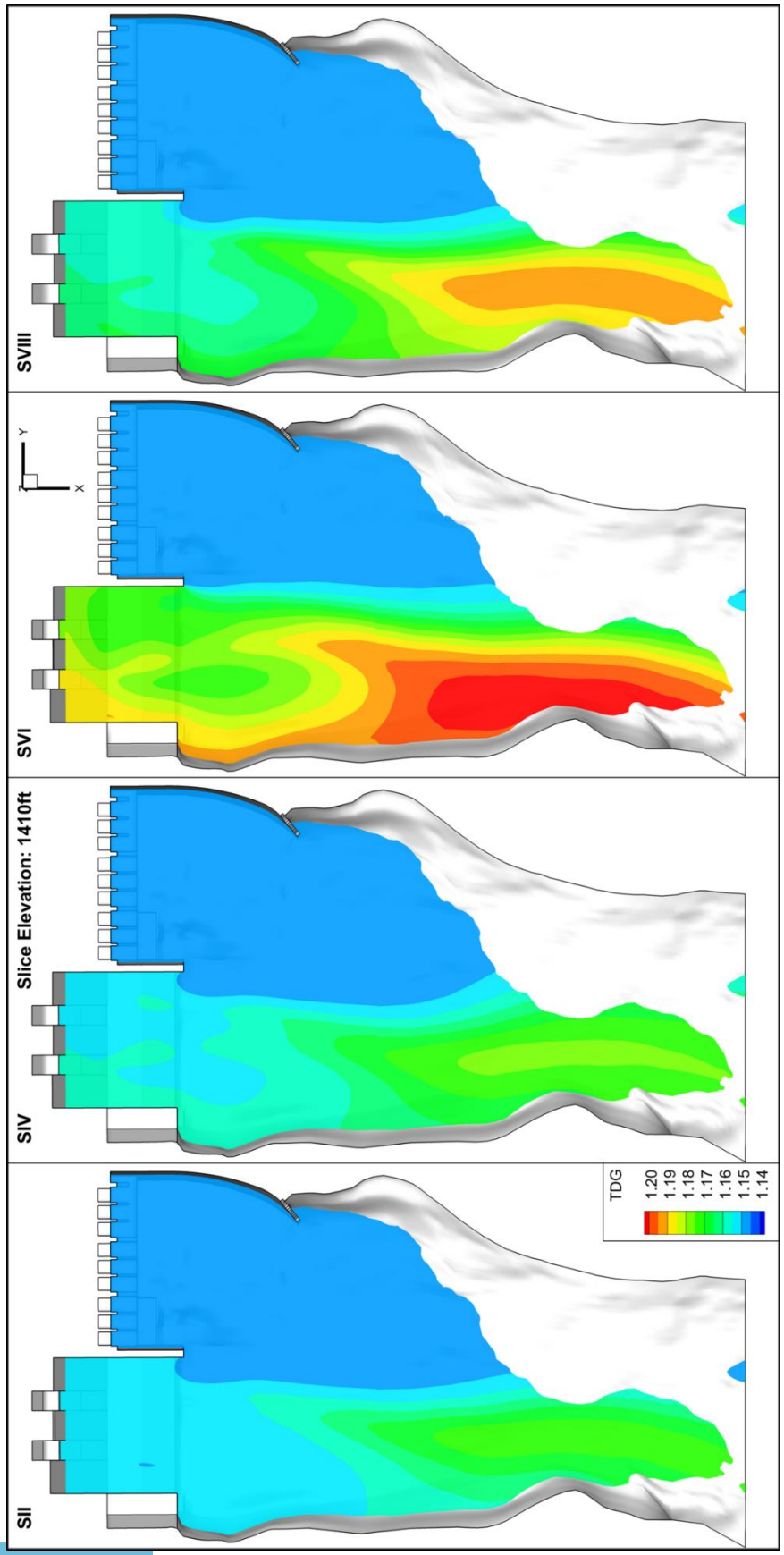

Figure 50. TDG contours at 1410 ft for 45 Kcfs

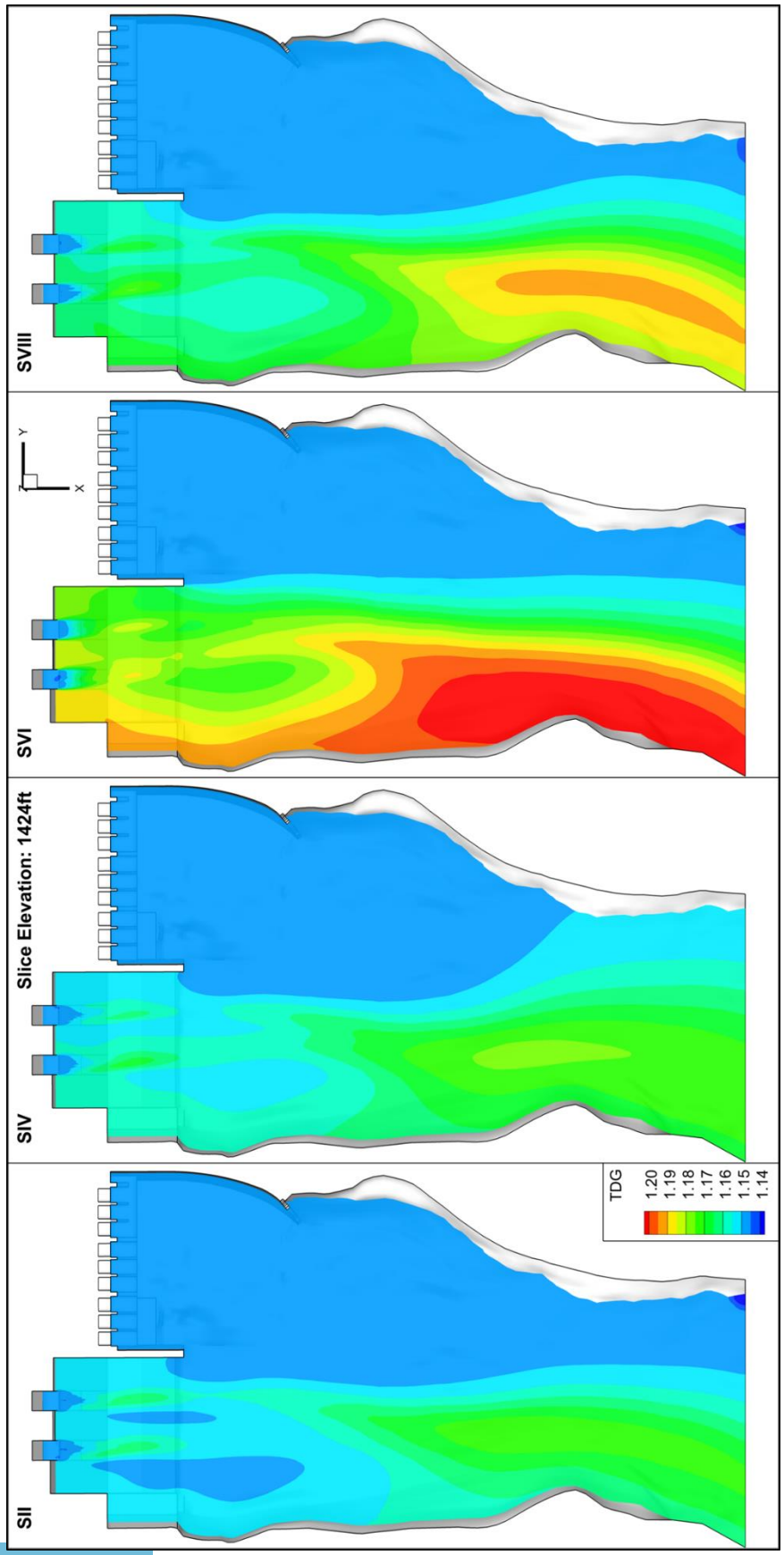

Figure 51. TDG contours at 1424 ft for 45 Kcfs

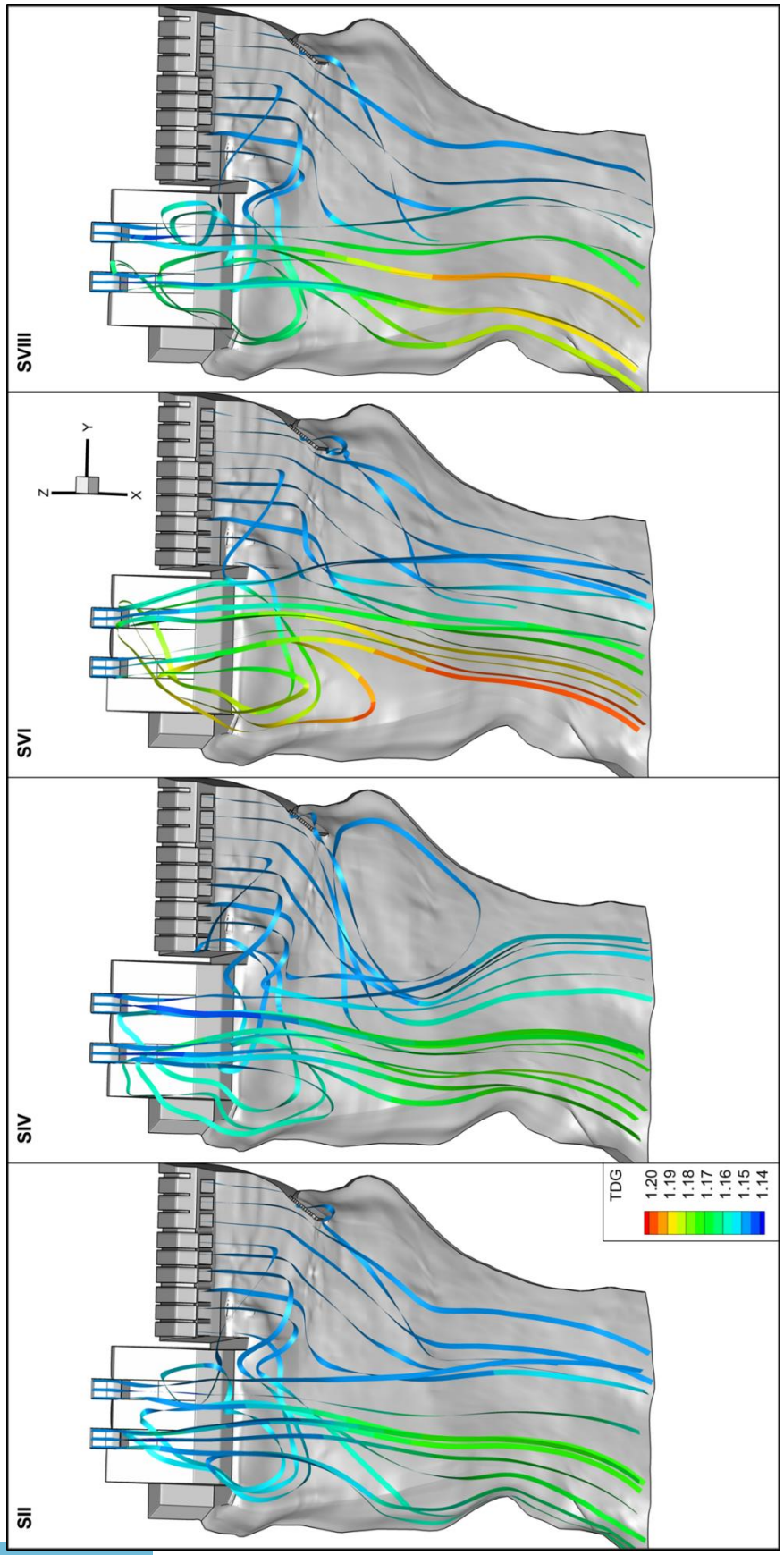

Figure 52. Streamlines colored by TDG for 45 Kcfs

Powerhouse Entrainment

Entrainment of powerhouse flow by the sluiceway jets improves the mixing of powerhouse flow and bubbly spillway flow, and may negatively affect fish migration or create undesired flow conditions (Turan et al., 2007). Proper estimation of entrainment began with determining a region were entrainment could be calculated for all simulations. The stilling basins training wall was chosen as the location to calculate entrainment. As seen in Figure 53, 9 planes were created perpendicular to the streamwise direction. The entrainment calculations were performed on the rigid-lid simulations. In order to compare the different simulations only the region of the plane inside the flow and with a negative y-direction, entraining flow, was considered in the calculation.

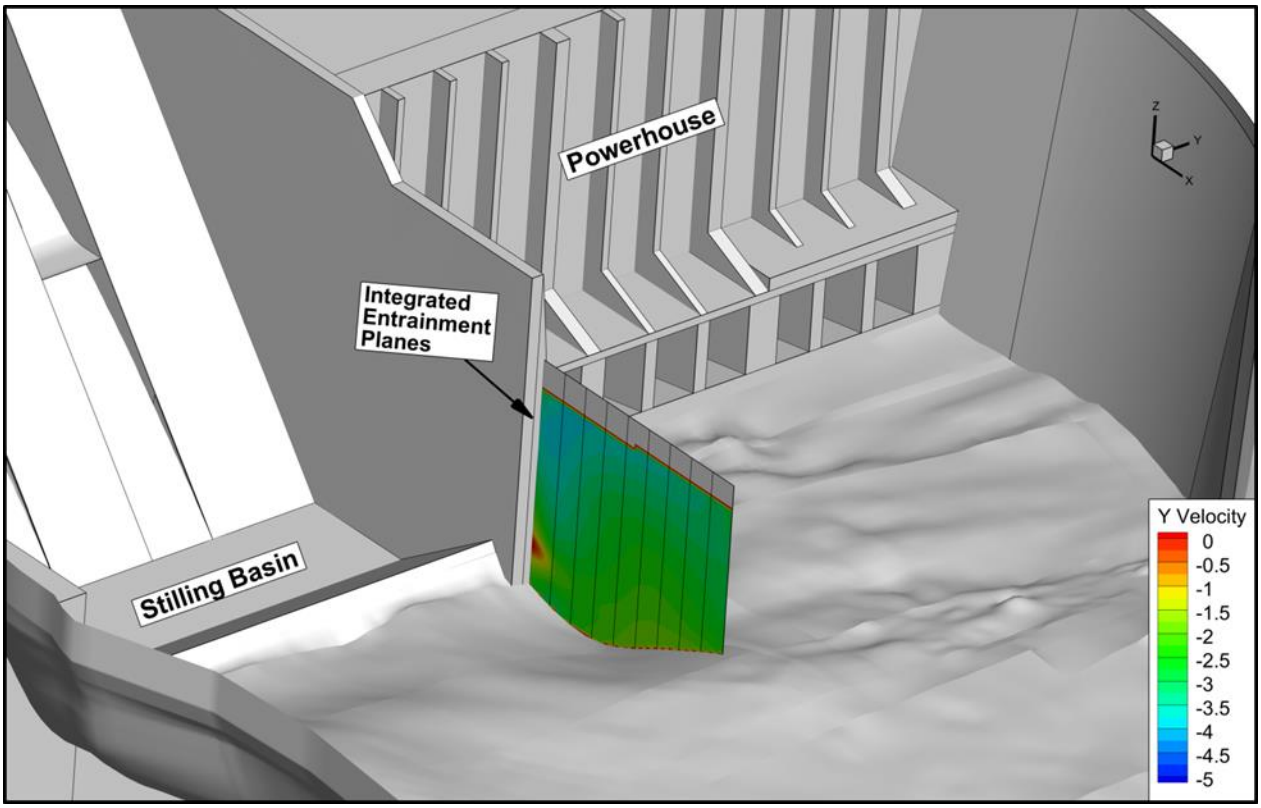

Figure 53. Segmented planes used to compute powerhouse entrainment

The entrainment values for the 25 Kcfs simulations was above the total powerhouse flow within 30 ft of the dividing wall's edge, Figure 54. This indicates the significant role the western eddy plays in the overall entrainment. Although the simulation with powerhouse 1 operating initially has more entrainment, the magnitude of the entrainment diminishes as the distance from the wall increases. The numerically lower entrainment value coincides with the weaker western eddy generated, as seen in Figure 34 or Figure 35. Net entrainment for SV_1 was less than the simulations operating with powerhouse 3. The entrainment for the raised deflector, SIII, as well as the deflector with the increased radius, SVII, was slightly greater than the simulation with the shortened deflector, SV_3, and the baseline deflector, SI. Entrainment for the 45 Kcfs simulations was shown to be significantly less than the 25 Kcfs flow entrainment, Figure 55. This was attributed to the absence of the western eddy, consequent of the increased streamwise flow from the powerhouse. SII was shown to have the least amount of entrainment, about 20% less than SVIII at a distance of 70 ft from the training wall. SIV, with the raised deflector, shows the greatest amount of entrainment maintaining a near linear increase over the distance of 90 ft from the training wall.

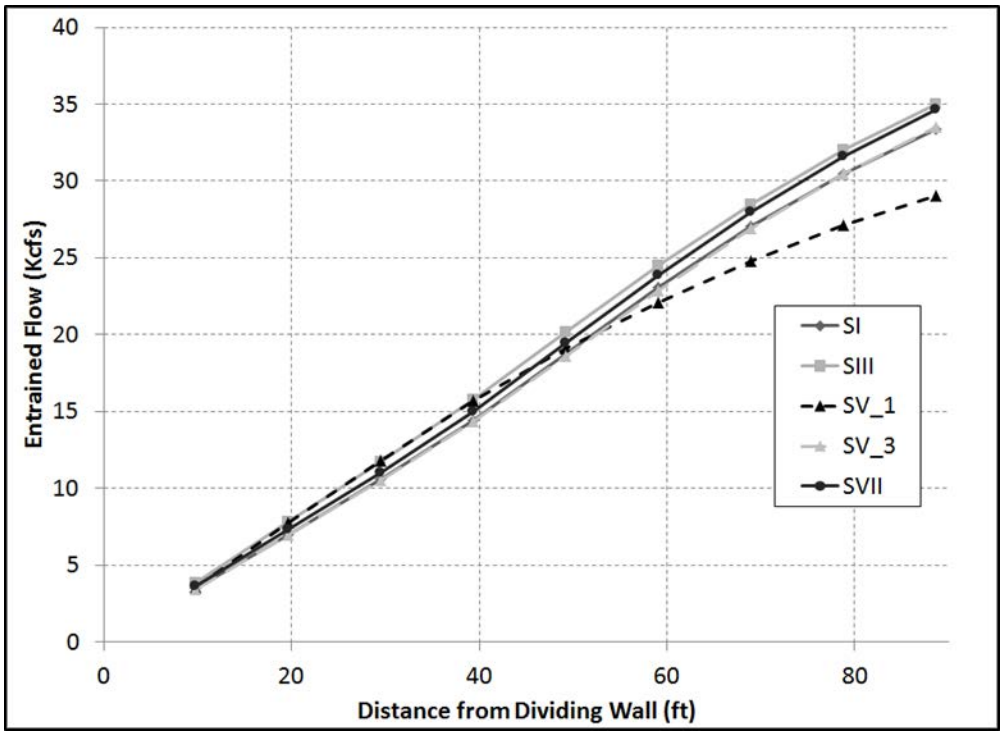

Figure 54. Powerhouse entrainment for the 25 Kcfs simulations

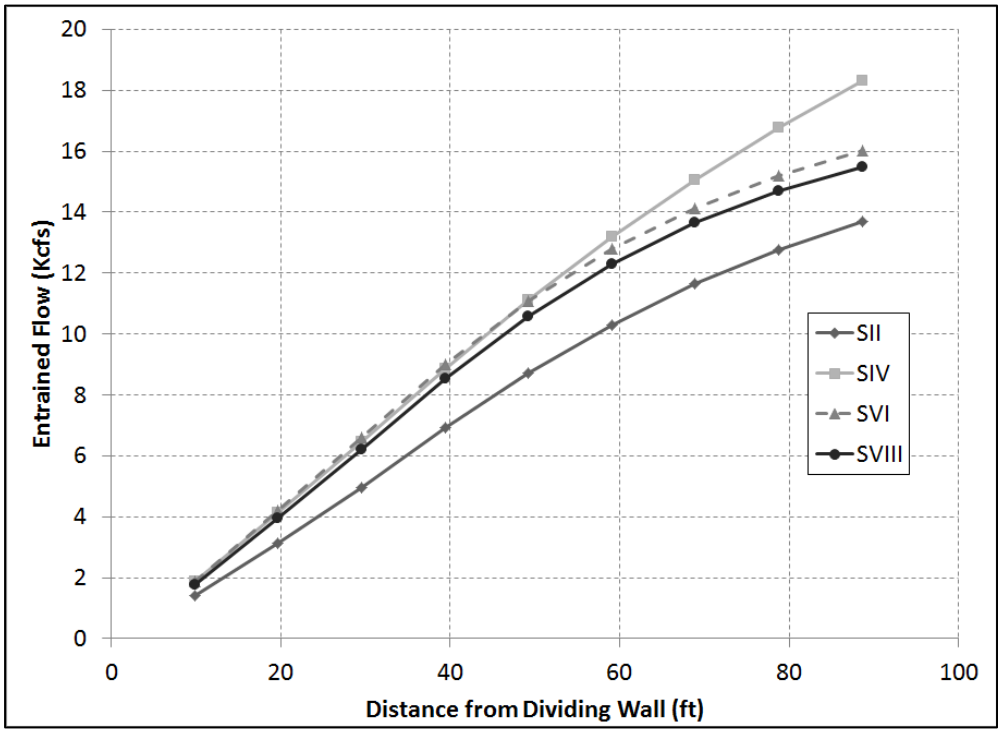

Figure 55. Powerhouse entrainment for the 45 Kcfs simulations

Water Surface Elevation near the Fish Trap

A secondary performance characteristic determined by IPC was the generation of waves near the already constructed fish trap. The fish trap consists of two different entrances, one for high flow and the other for low flow. For the 25 Kcfs and 45 Kcfs conditions the high flow entrance was above water and will therefore not be considered for these conditions.

Wave generation was estimated using the VOF simulations from earlier in Chapter V. Tecplot 360 was used to post process time dependent data files and extract water surface elevation at the fish trap. Located 230 ft downstream of the powerhouse draft tubes on the western bank. Figure 56 and Figure 57 show the water surface elevation at the fish trap lower entrance, for the 25 Kcfs and 45 Kcfs flows respectively. The initial instability in the plot stems from the stabilizing of the initialized VOF simulation, jets introduced to a stationary flow condition. The plots show otherwise that the wave height, for any of the simulations, was insignificant.

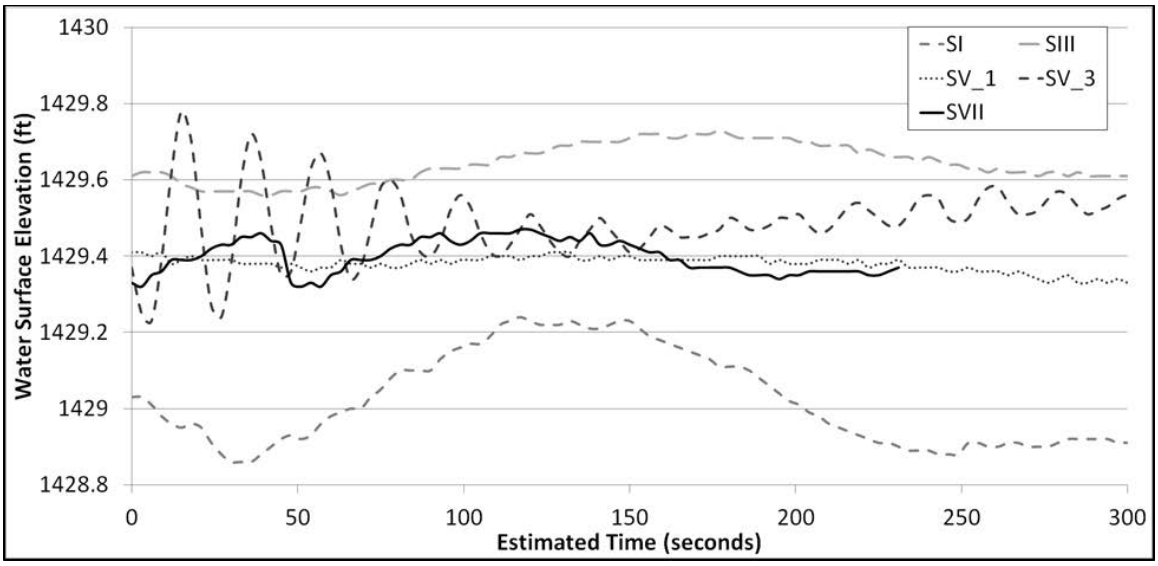

Figure 56. Near fish trap elevation for the 25 Kcfs simulations

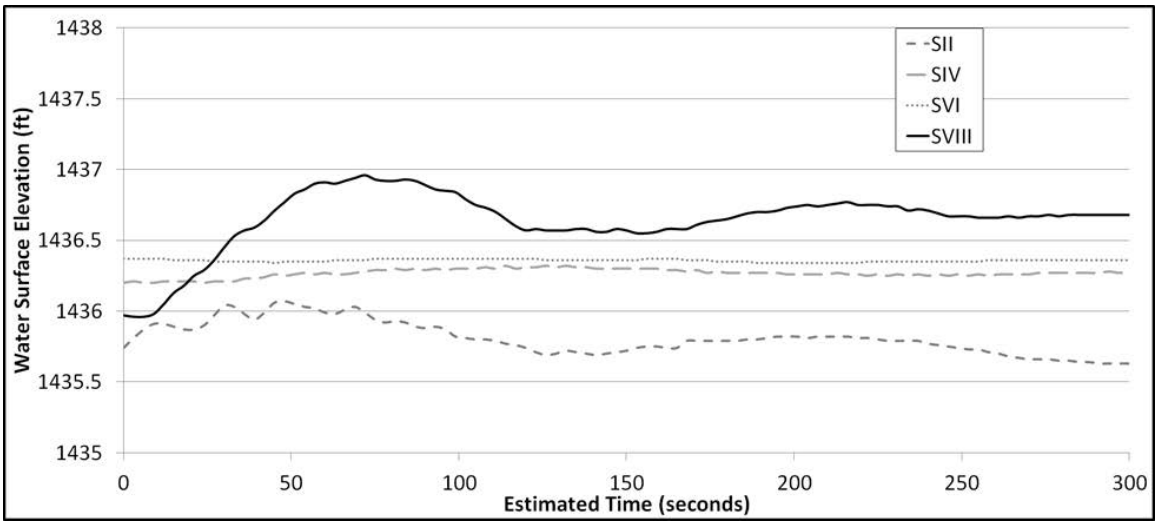

Figure 57. Near fish trap elevation for the 45 Kcfs simulations

Deflector Selection

Deflectors play a significant role in altering the tailrace flow. In all simulations with a 25 Kcfs flow rate as well as SVI, the raised deflector 45 Kcfs case, a large western eddy was present. This eddy presents issues by both changing the flow direction near the fish trap, altering the flow pattern it was designed for, as well as causing the entrainment of unsaturated powerhouse flow into regions where bubbles were present, thus increasing TDG production. For all other simulations the recirculation was negligible.

Low flow, 25 Kcfs, simulations had similar bubble transportation and TDG production. Concluding deflector geometries did not play a significant role at this elevation. For the high river flow, 45 Kcfs, simulations a high TDG values were seen with the shorter deflector, SIV, where water plunges to depth shortly after the stilling basin. This was followed by the increased transition radius producing the next most TDG

concentration. The baseline case as well as the simulation with the slightly higher deflector provided similar TDG values.

Given high TDG values were produced from the shorter deflector and the deflector with the larger transition radius, SIV and SVIII, those deflectors can be rejected as possible qualifying geometries. This leaves the similarly performing baseline and raised deflector. However, the shortened deflector causes a backflow and recirculation near the fish trap, an IPC established undesirable effect. The baseline deflector was chosen as the most effective to prevent TDG production as well as minimize changes in the flow field.

CHAPTER VI
DEFLECTOR PERFORMANCE

Volume of Fluid Simulations

Jet regimes at different IPC chosen flow rates of 37 Kcfs, 45Kcfs and 71.5 Kcfs were determined using the VOF approach. Figure 58 shows the free surface shape colored by elevation. Free surface shape for the 37 Kcfs flow was most closely related to that of a surface jump, where the jet was submerged. For this 37 Kcfs simulation, the powerhouse operation was at the full capacity of 30 Kcfs. The 45 Kcfs and the 7Q10 with deflector flows show a more surface jet flow regime. With the 7Q10 with deflector flow showing a large depression above the stilling basin due to the high velocity jets, this depression measures approximately 15 ft below the estimated tailwater elevation at the outflow. The 7Q10 flow without deflectors present shows an entirely chaotic flow where large waves were present in the stilling basin and propagating downstream toward the fish trap.

Figure 59 show the velocity components of the flow interpolated onto a structured plane. This structured plane shows the relative length of the jets as well as their directional tendencies. Showing the beginning of the jet for the 37 Kcfs flow tends to pitch upward whereas the 45 Kcfs and 71.5 Kcfs flows were directed heavily in the streamwise direction with very little angle present. A large western eddy was present in the 7Q10-D simulation. The 7Q10 no deflector case does not seem to contain any direction or control.

Slices through the sluiceways for the deflector cases are shown in Figure 60, whereas for the no deflector 7Q10 case slices are shown through the eastern and central spillways, 3 and 2 respectively. These figures show the velocity components of the flow

interpolated onto the vertical slice. The 37 Kcfs solution shows the weakness of the jet and the minimal effect it has on the flow just past the stilling basin. The 7Q10 deflector condition shows an extremely strong jet with high velocities extending far into the tailrace. Shortly after the stilling basin a hydraulic jump was visible downstream of sluiceway 1. Below the jet and the jump a vertical recirculation was visible moving water into the stilling basin. The recirculation was also visible below sluiceway 2 although it was milder. Strong flow was present until the bottom of the stilling basin in the no deflector case. High flow into the stilling basin causes a large hydraulic jump and induces back rolls in the stilling basin. Hydraulics jumps are indicative of areas where highly aerated flow will be introduced into the domain, making the simulation more diffusive.

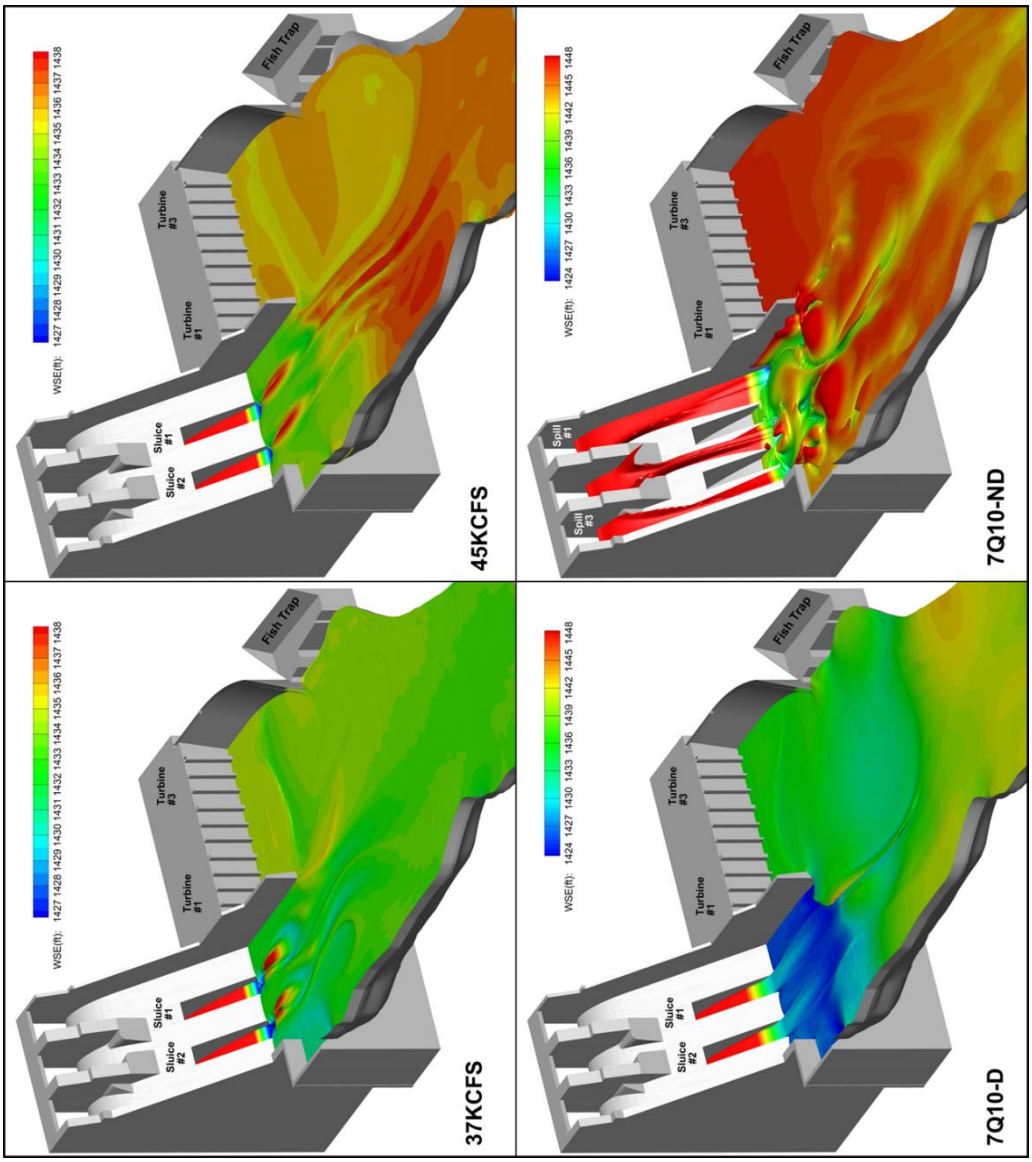

Figure 58. Free surface colored by elevation for the selected deflector

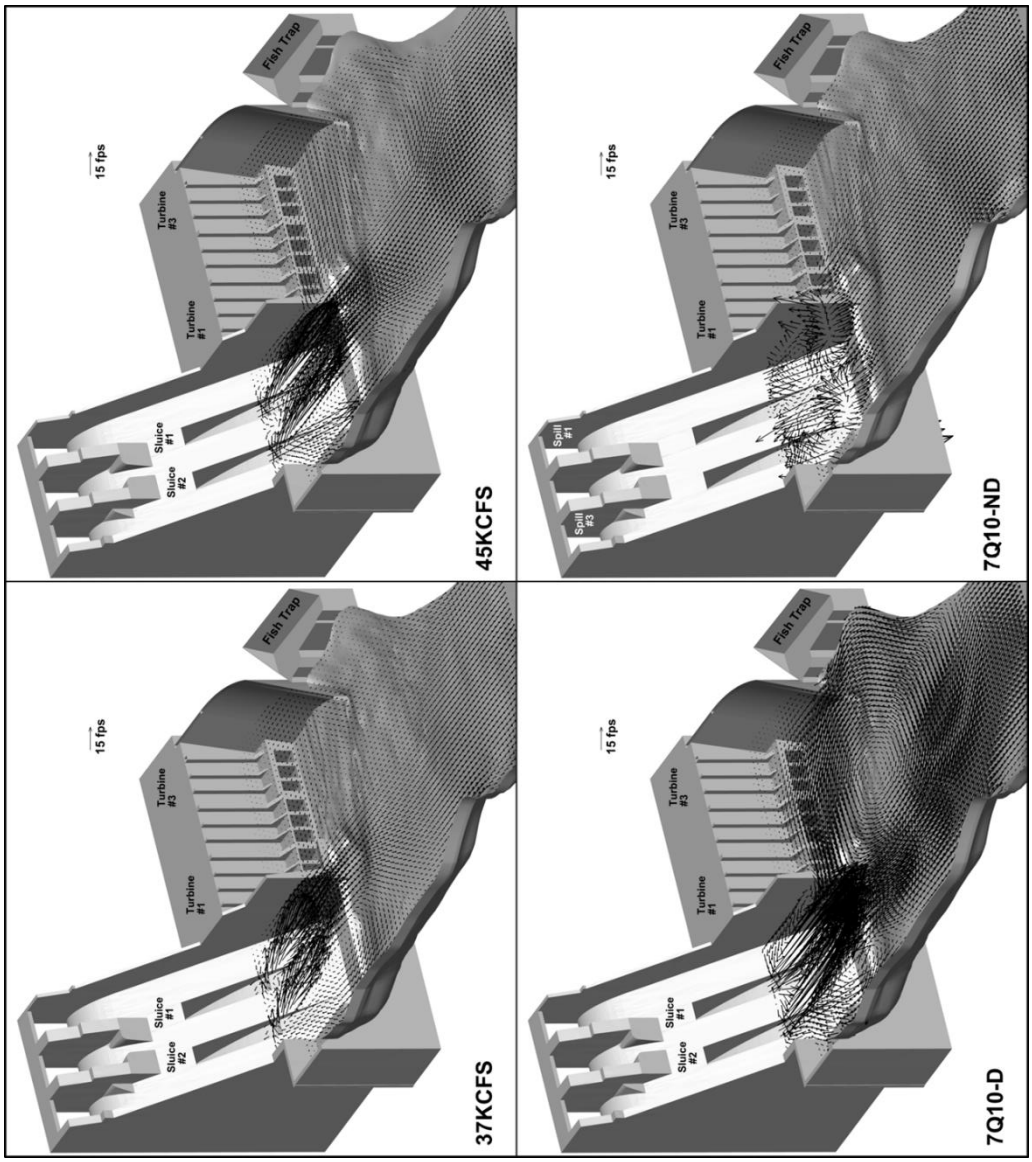

Figure 59. Velocity vectors at vertical slices just above the sluiceways for selected deflector

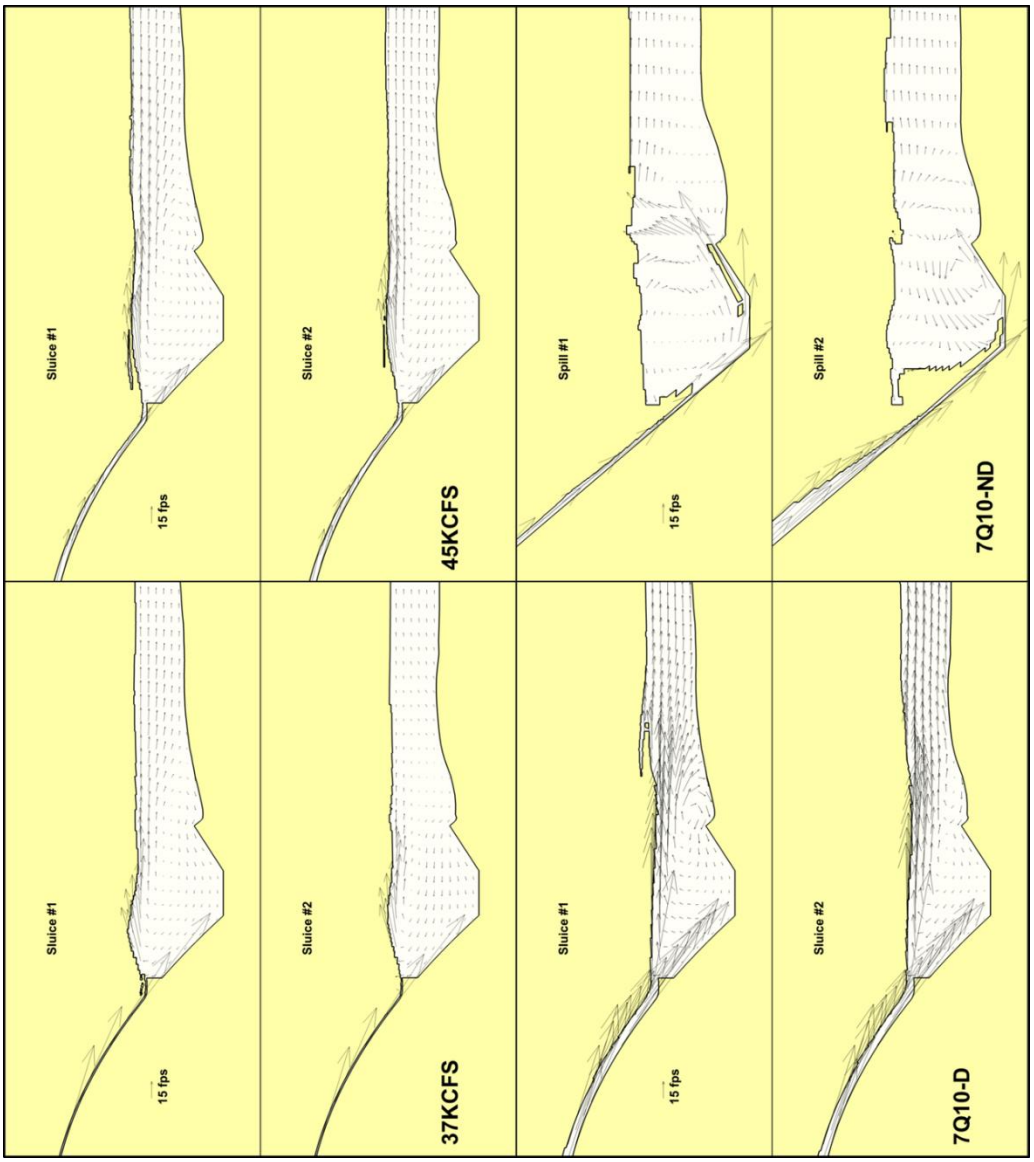

Figure 60. Velocity vectors at slices passing through the sluiceways for selected deflector and through spillway 1 and 2 for the no deflector case

Rigid-lid Simulations

Slices for comparing tailrace flow patterns were made at 1410 ft and 1424 ft, Figure 61 and Figure 62. The slices show the prominent eastern recirculation just downstream of the stilling basin for all of the simulations. For the 37 Kcfs and 45 Kcfs flow; the powerhouse flowrate was significant enough to overcome the western recirculation. For the high flow deflector case, the powerhouse flow was not strong enough to overcome the recirculation effects caused by the jet. A recirculation near the fish trap for the 7Q10 no deflector case was observed in both the high and low slices. Streamwise velocity contours are seen in Figure 63 and Figure 64. The lower slice shows the depth contrast of jet effects in the tailrace, where the 7Q10 jet effects the flow more deeply than the 37 Kcfs and 45 Kcfs flows. The difference in jet strength was seen in more detail in the higher slice where the velocity over seventy five feet per second extents past the stilling basin.

Figure 65 and Figure 66 show the gas volume fraction of the flow at 1410 ft and 1424 ft. 37 Kcfs and 45 Kcfs flows do not entrain bubbles back into the powerhouse region. Both 7Q10 flows deposit bubbles into the powerhouse region. However, the 7Q10 deflector case causes more bubbles to be present near the fish trap at depth increasing possible TDG production. Figure 67 shows the gas volume fraction at slices through the sluiceways. No bubbles were present deep in the stilling basin for the 37 Kcfs and 45 Kcfs flows. Bubbles plunge to depth in the stilling basin downstream of sluiceway 1 for all the simulations. The 7Q10 case with deflectors has a significant amount of bubbles present in the stilling basin downstream of sluiceway 1. Bubbly flow also has a significant presence in the stilling basin below sluiceway 2. The 7Q10 flow condition

without deflectors shows bubbles present in the entirety of the stilling basin at slices through all three of the spillways. Downstream of spillway 1 the water appears to contain bubbles only on the surface. This was due to the bubble free powerhouse flow being entrained into the flow. Spillway 2 shows a similar effect although the bubbles were not kept as high on the surface.

Figure 68 shows the TDG source for the selected deflector simulations. Plots showing TDG production in the 7Q10 flows are shown at a different scale than the 37 Kcfs and 45 Kcfs flows. Without a change in the scales the 7Q10 contours would be saturated. The TDG production for the 37 Kcfs was less than that of the 25 Kcfs cases, recalling Figure 38. Lower TDG production was attributed to the increased streamwise velocity from the 30 Kcfs powerhouse flow that does not let the large western eddy form. 7Q10 flow conditions show a significantly higher value of TDG production where the larger source values for the deflector case were present downstream and in the stilling basin for the no deflector case. The 7Q10 deflector case has high source values a similar distance downstream of the stilling basin as the optimization 25 Kcfs flow simulations, recall Figure 38. Both flow cases have a similar western eddy that brings bubbly flow from the jets around past the fish trap and underneath the jets, Figure 36 and Figure 66. Depicting the western eddy as some consequence of powerhouse flow and spillway jet flow. The 7Q10 flow without deflectors presents the largest TDG source values of any simulation. Without deflectors, bubbles were allowed to be transported to depth where hydrostatic forces were high and dissolution was rapid.

An isosurface of a gas volume fraction value $\alpha = 10^{-4}$ is found in Figure 69. At a gas volume fraction of 10^{-4}, 99.7% of bubbles have exited the domain. This means

that there was a negligible amount of possible TDG production downstream, or outside of, this isosurface. A corresponding TDG source isosurface of value $-2(10)^{-5}$ is shown in Figure 70, an isosurface corresponding to degasification from liquid to bubbles near the free surface. Downstream of these regions degasification only occurs at the free surface where the process is less efficient.

Total dissolved gas distributions are shown at 1415.6 ft and 1424.6 ft in Figure 71 and Figure 72. These height values were chosen to best show values shared by all 4 tailrace heights. Contour values are different for 7Q10 flow conditions to better visualize the lateral TDG distribution. The TDG contour values show the TDG past the stilling basin for the 7Q10 no deflector case was about 20% higher than the cases with the deflector present. However, without the deflector installed for the 7Q10 flow the large western eddy was not present and the flow past the fish trap does not have high values of TDG. Whereas with the deflectors installed the large western eddy brings high TDG flow near the fish trap. The maximum TDG values for the two 7Q10 flows were 1.38 with deflectors and 1.88 without deflectors. However, the maximum TDG values near the fish trap for the same simulations were 1.27 and 1.16, respectively.

Streamlines colored by TDG concentration illustrate the tailrace flow from the powerhouse and sluiceways in Figure 73 and Figure 74, respectively. Entrainment of flow into the stilling basin was seen for both the 37 Kcfs, 45 Kcfs and 7Q10 deflector flow condition, it was not seen in the 7Q10 no deflector condition. TDG values on the powerhouse streamlines increase as they enter the aerated sluiceway zone. TDG was also spread across the entire river width of the 7Q10 deflector because of the presence of the large western eddy. This reduced lateral gradient does not occur in any other performance

simulation. Some amount of entrainment was produced in the 7Q10 no deflector flow. This entrainment appears to be weaker and occurs more downstream than the flows with the deflector installed. Streamlines from the sluiceways or spillways in the case of the 7Q10 no deflector flow, Figure 74, show the tendency of flow to stay on the surface for the deflector cases. However, the weaker jet in the 37 Kcfs simulation was affected by the eastern eddy more so than the other simulations. This causes some of the aerated flow to reenter the bubbly flow from underneath the jet. Both the 45 Kcfs and 7Q10 deflector flow conditions show a jet that tends to not dissipate or be affected by an eddy. This was likely due to the high streamwise velocity produced by the jets. The no deflector 7Q10 flow shows streamlines that tend to follow the bottom surface of the stilling basin. Although some of the flow was trapped inside the stilling basin's rolling flow.

TDG equilibrium was determined by the depth of the flow as well as the local air temperature. Slices showing contours of TDG equilibrium as well as isolines of local TDG values are shown in Figure 75. Equilibrium TDG levels were determined by the maximum amount of air that can be dissolved by water. As previously mentioned, a major player in the solubility of water is the hydrostatic pressure, giving the maximum TDG contour the linear gradient. Local TDG was represented by lines on the slices, these lines are colored the TDG values they are associated with. If local TDG was higher than the equilibrium TDG degasification was promoted, this happens most frequently near the free surface. When the local TDG values were less than the equilibrium values and gas was present TDG can be generated. The 7Q10 deflector case shows the water entrained by the western eddy was capable of producing more TDG. The same occurs in the no

deflector case where the water entrained from the powerhouse was not saturated and therefor capable of generating TDG when introduced to bubbly flow.

Isosurfaces of gas volume fraction are shown in Figure 76 where a large percentage of the bubbles were present near the surface for the cases with the deflector, shown as the orange isosurface. For the no deflector case the high levels of bubbles were present deep in the stilling basin as well as on the surface downstream of the stilling basin. Figure 77 shows isosurfaces of TDG production where most TDG production occurred downstream of the stilling basin. However, as the flow rate increased the TDG production tended to move upstream. For the 7Q10 deflector case it is important to note the TDG production on the left bank near the entrance of the fish trap. This TDG production was supported by the western eddy transporting bubbles from the jets to nearby the fish trap. Major TDG production occurred in the stilling basin for the 7Q10 no deflector case. TDG isosurfaces in Figure 78, show for flowrates less than the 7Q10 flow rate the TDG values were transported directly downstream. The recirculation generated for the 7Q10 flow rate with deflectors causes TDG to be present near the fish trap as well as directly downstream of the fishtrap. 7Q10 flow without deflectors indicates large TDG values downstream and near powerhouse 1, although avoiding the fish trap entrance.

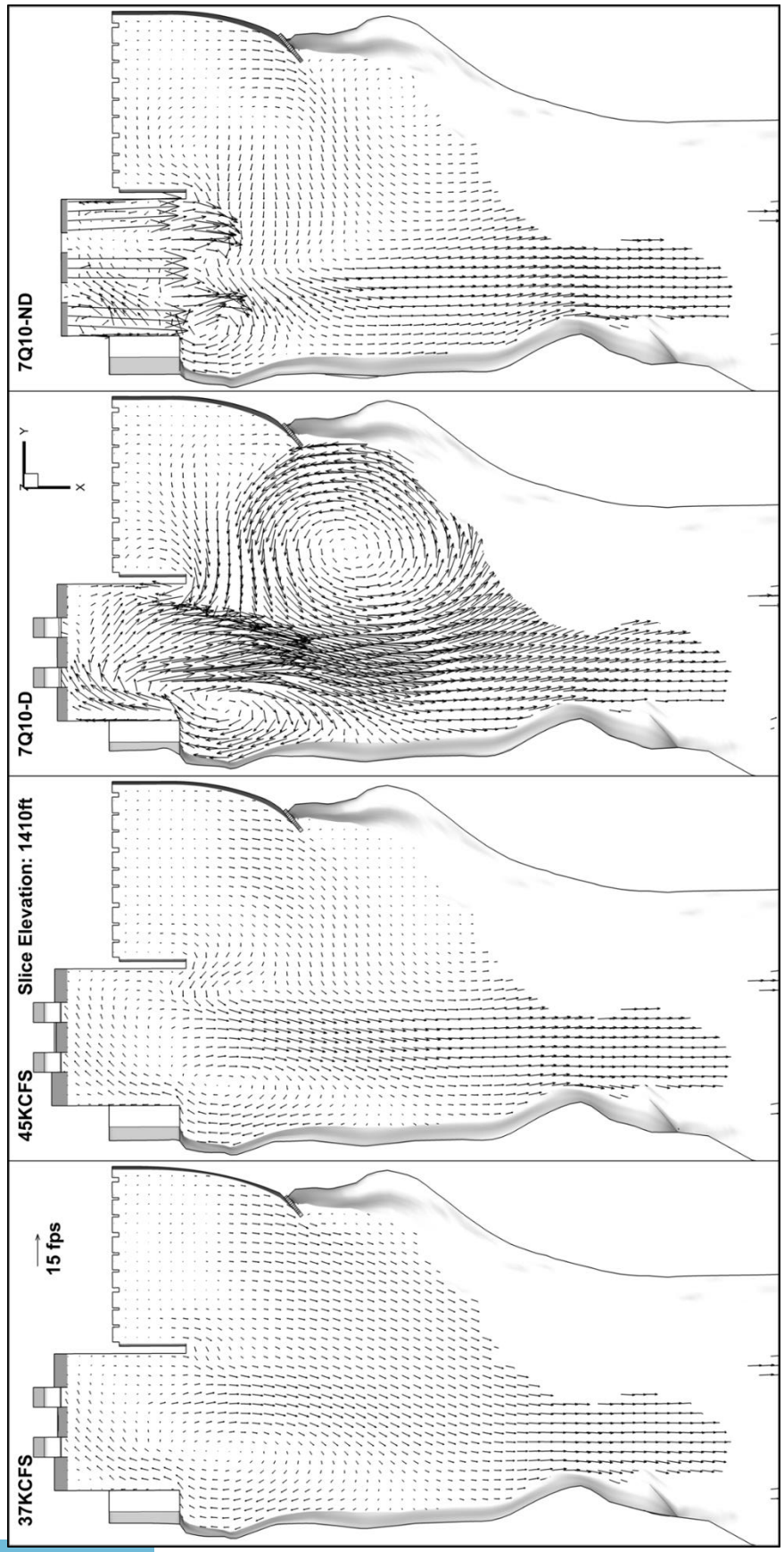

Figure 61. Velocity vectors at 1410 ft for the selected deflector

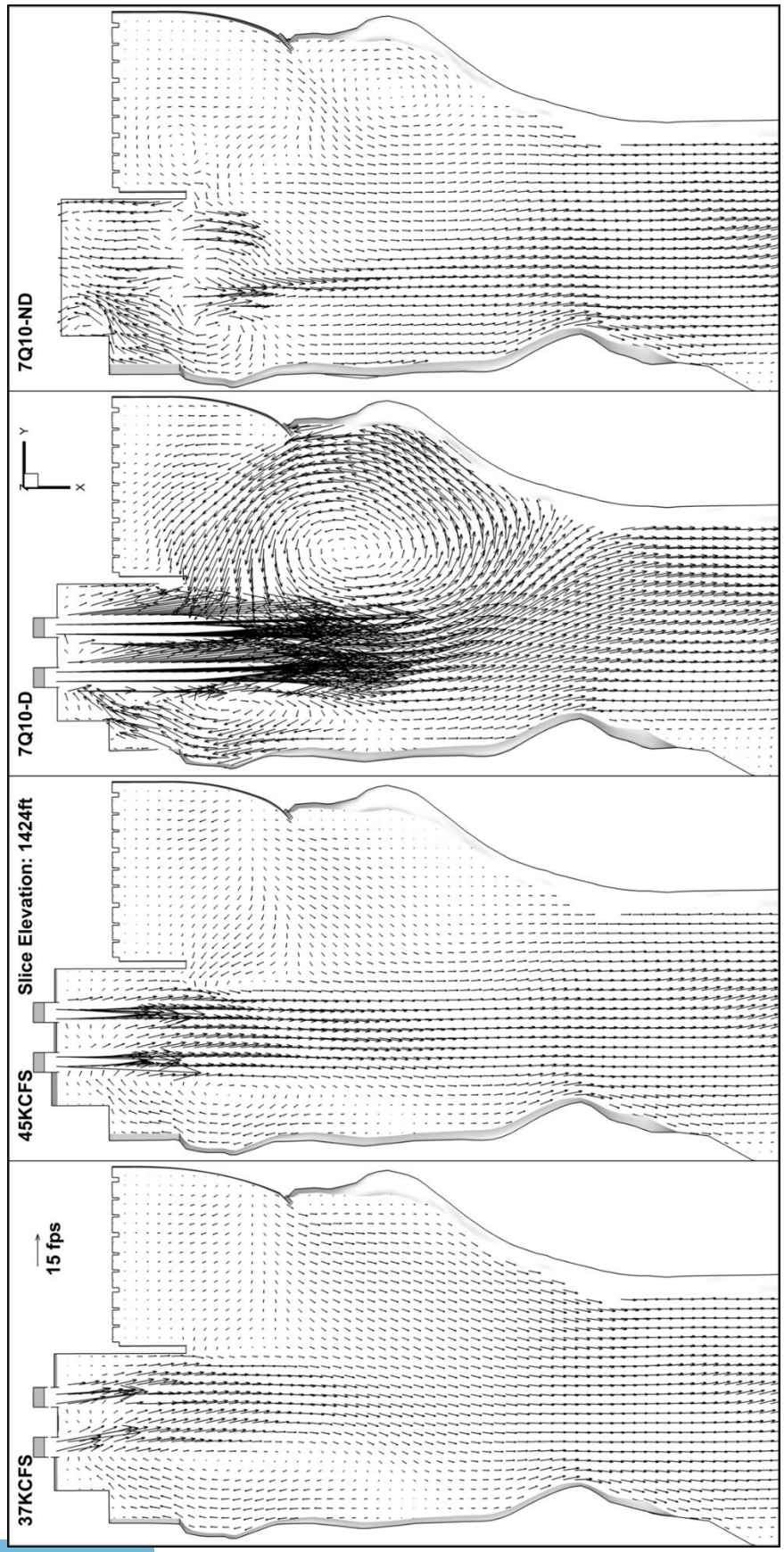

Figure 62. Velocity vectors at 1424 ft for the selected deflector

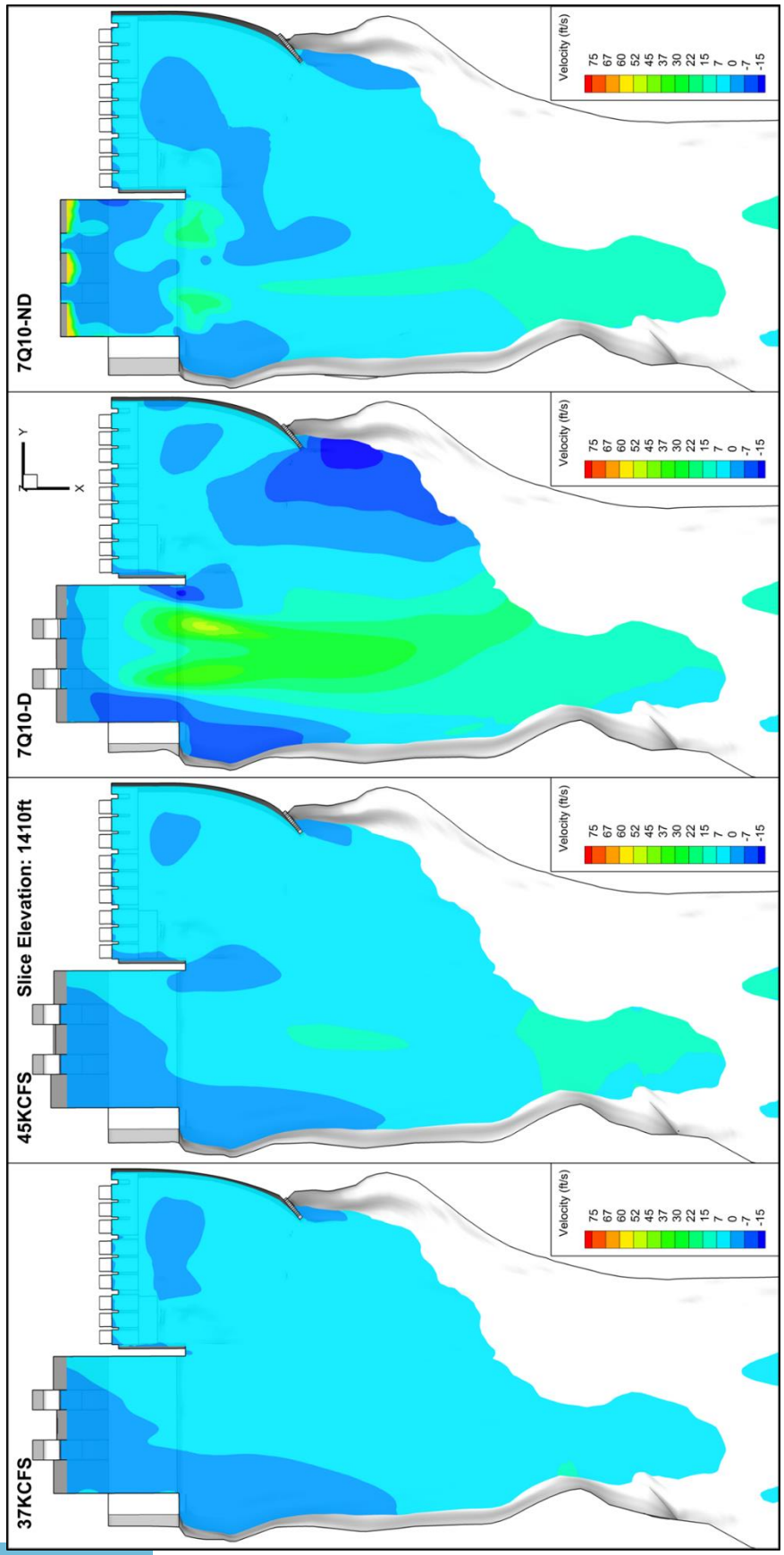

Figure 63. Velocity contours at 1410 ft for the selected deflector

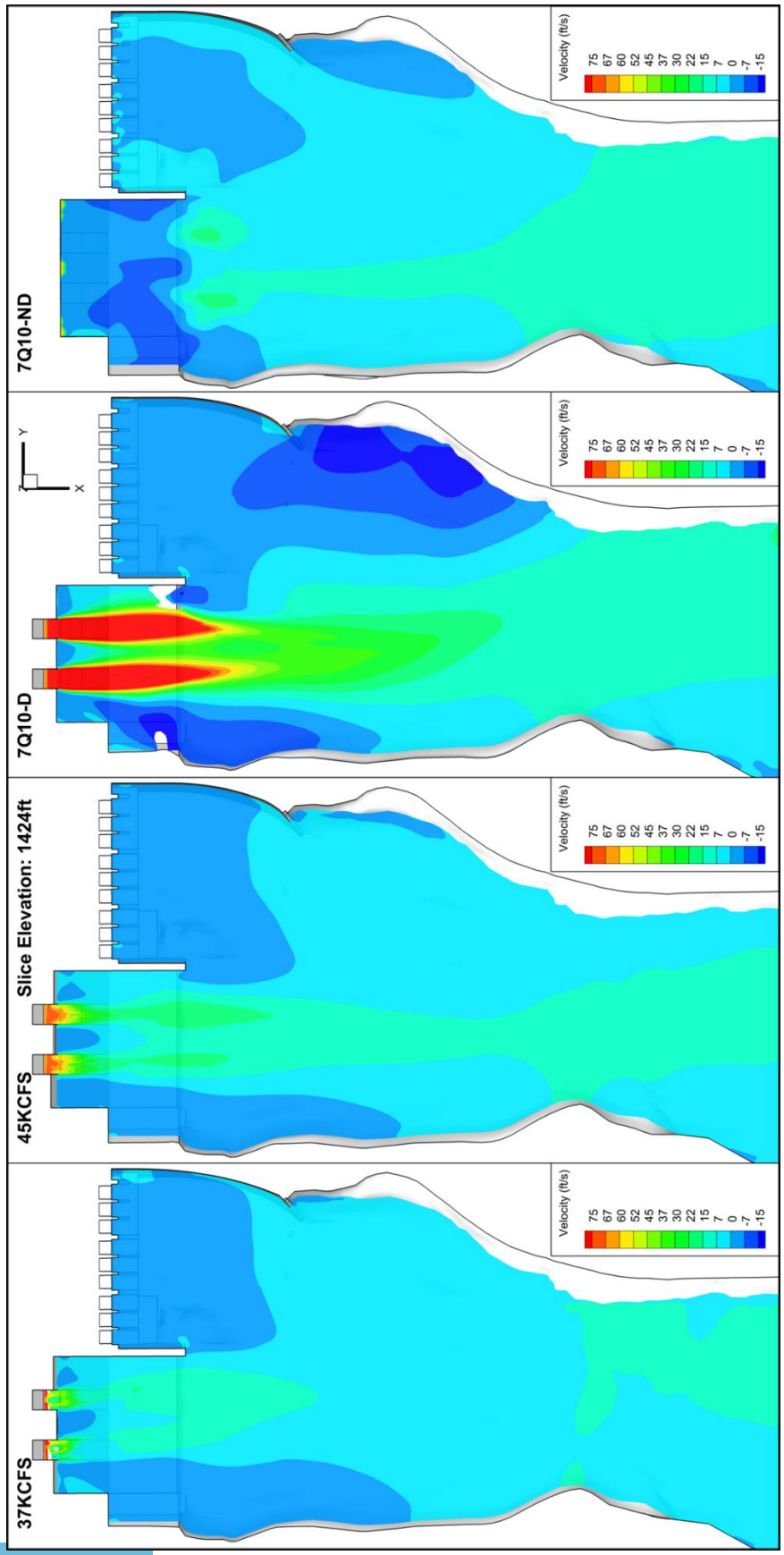

Figure 64. Velocity contours at 1424 ft for the selected deflector

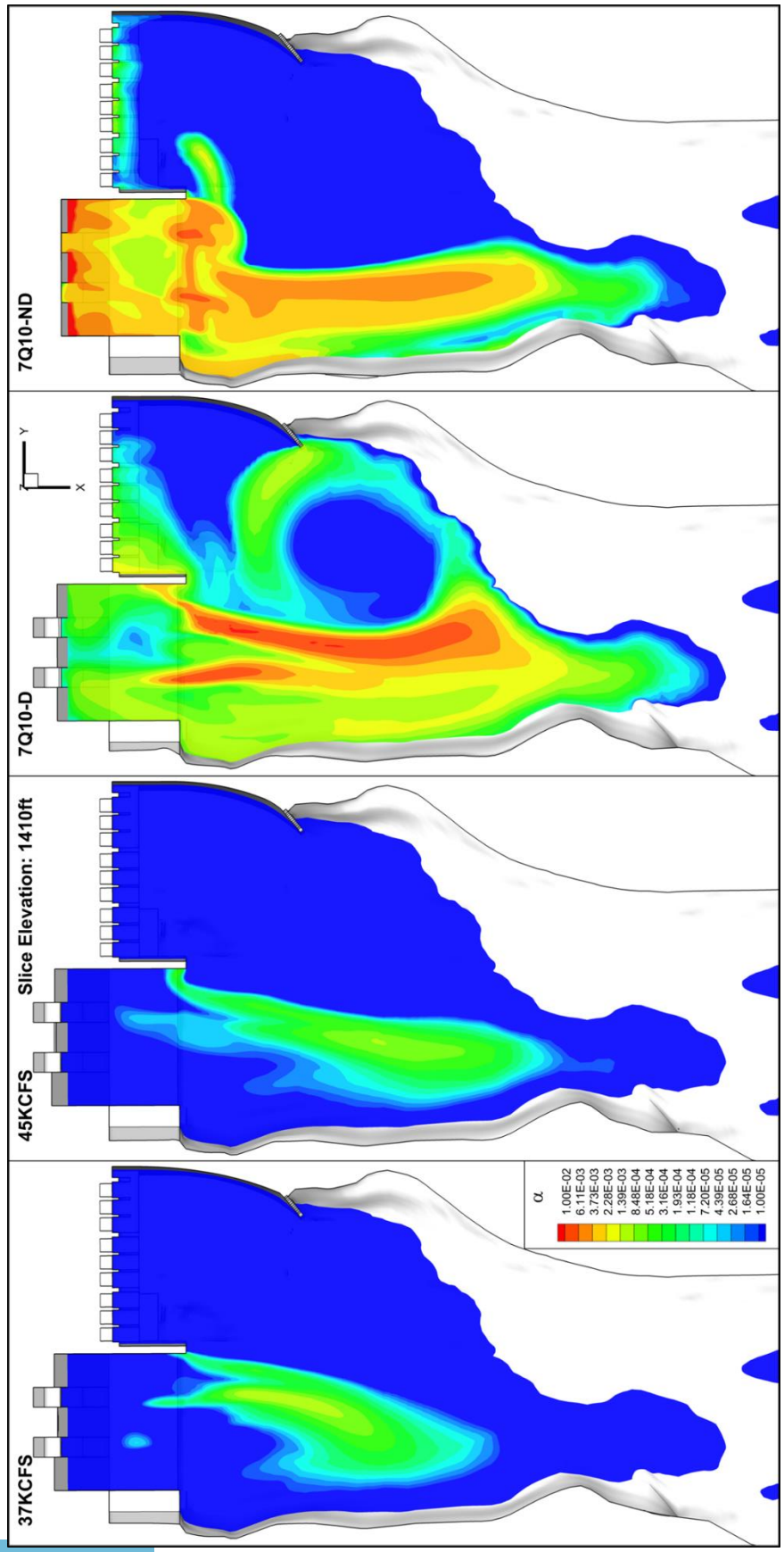

Figure 65. Gas volume fraction contours at 1410 ft for the selected deflector

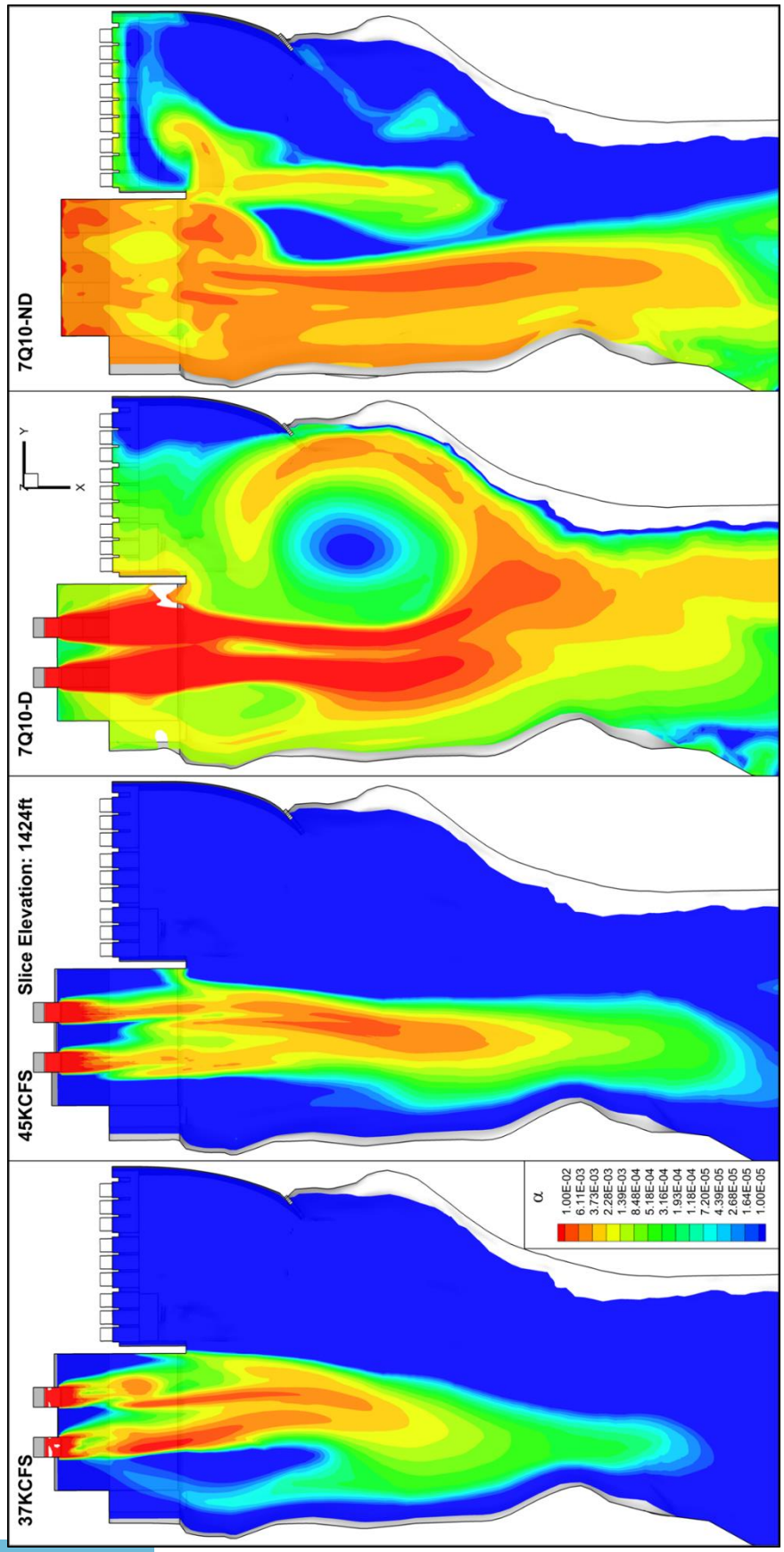

Figure 66. Gas volume fraction contours at 1424 ft for the selected deflector

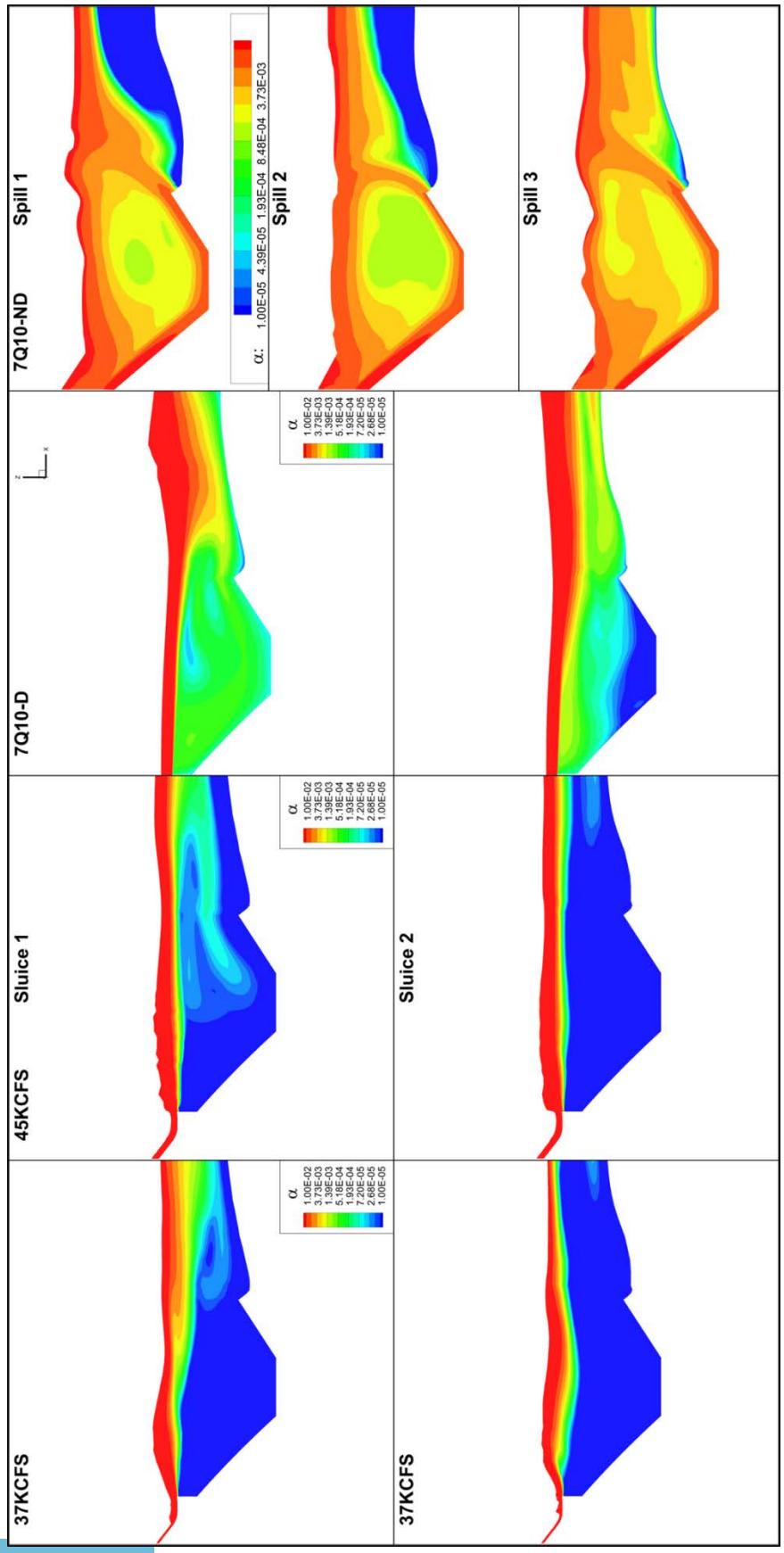

Figure 67. Gas volume fraction contours at vertical slices for the selected deflector

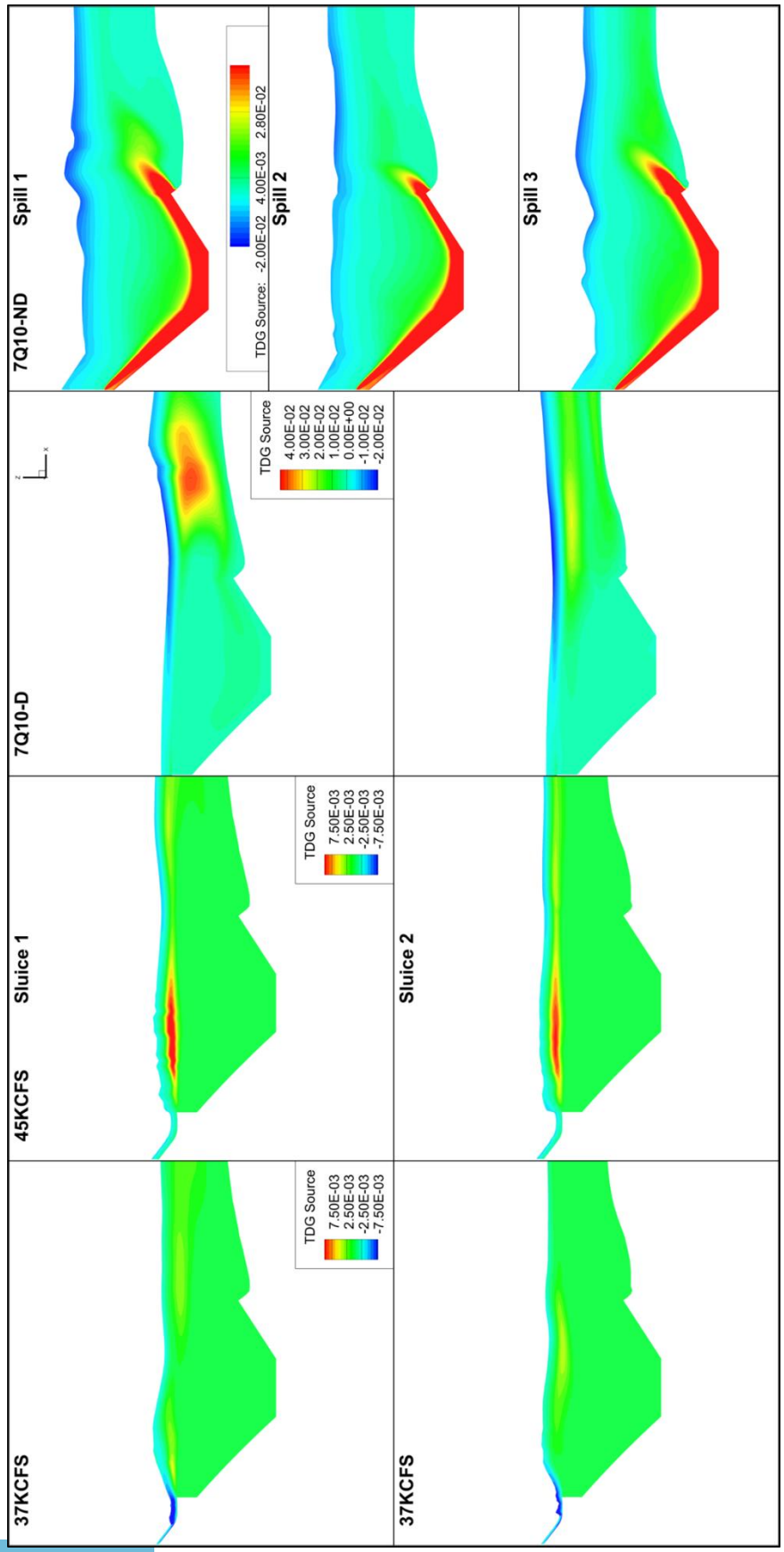

Figure 68. TDG source contours at vertical slices for the selected deflector

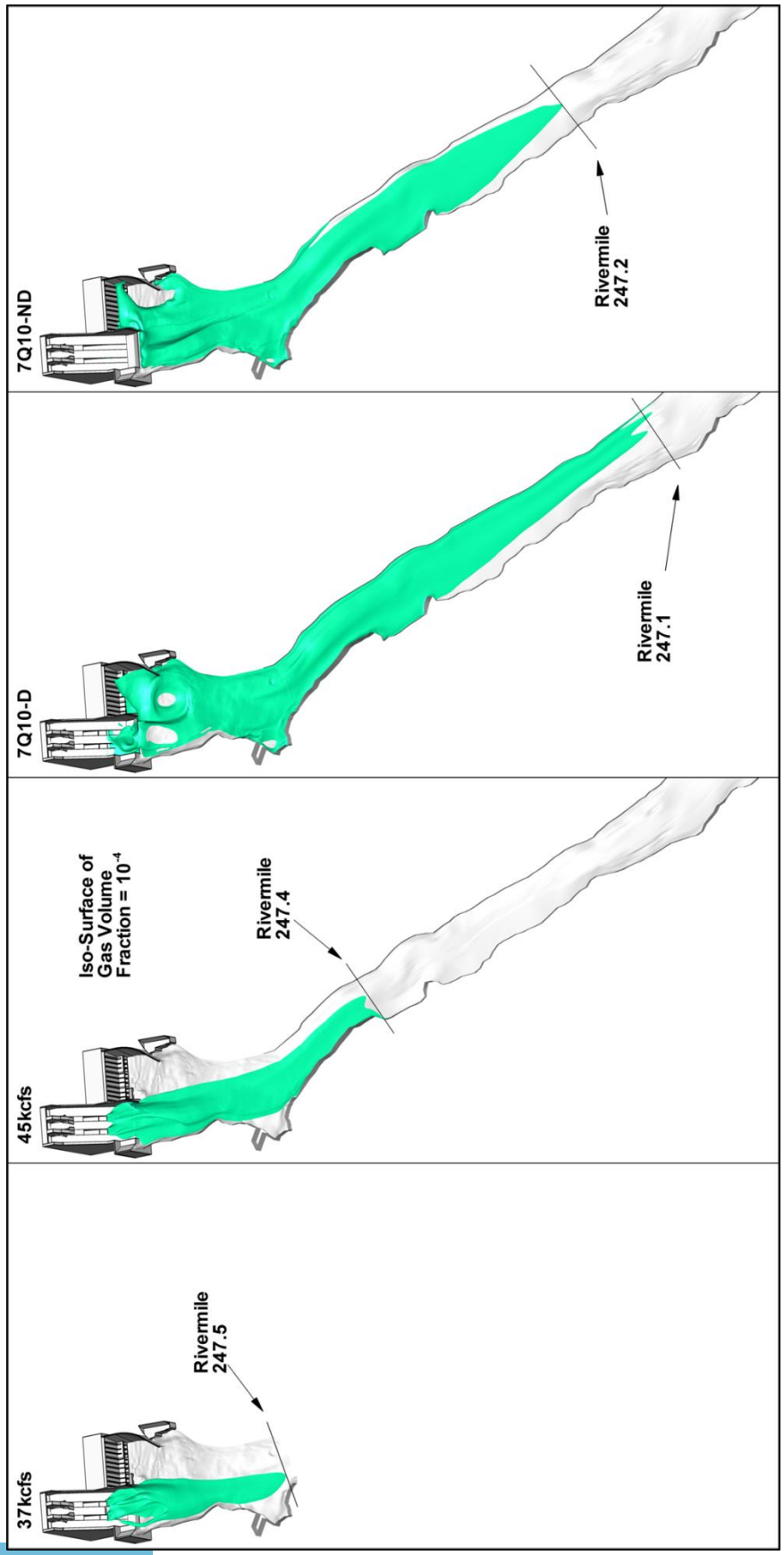

Figure 69. Isosurface of gas volume fraction 10^{-4}

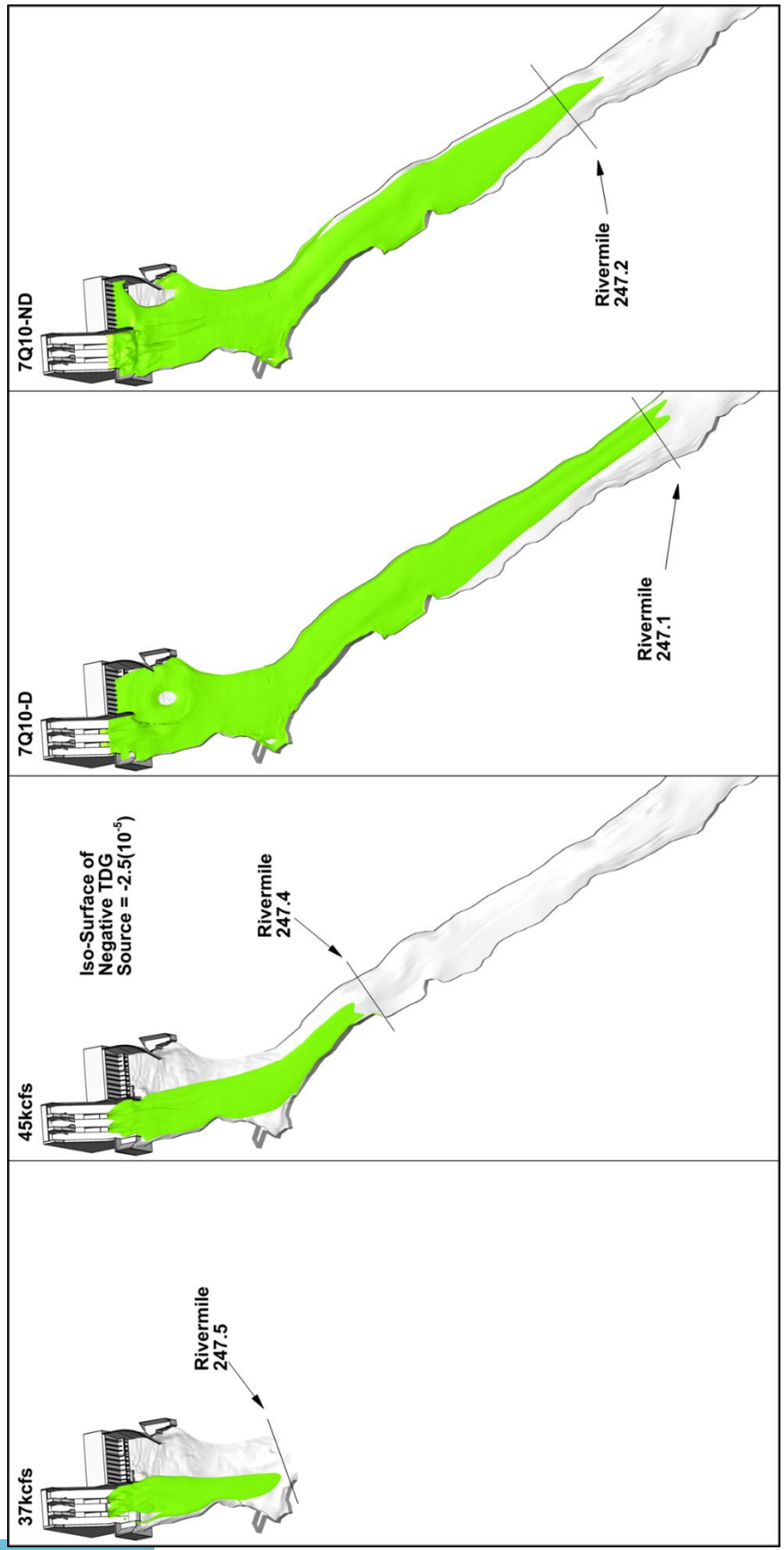

Figure 70. Isosurface of TDG source 2 10^{-5}

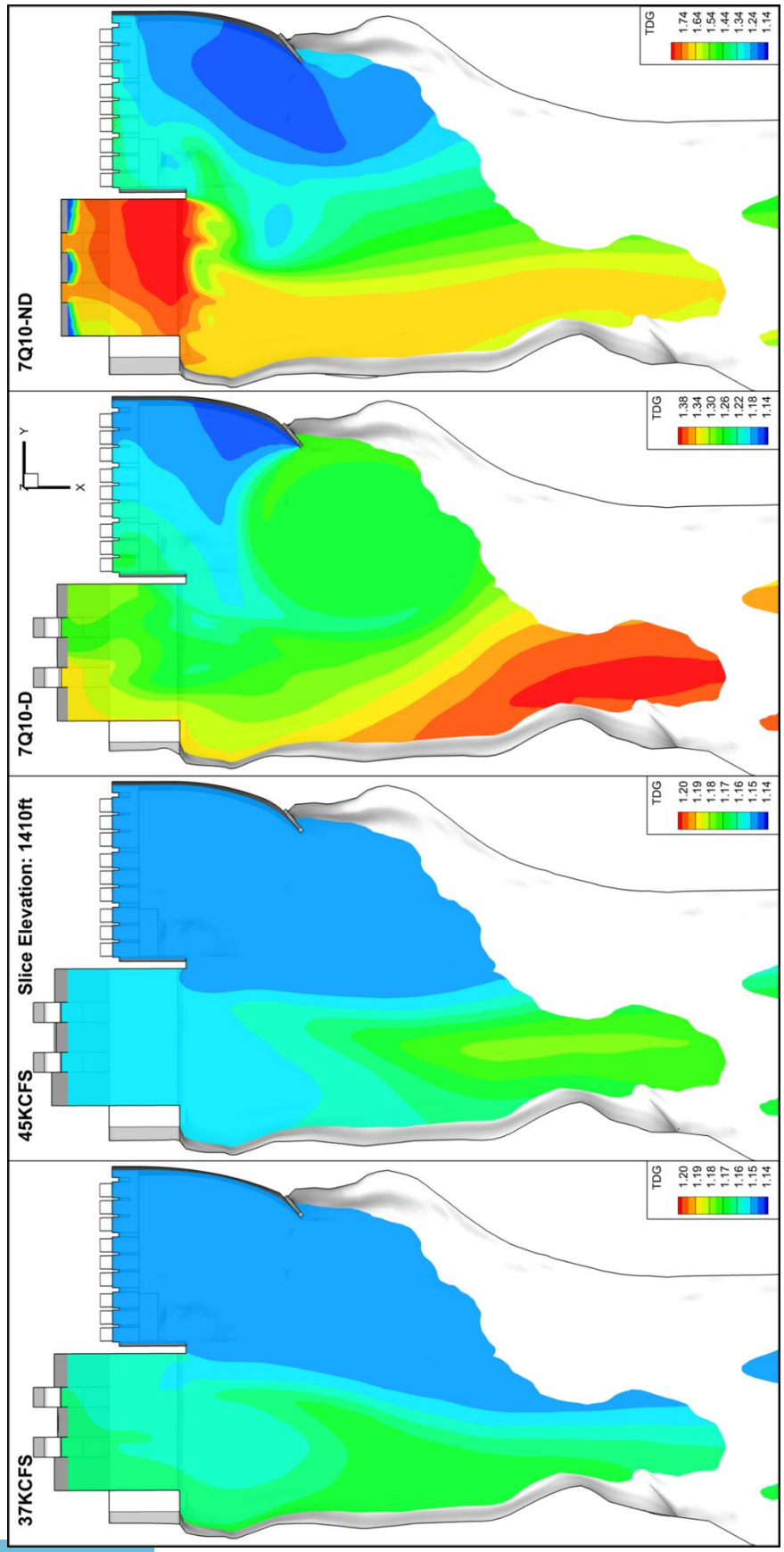

Figure 71. TDG contours at 1415.6 ft for the selected deflector

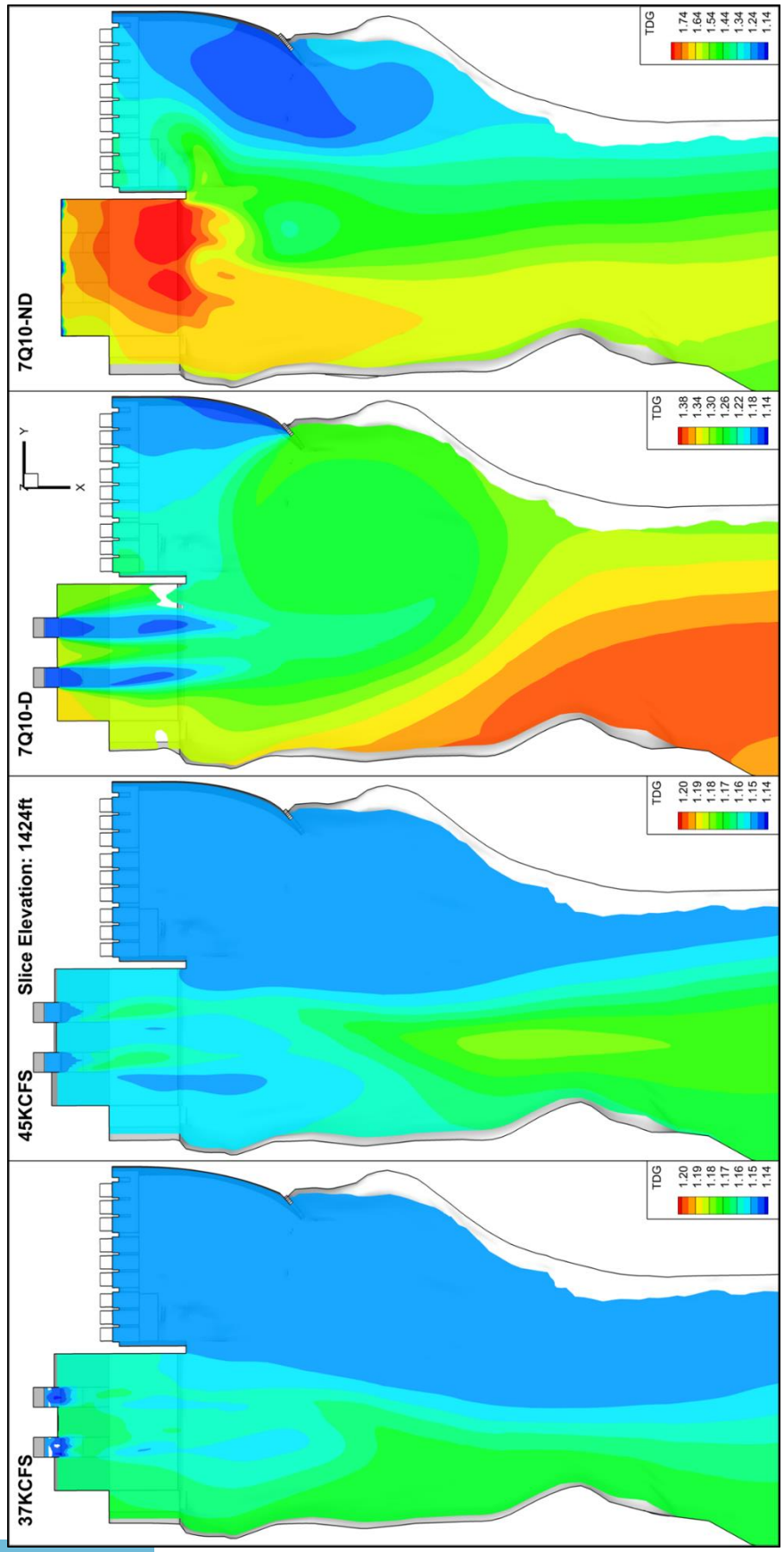

Figure 72. TDG contours at 1424.6 ft for the selected deflector

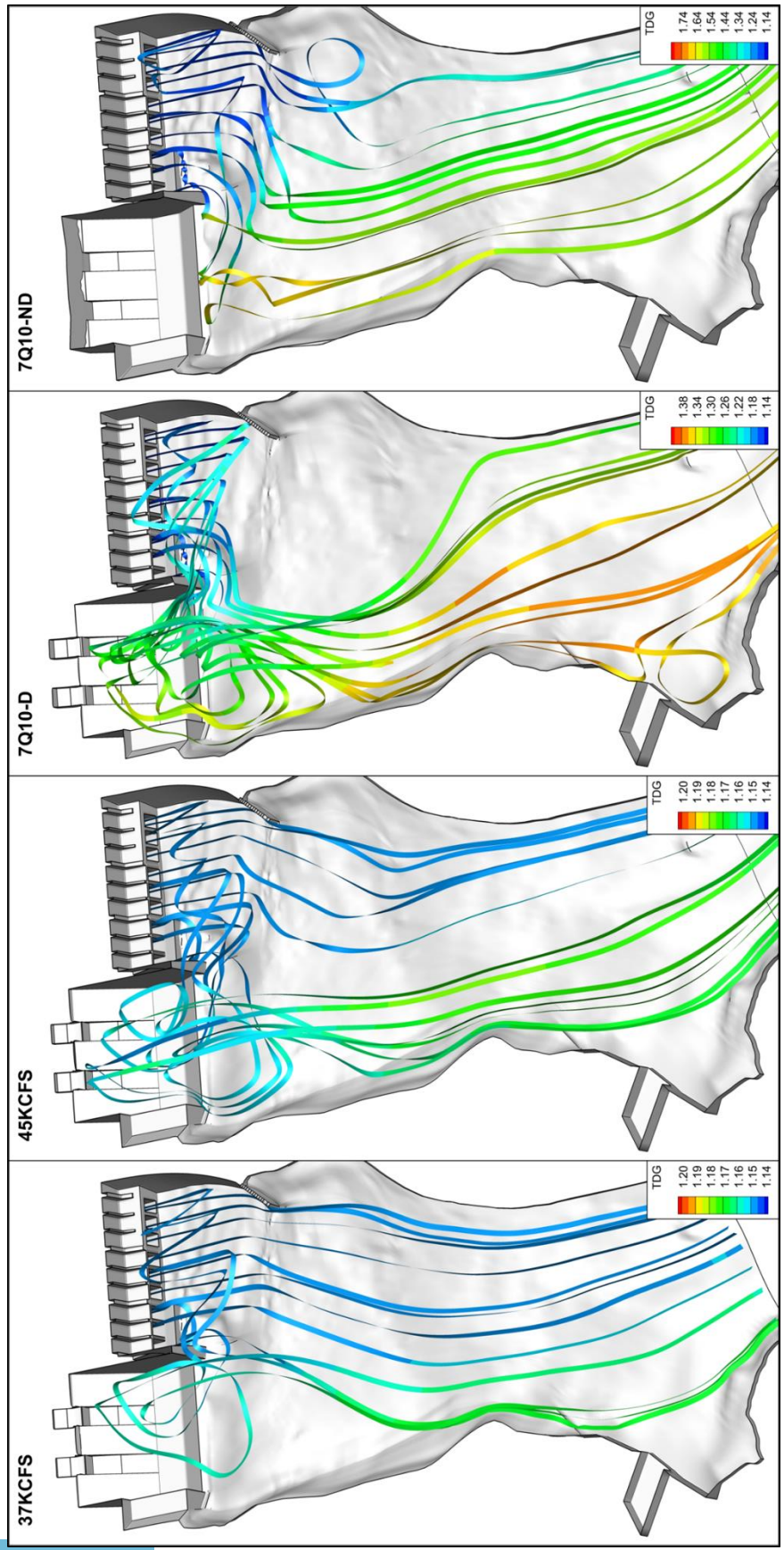

Figure 73. Streamlines released from the powerhouse colored by TDG for the selected deflector

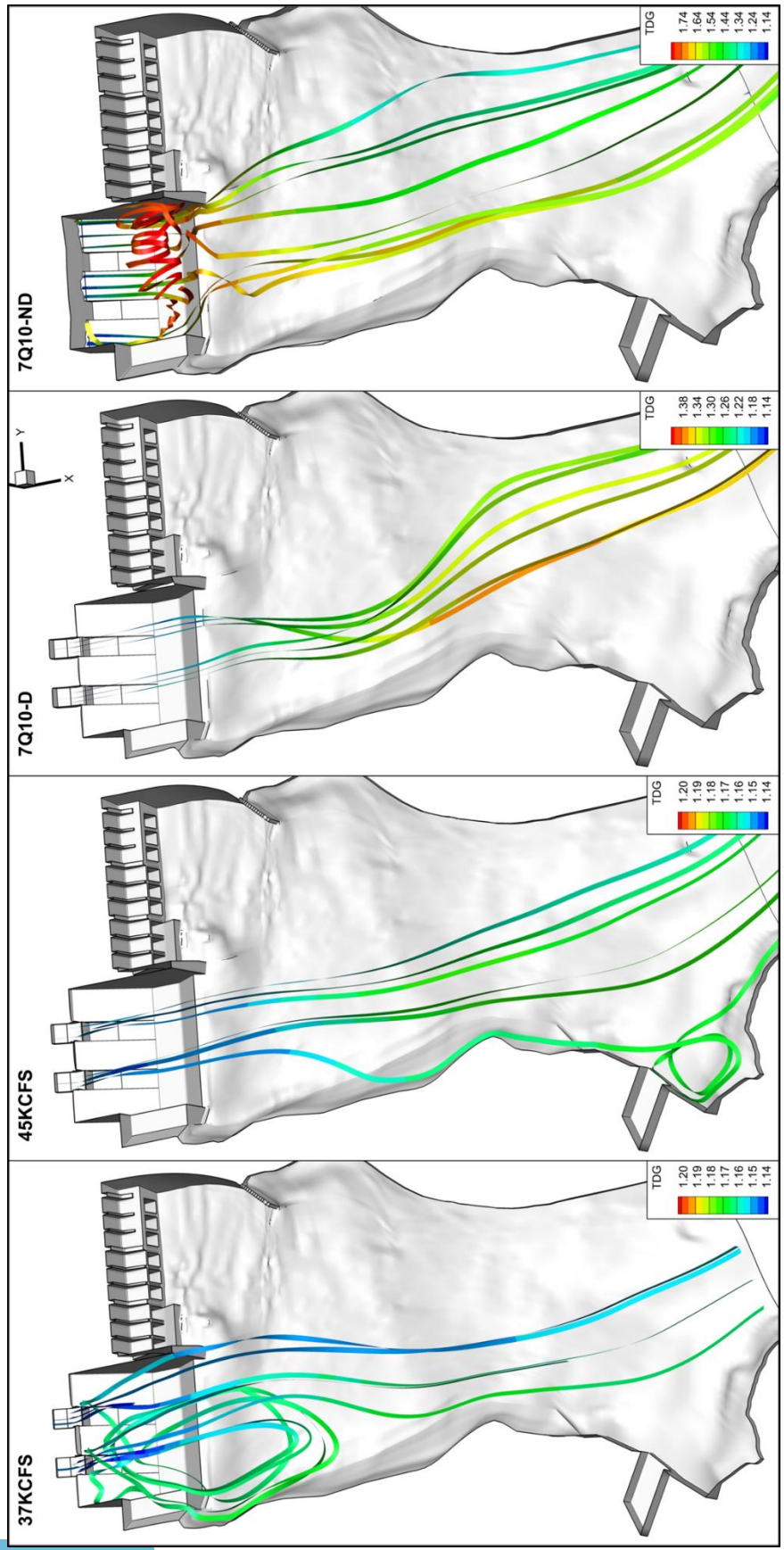

Figure 74. Streamlines released from the sluiceways and spillways colored by TDG for the selected deflector

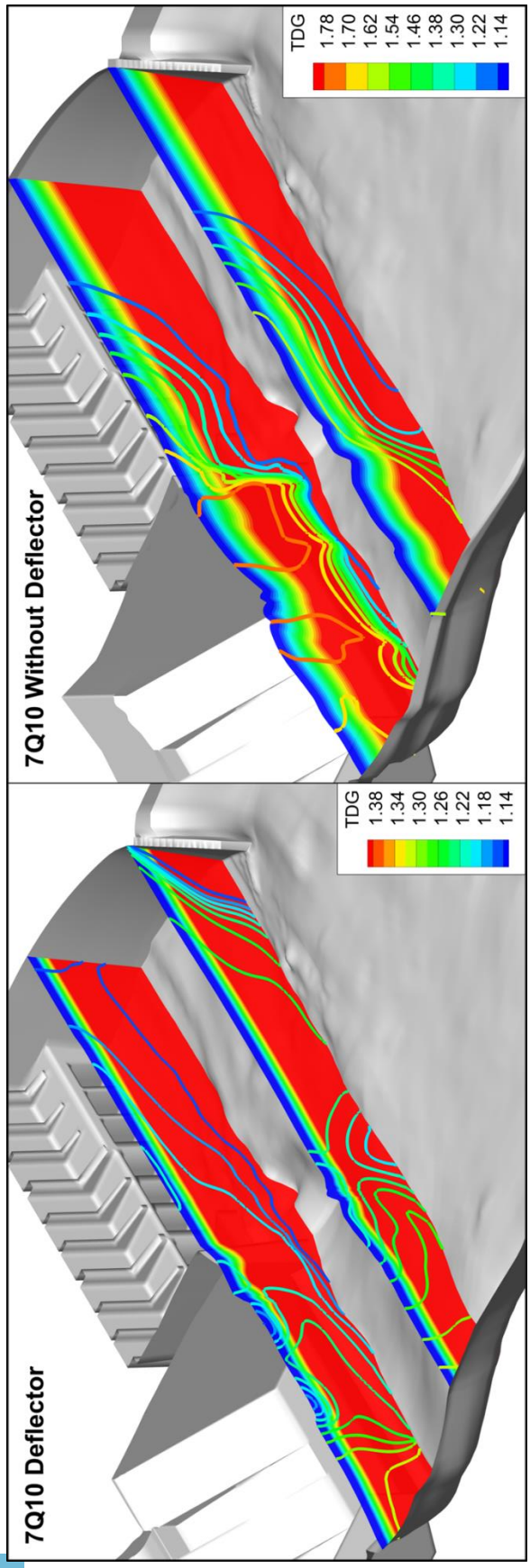

Figure 75. Local and equilibrium TDG for 7Q10 simulations

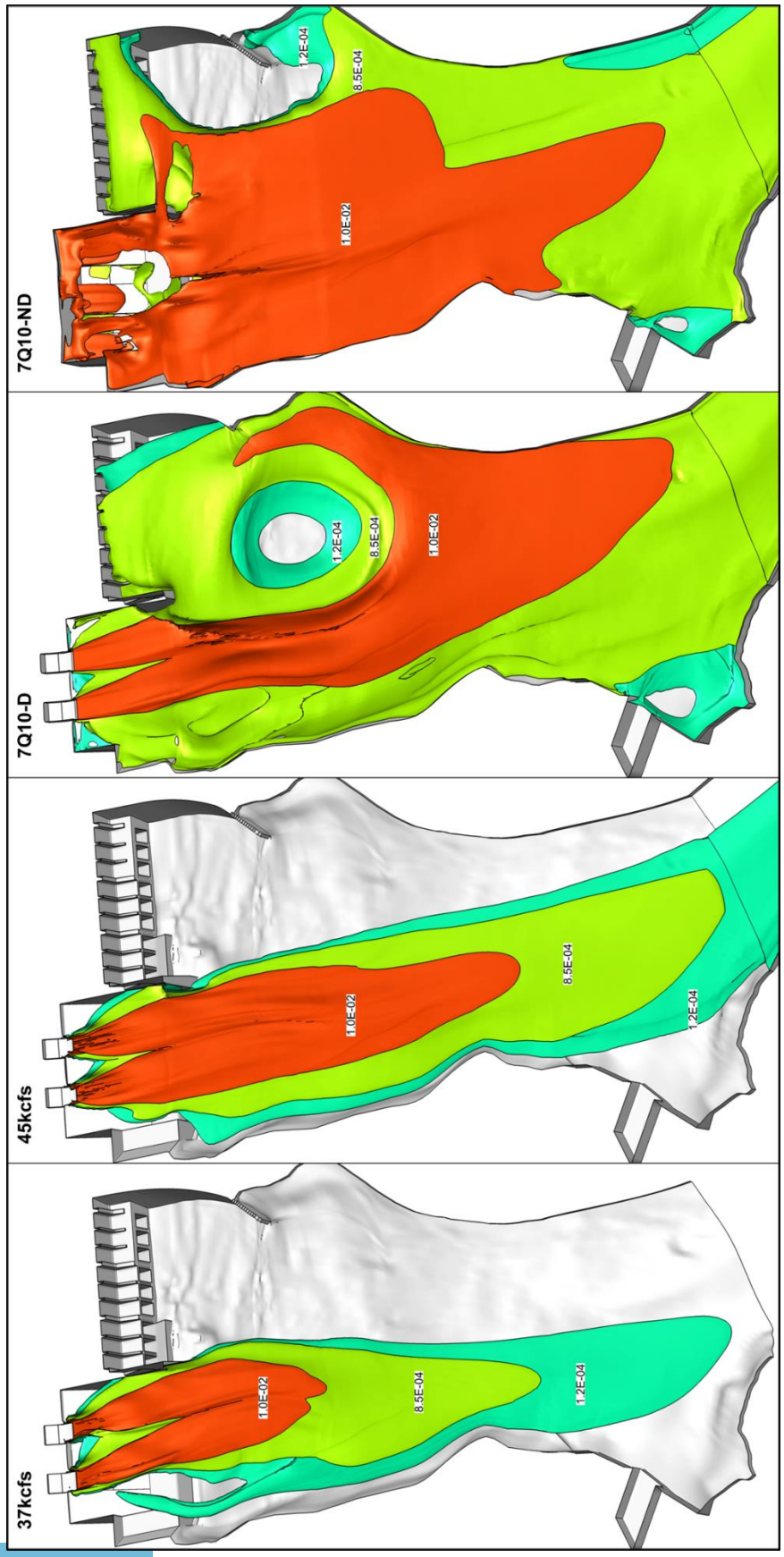

Figure 76. Gas volume fraction isosurfaces for the selected deflector

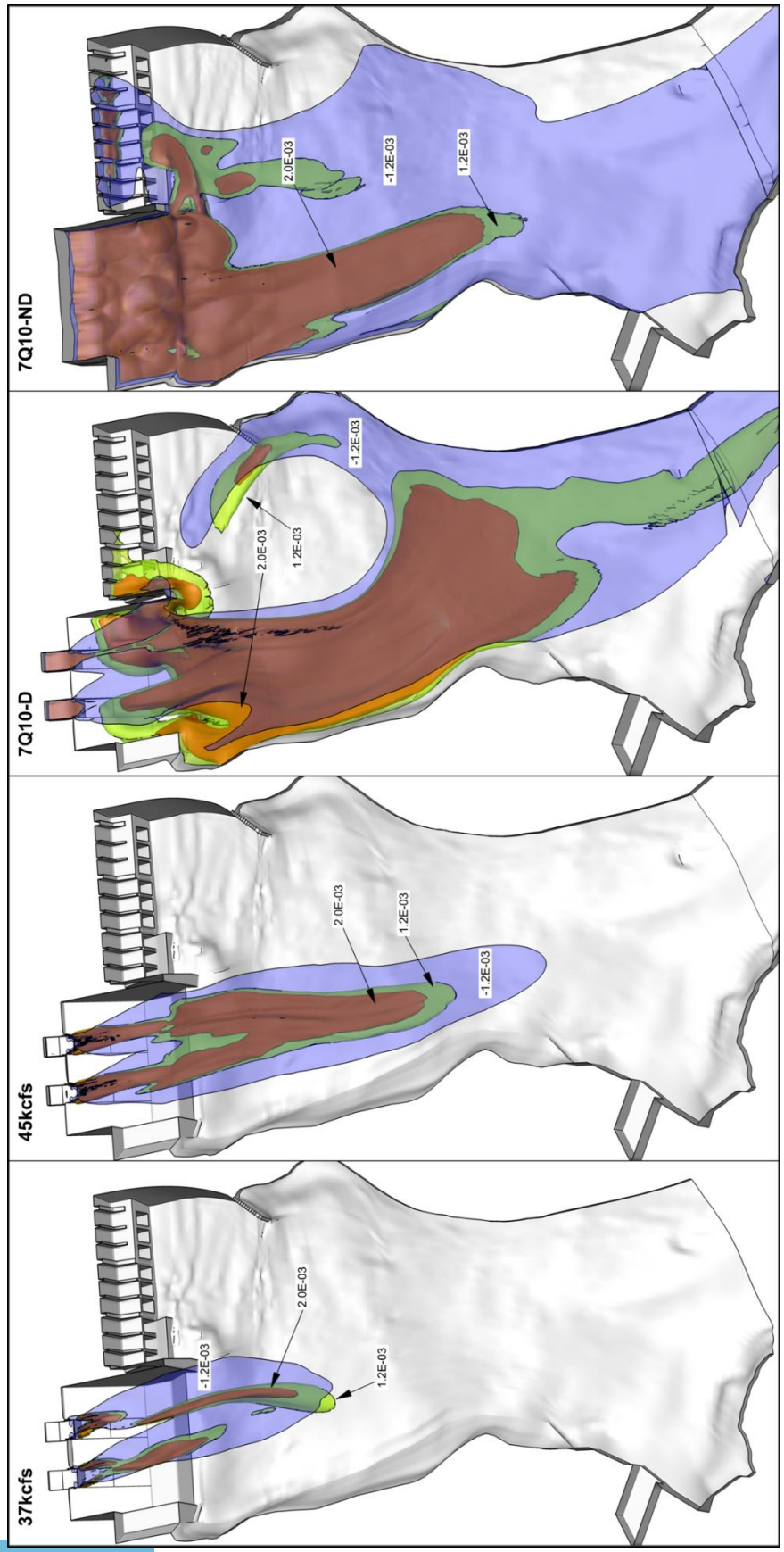

Figure 77. TDG source isosurfaces for the selected deflector

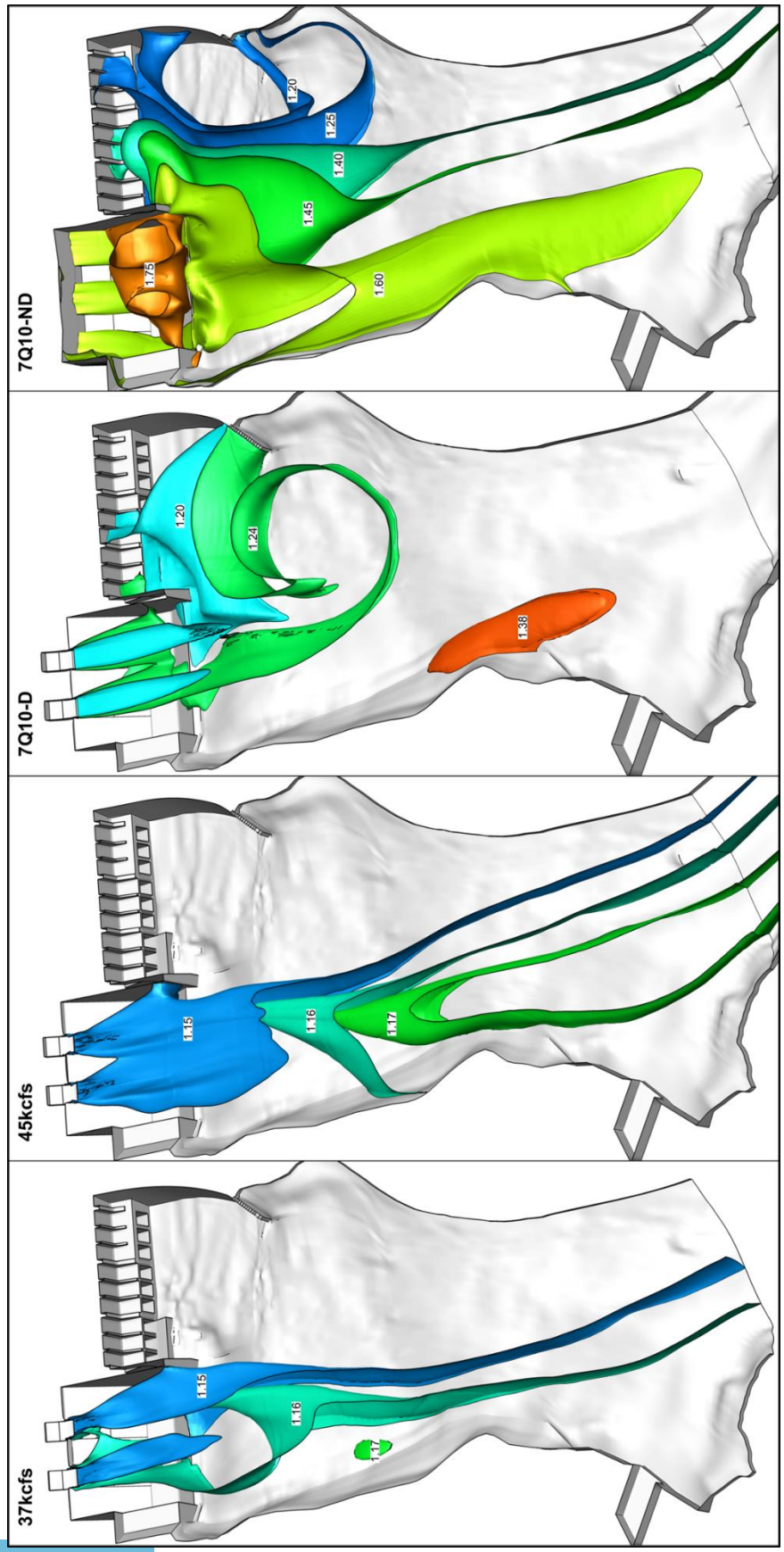

Figure 78. TDG isosurfaces for the selected deflector

Downstream Total Dissolved Gas Simulations

IPC request TDG be monitored far downstream of the dam to determine the range of the generated TDG. When the value of TDG downstream reaches that of the Hells Canyon's forebay, 1.15 or 115%, the effect of the TDG production at the dam was considered completed. To calculate when the TDG generation effects end, sample slices were taken at locations downstream, approximately separated by one half of a river mile. Figure 79 shows the tailrace colored by TDG at 6 different river miles, a slice was also present to show the vertical TDG gradient in the flow. It should be noted that in this figure the water elevation was very low and the TDG near the surface quickly diminishes. Figure 80 shows the same 6 river miles and vertical slices. This figure shows a reach that was slightly wider and deeper due to the higher flow rate. In the image of river mile 246, an evident lateral TDG gradient is seen, this gradient diminishes due to secondary flows existing in the turning river. Secondary currents created for the curving stream move water with low TDG, surface water, towards the outer bank and supersaturated water, deep water, to the inner bank. These currents induce new lateral TDG gradient. Figure 81 and Figure 82 show the 7Q10 flow at the same 6 locations. For this flow the river was wider, deeper and faster than the previous two flows. The vertical slices show apparent vertical TDG gradients throughout the reach. A lateral TDG gradient was present in the flow until river mile 243. Low TDG values at the surface were due to degasification by mass exchange with the atmosphere.

Table 4 shows the flow rate averaged TDG concentration at the forebay, dam, and each half of a river mile past the dam. 'Average TDG' values were generated by averaging TDG values over a slice at the river mile. While eastern and western TDG

values were the average of chosen values on the slice near the eastern and western bank respectively. According to the model, the average TDG produced by spill at Hells Canyon Dam disappears after one and three miles for the 37 Kcfs and 45 Kcfs, respectively. According to the model, TDG concentration of about 1.27 was predicted 7 miles downstream of the dam for the 7Q10 flow with deflectors and a value of 1.40 was predicted without deflectors.

Figure 83 shows values of flow rate averaged TDG plotted against river mile. TDG increases abruptly near the dam where bubble dissolution was occurring. Just past the dam in low pressure regions, bubbles were able to absorb air from supersaturated water. This was an efficient processes of degasification at regions of high TDG concentration; the process was most noticeable within one mile of the dam for the no deflector 7Q10 flow. After bubbles were no longer present in the domain, degasification can only occur as mass transfer at the surface.

Figure 84 shows the TDG values at the eastern and western banks at the forebay, dam, and each half river mile from the dam. The plot shows the low TDG values present in front of the powerhouse for all simulations. It also shows the mixing of supersaturated flow with unsaturated flow that occurs downstream due to secondary flows. For the cases with deflectors installed the TDG difference present on the western and eastern banks was less than 0.5% at 1.5 miles downstream of the dam. However, lateral TDG gradients can increase as the flow moves downstream.

Average TDG concentration and lateral TDG differences increase with the increase of river flow rate. For the 7Q10 flow without deflectors the lateral TDG gradients were the largest. Since mixing between the powerhouse flow and spillway flow

was less pronounced. For this flow TDG was generated deep in the stilling basin and tends to stay near the river bed where downstream secondary flows will move the supersaturated water to one bank again generating a large lateral TDG gradient.

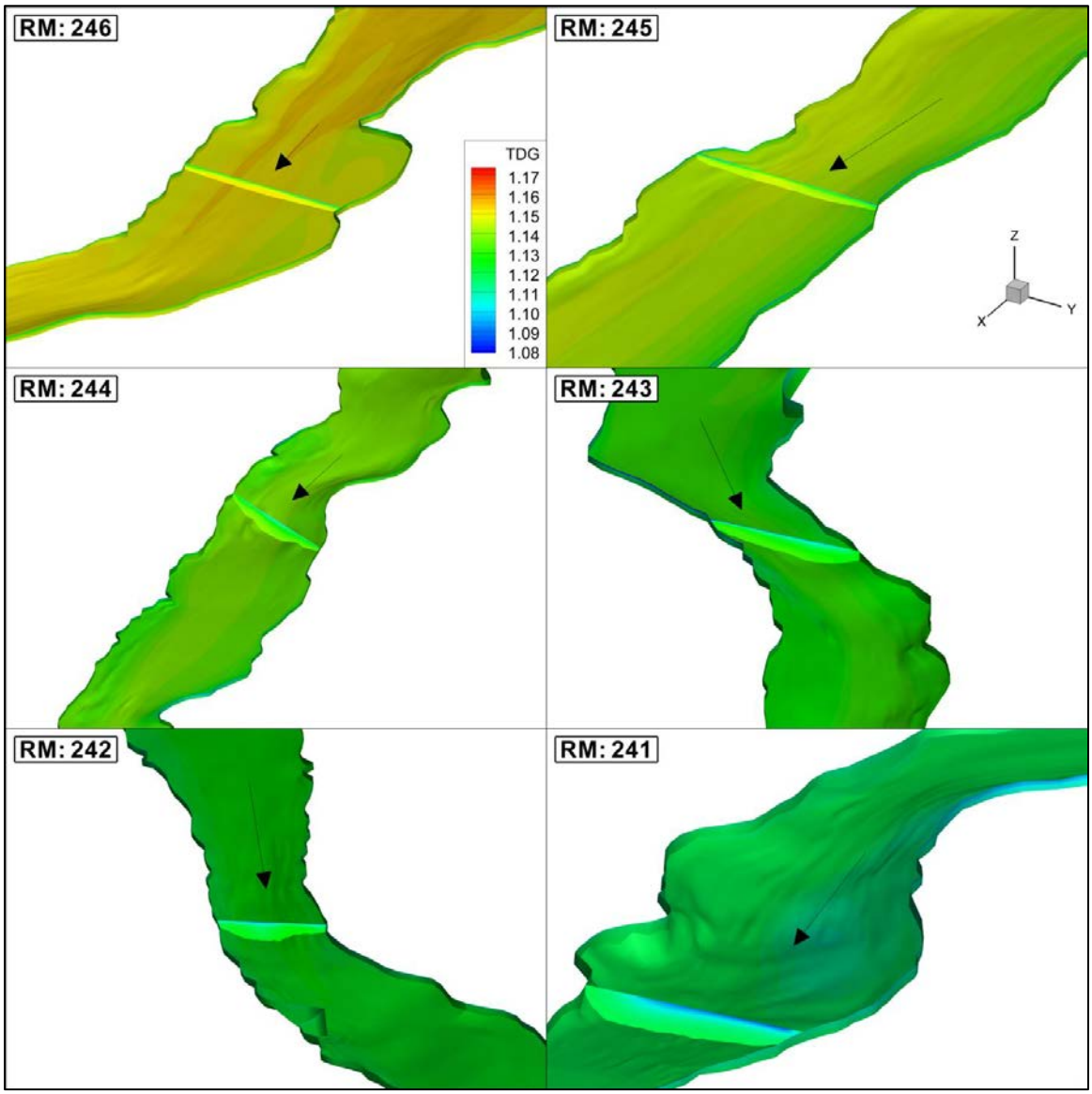

Figure 79. TDG in the downstream region displaying the distribution for 37 Kcfs

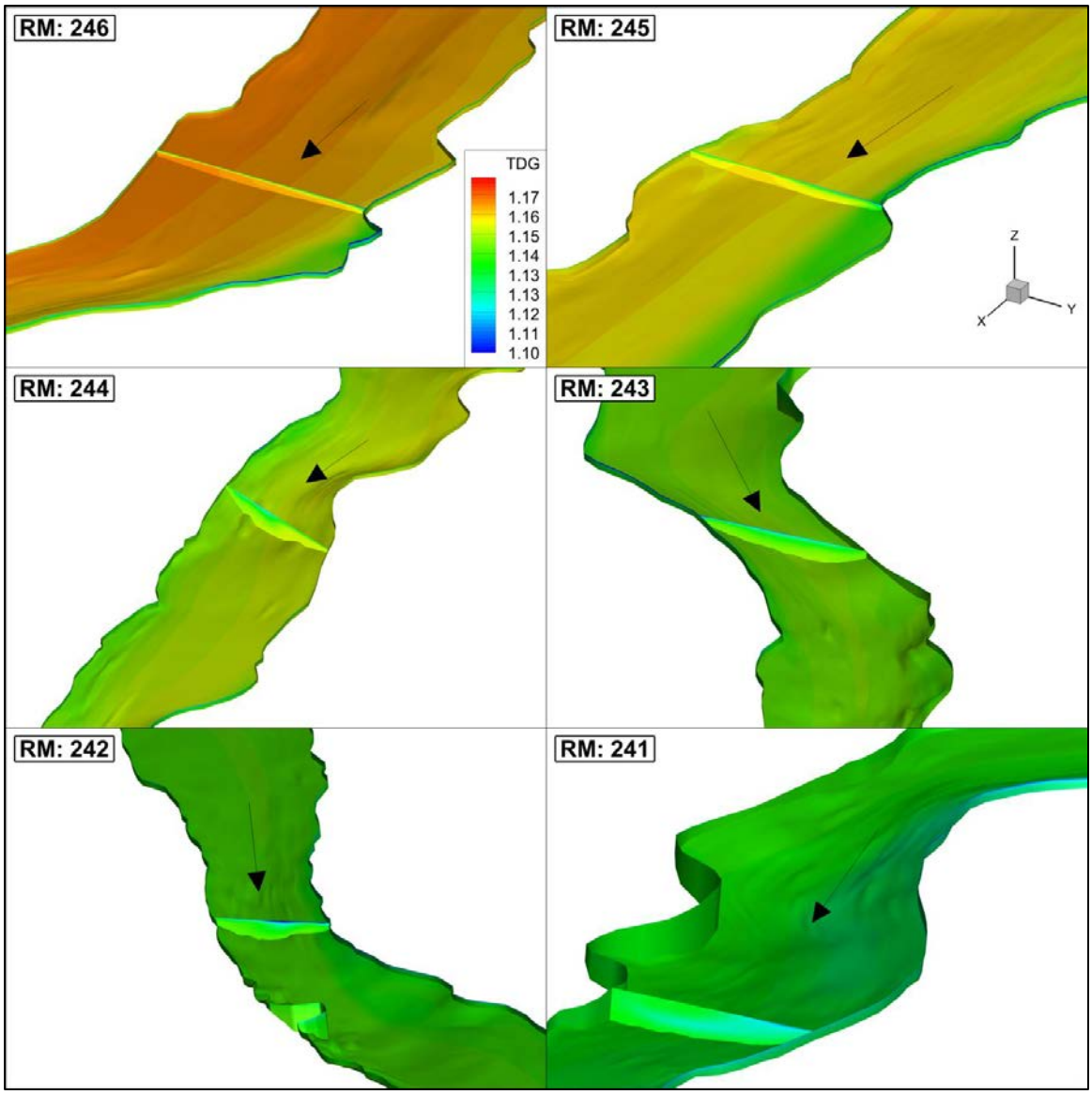

Figure 80. TDG in the downstream region displaying the distribution for 45 Kcfs

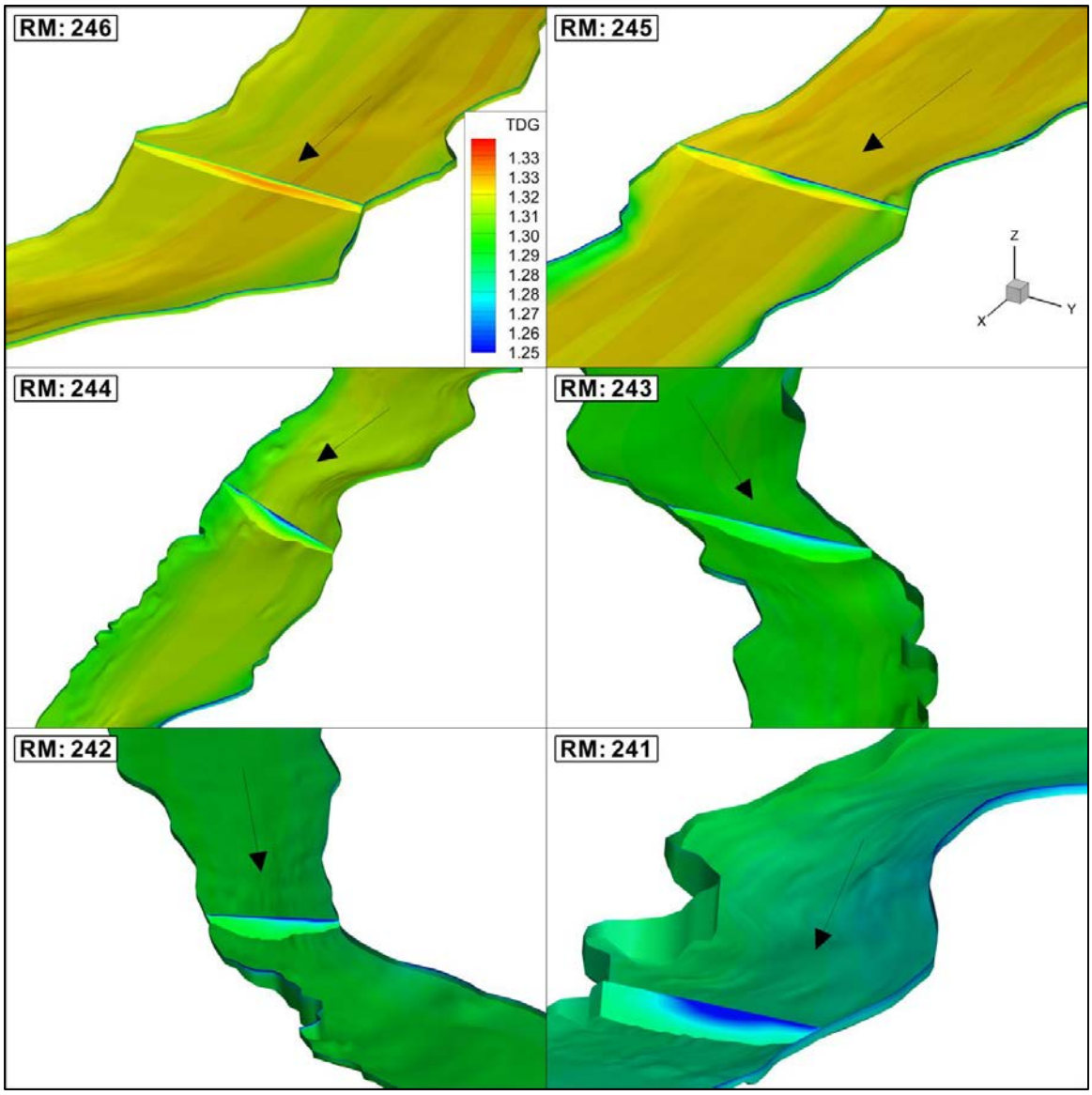

Figure 81. TDG in the downstream region displaying the distribution for 7Q10 deflector flow

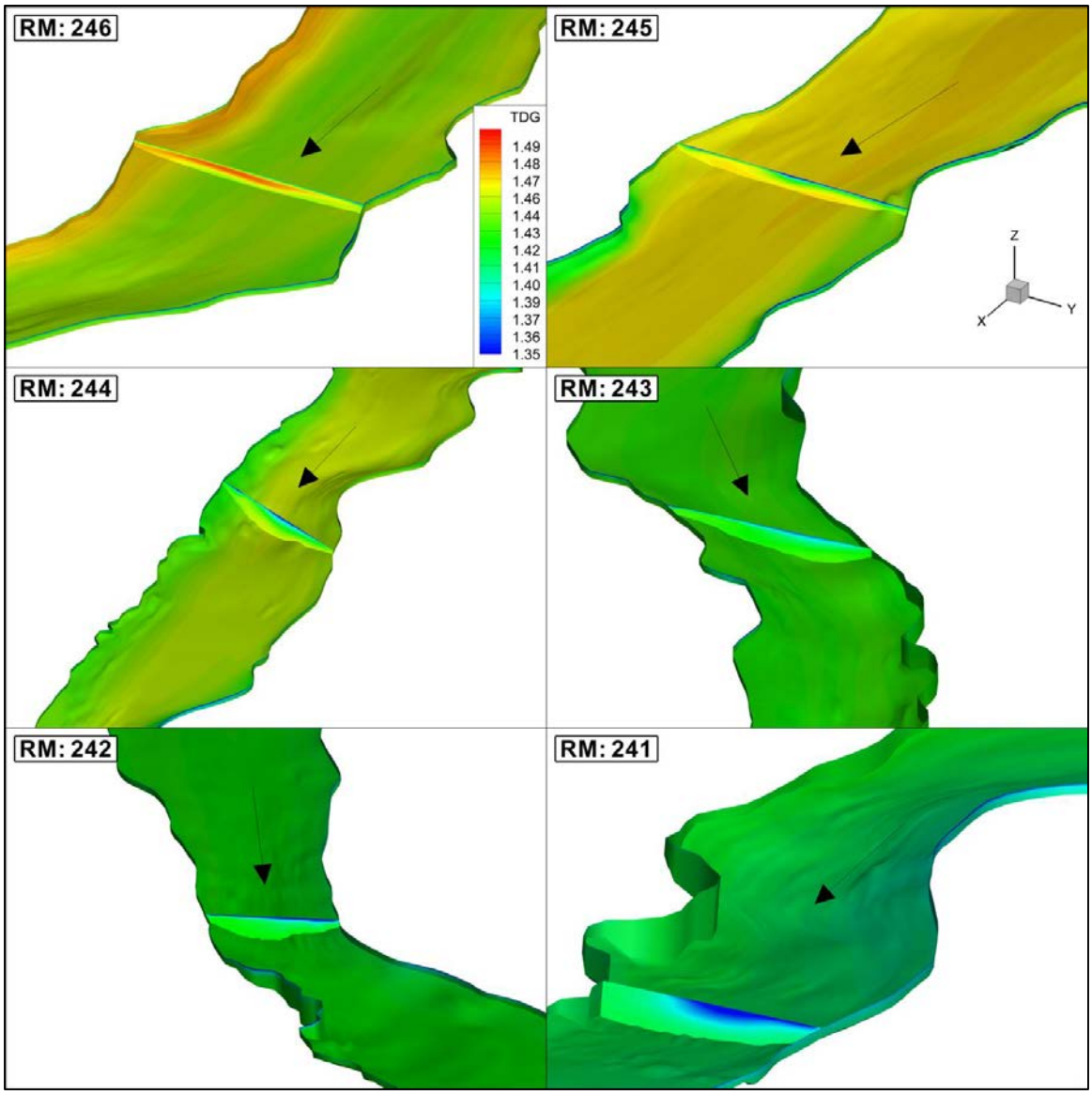

Figure 82. TDG in the downstream region displaying the distribution for 7Q10 deflector flow

Table 4. TDG concentration as a function of river mile. HCD is at RM 247.7 and RM 248 represents the forebay

TDG by River Mile												
	37kcfs			45kcfs			7Q10 Deflector			7Q10 No Deflector		
River Mile	Average	West Bank	East bank	Average	West Bank	East bank	Average	West Bank	East bank	Average	West Bank	East bank
248	1.150	1.150	1.150	1.150	1.150	1.150	1.150	1.150	1.150	1.150	1.150	1.150
247.6	1.155	1.169	1.151	1.152	1.157	1.151	1.209	1.321	1.164	1.501	1.205	1.674
247.5	1.159	1.171	1.151	1.168	1.169	1.151	1.352	1.368	1.287	1.518	1.210	1.656
247	1.154	1.160	1.151	1.169	1.174	1.159	1.339	1.352	1.295	1.479	1.313	1.553
246.5	1.151	1.156	1.152	1.166	1.171	1.163	1.326	1.329	1.330	1.476	1.391	1.524
246	1.147	1.152	1.143	1.163	1.165	1.152	1.321	1.322	1.320	1.468	1.465	1.483
245.5	1.144	1.150	1.137	1.158	1.164	1.158	1.313	1.322	1.319	1.456	1.455	1.477
245	1.140	1.145	1.133	1.154	1.159	1.141	1.306	1.322	1.310	1.446	1.461	1.450
244.5	1.135	1.139	1.134	1.151	1.159	1.154	1.301	1.306	1.322	1.438	1.441	1.464
244	1.132	1.137	1.132	1.148	1.150	1.157	1.297	1.307	1.309	1.432	1.468	1.441
243.5	1.130	1.137	1.131	1.146	1.150	1.155	1.294	1.307	1.305	1.428	1.453	1.440
243	1.126	1.133	1.127	1.143	1.148	1.147	1.290	1.302	1.295	1.422	1.444	1.448
242.5	1.125	1.130	1.130	1.142	1.149	1.146	1.289	1.298	1.287	1.421	1.428	1.438
242	1.122	1.123	1.122	1.139	1.147	1.140	1.283	1.296	1.288	1.412	1.427	1.429
241.5	1.118	1.117	1.118	1.135	1.138	1.135	1.278	1.288	1.281	1.404	1.412	1.431
241	1.116	1.116	1.116	1.133	1.136	1.130	1.273	1.285	1.274	1.398	1.408	1.423

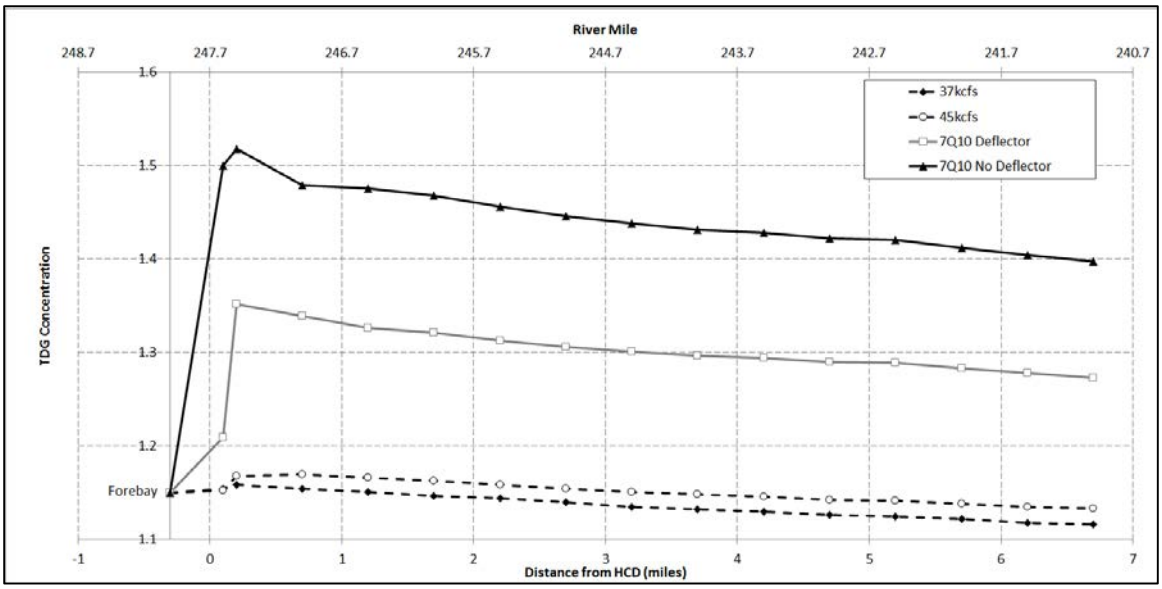

Figure 83. Average TDG downstream at selected distances

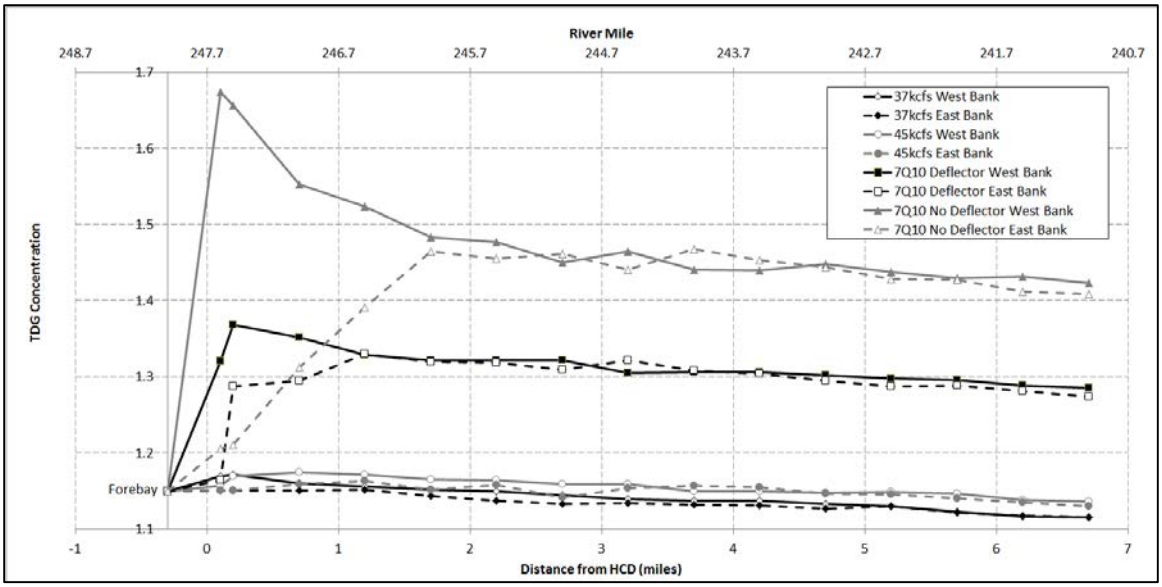

Figure 84. Downstream TDG at western and eastern banks

Powerhouse Entrainment

Jet entrainment of powerhouse flow is shown in Figure 85. Entrainment values were calculated based on the planes shown in Figure 53. The increase in sluiceway flow rate shows and increase in powerhouse entrainment. For the 7Q10 flow condition the inclusion of deflectors increases the level of flow entrainment by 30 Kcfs, an increase of approximately 150%.

Entrainment from the grid sensitivity analysis, Figure 22, is different from the rigid-lid data in the way entrainment was determined. Entrainment in the VOF grid sensitivity analysis was calculated without distinguishing the density of air and water. Also, it should be noted that conservation equations and turbulence models for the two models are different. The entrainment from the grid sensitivity 45 Kcfs VOF flow is on average 38% higher than the entrainment of the rigid-lid solutions.

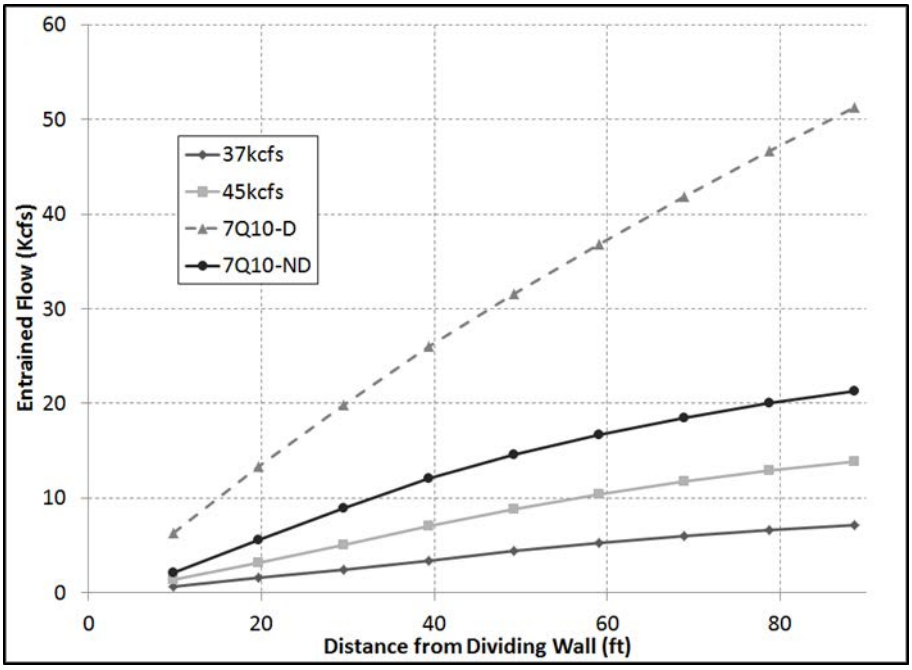

Figure 85. Powerhouse entrainment for the selected deflector at performance testing conditions

Fish Injury

Deng et al. (2005) determined curves of injury probability versus acceleration, as previously mentioned acceleration was the strongest predictive variable for determining probability of injury. Figure 86 and Figure 87 show the probability curve of the fish experience a major and minor injury, respectively. Whereas Figure 88 and Figure 89 show the probability curve of a fish experiencing injury to the eyes or operculum due to acceleration. For an acceleration of approximately 900 $\frac{ft}{s^2}$ the probability of major injury was below 0.05. At about 1500 $\frac{ft}{s^2}$, the probabilities of fish suffering minor and major injuries were 0.50 and 0.18 respectively. Life-threatening injuries were almost certain for accelerations above 4200 $\frac{ft}{s^2}$. Since the more comprehensive analysis was oriented to

acceleration, it will be considered the important factor in determining fish injury probability.

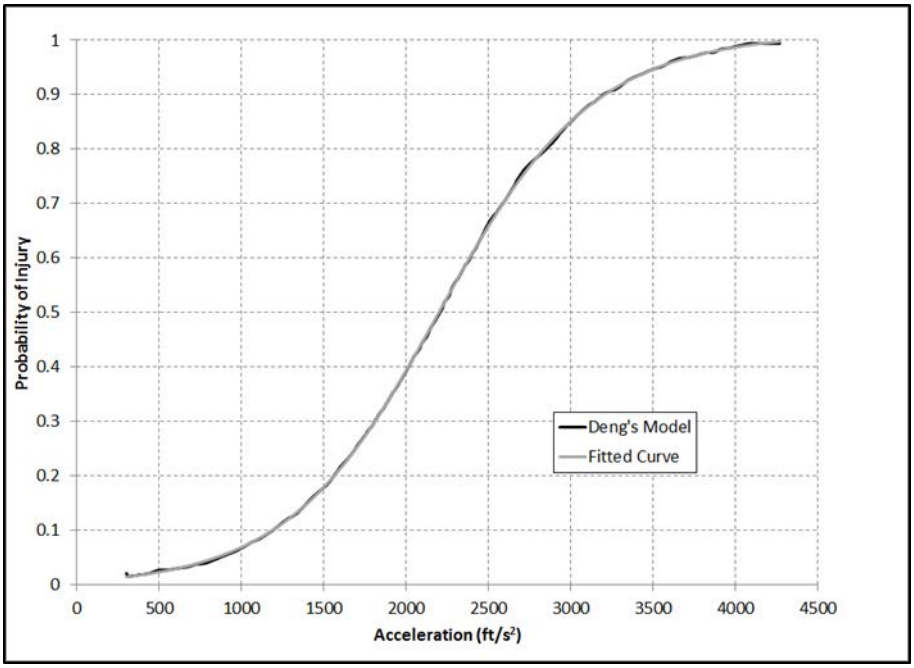

Figure 86. Probability of major injury

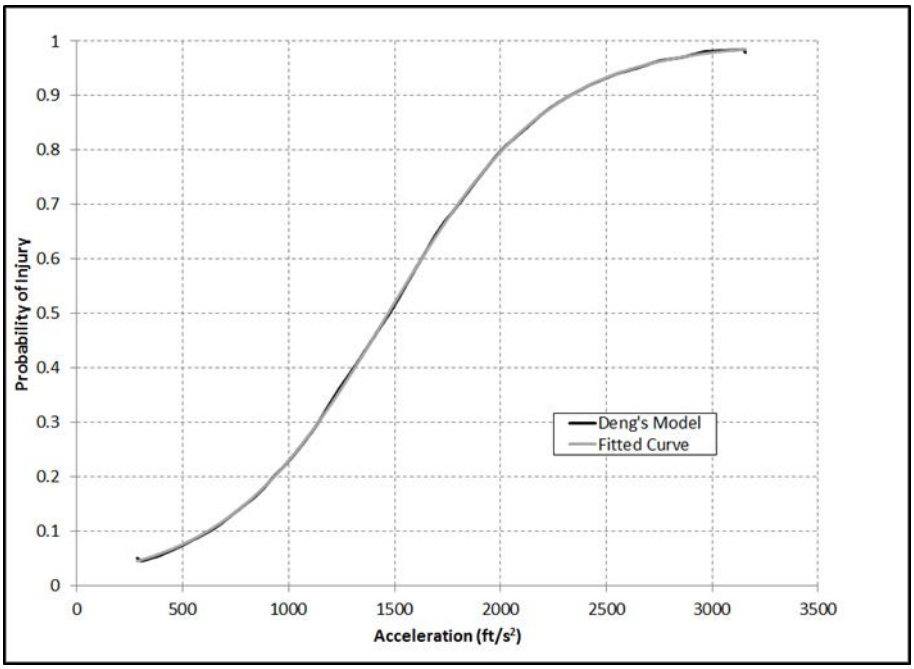

Figure 87. Probability of minor injury

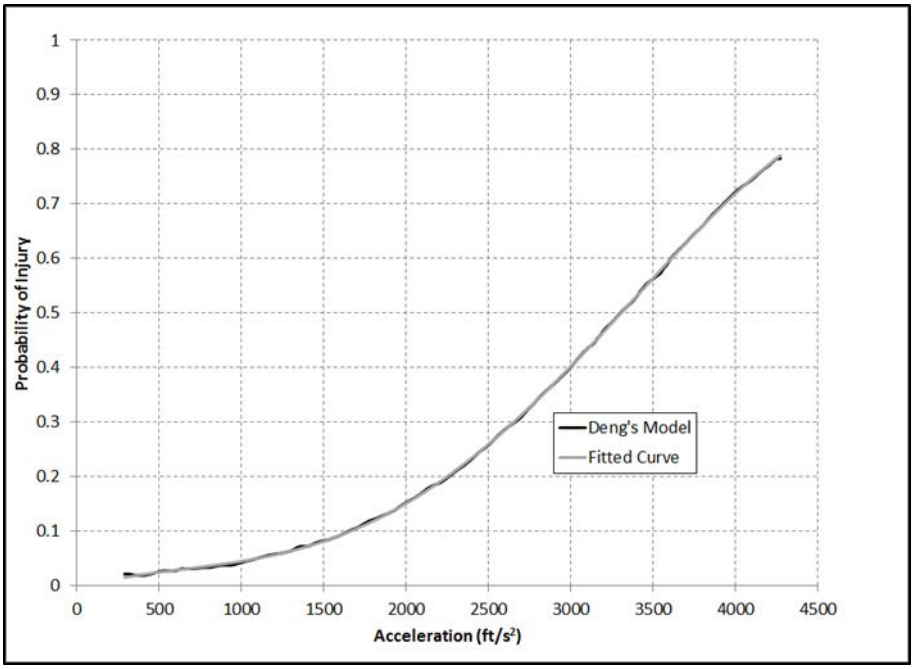

Figure 88. Probability of eye injury

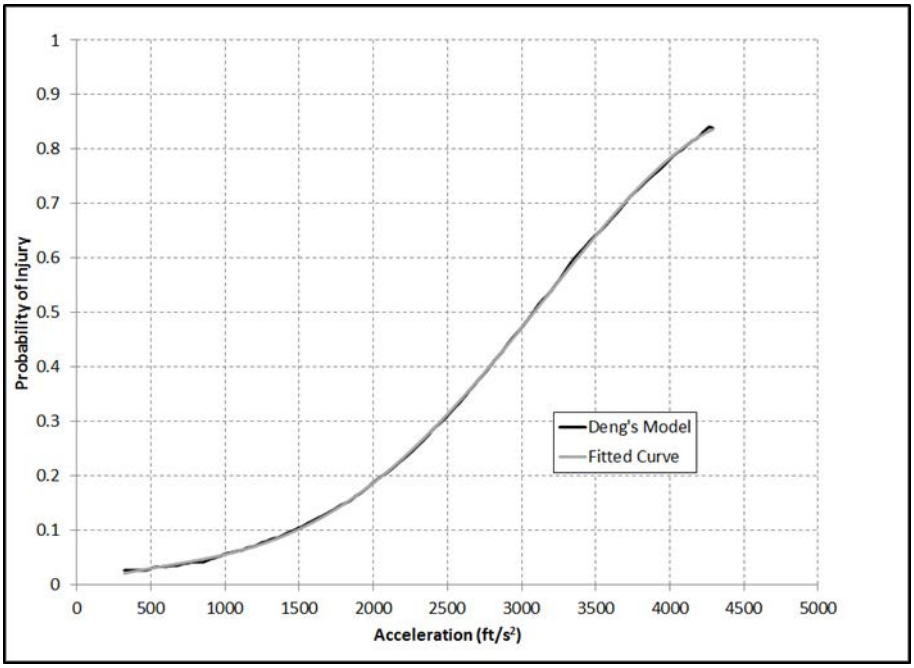

Figure 89. Probability of operculum injury

In order to estimate the overall probability of injury the probability of injury for each particle was calculated using curves fit to Deng's 4 probability curves shown previously, starting on page 129. In the probability curves shown there is a grey fit line

presented over the black line from the author. The curve fit was determined by digitizing the curves from the author to polynomial and sigmoidal functions. The below functions describe the injury probability curves for minor, major, eye and operculum respectively. Probability of injury was determined by releasing three thousand particles into the VOF flow from the two sluiceways and three spillways. The particles were released at 30% and 70% of the gate opening.

$$y = -0.0057 + 1.02059\left(\frac{0.7681}{1 + 10^{0.00331(665.60708-x)}} + \frac{0.2319}{1 + 10^{0.00221(706.05854-x)}}\right) \tag{23}$$

$$y = \frac{0.998}{1 + e^{-0.00847(x-447.33824)}} \tag{24}$$

$$y = -8.13649(10^{-13})x^4 + 2.02954(10^{-9})x^3 - 1.02567(10^{-6})x^2 + 3.14856(10^{-4})x - 0.00662 \tag{25}$$

$$y = -1.01137(10^{-12})x^4 + 2.33151(10^{-9})x^3 - 1.08654(10^{-6})x^2 + 3.38219(10^{-4})x - 0.0042 \tag{26}$$

Fish Injury Sensitivity Analysis

Particles were injected into the three converged solutions from the VOF grid sensitivity analysis, Figure 13, to compare the effects of grid density on the calculated probability of injury. Figure 90 shows the results for each of the tested VOF grids with the fine case showing the highest percentage of injury. The overall probability of injury is calculated from the acceleration data extracted from the path of each individual particle. Due to the probability of minor injury being most sensitive to changes in acceleration, it shows the largest difference in injury between the three simulations, calculated from Equation 24 and presented in Figure 87. The relative percent difference of injury probability between the fine and medium mesh was 9.5% and 9.4% between the medium and coarse mesh. This produced a difference of injury probability of 0.9% and 0.8% for the fine to medium and medium to coarse, respectively. Figure 91 and Figure 92 show the particle acceleration and strain rate averaged in space for all of the particles from sluiceway 1 and sluiceway 2, respectively. The trend for the average acceleration of the population is similar to the injury probability, where the largest average acceleration is present in the fine case. Damages due to strain rate were not considered important since they are an order of magnitude lower than the possibility of injury described in Foust et al. (2010).

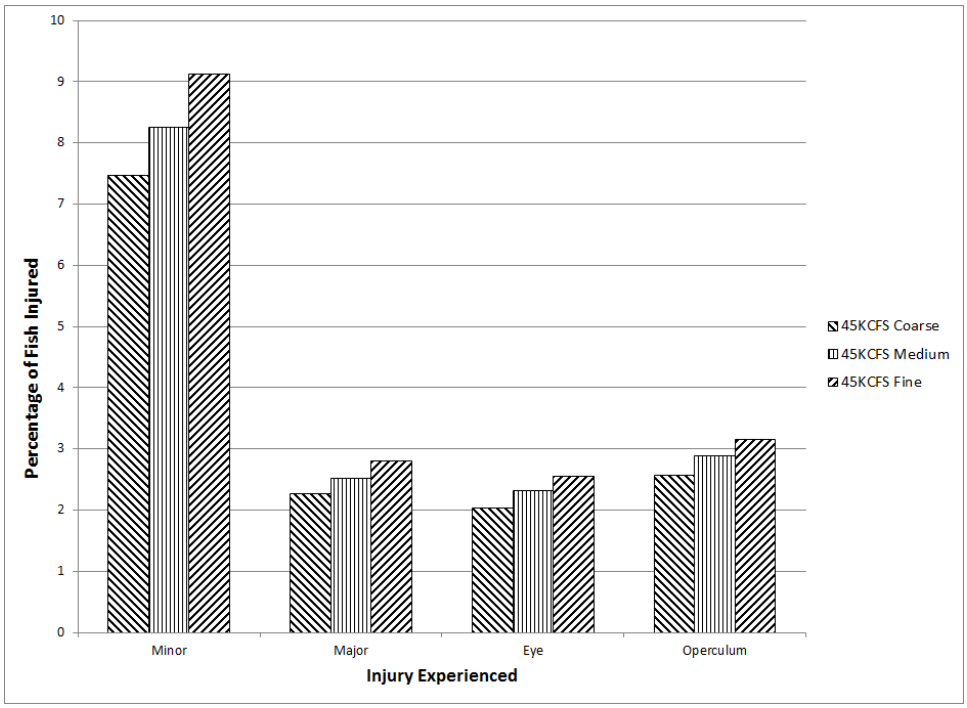

Figure 90. Injury experienced by the fish for the three grid densities

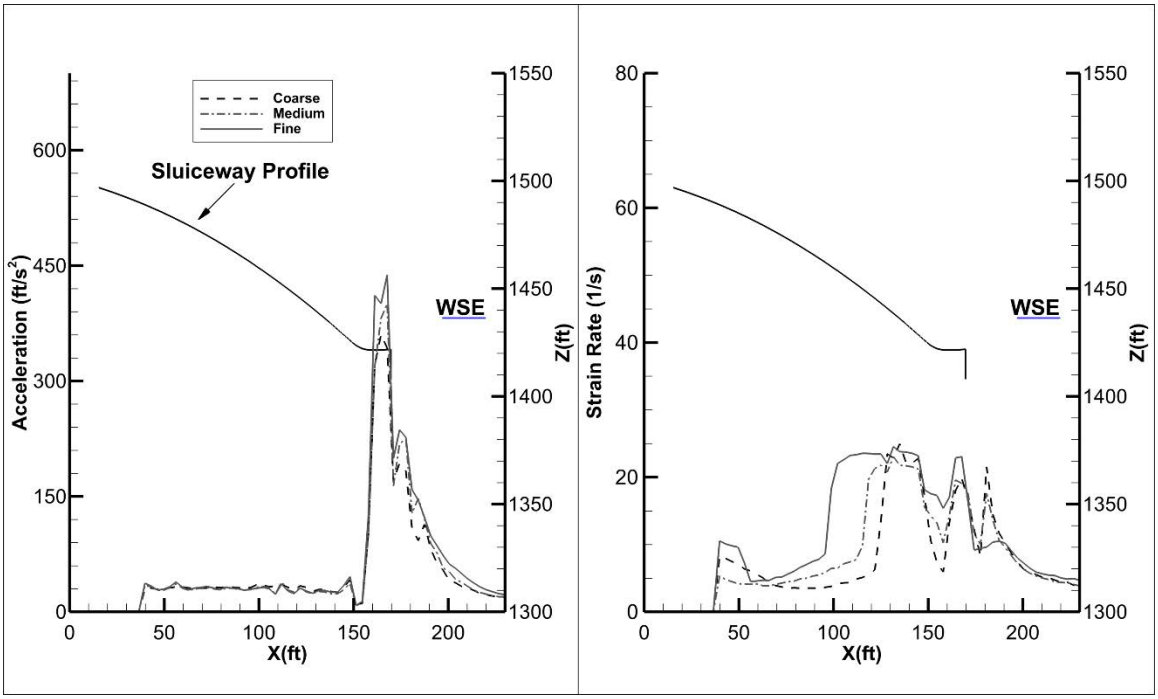

Figure 91. Acceleration and strain rate experienced by particles from sluiceway 1

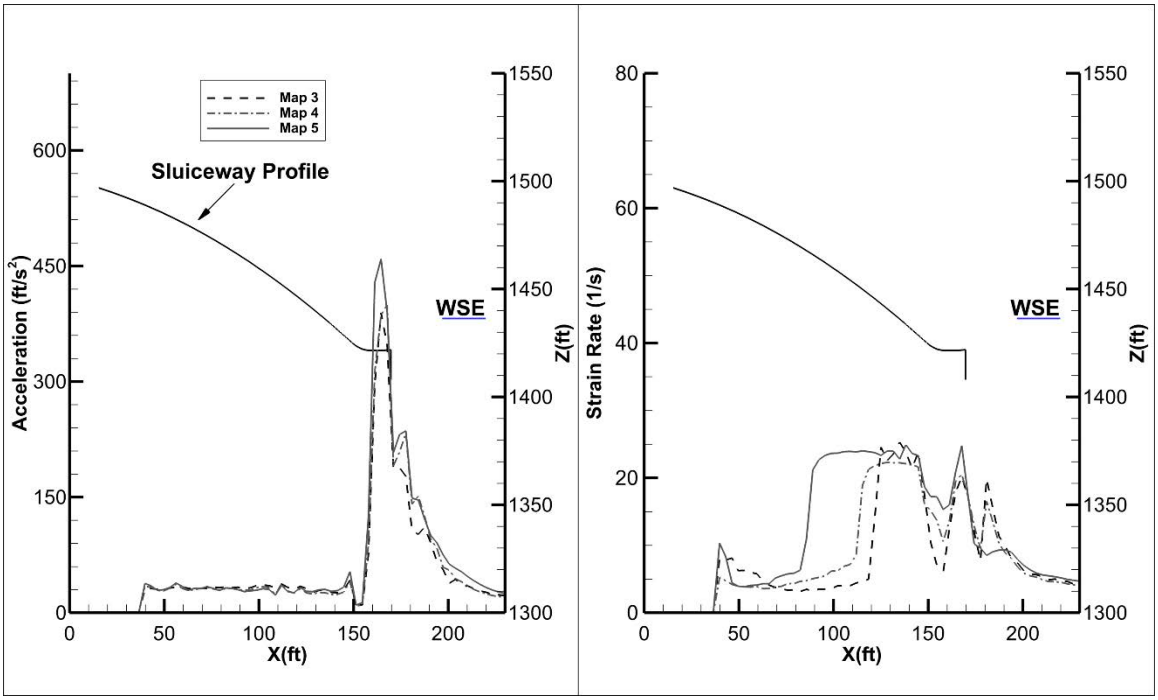

Figure 92. Acceleration and strain rate experienced by particles from sluiceway 2

The trends in Figure 90 to Figure 92 show the grids used in the sensitivity analysis are not converging to a value of injury probability or acceleration. Given this information the grid size should be increased to determine the value of convergence. However, the computational requirements of refining the grid, past the fine case of 6.5 million nodes, made the determining of the value of convergence infeasible for this study. Refining the fine grid using the 1.4 times increase of nodes per connector, used in determining the fine and coarse grid size, would produce a computational grid of approximately 17.8 million nodes. A grid that large could not be solved in a reasonable amount of time given the computational resources of this project. It is also not certain that one more refinement will indicate the value of convergence. Increasing the refinement near the walls may assist in converging the injury results. However, without further refinement away from the walls the accuracy of the flow field would be sacrificed.

Figure 93 shows contours of acceleration on slices through and across sluiceway 2; the acceleration data is extracted from Fluent. The slices are oriented to cross through the highest points of acceleration. With the constant X slice oriented perpendicular to the flow and near the location of maximum acceleration. The two slices down the spillway show the differences between accelerations near the wall and the center of the flow. Present on each slice is a white line, this line signifies the minimum gas volume fraction allowable for a particle to be counted in the injury analysis. This figure shows the refined grid resolving higher flow acceleration near the free surface. The percentage difference between the medium and refined case is on the order of 5%, calculated from sampling similar points relative to the structure.

Velocity data was extracted on the perpendicular slice from Figure 93, at the center of sluiceway 2, for each grid. Velocity profiles for the flow were generated with the extracted data, with the limitation that the velocities were collected within cells that have a gas volume fraction smaller than 0.5. Figure 94 shows the velocity profile for the flow in the center of the sluiceway for each of the grids involved in the grid sensitivity analysis. The medium and high sensitivity cases show a maximum difference of 1.5% and the coarse and medium cases show a maximum difference of -5.5%.

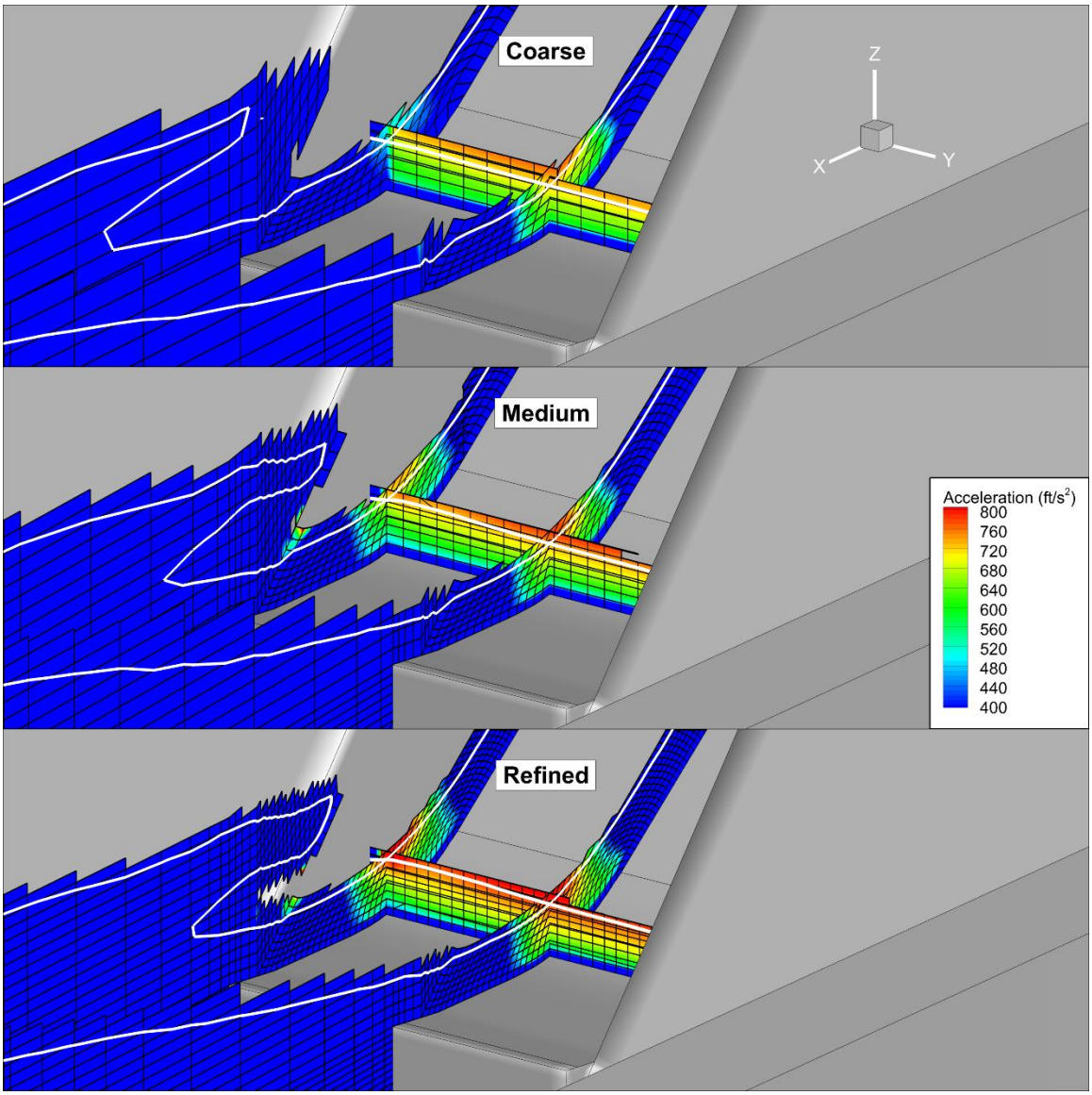

Figure 93. Slices showing the contour of acceleration on the grid where the white line signifies the allowable upper limit of gas volume fraction

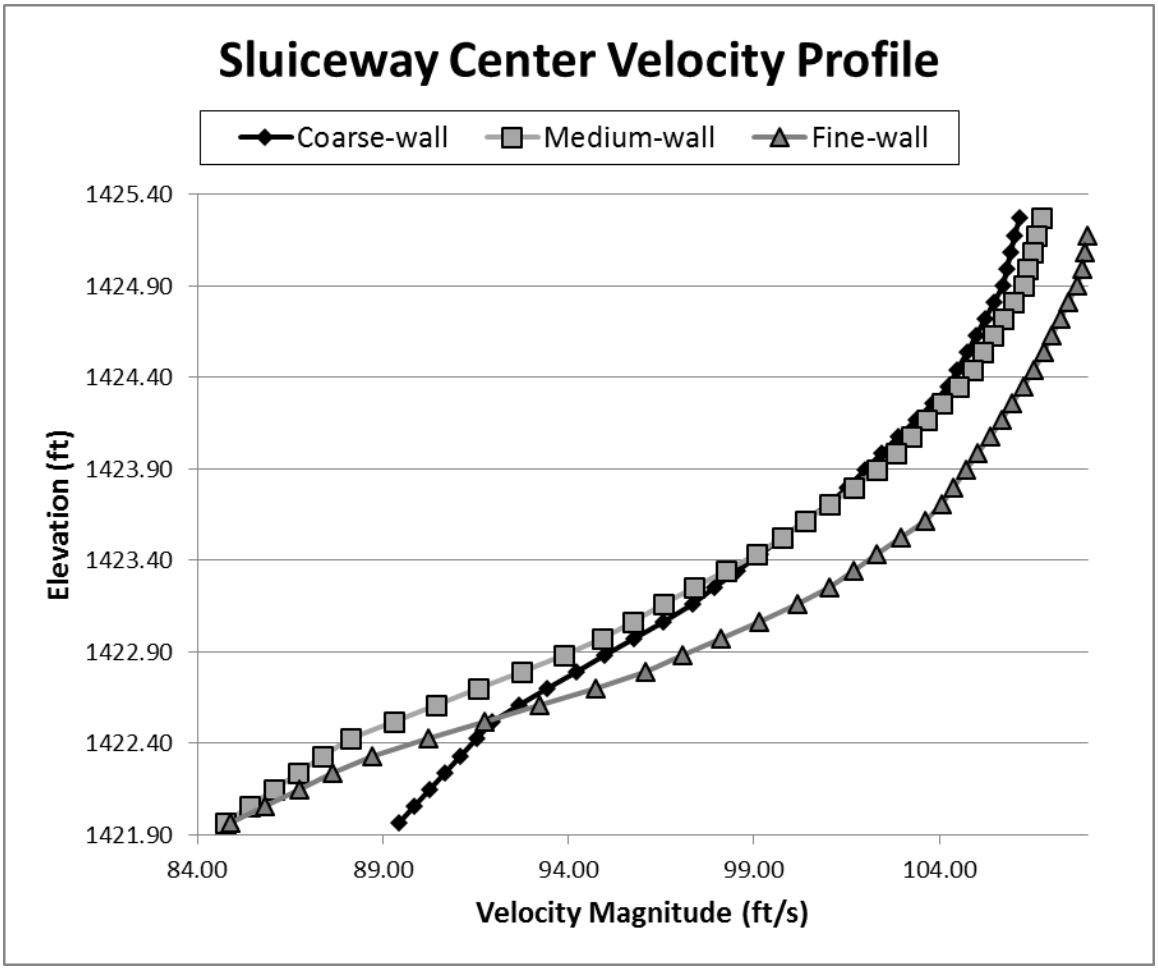

Figure 94. Velocity profile at the center of sluiceway flow for the grid sensitivity cases

Since the probability of fish mechanical injury was not the primary parameter for selecting the deflector, and is just used as an added measurement of deflector performance, the medium grid was used. The medium grid was shown in Chapter V to sufficiently converge the flow field, the medium grid was selected for the remaining studies presented in this work. Although not converged, the results from the medium grid will be used as a baseline to compare the differences in the probability of injury among the flow rates.

Fish Injury with Selected Deflector

Averaged acceleration and strain rate experienced by the particles for the 37 Kcfs, 45 Kcfs, and 7Q10 flows are shown in the below figures. Where the solid black line is the spillway face and the blue line is the tailwater elevation. Figure 95 shows the acceleration and strain rate experienced by the particles for the 37 Kcfs flow. For the 37 Kcfs flow a maximum acceleration was about 330 $\frac{ft}{s^2}$, with a maximum strain rate of 66 $\frac{1}{s}$. Figure 96 show the acceleration and strain rate for the 45 Kcfs. Maximum values for acceleration and strain rate for the 45 Kcfs were 165 $\frac{ft}{s^2}$ and 16 $\frac{1}{s}$ respectively. Figure 97 and Figure 98 show the acceleration and strain rate for the 7Q10 flows. Where the 7Q10 deflector case had the highest acceleration of 460 $\frac{ft}{s^2}$, approximately 155% larger than the no deflector case. In contrary the no deflector case has the higher strain rate at a value of 26 $\frac{1}{s}$, larger than the deflector case by 270%. The highest acceleration was experienced when the flow changes direction at the deflector and the greatest strain rate was experienced on the spillway face approximately 30 ft below the estimated water surface elevation.

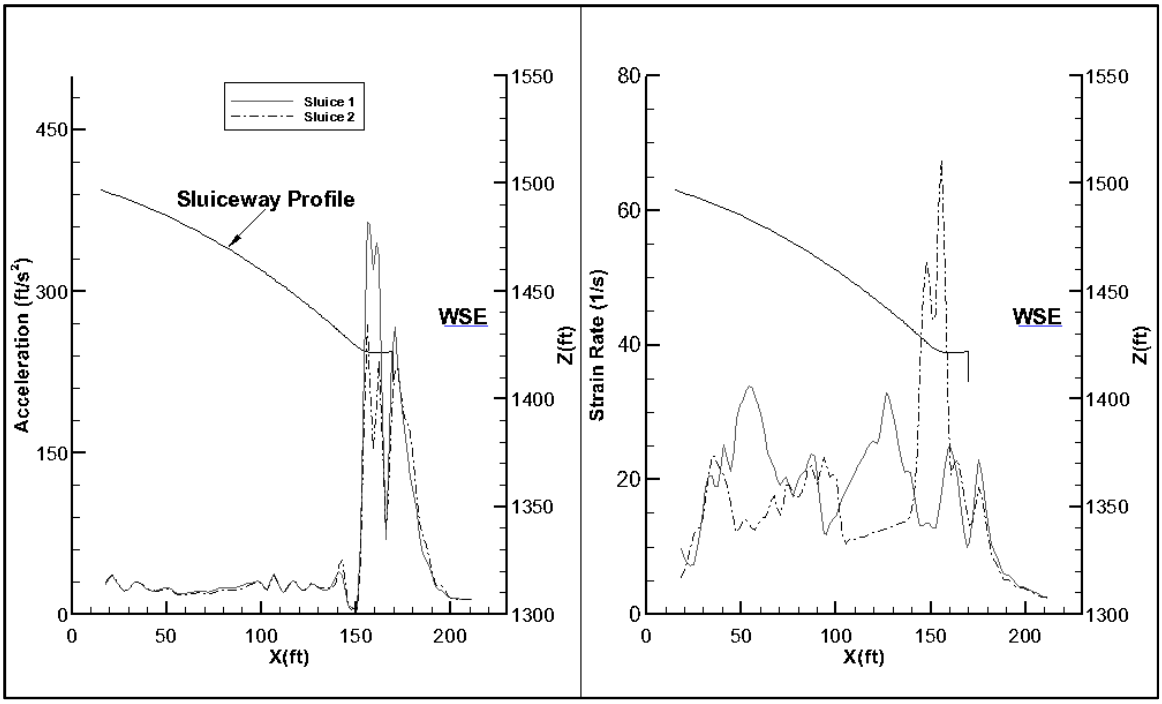

Figure 95. Acceleration and strain rate for 37 Kcfs

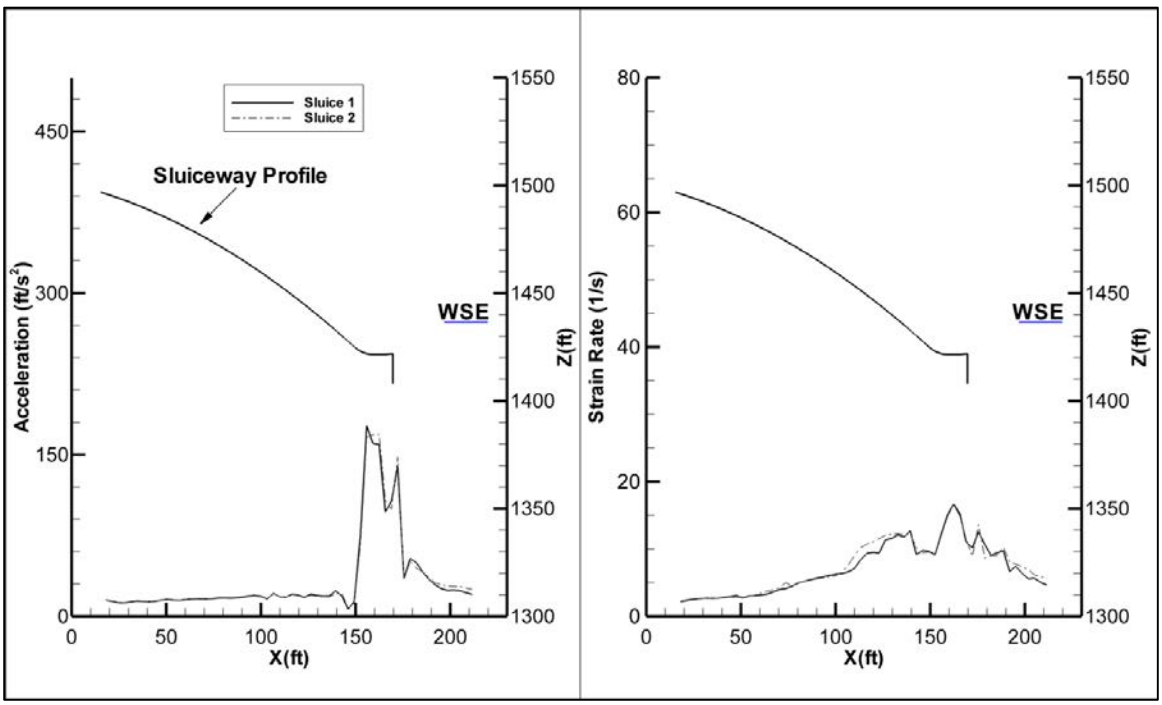

Figure 96. Acceleration and strain rate for 45 Kcfs

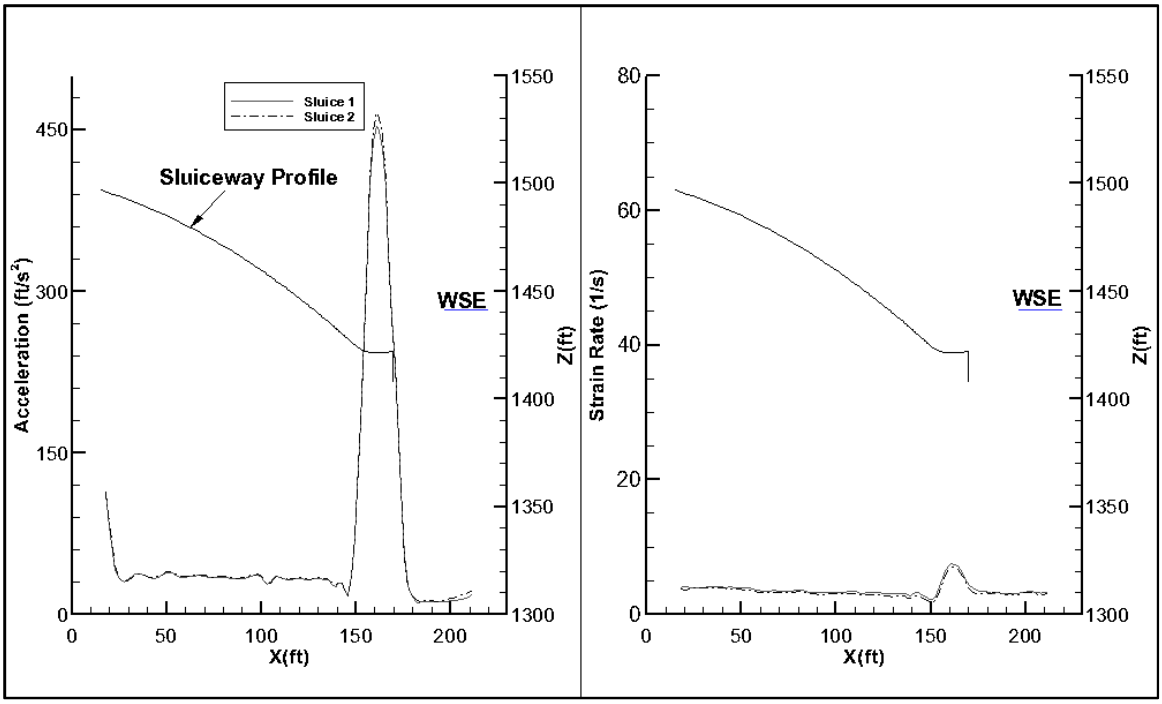

Figure 97. Acceleration and strain rate for 7Q10 with deflectors

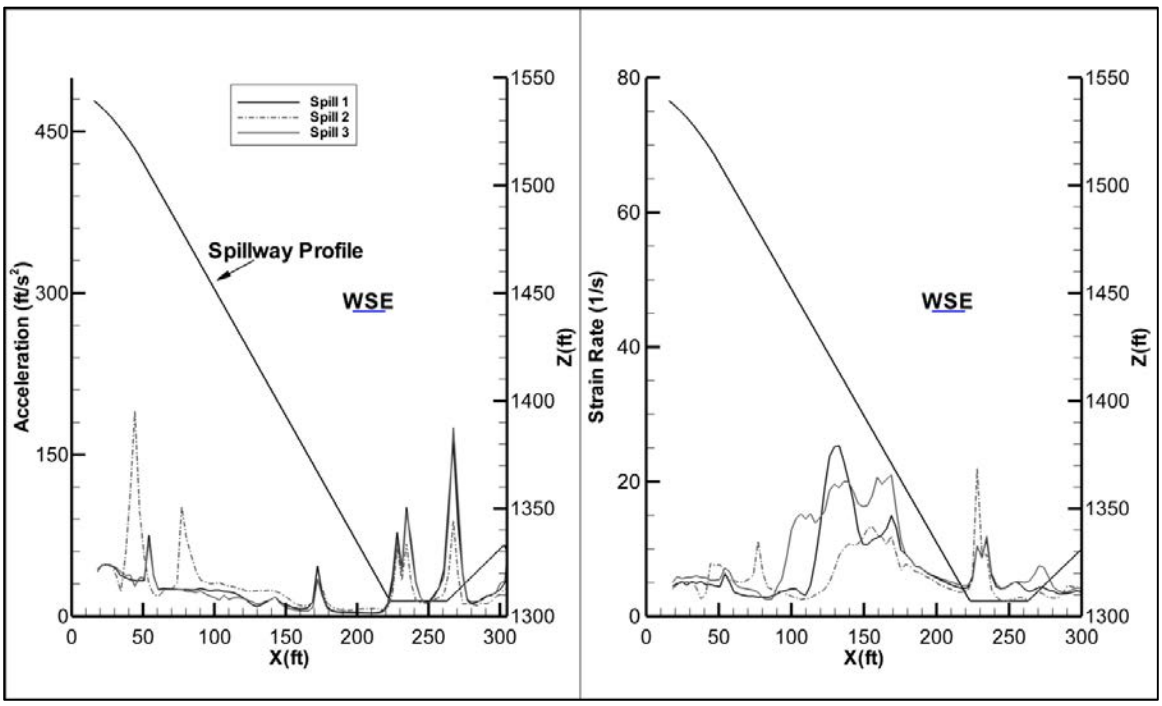

Figure 98. Acceleration and strain rate for 7Q10 without deflectors

Table 5 and Figure 99 show the different injury percentages for the respective flow conditions. The most serious conditions were present in the 37 Kcfs and 7Q10

deflector flow condition. Inclusion of deflectors in the 7Q10 condition increase the probability of major injury from 1.4% to 3.1% and from 4.6% to 10.2% for minor injuries.

Table 5. Injury percentage due to acceleration

Injury Percent				
	Minor	Major	Eye	Operculum
37Kcfs	10.9	3.4	3.0	3.7
45Kcfs	4.3	1.3	1.3	1.7
7Q10-D	10.2	3.1	2.9	3.5
7Q10-ND	4.6	1.4	1.3	1.8

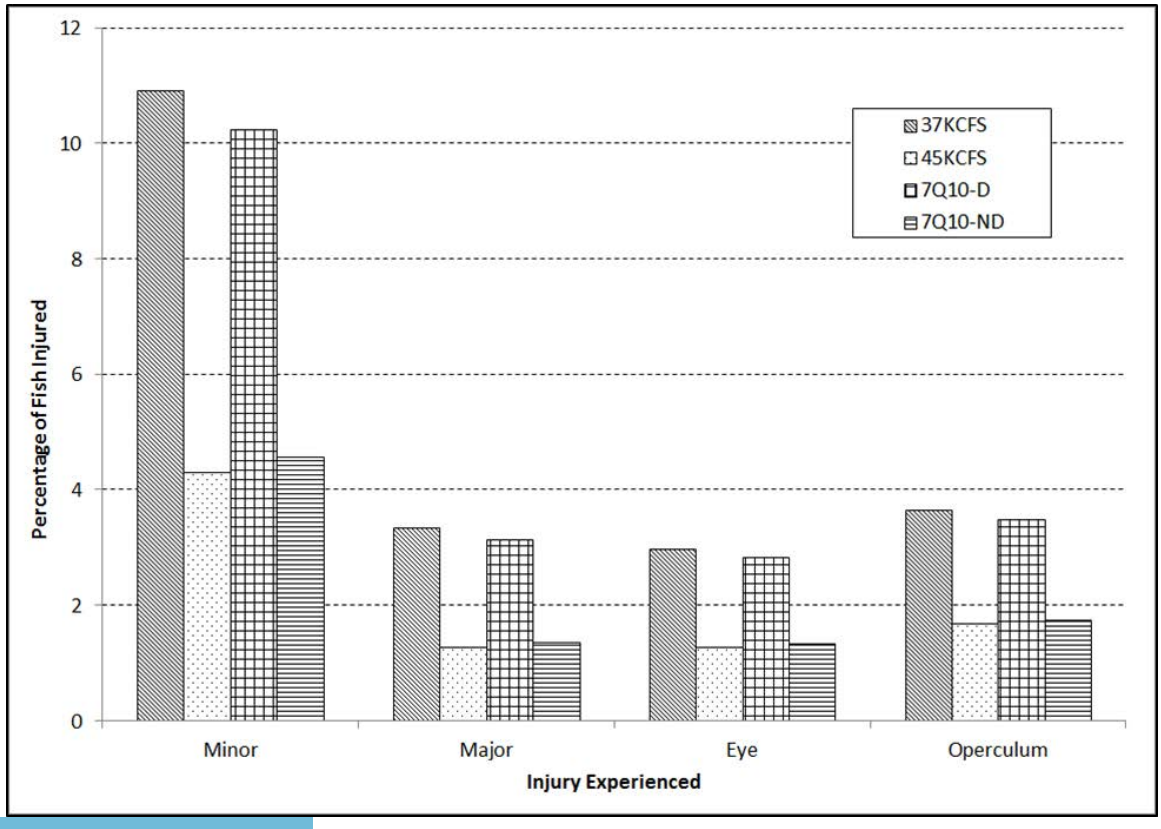

Figure 99. Percent of fish injuries based on acceleration

Residence Time

Tailrace residence time was calculated by releasing particles from all flow inlets and measuring the time elapsed before reaching a plane 650 ft downstream of the dam. The plane was chosen to be 650 ft downstream of the dam because it was contained in all 4 of the flow cases and past any recirculation region that may cause false readings. Number of particles released from each inlet was flow rate weighted to avoid misrepresentation of overall residence time. Table 6 shows the average, mean and standard deviation of the residence times for each flow case. It also shows the total number of particles present in the simulation.

Table 6. Tailrace residence time

Residence Time Statistical Summary				
	37Kcfs	45Kcfs	7Q10-D	7Q10-ND
Average Residence (s)	154.1	180.1	89.3	157.5
Mean Residence (s)	164.2	175.5	97.6	157.7
Standard Deviation (s)	154.1	101.7	65.2	111.8
Total Particles	4640	5643	8966	8966

Figure 100 and Figure 101 show the residence times for particles released from the sluiceways of the 37 Kcfs and 45 Kcfs flows, respectively. The particles released from the sluiceways for the 37 Kcfs simulation were slower than the 45 Kcfs; as expected given the higher velocity present in the sluiceway jets.

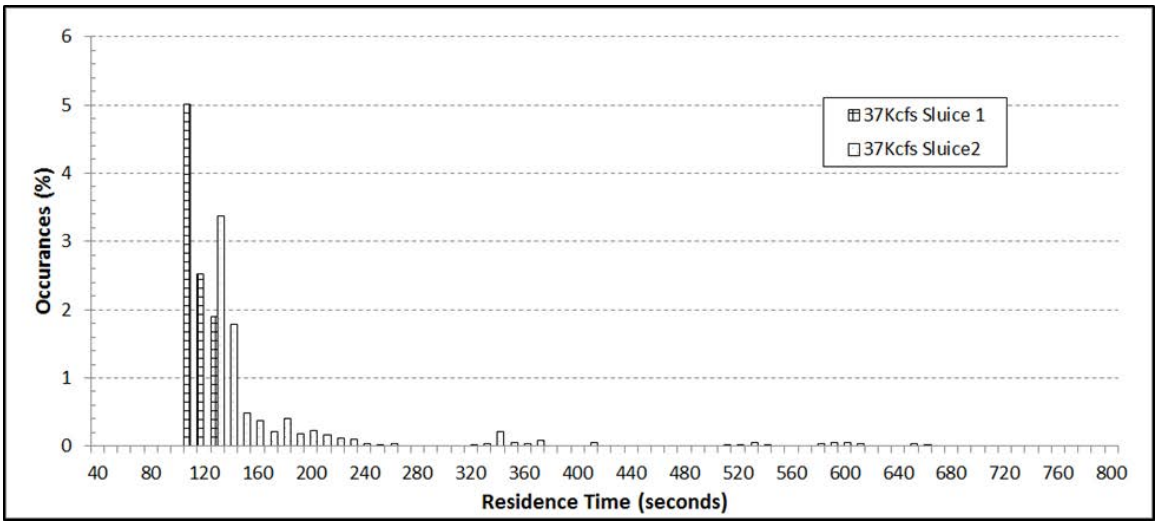

Figure 100. Residence time of particles released from the sluices for 37 Kcfs

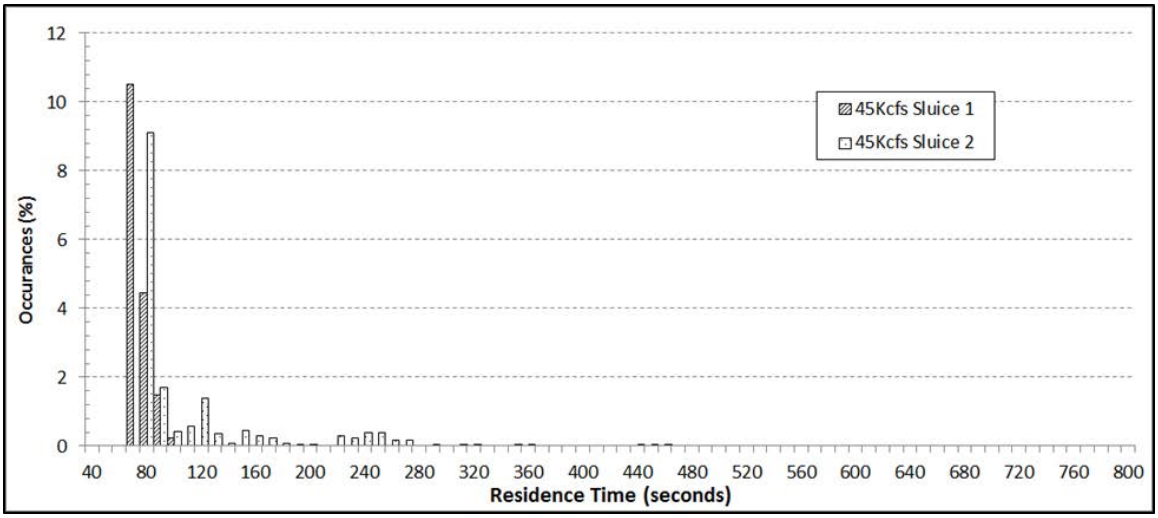

Figure 101. Residence time of particles released from the sluices for 45 Kcfs

Figure 102 and Figure 103 show particle residence times for the 7Q10 flow conditions. For the flow with deflectors the particles can be present in the 650 ft past the spillway for as low as 40 seconds; with the highest number of particles passing the plane between 40 and 80 seconds. It should be noted that some particles can take upwards of 200 seconds to exit the domain, these particles likely entered the large western eddy. For the flow

without deflectors the particles can still exit the domain quickly they were however more likely to spend more time within the 650 ft boundary of the dam.

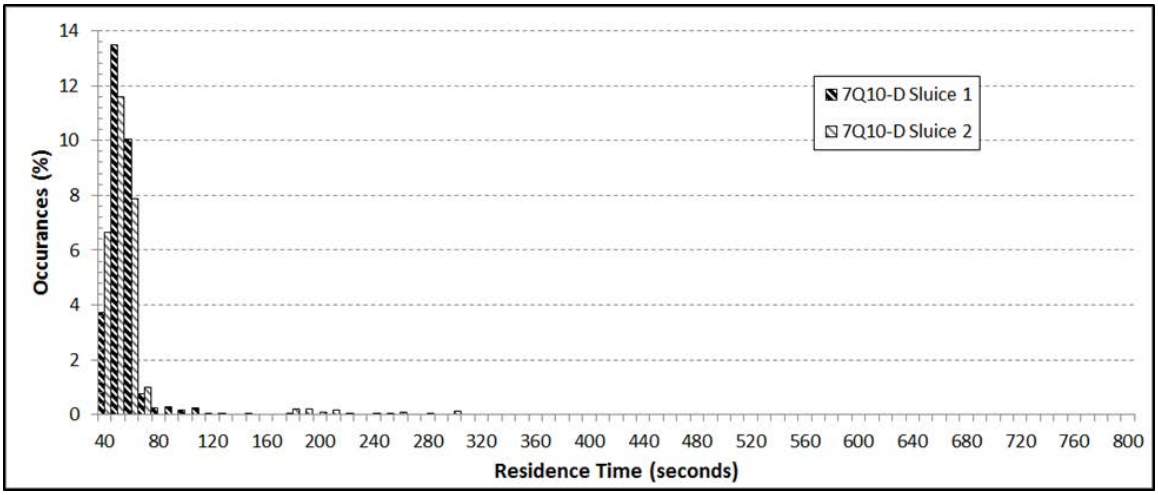

Figure 102. Residence time of particles released from the sluices for 7Q10 with deflectors

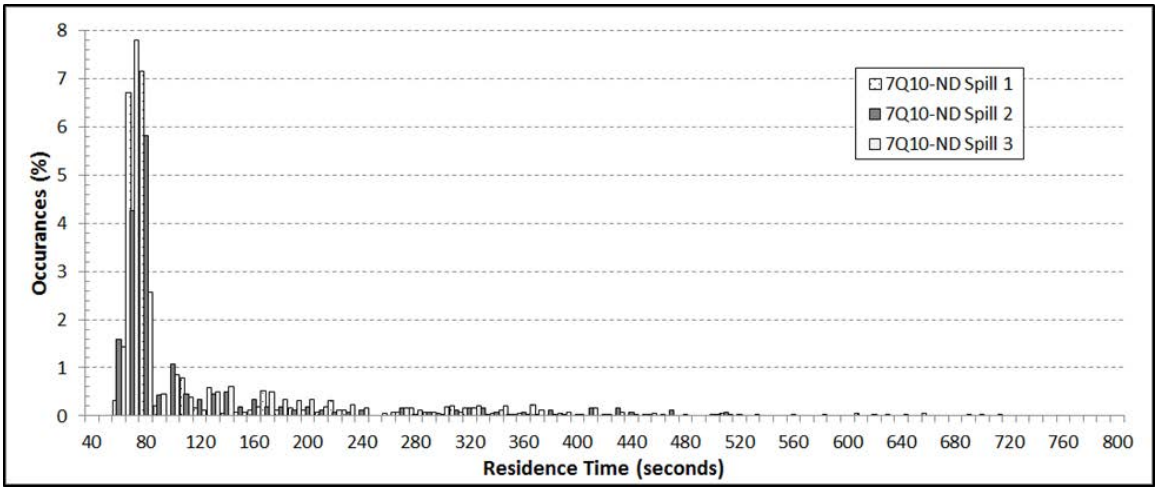

Figure 103. Residence time of particles released from the spillway for 7Q10 without deflectors

Figure 104 shows the residence time of particles released from the turbine draft tubes of the 37Kcfs and 45 Kcfs flows. It should be noted the residence time for particles in the 37 Kcfs case was lower than the particles in the 45 Kcfs case. The lower residence time from the 37 Kcfs flow was attributed to the lower entrainment and the particles being more likely to travel in the streamwise direction undisturbed. Figure 105 shows the comparison

of the particles released from the turbine draft tubes of the 7Q10 simulations. For the case with the deflectors residence time varies greatly with some particles exiting the domain in 40 seconds and a significant number of particles remaining in the domain past 200 seconds. Particles leaving the domain quickly were joining the high velocity jets of the sluiceway. Whereas the particles that were tending to take significant time were likely caught in the large western eddy or in below the jets in a back roll.

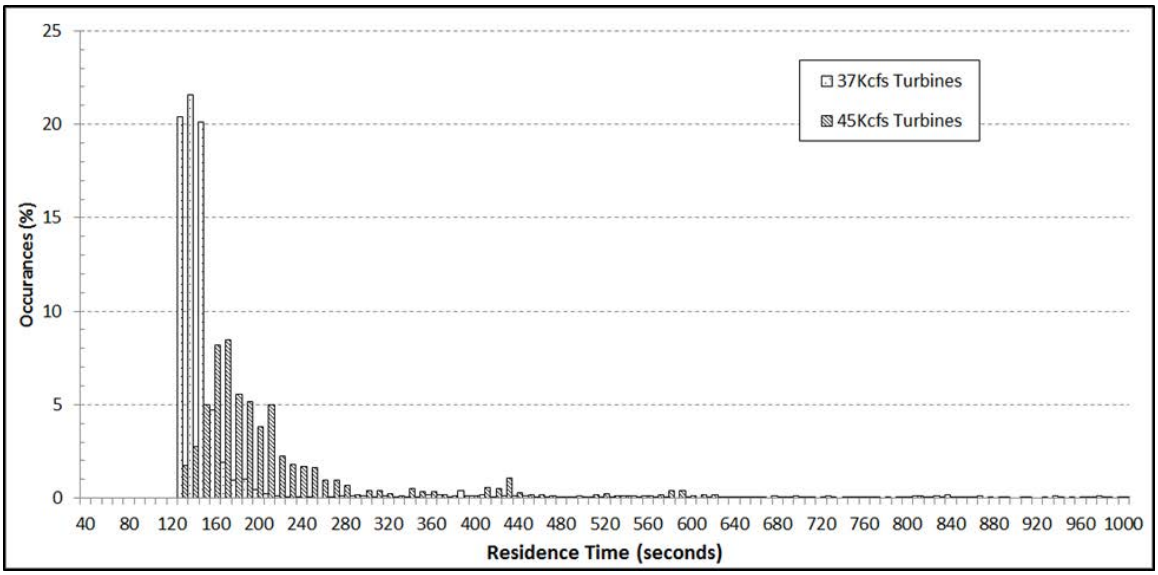

Figure 104. Residence time of particles released from the turbine draft tubes for 37 Kcfs and 45 Kcfs

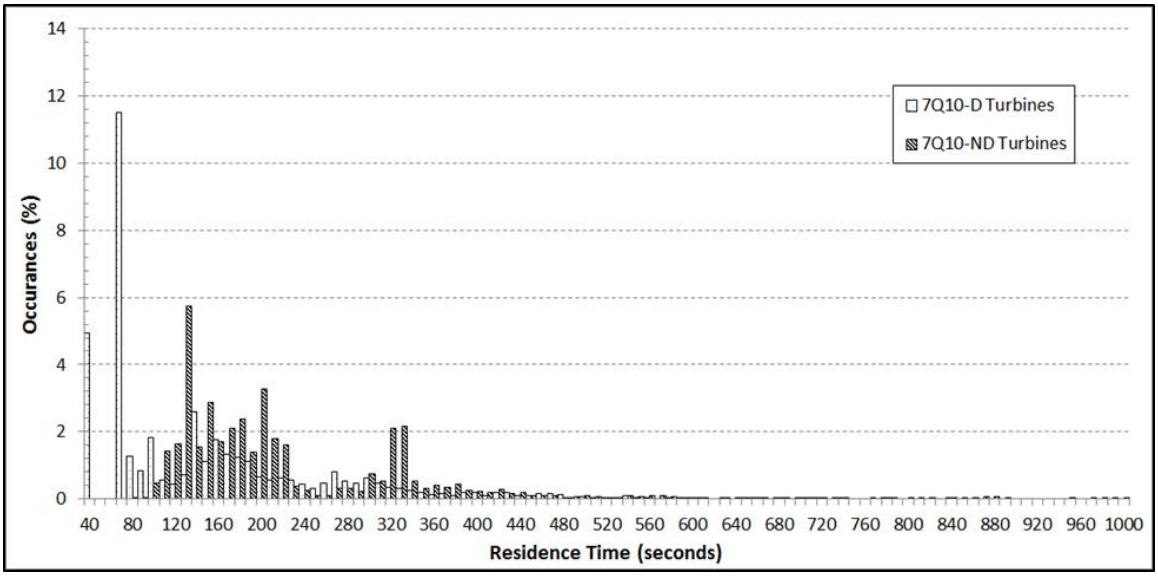

Figure 105. Residence time of particles released from the turbine draft tubes for a 7Q10 flow

The path of all particles released from the 37 Kcfs case are shown in Figure 106, sluiceways, and Figure 107, powerhouse. Particles released from sluiceway 2 can be trapped in the small eastern recirculation and pulled to depth in the stilling basin, thus increasing residence time. As previously mentioned, the low entrainment levels allow the particles released from the powerhouse to travel downstream most undisturbed although a few particles were mixed in with the sluiceway flow.

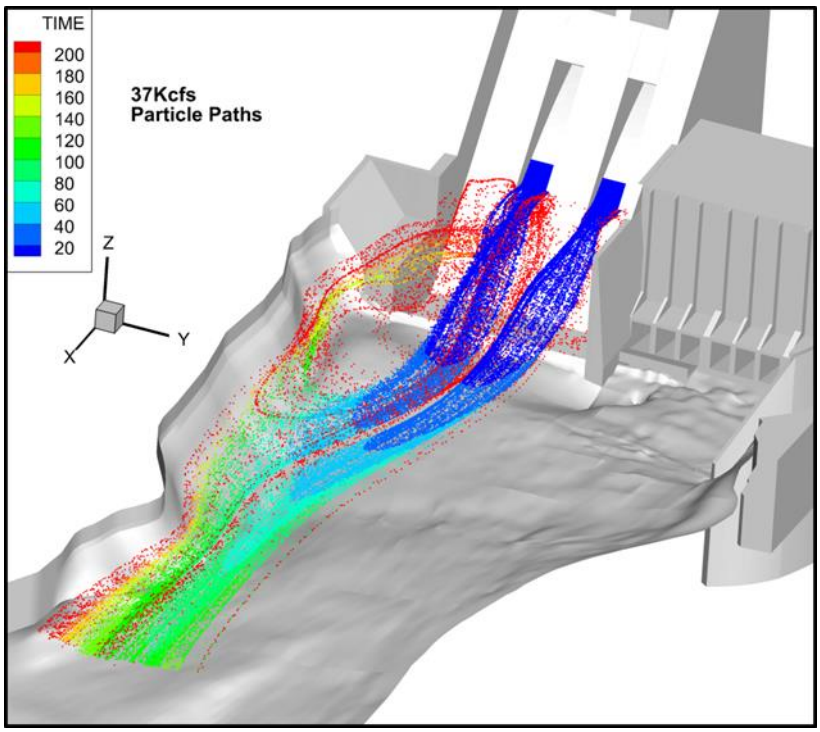

Figure 106. Paths of particles released from the sluices colored by time, in seconds, for 37 Kcfs

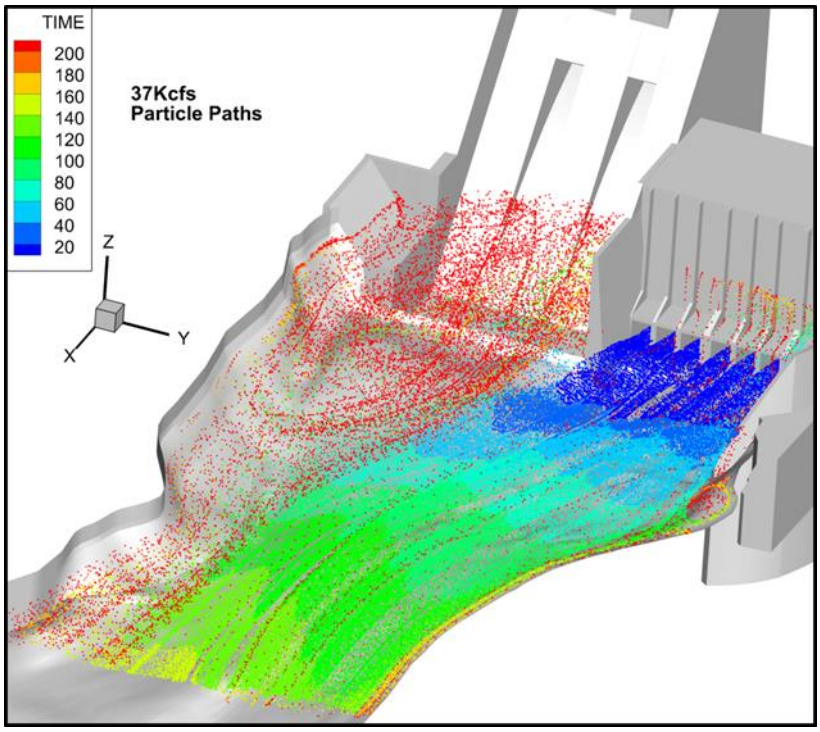

Figure 107. Paths of particles released from the powerhouse colored by time, in seconds, for 37 Kcfs

Figure 108 and Figure 109 show particles released from sluiceways and powerhouse, respectively, for the 45 Kcfs flow condition. Although it was not a common occurrence some particles from sluiceway 2 enter the eastern eddy and were taken back to the stilling basin to rejoin the jet. Particles released from the turbines of the 45 Kcfs flow have a chance to be entrained into the sluiceway region bringing the particles to depth and increasing their residence time.

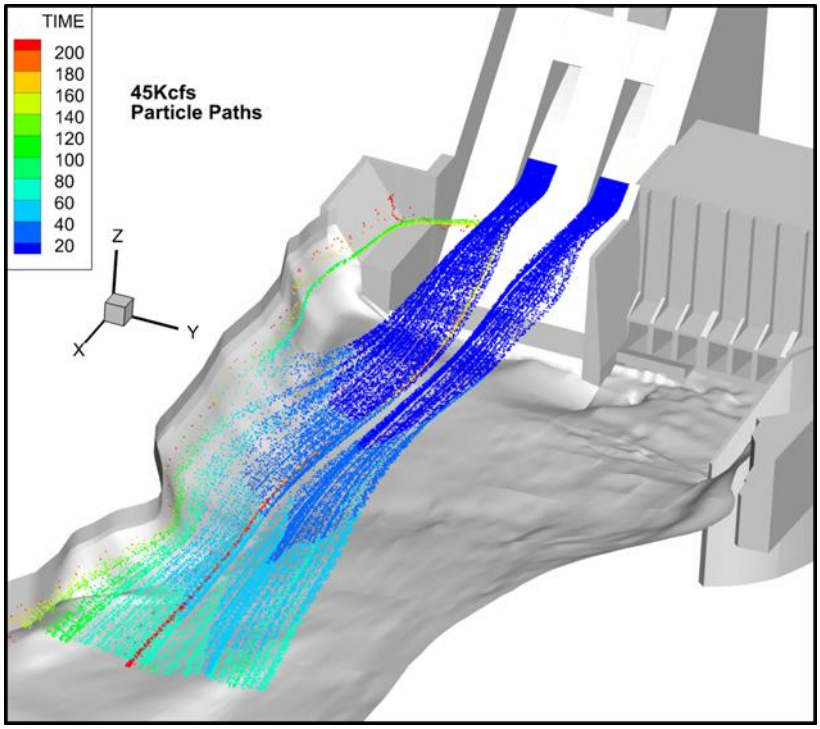

Figure 108. Paths of particles released from the sluices colored by time, in seconds, for 45 Kcfs

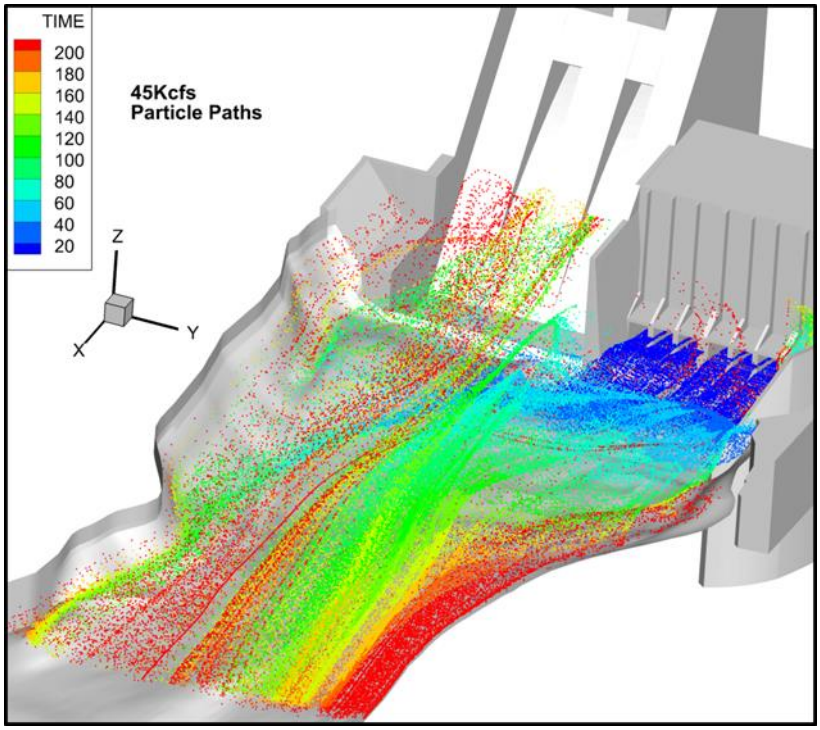

Figure 109. Paths of particles released from the powerhouse colored by time, in seconds, for 45 Kcfs

Figure 110 shows the particles released for the 7Q10 flow from the sluiceways. Particles released from the sluiceways were quickly ejected from the domain; with a small number of particles joining the western eddy and becoming entrained by the jets into the stilling basin. Figure 111 shows the particles released from the powerhouse units. These particles have a generally high residence time with few particles exiting the domain quickly. Most of the particles directly enter the large western eddy and were transported to various regions in the tailrace. However, some particles released from the powerhouse unit 1 were directly entrained in the jet flow and exit the domain quickly.

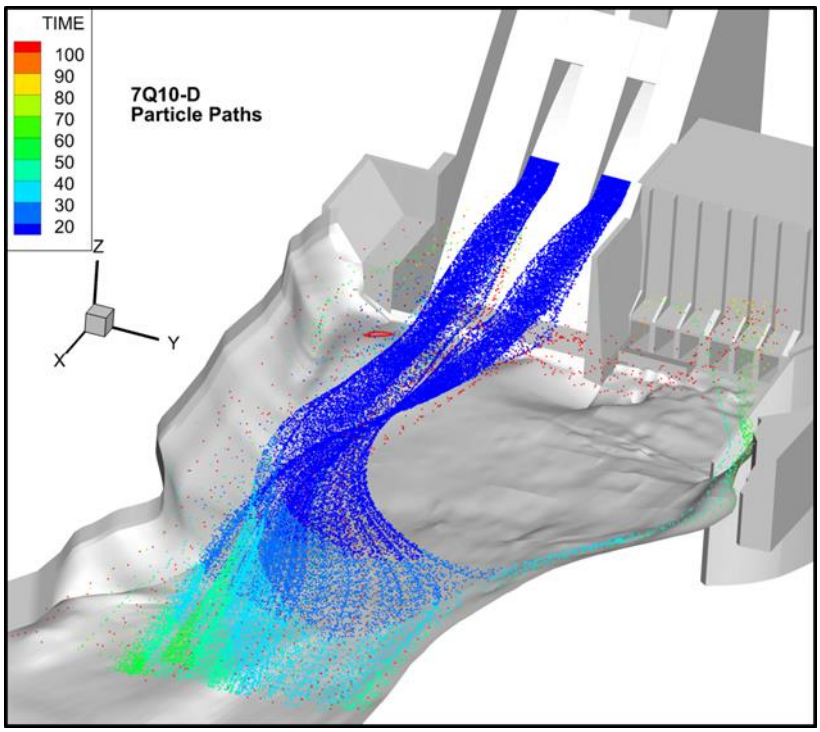

Figure 110. Paths of particles released from the sluices colored by time, in seconds, for a 7Q10 flow with deflectors

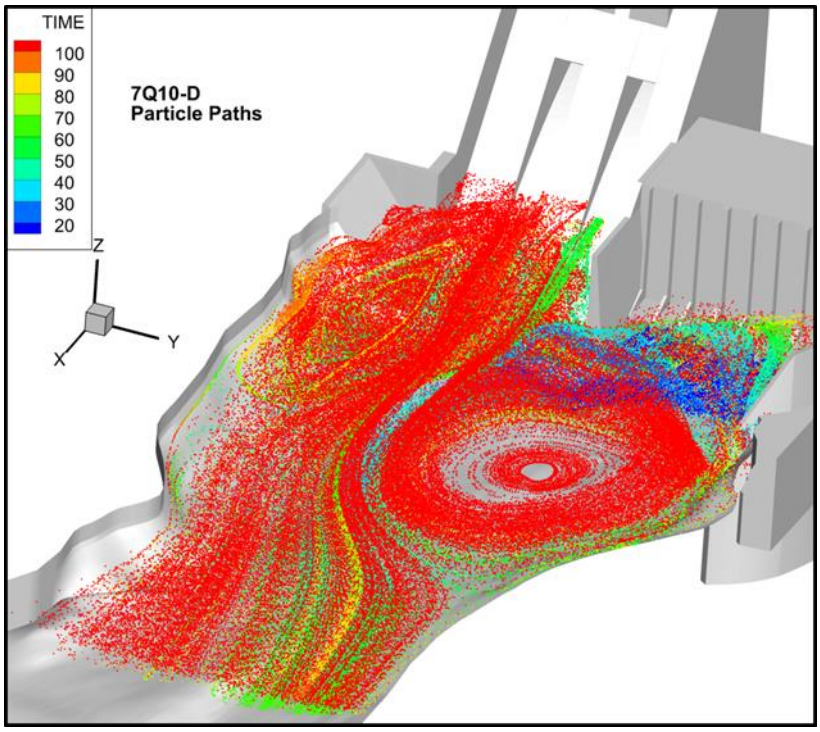

Figure 111. Paths of particles released from the powerhouse colored by time, in seconds, for a 7Q10 flow with deflectors

Particles released from the spillways of the no deflector 7Q10 flow are seen in Figure 112 with the particles released from the powerhouse units in Figure 113. Particles released from the spillways have a chance to be pushed out of the stilling basin and exit the domain in a short time. Other particles were trapped in the back rolls in the stilling basin and take a more significant amount of time to exit the domain. Particles released from the powerhouse draft tubes seem to be distributed around the tailrace in various manners with some entering the stilling basin and other present above the powerhouse units near the free surface. Regardless the path of the particle, the residence time was above 80 seconds. The particles released from both the spillways and the powerhouses show the presence of a small recirculation region east of the fish trap that is not present in the streamlines or vector plots.

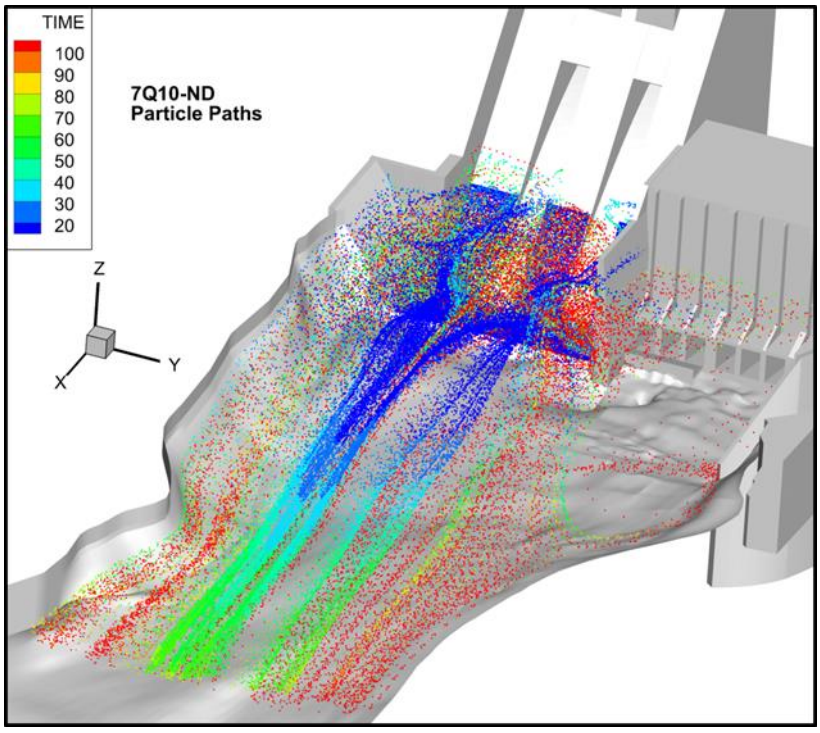

Figure 112. Paths of particles released from the sluices colored by time, in seconds, for a 7Q10 flow without deflectors

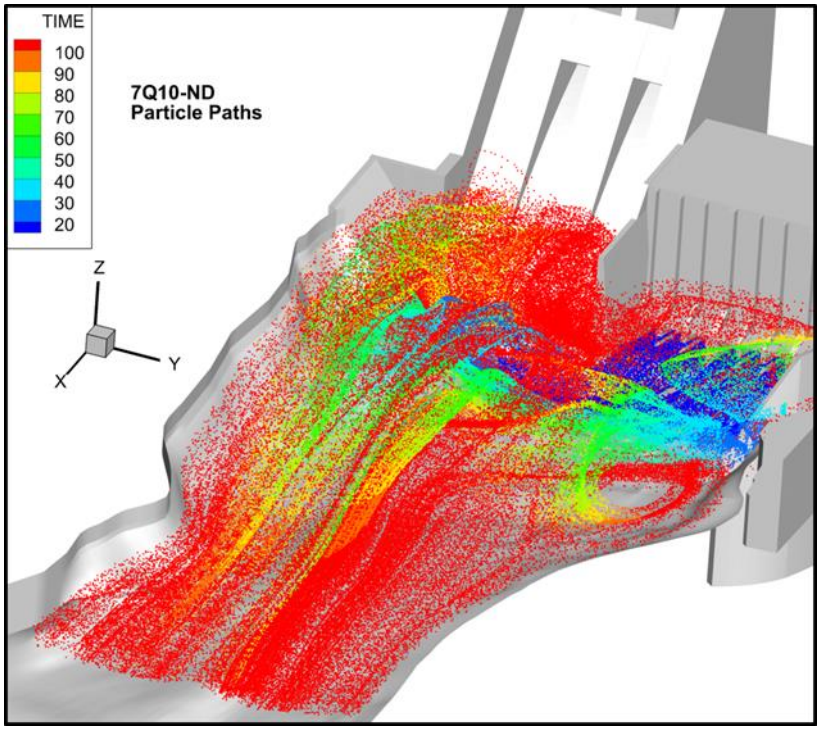

Figure 113. Paths of particles released from the powerhouse colored by time, in seconds, for a 7Q10 flow without deflectors

To more clearly show the residence paths, one particle from each release location is plotted for a given flow condition. Figure 114 shows three particles released into the 37 Kcfs flow domain. The particle released from sluiceway 2 enters the eastern eddy whereas the particle from powerhouse unit 1 and sluiceway 1 tend to a streamwise direction and exit the domain quickly. Figure 115 shows the particles released for the 45 Kcfs flow condition. The 2 particles released from the sluiceways tend to exit the domain directly. However, the particle released from powerhouse unit 1 was affected by entrainment and brought into the eastern eddy and back into the jets.7Q10 flow particles, Figure 116, show particles released from all three locations exiting the domain quickly. The 7Q10 no deflector flow contains 4 particle tracks, one from each of the three sluiceways as well as powerhouse unit 1, shown in Figure 117. Particles released from

spillway 2 and 1, represented by a circle and square respectively, leave the domain quickly and avoid any back rolls or recirculations. The particle released from powerhouse 1 and from spillway 3, a triangle and diamond respectively, were both found caught in a back roll in the stilling basin. The back roll increases the residence time of the particle released from the spillway more so than the particle released from the powerhouse unit.

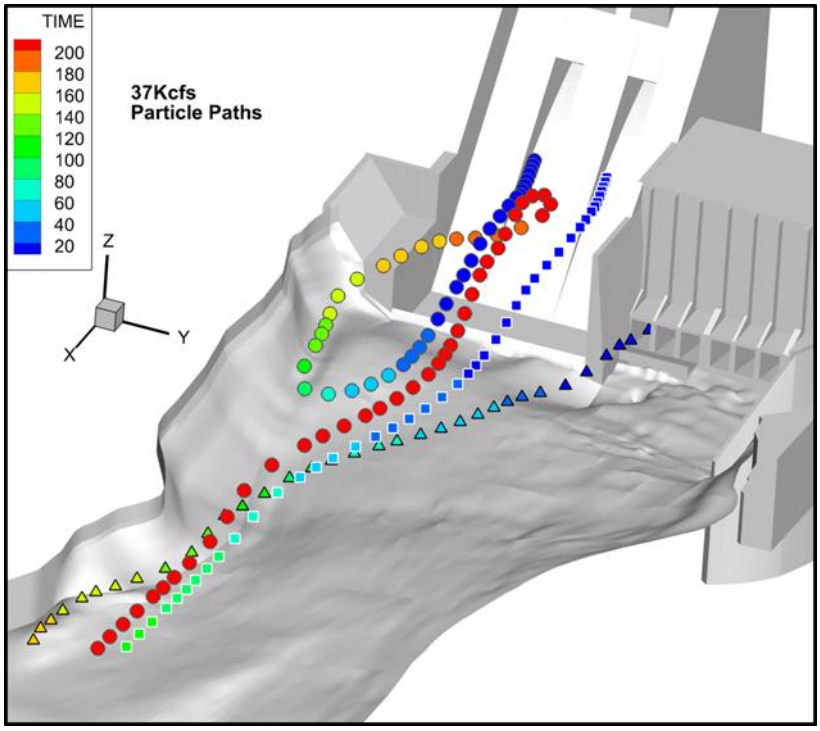

Figure 114. Path of a particle from each injection site colored by time, in seconds, for 37 Kcfs

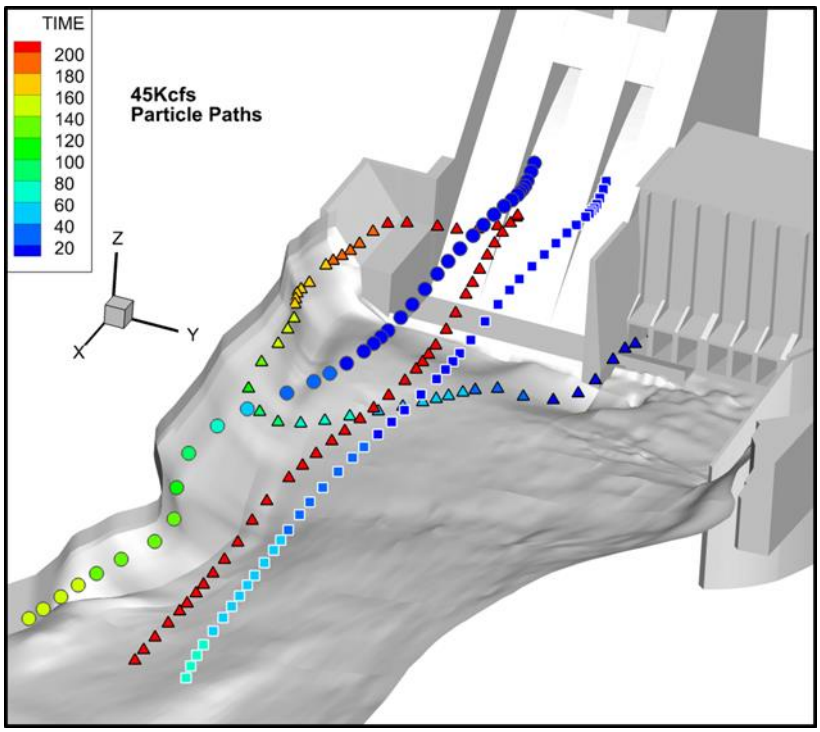

Figure 115. Path of a particle from each injection site colored by time, in seconds, for 45 Kcfs

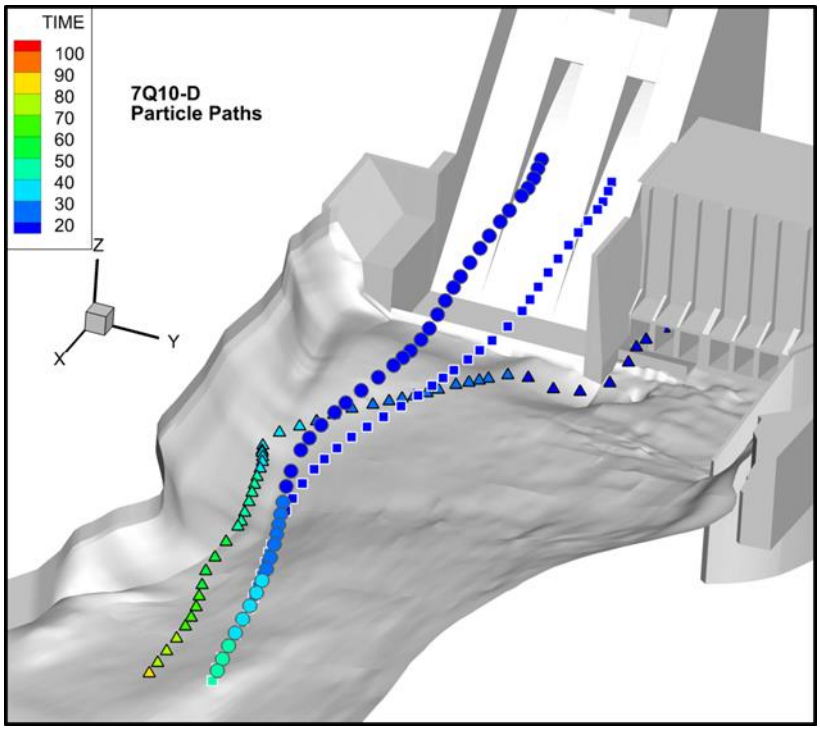

Figure 116. Path of a particle from each injection site colored by time, in seconds, for 7Q10 flow with deflectors

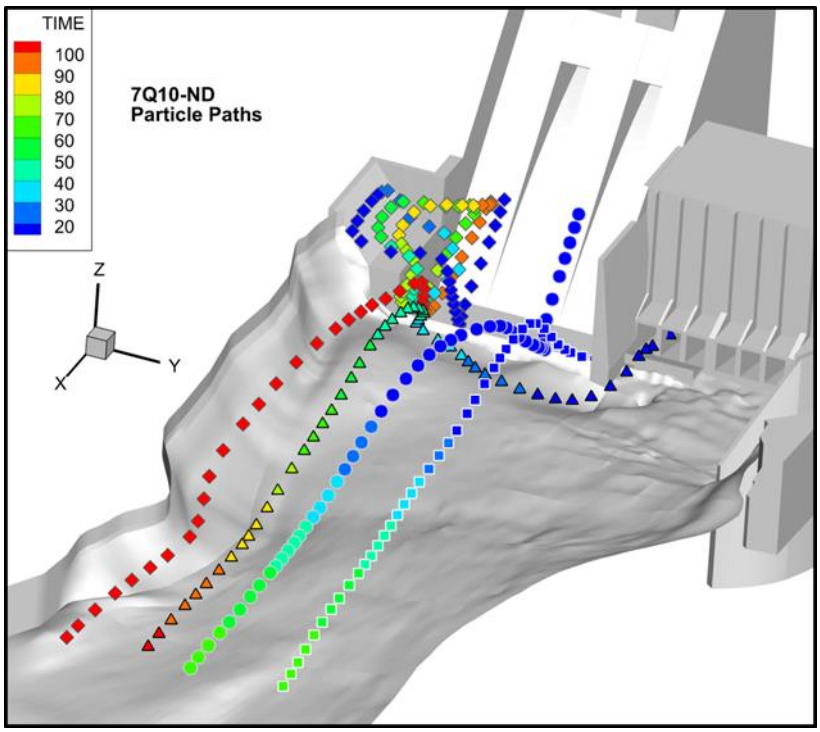

Figure 117. Path of a particle from each injection site colored by time, in seconds, for 7Q10 flow without deflectors

Water Surface Elevation near the Fish trap

Water surface elevations for 37 Kcfs and the 7Q10 simulations are shown in Figure 118. For the 37 Kcfs simulation, water surface elevation was extracted only near the lower fish entrance. As observed earlier for 25 Kcfs and 45 Kcfs, predicted water surface fluctuations were negligible for a 37 Kcfs flow. The amplitude of the waves for the high and low fish entrances in a 7Q10 flow was similar. According to the model, deflectors reduce the generation of high frequency surface waves.

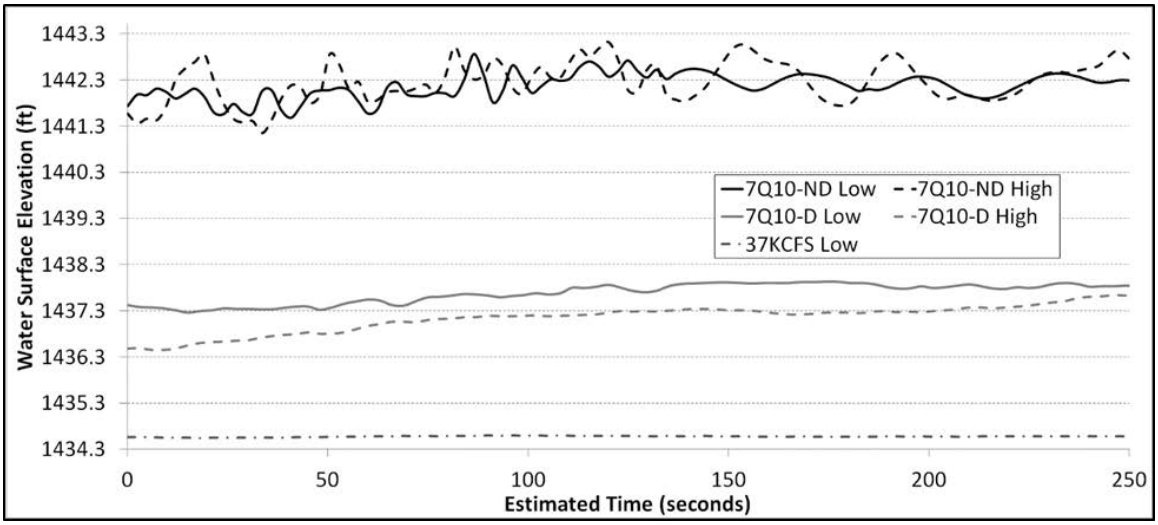

Figure 118. Water surface elevation al the low and high fish trap entrances for a 7Q10 flow

CHAPTER VII
CONCLUSIONS AND FUTURE WORK

Conclusions

A numerical model was developed to evaluate spillway deflector performance and possible fish injury caused by deflectors in Hells Canyon Dam. A mixture two-phase flow model presented in Politano et al. (2009a) was used to simulate the hydrodynamics and TDG field. The model parameters used were a bubble diameter of $0.8\ mm$ and gas volume fraction of 4% in the spillways and sluiceways.

Surface jets and transition to surface jumps were predicted for simulations with total river flow of 25 Kcfs and 45 Kcfs, respectively. For all simulations, the water surface elevation close to the fish trap was not significantly affected by the sluiceway deflectors. Sluiceway 1, closest to the powerhouse, had a jet that showed a slight tendency to plunge. VOF results predicted back-rolls within the stilling basin, being more important downstream of sluiceway 1.

Results show that a negligible amount of bubbles were transported to depth and TDG production was small for all the simulated deflector geometries. Deflector geometries were altered by increasing 1ft in elevation, decreasing 1 ft in length, and increasing the transition radius by 10 ft from a base deflector. The base deflector had an elevation of 1421.6 ft, a length of 16 ft, and a 15 ft transition radius. For the 25 Kcfs flow altering deflector geometries did not generated an appreciable difference in TDG production. In these cases, a recirculation zone was predicted in the eastern region of the tailrace. Altering geometries for the 45 Kcfs case generated distinguishable differences in TDG. The highest TDG production was found for the shortest deflector, 120%; compared to the base case at 117% . A larger deflector transition radius yielded slightly

more TDG production, than the base case, approximately 2% greater. A higher deflector elevation resulted in a recirculation in the eastern region of the tailrace, an undesired flow effect. According to the model, the deflector designed at the 1:48 laboratory scale model was the most appropriate to reduce TDG concentration and avoid negative flow patterns that could affect the operation of the fish trap.

Particle tracking was performed on the VOF solutions to evaluate possible fish injury and it was determined in this thesis to be an inconclusive study. The grid sensitivity analysis did not converge to a value of injury probability with the tested grid densities. Comparatively, particles moving over the sluiceways, with deflectors present, were exposed to higher accelerations than particles moving over the spillways, where deflectors were not present; a difference of 5.6% with a 7Q10 flow. Given this information it is likely that the inclusion of the deflector increases the injury probability although a more comprehensive analysis would be required to have definite results.

Future Work

The present study investigated only the effects of adding a deflector onto the face of the spillway to reduce TDG generation. However, there may be other methods to reduce TDG generation. Increasing the length of the wall that divides the stilling basin and the powerhouse units may decrease the entrainment present in the tailrace. It may also help direct the flow downstream reducing the impairing effects of the large western eddy.

Powerhouse operation in this study was limited from one powerhouse operating full capacity to all three operating full capacity. It may be beneficial to investigate the

tailrace effects of alternative powerhouse operation. More specifically using powerhouse unit 2, the middle powerhouse, as the single fully operating powerhouse unit.

A computationally cost effective method to determine the convergence of fish injury probability could be pursued. Removing the unneeded regions of the computational grid would be a method of reducing the time requirement of performing the increasing higher resolution VOF simulation. Since it was seen that the acceleration is highest just prior to the spillway deflector, a region of super critical flow, it would be possible to eliminated the grid near and including the powerhouse, as well as everything downstream of the stilling basin. If Fluent requires a longer computational domain to converge an easily generated orthogonal mesh could be used to extend the domain. Since the area of focus is located in the supercritical flow upstream, disregarding changes in the bathymetry downstream will not affect the flow and consequently the probability of injury results.

Combining the process for determining TDG and free surface shape would also be worth investigating. This is given much of the time spent on this study was running simulations to determine free surface shape and creating a best fit rigid free surface computational grid from those results. With the combined calculations it would lead to determining results with a more true surface shape, potentially more accurately.

REFERENCES

Antal, S.P., R.T. Lahey Jr., and J.E. Flaherty. 1991. *Analysis of phase distribution in fully developed laminar bubbly two-phase flow*. International Journal of Multiphase Flow. 17(5): 553-682

Carrica, P.M., D. Drew, F. Bonetto, and R.T. Lahey Jr. 1999. "A polydisperse model for bubbly two-phase flow around a surface ship." *International. Journal of Multiphase Flow.* 25: 257-305.

Drew, D.A. and S.L. Passman. 1998. "Theory of Multicomponent Fluids." *Applied Mathematical Sciences,* Springer 135.

Deng, Zhiqun, Gregory Guensch, et al. 2005. *Evaluation of Fish-Injury Mechanisms During Exposure to Turbulent Shear Flow*. Richland: Pacific Northwest National Laboratory, Print/Web. <http://cjfas.nrc.ca>.

Dierking, P. B., and L. J. Weber. 2002. *Hydraulic modeling of Hells Canyon dam for spillway deflector design: Phase one – deflector design*. IIHR.

Fluent, 2001a. "20.3 Mixture Model." Accessed April 10, 2013. http://combust.hit.edu.cn:8080/fluent/Fluent60_help/html/ug/node689.htm.

Fluent, 2001b. "19.2.1 Equations of motion for particles" Accessed April 10, 2013. http://combust.hit.edu.cn:8080/fluent/Fluent60_help/html/ug/node607.htm.

Fluent, 2009. "4.12.2 Standard Wall Functions." Accessed April 30, 2013. https://www.sharcnet.ca/Software/Fluent12/html/th/node99.htm.

Foust, J. M., Stuart Coulson, George E. Hecker, Gregory S. Allen, and Douglas A. Dixon. 2010. "Design considerations for the alden fish friendly hydro turbine." *Hydrovision International*.

Harrison, John. 2013. "Hells Canyon." *Northwest Power and Conservation Council*. Northwest Power and Conservation Council, Accessed Oct 31, 2008. <http://www.nwcouncil.org/history/HellsCanyon>.

Haug P. E. and Weber L.J. 2002. "Hydraulic modeling for Hells Canyon Dam spillway deflector design: phase two – three dimensional model." IIHR LDR 304

"Hells Canyon Dam - Hydroelectric Project Information." 1997. *Columbia Basin Research*. N.p. Accessed March 14, 2013. <http://www.cbr.washington.edu/hydro/hellscanyon>.

EPA. 2012. "Hydroelectricity." *EPA:U.S. Environmental Protection Agency*. U.S. Environmental Protection Agency. Web. Accessed Mar 11, 2013. <http://www.epa.gov/cleanenergy/energy-and-you/affect/hydro.html>.

Kolosseus, Andrew. 2009. "Evaluation of the 115 Percent Total Dissolved Gas Forebay Requirement for the Columbia and Snake Rivers." *Washington Department of Ecology, Water Quality Program*. Accessed April 10, 2013. http://www.ecy.wa.gov/programs/wq/tmdl/ColumbiaRvr/AMTfaqTDG.pdf.

Lane, G.L., M.P. Schwarz, and G.M. Evans. 2005. "Numerical modeling of gas-liquid flow in stirred tanks." *Chemical Engineering Science*. 60: 2203–2214.

Lopez de Bertodano, M.L., R.T. Lahey Jr, and O.C. Jones. 1994. "Development of a model for bubbly two-phase flow." *Journal of Fluids Engineering.* 116: 128-134.

Meyers, Theodore, Tamara Burton, Collette Bentz, and Norman Starkey. 2008. "Common Diseases of Wild and Cultured Fishes in Alaska." *Anchorage: Fish Pathology Laboratories*. <http://www.adfg.alaska.gov/static/species/disease/pdfs/fish_disease_book.pdf>.

NPARC, 2002. "Conducting & Reporting CFD Analyses." lecture., NASA. www.grc.nasa.gov/WWW/wind/class2002/Reporting.ppt.

Neitzel, D.A., Richmond M.C., Dauble D.D., Mueller R.P., Moursund R.A, Abernethy C.S., Guensch G.R., and Čada G.F.. 2000. "Laboratory studies on the effects of shear on fish: final report." U.S. Department of Energy, Idaho.

Neitzel D.A., Dauble D.D., Čada G.F., Richmond M.C., Guensch G.R., Mueller R.P., Abernethy C.S. and Amidan B. 2004. Survival estimates for juvenile fish subjected to a laboratory-generated shear environment. *Transactions of the American Fisheries Society* 133:447-454.

Orlins, J.J. and J.S. Gulliver *Dissolved Gas Supersaturation Downstream of a Spillway: Computational Model* Journal of Hydraulic Research (2000), 38(2), 151-159.

Oxbow Fish Hatchery Idaho Fish and Game. Idaho Department of Fish and Game, 24 May 2012. Web. 15 Mar 2013. <http://fishandgame.idaho.gov/public/fish/?getPage=101>.

Paul B., Dierking, and Weber Larry J. 2001. "Hydraulic Modeling of Hells Canyon Dam for Spillway Deflector Design." *Iowa Institute of Hydralics Research*, 30-33,40.

Politano, M.S., P.M. Carrica, C. Turan, and L. Weber. 2007. "A multidimensional two-phase flow model for the total dissolved gas downstream of spillways." *Journal of Hydraulic Research* 45(2): 165-177.

Politano, M.S., P.M. Carrica, and L. Weber. 2009a. “A Multiphase Model for the Hydrodynamics and Total Dissolved Gas in Tailraces.” *International Journal of Mutliphase Flow*. 35.: 1038-1040. Print.

Politano, M.S., A.A. Arenas, and L. Weber. 2009b. “An investigation into the TDG dynamics of the Wells project.” FERC Report No 2149.

Politano, M.S., A.A. Arenas, and Y. Wang. 2010. “Hells Canyon Total Dissolved Gas Modeling.” *IIHR Hydroscience and Engineering*. 8-9. Print.

Turan, C., M.S. Politano, P.M. Carrica, and L. Weber. 2007. "Water Entrainment Due to Spillway Surface Jets." *International Journal of Computational Fluid Dynamics*. 137-153.

Urban, A.L., J.S. Gulliver, and D.W. Johnson. 2008. "Modeling Total Dissolved Gas Concentration Downstream of Spillways." *Journal of Hydralic Engineering*. 550-552. Print.

Weitkamp, Don. 2008. “Total Dissovled Gas Supersaturation Biological Effects” *Parametrix*, http://www.ecy.wa.gov/programs/wq/tmdl/ColumbiaRvr/062308mtg/TDGeffectsLitRev080615.pdf.